MEASUREMENT OF TRANSVERSE SPIN ASYMMETRIES IN POLARIZED PROTON-PROTON COLLISIONS, AND THE REALIZATION OF NEW ELECTROMAGNETIC CALORIMETERS FOR FORWARD PHYSICS

BY

JOHN KOSTER

DISSERTATION

Submitted in partial fulfillment of the requirements
for the degree of Doctor of Philosophy in Physics
in the Graduate College of the
University of Illinois at Urbana-Champaign, 2010

Urbana, Illinois

Doctoral Committee:

Professor Jen-Chieh Peng, Chair
Associate Professor Matthias Große Perdekamp, Director of Research
Professor Laura Greene
Professor John Stack

Abstract

Single transverse spin asymmetries in polarized proton-proton collisions, A_N, are extracted at mid-rapidity and at forward-rapidity. The forward-rapidity data is acquired with a pair of electromagnetic calorimeters which were built as part of the thesis. All aspects of the calorimeters from design to data analysis are discussed. The calorimeters are used to measure non-zero asymmetries at forward-rapidity. The measurements extend to higher p_T than previously measured. The data for p_T >3 GeV/c are consistent with a $1/p_T$ falloff. A constant asymmetry at high p_T is excluded at the two sigma level. At mid-rapidity, precision asymmetries for neutral pions and η mesons are measured. These asymmetries are consistent with zero, and are expected to place bounds on the gluon Sivers function. Lastly, an exploratory double transverse spin asymmetry, A_{TT}, measurement is carried out using coincidences between the two forward calorimeters.

Acknowledgments

Many people have encouraged and supported this work. An accurate accounting of the acknowledgments would include at least entire PHENIX collaboration and stretch for several pages. With this caveat, I will acknowledge a subset:

My advisor Matthias Große Perdekamp and my unofficial co-advisor Mickey Chiu. Working closely with both of them has been a fantastic and educational experience. Matthias' infectious enthusiasm has been a great motivator. I have learned a lot from him on heavy ion physics to wire chambers. Mickey and I have been working together since nearly my start in Matthias' group. I learned a great deal from his systematic and logical approach to hardware and analysis work.

The main work of the thesis has been to upgrade PHENIX for the measurements of this thesis. On the hardware side of this upgrade, many people contributed: Terry Awes, Mickey Chiu, Frank Ellinghaus, Oleg Eyser, Matthias Große Perdekamp, John Haggerty, David Kawall, Andrey Kazantsev, David Layton[1], Nathan Means[1], Ed O'Brien, Kenneth Sedgwick, Toru Sugitate, Aaron Veicht[1], Cole Watts, Ryan Wright and Chun Zhang. The technical and engineering staff deserve special praise for building and installing a detector on a timescale of six months. From NPL: John Blackburn, Penny Sigler and Eric Thorsland. From PHENIX/Brookhaven National Laboratory: Jimmy LaBounty, Carter Biggs, Steven Boose, Paul Giannotti, Matthias Große Perdekamp, Kenny Jones, Michael Lenz, Don Lynch, Salvatore Marino, Salvatore Polizzo, Richard Ruggiero, Frank Toldo and John Tradeski. On the calibration/analysis side of the upgrade: Mickey Chiu, Kwang-Bok Lee, Beau Meredith, Chris Pinkenburg, Aaron Veicht, Anselm Vossen, Scott Wolin and Ruizhe Yang have been extremely important.

Lastly, I thank my friends - many of whom are mentioned above - and family. Their support and collaboration are very important to me and to this work.

[1] Team Zero

Table of Contents

Chapter 1

Introduction

Early β decay experiments are some of the first experiments in the field of nuclear and particle physics. The theoretical and experimental understanding of the decay: $n \rightarrow p + e^- + \bar{\nu}_e$, advanced quite far before the discovery of parity violation in the weak interaction. The experiment, proposed by T.D. Lee and C.N. Yang[1] and carried out by Wu[2], uses a *polarized* cobalt-60 source to show that the electrons are emitted preferentially with respect to the polarization direction. Until that time, parity had been considered a fundamental symmetry of nature and had been tested by experiments sensitive to either the electromagnetic and strong interactions, but not to the weak interaction.

At present an experimental and theoretical program has shown that Quantum Chromodynamics (QCD) successfully describes a wide variety of physical systems. Together, they have revealed a great deal about the structure of hadrons. As with the early work on β decay, the bulk of experiments have not employed spin. While none of the spin-dependent experiments have cast doubt on the theory, there are many as-of-yet unexplained results. This introduction discusses the production of hadrons from the collision between two polarized protons. The spins can be averaged over to produce a spin-averaged cross-section, and this is discussed first. At high enough p_T and center-of-mass energy, pQCD agrees well with experiment. Since pQCD agrees well with the spin summed cross-section, it is natural to apply it to the study of the difference of cross-sections between different proton spin-states. The next two sections review some of the work with longitudinally polarized beams and with transversely polarized beams. Hadron production from transversely polarized beams is the focus of this thesis. This topic has generated a great deal of recent interest. Large and surprising spin effects have been measured which are challenging theoretical interpretation.

1.1 Applying Perturbative QCD to Proton-Proton Collisions

1.1.1 Unpolarized Proton Structure

The inclusive production of a hadron from the collision between two protons, A and B, is characterized by the center of mass energy of the $p+p$ system, $\sqrt{s}$, and the four-momentum of the produced hadron. Various quantities used to measure the hadron, h, are:

E, p_X, p_Y, p_Z	The hadron four momentum, where p_Z is parallel and $p_{X,Y}$ are perpendicular to the initial proton momenta.
ϕ	The azimuthal angle of the hadron around the beam axis.
x_F	$p_z/p_{z(max)}$, where $p_{z(max)}$ is the maximum momenta along the z-direction.
p_T	$\sqrt{p_x^2 + p_y^2}$, the total transverse momenta.
θ	$tan(\theta) = p_T/p_Z$, the polar angle measured from the beampipe.
η	$-ln(tan(\theta/2))$, referred to as pseudorapidity. Approximates the boost-invariant quantity rapidity at high energies. Equals 0 for hadrons produced perpendicular to the beams (mid-rapidity) and increases in magnitude to ± infinity for angles parallel to the incoming protons (forward/backward rapidity).

The cross-section for the collision between two high energy protons producing a high p_T hadron can be written as:

$$E\frac{d^3\sigma_{A+B\to h}}{d^3p} = \Sigma_{abc}\int dx_1 f_a(x_1)\int dx_2 f_b(x_2)\int \frac{dz}{z}\left(E_c\frac{d^3\sigma^{a+b\to c+X}}{d^3p_c}\right)\frac{D_{c\to h}(z)}{z} \tag{1.1}$$

at leading order and twist in a collinear picture where:

a, b	Flavor of colliding partons, i.e. quarks or gluons.
c	Flavor of one of the fragmenting final state partons.
$x_{1,2}$	Fraction of the proton momenta carried by each parton.
z	Fraction of the scattered quark momenta carried by the observed hadron.
$f_a(x)$	Number density of finding a parton of identity a and momentum fraction x.
$D_{c\to h}(z)$	Fragmentation probability function of producing a hadron, h, from a parton of type c.

Expressing the cross-section in such a form makes use of several theoretical assumptions. The first is factorization. Factorization separates the cross-section into hard and soft parts. The hard part ($E_c\frac{d^3\sigma_{a+b\to c}}{d^3p_c}$) is calculable in pQCD. The soft parts ($f_a(x)$ and $D_{c\to h}(z)$) are not calculable and must be measured. The measurement of the cross-section's soft parts involves the second assumption referred to as universality. Similar factorized cross-sections can be constructed for other processes such as Deep Inelastic Scattering ($e(\mu) + p(d, He^3, etc) \to e(\mu) + X$, known as DIS) or electron positron annihilation ($e^+ + e^- \to h + X$). Universality states that the soft parts, parton distribution functions and hadron fragmentation functions, of the factorized cross-section are the same in $p + p$ collisions, DIS or $e^+ + e^-$ annihilation. The present understanding of the proton's unpolarized structure is based on a global analysis of all the world data in high energy collisions of $p + p$, DIS and $e^+ + e^-$ annihilation. Current parametrization of the parton distribution functions are shown in figure 1.1. The major pattern is the dominance of valence quark distributions at high

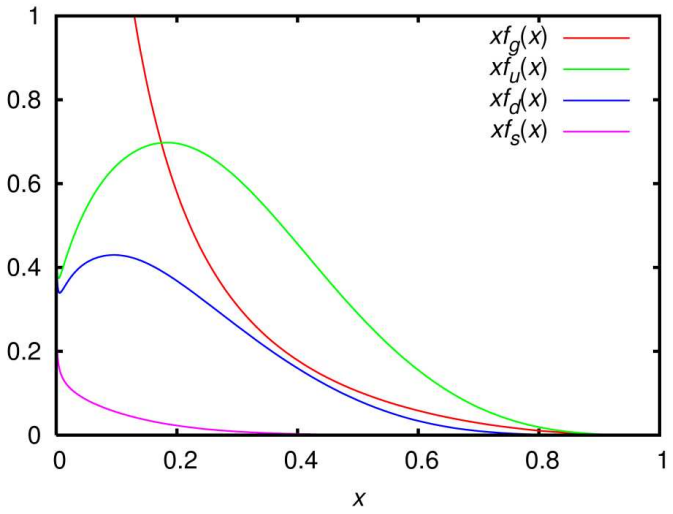

Figure 1.1: Unpolarized parton distribution functions from the CTEQ Collaboration[3].

x and the gluon distribution at low x. The determination of parton distribution functions are dominated by the DIS data, and at high x by Drell-Yan experiments.

After the soft components of equation 1.1 have been measured, it is possible to use pQCD to predict the cross-sections for a wide variety of phenomena. Figure 1.2 shows a comparison between theory and experiment for the case of inclusive hadron production from proton-proton collisions at different center of mass energies.

The good agreement between the theoretical predictions and the experimental data for $\sqrt{s}$ $\geq$62 GeV indicates that the framework of perturbative QCD, factorization and universality describes the production of hadrons at high p_T. To gain insight into the underlying kinematics of quarks and gluons, a leading order Monte-Carlo simulation of $p+p$ collisions called Pythia[6] is used. The simulation is used to estimate how the hadron samples the underlying sub-processes (quark-quark, quark-gluon, or gluon-gluon) and $x_{1,2}$ distributions. Similar studies are also possible using more sophisticated theoretical techniques. The study is done using the two scattering angles measured in this thesis. It is possible to tune Pythia to match experimental observables. The tuning and details of the simulation are described in section 8.3.

The results of the Pythia study are shown in figure 1.3. The figure shows that mid-rapidity production, by virtue of its symmetry around $\eta = 0$, has identical distributions of x_1 and x_2. Production at low p_T is dominated by gluon-gluon scattering. As p_T increases, quark scattering begins to dominate. In contrast to mid-rapidity, at forward rapidity the distributions are asymmetric between x_1 and x_2. This corresponds to a high momentum parton scattering against a low momentum parton. The reach in x_2 at the forward region extends below the range accessible at mid-rapidity. Forward hadron production is dominated by quark-gluon

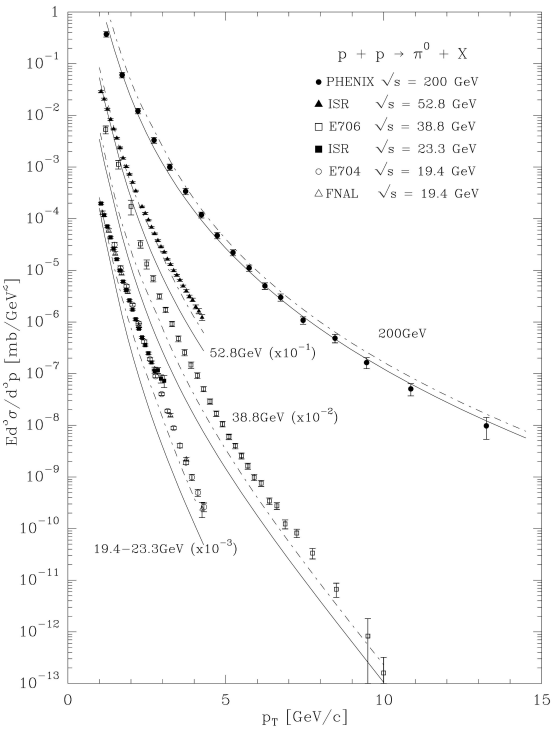

(a) Theoretical predictions calculated at next-to-leading order (NLO). Figure taken from reference [4].

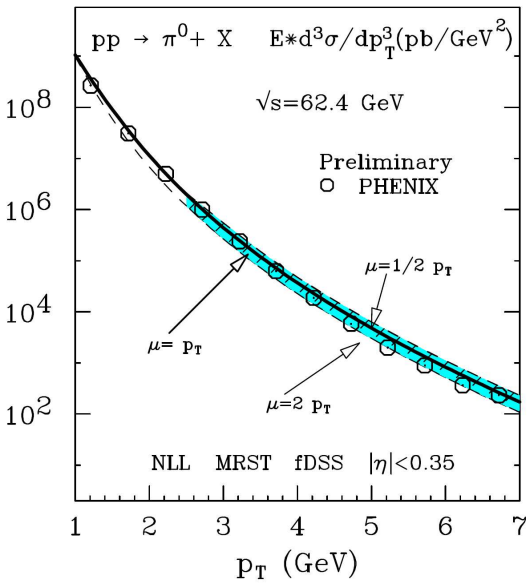

(b) Theoretical predictions calculated at next-to-leading order and with next-to-leading logarithm (NLL) accuracy. Figure taken from reference [5].

Figure 1.2: Comparison between experimental inclusive π^0 cross-sections for p+p collisions at different center of mass energies at mid-rapidity compared to pQCD calculated predictions. Good agreement between data and NLO pQCD is found for $\sqrt{s} \geq 62$ GeV.

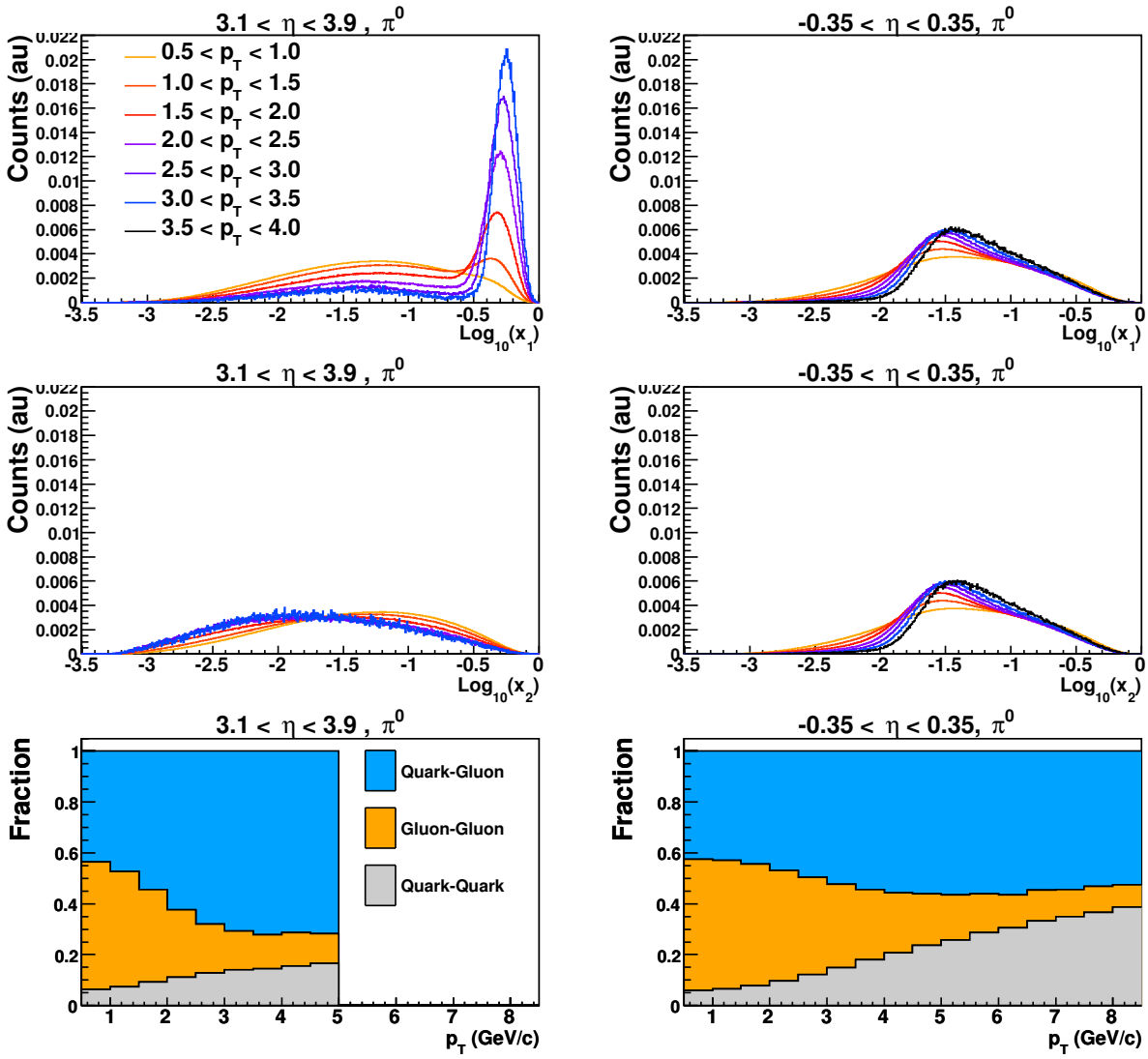

Figure 1.3: Results from a Pythia simulation of proton+proton collisions. The distribution of x_1 and x_2 are shown for the production of π^0's in the experimentally accessible region of PHENIX. The top and middle panels show the distribution of x_1 and x_2 in bins of $p_T^{\pi^0}$. Each distribution is normalized to one. The bottom panel shows the fraction of events originating from either quark-quark, gluon-gluon or quark-gluon scattering. The role of other types of processes are demonstrated in section 8.3 of the thesis.

scattering which follows from the relative sizes of the quark and gluon distributions at low and high x shown in figure 1.1.

1.1.2 Proton Helicity Structure

When colliding longitudinally polarized protons, single and double spin asymmetries can be constructed, A_L and A_{LL}, which are defined as:

$$A_L = \frac{\sigma^{+,\circ} - \sigma^{-,\circ}}{\sigma^{+,\circ} + \sigma^{-,\circ}} \quad A_{LL} = \frac{\sigma^{+,+} - \sigma^{+,-}}{\sigma^{+,+} + \sigma^{+,-}} \tag{1.2}$$

where +, - and $\circ$ denote the protons with either positive helicity, negative helicity or are unpolarized. A_L is parity violating. Using a leading order treatment the double spin asymmetry is equal to:

$$E\frac{\Delta d^3\sigma_{A+B\to h}}{d^3p} = \Sigma_{abc}\int dx_1 \Delta f_a(x_1)\int dx_2 \Delta f_b(x_2)\int \frac{dz}{z}\left(E_c\frac{d^3\Delta\sigma_{LL}^{a+b\to c}}{d^3p_c}\right)\frac{D_{c\to h}(z)}{z} \tag{1.3}$$

where $\Delta f_a(x) = f_a^{++}(x) - f_a^{+-}(x)$ is the helicity difference between the probabilities densities to find partons polarized parallel $(++)$ versus anti-parallel $(+-)$ with the parent proton spin, and $E_c\frac{d^3\Delta\sigma_{LL}^{a+b\to c}}{d^3p_c}$ is the partonic double spin asymmetry calculable in pQCD. Like the unpolarized distribution functions, the helicity distribution functions are determined by global analyses[7, 8, 9, 10, 11]. Results from the DSSV collaboration's analysis[11] are shown in figure 1.4.

The main features of the distributions are:

- Up and down quark distributions are known with good precision. Their determination is dominated by data from lepton scattering experiments.
- Gluon distribution appears small but has large uncertainties. The determination of the gluon distributions are dominated by inclusive probes at RHIC. The data constraints $\Delta G(x)$ in a range of $0.05 \leq x \leq 0.2$. Continued measurements at a variety of energies and with di-jets will further constrain the helicity distribution to smaller x.
- The sea quark distributions are poorly constrained. The upcoming $A_L^{W^\pm}$ program at RHIC will help to determine these distributions.

1.1.3 Transverse Proton Spin Structure

When colliding a transversely polarized proton beam with an unpolarized proton beam, the spin-direction makes it possible to measure azimuthal asymmetries with respect to the spin-direction of the polarized

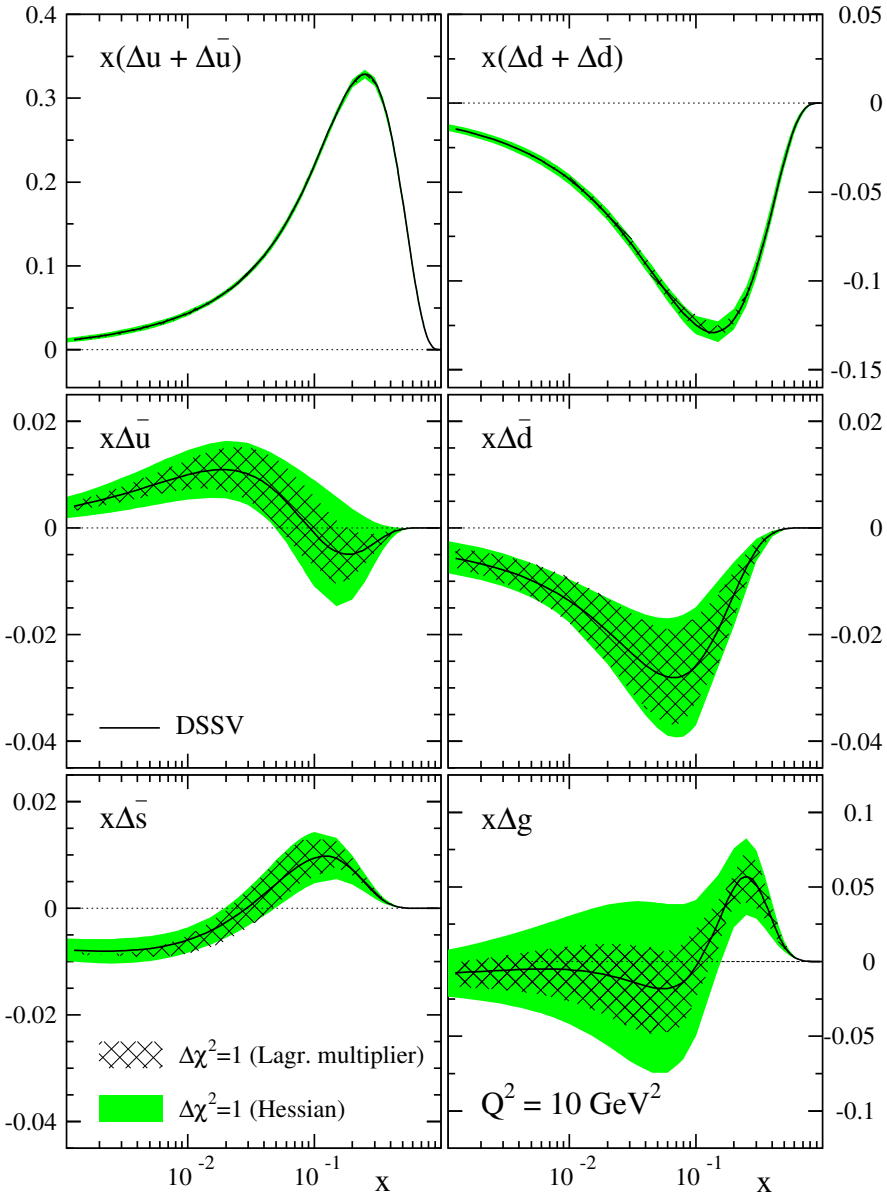

Figure 1.4: Quark and gluon helicity distribution functions from the DSSV collaboration (figure taken from reference [11]). The green bands represent experimental uncertainties propagated through the theoretical fitting analysis.

proton beam. This asymmetry is denoted as A_N and is given as:

$$A_N = \frac{\sigma^{\uparrow} - \sigma^{\downarrow}}{\sigma^{\uparrow} + \sigma^{\downarrow}} \tag{1.4}$$

In the framework of pQCD, this asymmetry was expected to be small at high p_T[12]. Early experiments date back to the 1970's[13, 14, 15, 16, 17], but they were carried out at an energy below the level for which pQCD has successfully predicted the unpolarized cross-sections. The E704 collaboration continued the measurement of A_N to higher center of mass energies ($\sqrt{s}$=19.4 GeV), and found that, surprisingly, the asymmetries persisted[18, 19, 20, 21, 22, 23, 24, 25]. More recently and at even higher center of mass energies the STAR, BRAHMS and PHENIX collaborations measured these asymmetries and found that the asymmetry magnitude and general behavior does not change. This is surprising since figure 1.1 shows that pQCD fails to describe hadron production for low $\sqrt{s}$, but succeeds at high $\sqrt{s}$. The asymmetries measured by the four collaborations are shown in figure 1.5. The major features of the asymmetries are:

- Little dependence on the center of mass energy of the system (figures 1.5(a) and 1.5(b))
- At mid-rapidity the asymmetries are consistent with zero (figure 1.5(b)) while at forward-rapidity the asymmetries are non-zero and increase in magnitude with x_F (figure 1.5(c)). The difference can be explained by the difference in sub-process fractions and mean kinematics between hadrons produced at mid- and forward-rapidity (figure 1.3).
- The magnitude and sign of the forward-asymmetry depends on the charge of the pion (figure 1.5(c)). This pattern is consistent with the measurements at lower center of mass energies.

At present, two theoretical approaches are under active research to explain the origin of single spin asymmetries:

1. Transverse momentum distributions (TMD) which include transverse momentum dependence to the distribution functions of equation 1.1. This approach goes beyond collinear factorization.
   - $f_{1T}^{\perp a}(x, k_T) D_{c\to h}(z)$ correlates the proton transverse spin with the parton transverse momentum (k_T). This effect introduces k_T in the initial state. This function is commonly referred to as the Sivers function and was first proposed in 1990[31].
   - $\delta f_a(x) \cdot H_1^{\perp}(z, p_T)$ This effect introduces a spin-dependent parton distribution function $\delta f_a(x)$ called transversity. This distribution is similar to the helicity distribution but for transversely polarized quarks and protons. It can then couple to a spin-dependent fragmentation function $H_1^{\perp}(z, p_T)$ which introduces a correlation between the transverse quark spin and the hadron

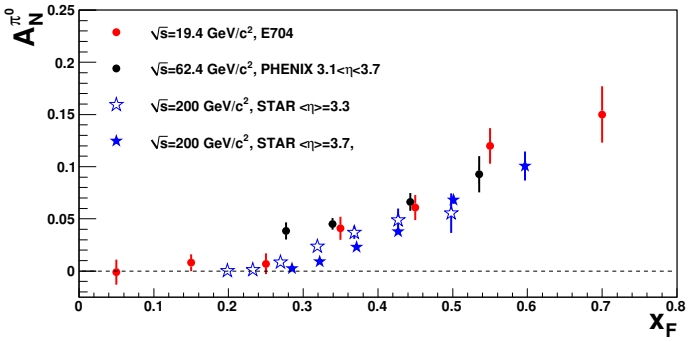

(a) A_N for neutral pion production for $p+p$ at $\sqrt{s}$=19.4, 62.4 and 200 GeV/c^2 from the E704[22], PHENIX[26, 27] and STAR[28] collaborations at forward rapidity.

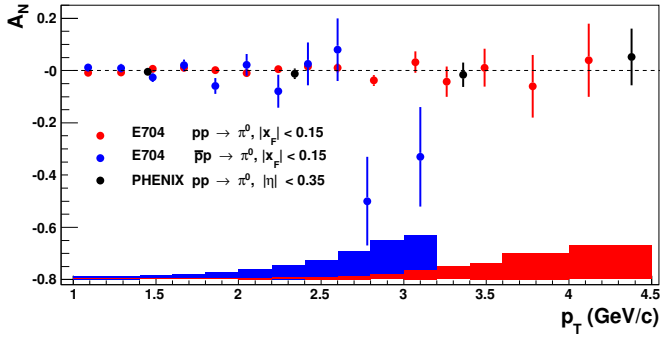

(b) A_N for neutral pion production at $\sqrt{s}$=19.4 and 200 GeV/c^2 from E704[23] and PHENIX[29] at mid-rapidity. The χ^2/NDF to $A_N = 0$ are: 11.1 / 15 for the E704 pp results, 12.2 / 11 for the E704 $\bar{p}p$ results, and 0.877 / 4 for the PHENIX pp results. The total error for each point is calculated as the statistical and systematic errors summed in quadrature.

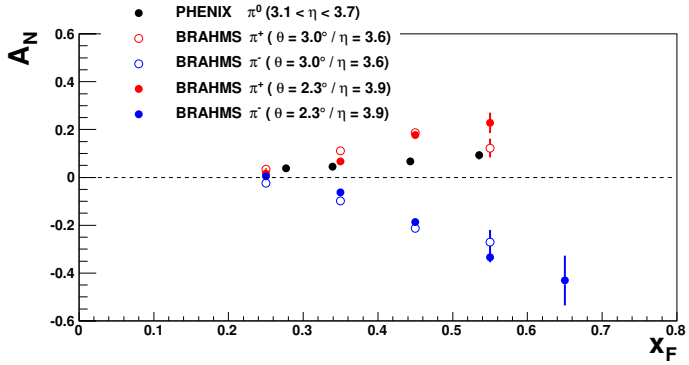

(c) A_N for charged and neutral pion production for $p+p$ at $\sqrt{s}$ = 62.4 GeV/c^2 from the BRAHMS[30] and PHENIX collaborations[26, 27]

Figure 1.5: A_N for $p+p^{\uparrow} \rightarrow h+X$ at various center of mass energies as a function of p_T and x_F.

momentum transverse to the quark momentum, p_T. This fragmentation function is commonly referred to as the Collins Function and was first proposed in 1993[32]. This effect introduces a transverse momentum effect in the fragmentation. Since the overall effect relies on the convolution of two functions, if either function is proved to be zero then the magnitude of the other is unimportant with regards to spin-dependent hadron production. The Collins fragmentation function has been recently measured to be large and non-zero in $e^+ + e^-$ collisions[33].

2. Collinear twist-3 quark-gluon correlation functions in either the initial or final state. The idea that the asymmetries may originate from twist-3 rather than leading twist contributions was first proposed in references [34, 35]. Subsequently, the idea was developed as an initial state[36] and final state[37] effect. The combined asymmetry difference, $\Delta\sigma$, between spin up and down is given in reference [38] as:

$$\begin{aligned}\Delta\sigma = G^{(3)}(x_1, x_2) \otimes f(x') \otimes D(z) \otimes \hat{\sigma}_A \\ + h(x) \otimes f(x') \otimes \hat{E}^{(3)}(z_1, z_2) \otimes \hat{\sigma}_B \\ + h(x) \otimes E^{(3)}(x_1', x_2') \otimes D(z) \otimes \hat{\sigma}_C\end{aligned} \tag{1.5}$$

where:

- f(x) and D(z) are the unpolarized parton distribution and fragmentation functions introduced in equation 1.1.
- $\delta q(x)$ is the transversity distribution.
- $G^{(3)}(x_1, x_2)$ twist-3 distribution function for the polarized proton.
- $E^{(3)}(x_1', x_2')$ twist-3 distribution function for the unpolarized proton.
- $\hat{E}^{(3)}(z_1, z_2)$ twist-3 fragmentation function for the final hadron.

In the kinematic regime where they both are valid, the Sivers function and the higher twist correlation functions have been proven to produce consistent results[39]. At high p_T only the twist-3 is valid. It is in the twist-3 framework that a $1/p_T$ falloff for A_N is expected[36]. Phenomenological studies using both approaches have been successful at describing existing data. Examples from both sets of approaches are shown in figure 1.6. At present, on the theoretical side, phenomenological studies of the asymmetries are an active area of research. To determine the various functions, the existing measurements are being pushed to higher or lower energies and with greater precision. In addition, experiments at DESY, CERN, Jefferson

Laboratory, and KEK not discussed in the thesis are using Semi-Inclusive Deep Inelastic Scattering, Drell-Yan production and electron positron annihilation to isolate each of these effects and others.

1.2 Motivation to Build Forward Calorimeter

I have played a leading role in the design, construction, installation, running, calibration and analysis of a pair of forward electromagnetic calorimeters called the Muon Piston Calorimeter (MPC). This section describes the physics which motivate the upgrade.

1.2.1 Transverse Spin Physics

A forward calorimeter, not only gives access to testing the p_T dependence of the $A^{\pi^0_N}$ as was discussed previously, it also allows the possibility to study the $\sqrt{s}$ dependence of the asymmetry over a wide range of energy. The $A_N^{\pi^0}$ at $\sqrt{s}$=62 GeV data from figure 1.5(c) was collected in 2006 using the MPC. For more information on the analysis see references [27] and [26].

1.2.2 Longitudinal Spin Physics

A comparison between the single transverse spin asymmetries at mid and forward rapidity demonstrate that the sub-processes and parton momentum fractions are dramatically different between the two regions. The forward region is dominated by one high momentum parton colliding with a low momentum parton. This type of kinematic selection naturally leads to quark-gluon scattering because of the unpolarized distribution functions. Therefore, a measurement of A_{LL} in the MPC will be naively be dominated by $\Delta q(x_1) \cdot \Delta g(x_2)$ where the integral over x, summation over partons and fragmentation functions have been dropped. The factor of $\Delta q(x_1)$ is an advantage: it is known from DIS experiments to be non-zero and large (see figure 1.4 for the helicity distributions.). Moreover, since the x_2 range of the forward measurement extends *below* the range currently accessible by experiment, the only bound on $\Delta G(x)$ is $G(x)$ – not the current best fits which are based on data above $x \sim 0.02$. One drawback of using π^0's is that there will be cancellations between the u and d quarks which have opposite signs for $\Delta q(x)$.

Presently, double-longitudinal spin asymmetry measurements at RHIC have focused on inclusive probes such as A_{LL} from hadrons, jets or direct photons. As luminosity and polarization continue to improve, the asymmetries di-jet, di-hadron, or γ-jet production will become viable. These channels are interesting since the kinematics of two scattered partons are constrained rather than just one. At leading order and ignoring parton masses, the inelastic proton-proton collision can be viewed as relativistic elastic scattering of two

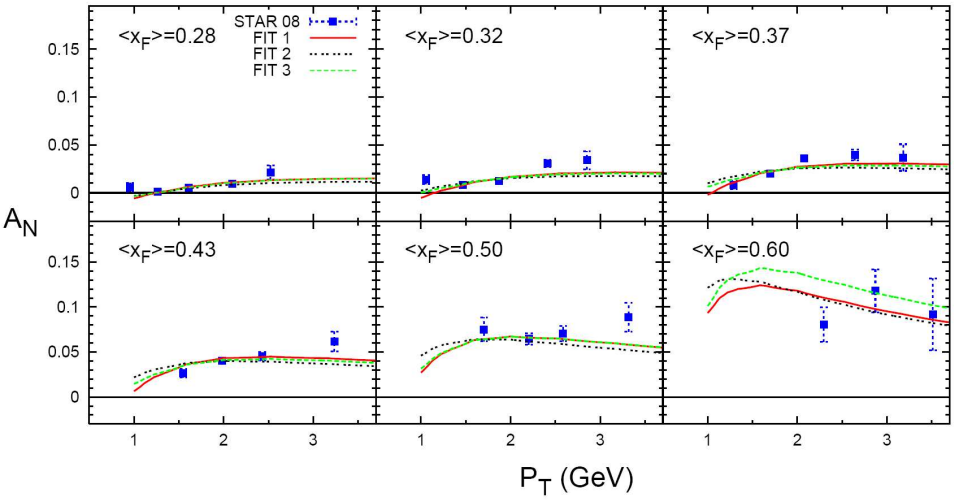

(a) Comparison between the measurement of $A^{\pi^0}_N$ by the STAR collaboration at forward rapidity and $\sqrt{s}$=200 GeV([28]) and a numerical analysis in the twist-3 framework[38]. The various fits are explained in that reference.

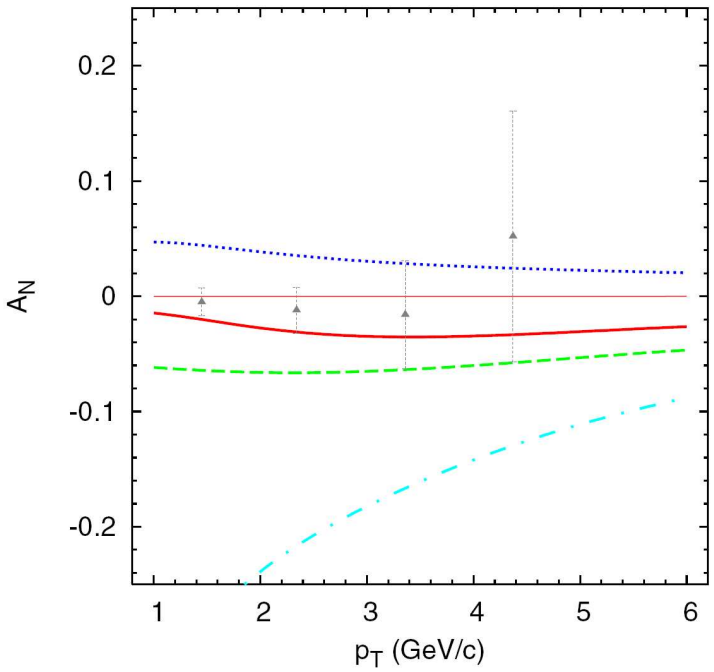

(b) Comparison between the measurement of $A^{\pi^0}_N$ by the PHENIX collaboration at mid-rapidity and $\sqrt{s}$=200 GeV([29]) and a phenomenological analysis using the Sivers function [40]. The various theoretical fits are explained in that reference.

Figure 1.6: Two theoretical analyses using the tools of pQCD compared to measured values of A_N at $\sqrt{s}$= 200 GeV from the STAR and PHENIX collaborations.

partons. The proton momenta are known, but the momentum fractions of the partons are not. If both scattered parton momenta are measured (in the form of final state jets or hadrons), then equation 1.6 can be used to determine the initial parton momenta.

$$x_1 = \frac{p_T}{\sqrt{s}}\left(e^{y_1} + e^{y_2}\right), x_2 = \frac{p_T}{\sqrt{s}}\left(e^{-y_1} + e^{-y_2}\right) \tag{1.6}$$

where y is the parton rapidity, $y = \frac{1}{2}ln\left(\frac{E+p_z}{E-p_z}\right)$. In the high energy limit, this is equivalent to the pseudo-rapidity (defined above). A measurement with a single jet fixes y_1 or y_2, leaving the other to be integrated over. By fixing both y_1 and y_2, the range of x_1 and x_2 is constrained. At PHENIX, the proposed measurements use hadrons instead of reconstructing jets. This will smear the resolution of the final state jet p_T and rapidity. The level of smearing can be estimated using Monte-Carlo.

1.2.3 Parton Distributions at Extreme Density

The previous sections have explored the spin degrees of freedom by introducing spin-dependent distributions, e.g. $f_a(x)$, $\Delta f_a(x)$ and $\delta f_a(x)$ for a parton of flavor a in a proton. In the discussion, only the proton is considered. Another area of research studies the nuclear dependence of the unpolarized distribution function, e.g. $f_a(x)$ for copper or for iron. Past DIS experiments using nuclear targets have shown that the structure of a nucleus cannot be described by a simple sum of the proton or neutron structure functions[41]. Results from RHIC have shown that this is also true for the collisions between deuteron ions and gold ions ($d + Au$). The experiments measure R_{dA}, the ratio of cross-sections between hadrons produced in deuteron-gold collisions and in proton-proton collisions scaled by the number of binary collisions[42, 43]. In the absence of nuclear medium effects, the ratio will be one. However, the ratio has been demonstrated to vary with p_T, with the production angle of the hadron, and with the centrality (roughly the impact parameter) of the collision. The results can be interpreted within the framework of multiple theories. To provide distinguishing power between the theories, the experimental program is: 1) determining the R_{dA} suppression factors with greater precision, and 2) moving beyond inclusive hadron production to ratios determined from di-hadron angular correlations. Different explanations for the patterns of R_{dA} predict different correlations in the back-to-back azimuthal distributions of hadron or jet pairs. The effects are expected to vary with both the rapidity difference of the hadrons, and on the individual rapidities (which help determine the underlying x_1 and x_2 distributions). Using the baseline PHENIX detector, this di-hadron analysis was carried out using hadrons at mid-rapidity ($|\eta| < 0.35$) and hadrons at forward rapidity ($1.4 < |\eta| < 2.0$)[44].

The construction of forward electromagnetic calorimeters enables PHENIX to measure hadrons at high

p_T using five instead of three rapidities. After the upgrade was completed, pairs between any of the following scattering angles became possible: $-3.9 < \eta < -3.1$, $-2.0 < \eta < -1.4$, $-0.35 < \eta < 0.35$, $1.4 < \eta < 2.0$, $3.1 < \eta < 3.7$. Therefore, each theoretical effect can be tested against angular correlations for many different pairs of scattering angles. In particular, the low-x region, accessible with forward detectors, is expected to provide distinguishing power. At low-x and high gluon densities some of the theories predict novel effects from gluon saturation.

Chapter 2

RHIC

Producing polarized protons and maintaining their polarization through acceleration and storage has been achieved at the Relativistic Heavy Ion Collider (RHIC) located at Brookhaven National Laboratory on Long Island. However, the experimental demand for high polarization and higher luminosity drive continued accelerator research. The accelerator chain and some of the instrumentation relevant to polarization are reviewed. Reference to work on detailed technical aspects of the of polarized proton acceleration are given throughout the discussion in this chapter. For an overall summary see reference [45].

2.1 Acceleration Chain

The accelerator complex is shown in figure 2.1, summarized in table 2.1 and explained in the text.

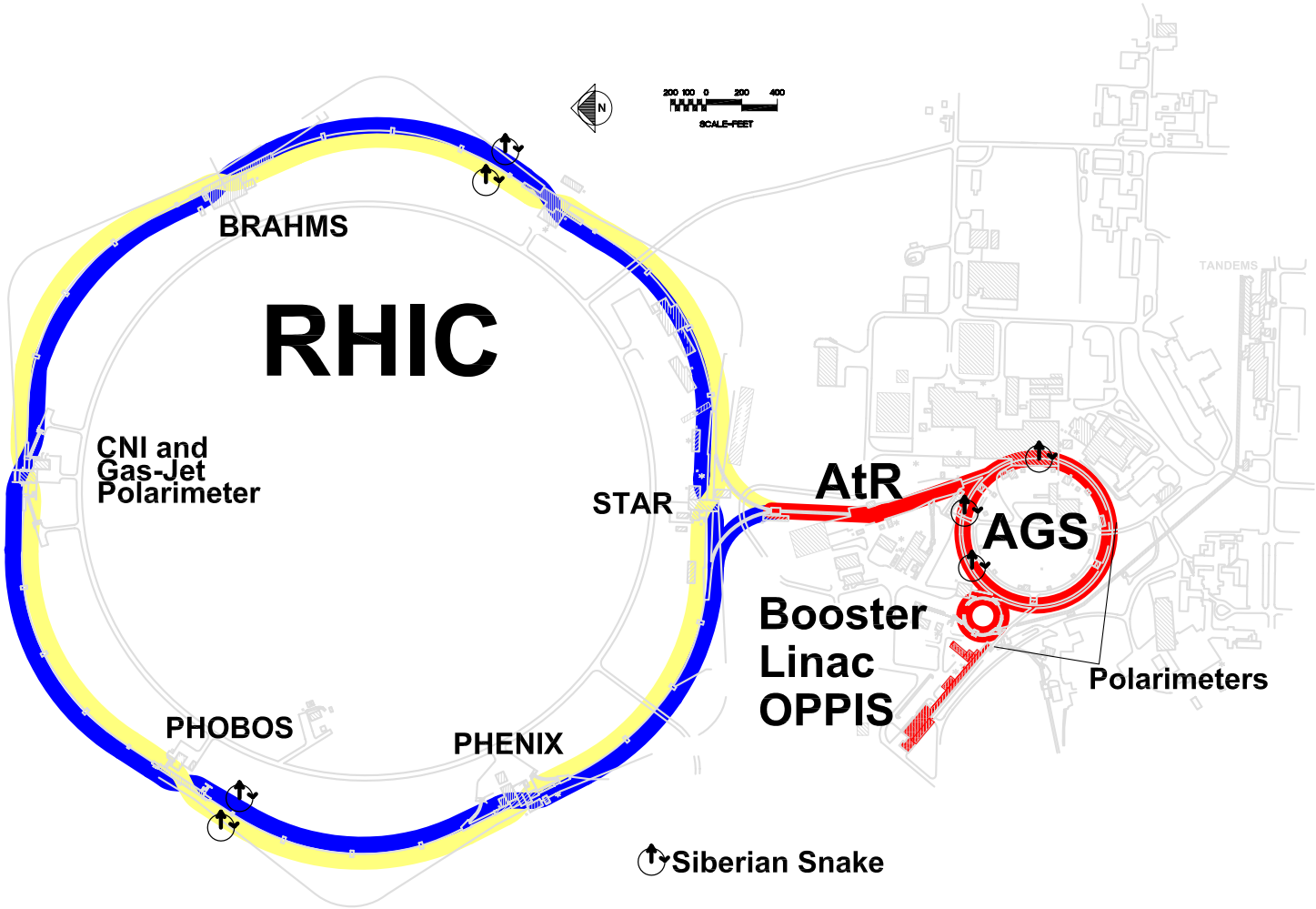

Figure 2.1: The acceleration chain of RHIC and the location of some of the important accelerator systems for accelerating and storing polarized proton beams: Polarized proton source (OPPIS), polarimeters and Siberian Snakes. Also shown are the locations of four experimental detector systems at RHIC.

Stage	**Energy**	**Protons per bunch** [10^{11}]	**Polarization** [%]
OPPIS+RFQ	750 keV	10	80
LINAC	200 MeV	5	80
Booster	2.35 GeV	2	-
AGS	24.3 GeV	1.7	65
RHIC	31.2 GeV	1.4	50
	100 GeV		56
	250 GeV		39

Table 2.1: Proton energy, population and polarization at each stage of acceleration. The figures shown in the table are taken from references [46, 47, 48].

2.1.1 OPPIS

The Optically Pumped Polarized Ion Source (OPPIS) produces a 400 μs pulse of 10^{12} nuclearly polarized H^{1-} atoms with 35 KeV of kinetic energy. These atoms are produced in several steps. First, 3 KeV unpolarized protons (H^{1+}) pass through an optically pumped rubidium gas in a 4 T magnetic field producing a beam of electron-spin polarized H^0 and un-reacted H^{1+} atoms. The H^{1+} ions are swept from the atomic beam by deflector plates and then the electron spin is transferred to the proton through a Sona transition. The Sona transition adiabatically brings the magnetic field from large positive to large negative values with a rapid jump between $\pm$ 1 gauss. During the adiabatic ramps, the atoms follow energy levels according to the usual Zeeman and hyperfine effects, but the rapid jump causes the atoms to jump from electron-spin polarized atoms to nuclearly polarized atoms. To facilitate acceleration, H^{1-} atoms are formed by passing the beam through a Na-jet vapor cell. Then the atoms are accelerated by a radio frequency quadrupole (RFQ) to 750 keV. The Sona transition is more thoroughly described in [49] and the full system in [47, 50].

2.1.2 LINAC

The LINAC is a 200 MHz linear accelerator which brings the nuclearly polarized H^{1-} atoms to 200 MeV and strip-injects the ions into the Booster.

2.1.3 Booster

The Booster, a fast cycling synchrotron, captures the 400 μs pulse into a single bunch of protons, accelerates them to 2.35 GeV and injects them into the AGS. The Booster acceleration stage is spin-transparent.

2.1.4 AGS

The Alternating Gradient Synchrotron (AGS) further accelerates the polarized protons to 24.3 GeV. Depolarizing resonances in the AGS are overcome by RF dipoles and Siberian Snakes (see section 2.2.1 for details). Polarized protons pass from the AGS to RHIC along the AGS to RHIC transfer line (AtR).

2.1.5 RHIC

Starting in the year 2000, RHIC has been colliding at center of mass energies ranging from 7.7 to 200 GeV for heavy ions and 62.4 to 500 for polarized protons. Several features of the accelerator make it unique: collisions of non-symmetric ions are possible; it was designed to operate at many energies rather than a single peak energy; and it is the only facility colliding polarized protons. The accelerator is a synchrotron in that the ions are accelerated in packets as opposed to a continuous stream. The packets of particles, called bunches, are accelerated by two independent accelerator rings called Blue (clockwise) and Yellow (counterclockwise), provide collisions for roughly eight hour periods during which time the beam luminosity drops, and then the beams are dumped. Each packet contains roughly $1.4 \cdot 10^{12}$ protons which are separated from one another by 106 ns. The accelerator has room for 120 packets in each ring however approximately 10 utility "buckets" are left empty – the bulk of which are called the "abort gap" [1]

RHIC is the first and only polarized collider, but not the first facility available for investigating polarized proton structure. Most of RHIC's predecessors used polarized fixed targets whose orientation could only be flipped on a multi-hour time scale. In that time period, acceptances may drift, introducing false spin asymmetries and reducing the systematic precision of the measurement. RHIC sidesteps the issue by setting the spin direction – up or down – of each ring's 120 bunches in a semi-random fashion. Therefore, the spin flips on the interbunch spacing timescale (106 ns), and the problem of time-dependent acceptance drifts is dramatically reduced. The alternating sequence of spin orientations is called the "spin pattern". There are four spin patterns which are cycled through in a fixed order from fill to fill. More combinations are possible, but four patterns strike the balance between sampling each pattern several times per week during both day and night cycles, and decreasing the odds that a spin-pattern induced systematic effect eludes notice.

The important parameter for any accelerator is the luminosity, $\mathcal{L}$, and, for spin asymmetry measurements, the beam polarization(s), P. The luminosity integrated over time measures the number of proton-proton collisions sampled by the experiment. The two parameters can be used to define a figure of merit (FoM) for different types of asymmetry measurements, and used to compare performance from year to year. For single

[1] When it comes time to dump the beams, a kicker magnet sweeps the ions out of their RHIC orbit and into a beam dump. The magnet has a finite ramp time, so 10 bunches are kept empty to allow the magnet to ramp up fully rather than trigger an uncontrolled spray of particles between the beamline and the beamstop.

Year	$\sqrt{s}$	**Polarization**	**Longitudinal**		**Transverse**	
	[GeV]	[%]	$\int \mathcal{L}$ [pb^{-1}]	$\int \mathcal{L}$P^4 [pb^{-1}]	$\int \mathcal{L}$ [pb^{-1}]	$\int \mathcal{L}$P^2 [pb^{-1}]
2002	200	15	-	-	0.15	$3.4 \cdot 10^{-3}$
2003	200	27	0.35	$1.9 \cdot 10^{-3}$	-	-
2004	200	40	0.12	$9.0 \cdot 10^{-3}$	-	-
2005	200	48	3.4	$2.0 \cdot 10^{-2}$	0.16	$3.5 \cdot 10^{-2}$
2006	200	54	7.5	$7.9 \cdot 10^{-1}$	2.7	$7.0 \cdot 10^{-1}$
2006	62	48	0.08	$4.2 \cdot 10^{-3}$	0.02	$4.6 \cdot 10^{-3}$
2008	200	46	-	-	5.2	$1.1 \cdot 10^{0}$
2009	500	35	14	$2.1 \cdot 10^{-1}$	-	-
2009	200	55	16	$1.5 \cdot 10^{0}$	-	-

Table 2.2: RHIC performance history for polarized protons. All measurements in this thesis are from data generated in 2008.

spin asymmetries such as A_L and A_N, the FoM is $\int \mathcal{L}P^2$ and for double spin asymmetries such as A_{LL} and A_{TT} it is $\int \mathcal{L}P^4$. Each year's energies and performance of RHIC are summarized in table 2.2[2].

In their normal orbit around RHIC, the two beams are stored in separate beampipes. However, the beampipes merge before and separate after each of the six collision points. The collision points are enumerated by their position along the ring like in a clock. The beams are merged by using dipole magnets called DX magnets (illustrated in figure 2.2). Four collisions points were originally instrumented. BRAHMS[3] and PHOBOS are two smaller special-purpose detectors which have completed their physics goals and are now dismantled. STAR[4] and PHENIX[5] are two larger general-purpose detector and are still active. Due to the size of each beam, collisions are spread around the center of each experiment with roughly σ=50cm in the direction parallel to the beams and σ= 100's μm in the direction transverse to the beams.

2.2 Beam Instrumentation

2.2.1 Siberian Snakes

At any point in the acceleration process, the beam polarization may be lost due to two types of resonances: imperfection resonances, caused by dipole errors leading to small radial field components and quadrupole misalignments; and intrinsic resonances, caused by the spin precession around the radial field components in the focusing magnets. Both types of resonance are overcome using "Siberian Snakes" which rotate the spin direction of the polarized beams by a fixed amount. A 9 degree partial snake is installed in the AGS,

[2]Only the polarized performance is shown. The experimental program with heavy ions has also made great strides in parallel to the polarized program.
[3]Broad Range Hadron Magnetic Spectrometers Experiment at RHIC
[4]Solenoidal Tracker at RHIC
[5]Pioneering High Energy Nuclear Interaction eXperiment

and two full 180 degree snakes are installed in each RHIC beam[6]. A single Siberian snake is made up of four helical dipoles.

2.2.2 Spin Rotator

The stable spin direction at RHIC is vertical (i.e. either toward or away from the sky), but the spin delivered to each experiment may be rotated prior to the collision and then rotated back for continued orbit in RHIC using spin rotators. The spin rotators use the same set of four helical dipole magnets as a Siberian snake, but the currents in each helical dipole are set differently. These currents are tuned before each RHIC run with feedback from the local polarimeters of each experiment. In the past, the spin rotators have delivered beams in three orientations: vertical ($\pm\hat{z}$, pointing toward and away from the sky), radial ($\pm\hat{r}$, pointing toward and away from the center of the RHIC ring) and longitudinal ($\pm\hat{\phi}$, pointing parallel or anti-parallel to the proton momentum), where a cylindrical coordinate system is used to describe the orientations. The collision of vertically and radially polarized protons are equivalent in terms of physics, but for azimuthally asymmetric detectors like PHENIX each has its own advantages.

2.2.3 Polarimetry

Polarimetry at RHIC is done using three polarimeters. All three measure the left-right asymmetry, A_N, of the final state from the scattering of a vertically polarized proton against an unpolarized target. Near the 12 o'clock position, the Coulomb Nuclear Interference Polarimeter (CNI) provides a high-precision but uncalibrated measurement. At the 12 o'clock position, the Hydrogen Jet Polarimeter (H-Jet) measures the absolute polarization but with much less statistical power than the CNI. Together, the two provide a polarization measurement with a precision of O(5%). The last polarimeter, traditionally not considered part of the accelerator complex, is built into each experiment and measures the polarization delivered to each experiment. This last "local" polarimeter guarantees that the polarization measured by the CNI and H-jet polarimeters at the 12 o'clock position matches the expected polarization at the 8 o'clock position in PHENIX. For longitudinal running, the combined measurement outside of PHENIX of polarization using the CNI+H-Jet and a negligible asymmetry at PHENIX indicate that the polarization is forced into the longitudinal direction by the spin rotators. Local polarimetry is less crucial in transverse spin running, but is still performed in case the beams are not delivered to PHENIX in the pure vertical or radial direction. The importance of local polarimetry at PHENIX is underscored by the analysis reported in chapter 7 which

[6]Two weak depolarizing resonances in the Booster are overcome with beam-tuning techniques. These techniques were used in the AGS and could be used in RHIC, but the tuning would have to expand from overcoming two resonances in the Booster to hundreds in the AGS and RHIC.

shows that contrary to the expected pure vertical beam, in 2008 there was also a significant radial polarization.

Hydrogen Jet Polarimeter

The H-jet polarimeter produces a dilute gas-jet of polarized protons which is periodically brought into collision with each polarized RHIC beam. The left-right asymmetry, A_N, for elastically scattered protons is measured using both a polarized beam and target. The target (hydrogen-jet) polarization is known by using a Breit-Rabi polarimeter. Since elastically scattered protons are measured, the physics asymmetry, A_N must be the same for both measurements. The physics asymmetry is calculated as: $A_N = \epsilon_{Beam}/P_{Beam} = \epsilon_{Target}/P_{Target}$, where ϵ is the raw asymmetry and P is the polarization. The H-jet polarization (P_{target}) is known, and the raw asymmetries, ϵ_{target} and ϵ_{beam} are measured. Rearranging terms gives: $P_{beam} = P_{target} \cdot \epsilon_{beam}/\epsilon_{target}$. References [51, 52] provide details of the hardware and analysis. The major drawback of the H-jet polarimeter is that due to its dilute target the count rates are low. Therefore, another polarimeter with large count rates but without an absolute polarization scale is used.

CNI Polarimeter

The Coulomb-Nuclear Interference polarimeter measures the left-right asymmetry of recoil carbon at about 90 degrees in the reaction $p^{\uparrow}$+C→p+C. The left-right asymmetry is measured by inserting a thin ribbon of carbon into the RHIC beam, and then counting the asymmetry using six silicon strip detectors. The cross-section is large, which allows precision asymmetries in approximately one minute of data-taking. This makes it possible to monitor the polarization as a function of time in a store/fill. Reference [53] provides more details on the hardware and analysis.

Local Polarimeter

The Zero Degree Calorimeter (ZDC), a 6 nuclear interaction length (λ_0) hadronic calorimeter, is installed at all RHIC experiments and is used as a common luminosity monitor between each interaction point. In addition, it is used at PHENIX as the local polarimeter. It is located at either end of the PHENIX interaction region near the DX magnet. See figure 2.2 for an illustration. The DX magnets sweep charged particles away from the detector leaving only neutral particles such as photons or neutrons to hit the calorimeter face. It covers a solid angle of roughly ± 2.8 mradian around a scattering angle of zero. Each calorimeter is broken into three longitudinal segments with independent readout to give discriminating power for hadronic versus

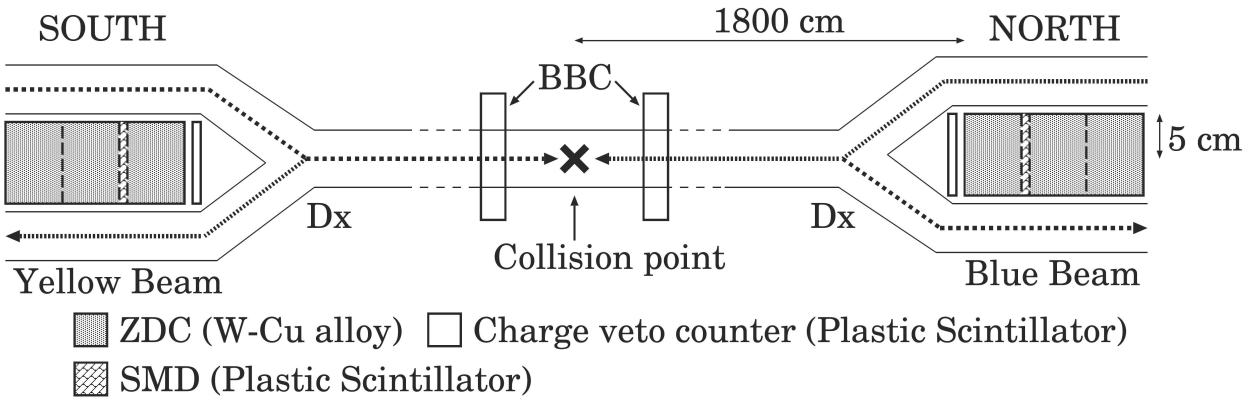

Figure 2.2: Diagram of ZDC detector and the magnet elements which join and separate the beams around the PHENIX experimental hall. Taken from [54].

electromagnetic showers. A hodoscope array of scintillators called the Shower Maximum Detector (SMD) is embedded in the ZDC after the first longitudinal segment. The SMD is used to reconstruct the position of high energy neutrons which shower in the calorimeter. It is composed of 8 (7) scintillator strips of width 2 (1.5) cm in the vertical (horizontal) direction. These extremely forward neutrons were found to have a left-right asymmetry in the scattering of transversely polarized protons by a dedicated RHIC experiment searching for asymmetries suitable for local polarimetry at RHIC[55]. The origin of the asymmetry remain as a challenge to theory. The details of the 2008 local polarimetry analysis are discussed in chapter 7. Details of hardware and its construction are available in reference [56].

Chapter 3

PHENIX

The PHENIX[1] detector is a large general purpose detector. As shown in figure 2.1 the experiment is located at the 8 o'clock position of the RHIC ring. It has been in operation since 2000. Its design is optimized to measure rare probes in both high-multiplicity Gold+Gold collisions and high-rate proton+proton collisions. Conceptually the detector is broken into two parts: the central detector and muon detector with several other subsystems providing key contributions. After a brief introduction, the parts are explained.

Measurements at PHENIX are done in two stages: trigger and offline. The two stages are necessary because of the large difference between the crossing rate (9.4 MHz) and the maximum rate which each event's digitized signals can be written to disk (∼7 kHz). The trigger produces a set of fast but simple measurements which are used to determine if an event is recorded, e.g. events with high energy photons promise to be interesting and can be flagged by their large energy deposits in the electromagnetic calorimeter. In some cases, the intrinsic timescale of a detector is too slow for it to participate in the trigger decision and it must rely on other detectors to select events. After the selected events are written to disk, the offline analysis uses all the detectors, fast or slow, to reconstruct an event in fine-grained detailed. The PHENIX detector is shown in figure 3.1 with the trigger-capable detectors highlighted in green. The triggering system

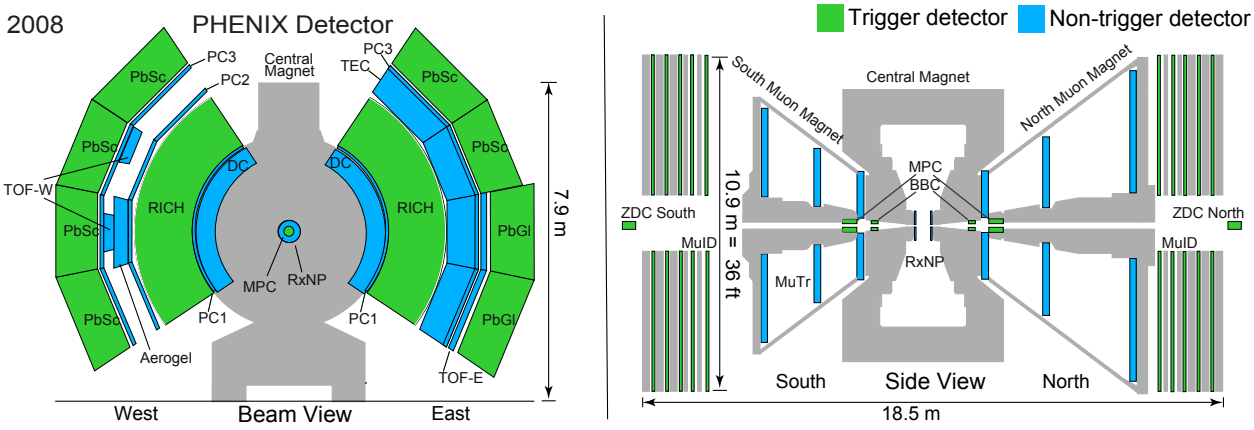

Figure 3.1: Diagram of the PHENIX detector. Detectors generating triggers are highlighted in green – others in blue.

[1]Pioneering High Energy Nuclear Interaction eXperiment

of PHENIX makes a fast decision (<4μs) to either ignore or collect the experiment's digital signals for each crossing. Triggers are formed with six detector systems: the Beam Beam Counter (BBC), the Muon Identifier (MuID) and three calorimeter based triggers: the Zero Degree Calorimeter (ZDC), the EMC-RICH Trigger (ERT) and the Muon Piston Calorimeter (MPC).

3.1 Muon Spectrometer Arms

The muon arms are designed to measure muons. The acceptance between the North and South arms are not identical ($1.2 < \eta < 2.4$ in the North and $-2.4 < \eta < 1.4$ in the South). This feature allows for independent measurements and consistency checks between spectrometer arms. A particle in the muon arm acceptance traverses five elements of the PHENIX detector, two of which produce analyzable data. First, the muons pass through the Central Magnet. Next they enter a radial magnetic field set up by the muon magnet system. Three stations of cathode strip chambers (Muon Tracker, MuTr) measure the muon deflection to reconstruct momenta and charge-sign. Lastly the muons traverse five layers of steel walls and stacked Iarocci tubes (Muon Identifier, MuID). Only muons with energy above 2.7 GeV have the penetrating power to reach the last layer of the Muon Identifier, so it is used to both identify muons and provide a fast trigger. The Muon Tracker was initially too slow to participate in the trigger decision but an upgrade is eliminating this limitation. Further documentation is available in reference [57].

3.2 Central Arm Spectrometers

The central detectors are used to reconstruct identified charged particles, direct photons and neutral hadrons at mid-rapidity ($|\eta|$ <0.35). This is done with a magnet system, a drift chamber, two flavors of time of flight detectors, three layers of multi-wire proportional chambers with pad readout (Pad Chamber, PC1,2,3), an aerogel Cerenkov detector, a time expansion chamber, a ring imaging Cerenkov detector (RICH) and an electromagnetic calorimeter (EMC). The measurements of my thesis use the EMC and the last layer of the pad chamber (PC3) which sits just in front of the calorimeter for charged particle rejection. The other detectors and the techniques used for charged particle tracking are not used. See reference [58, 59, 60] for more information.

The electromagnetic calorimeter (EMC) is divided into eight sectors: six sectors are Lead-Scintillator sampling calorimeters (PbSc), and two sectors are Lead Glass homogeneous calorimeters (PbGl). A sector of the lead scintillator (lead glass) is composed of a grid of 72 by 36 (96 by 48) towers in the z and y coordinate of PHENIX where each tower covers approximately 0.01x0.01 (0.008x0.008) in $\Delta\eta\Delta\phi$ space. The

calorimeters are described in detail in references [61, 62, 63], and their readout and triggering electronics in section 4.4.3.

3.3 Global Detectors

The global detectors include the Beam-beam counter (BBC), Zero Degree Calorimeter (ZDC) and the Reaction Plane Detector. The reaction plane detector is only used in heavy ion measurements and won't be described here or in this thesis; the ZDC was already described in section 2.2.3.

The two BBC arms sit ±144 cm from the nominal interaction point with a pseudorapidity coverage of $3.1 < |\eta| < 3.9$. Each arm is composed of 64 3-cm thick Cerenkov ($\beta_{threshold} = 0.7$) radiators read-out with mesh-dynode photomultiplier tubes. The time difference between each arm is used to reconstruct the collision point along the beamline. The sum gives the start time for time of flight measurements. The z-vertex reconstruction is done both online in the trigger and offline with better precision. The multiplicity of active towers and the online measurement of the z-vertex is used to construct a minimum-bias trigger, i.e. one which fires for a large fraction of collisions and selects inelastic collisions without a selection bias. The trigger fires so frequently that not all events are collected. In fact, it fired at about 100 kHz in 2008, and most of its events were not written to disk. However, minimum bias triggered events serve an important purpose. The other PHENIX triggers are designed to select and collect rare events while discarding as few as possible. They may introduce a measurement bias. Comparing an analysis done with the minimum bias triggered data sample and to an identical analysis done with a selectively triggered data sample reveals the trigger bias and can often be used to correct it.

3.4 Luminosity Monitors

Two sets of scaler boards are used to measure the integrated luminosity delivered to PHENIX. The first board, GL1, counts the number of times a set of triggers fire. It scales each trigger three times with two additional coincidences placed on each trigger. The first scaled trigger, called "Raw", is the simple sum of the number of times a trigger fires. This number is equal to the integrated luminosity multiplied by the cross-section of each trigger[2]. The second scaled trigger, called "Live", is the same as raw, but places the additional requirement on each trigger that the DAQ is ready to take data. This does not correspond to the number of events taken with each trigger, since the DAQ does not collect data from every event. The last

[2]For simplicity, the issue of more than one collision in a given crossing is ignored. It is not of large concern from the Run-8 dataset. The interaction rate was O(100 kHz) and the crossing rate is 9.4 MHz. Therefore, the Poisson probability for multiple collisions for more than one collision in a crossing is quite low.

trigger, called "Scaled", scales the number of events triggered and written to disk for each trigger.

The second board is motivated by spin asymmetries. Of particular interest to spin asymmetries is the ratio of luminosities between different combinations of spin states. For example, the ratio of luminosity for the blue beam with spin up as compared to spin down. Section 6.1.2 motivates the need to measure the spin state orientation dependent luminosity, but it is accomplished by the second board. A scaler board called GL1−1P scales the number of times a trigger fires but separates the scaling between each of the 120 bunch crossings at RHIC. Therefore, with appropriate sums of counts, the spin-dependent luminosities can be determined.

3.5 Data Acquisition System

The PHENIX DAQ has for many years led the world's high energy physics experiments in data volume written to disk. At peak running, data is written at a rate of 700 MB/s. Data flows from each subsystem's front end electronics in the interaction region over fiber optic cables to data collection modules (DCM) located outside the interaction region. The DCM's pass the data to the Sub Event Buffers (SEB) which then pass the data to the Assembly and Trigger Processor (ATP). The ATP's assemble each the event's data from the individual subsystems and pass the data to one of a series of buffer boxes for archiving. The buffer boxes are composed of seven machines each with 15 terabytes of hard-drive space. All machines are written to in parallel, but each one's capacity is split into four filesystems: `a`, `b`, `c` and `d`. During normal operations data is written in sequence to `a`, `b`, `c`, `d` and then starts again at `a`. Swaps between filesystems are done once a filesystem reaches maximum capacity. After a swap, data is immediately copied to a tape robot with multi-petabyte storage capacity. The computing facility which houses this tape robot is called the RHIC Computing Facility (RCF). RCF provides support to all RHIC experiments. The facility maintains a computing farm of several thousand machines used for reconstructing and analyzing data and a smaller set of machines for interactive use.

Data is written to the buffer box in a binary format called `PRDF`[3]. The `PRDF` internal structure is based around a packet ID unique to each data collection module.[4]

After the data has been copied, it is safe to delete it from the buffer box but it is not done until the last possible moment. Since PHENIX writes such large volumes of data, running even a simple analysis over the entire dataset requires significant resources. However, the data is kept locally on the buffer boxes for approximately twelve hours which allows simple analyses to be run over the data. Two types of analysis

[3]PHENIX Raw Data Format

[4]Data extraction can be done quickly using the utilities: `dlist` and `ddump` which list and fetch packet information, or with compiled code linked against data extraction libraries.

are done. The first is called Online Monitoring. It produces a simple but fast display of each detector's performance. These plots are closely tracked by the shift crew 24 hours a day, 7 days a week during each half-year long RHIC run. The detector performance plots from the online monitoring are designed to automatically alert the shift crew in case of any problems. The second type of analysis is online calibration. Online calibration gives the subsystem experts a first iteration on calibrating their detector, and greatly speeds up the path to publication. It also gives the subsystem experts more sophisticated feedback on the performance of their subsystem.

Chapter 4

Muon Piston Calorimeter Upgrade

The Muon Piston Calorimeter, a pair of forward electromagnetic calorimeters, significantly extends the capabilities of the PHENIX detector. This chapter reviews the detector development from idea to installation in PHENIX. The next chapter describes the detector calibration and reconstruction. This chapter consists of:

- Introduction to calorimetry.
- Overview of: the detector design, the location, the tower material, the mechanical structure and the monitoring system.
- Construction of the detector shells and the preparation of the crystals.
- Readout and trigger electronics.
- Integration into the slow control and safety systems of PHENIX.
- Reconstruction algorithm.

Placing an electromagnetic calorimeter in the muon piston holes was originally proposed but not implemented by Ken'ichi Imai in 1999[64]. The idea was independently proposed by Terry Awes, Mickey Chiu and Matthias Große Perdekamp in 2005. Along with others, they developed the Letter of Intent[65] laying out the physics goals and apparatus. The South arm design was finalized in the fall of 2005. The South detector was built and installed in roughly six months, and took data and triggered on events successfully in the 2005/2006 run[1]. The North arm first took data in the 2006/2007 run[2]. Major construction ended in 2007 when the south arm and a new monitoring system were designed and built for the 2007/2008 run[3]. The detector recently completed its fifth successful data collection period. The author of this thesis contributed to the project from the beginning in 2005 and made significant contributions to the design, prototyping and test beam studies, construction, integration, software development, operations, calibrations and analysis.

[1] Longitudinally and transversely polarized proton-proton at $\sqrt{s}$=62 and 200 GeV
[2] Gold-Gold at $\sqrt{s}$=200 GeV
[3] Deuteron-Gold and transversely polarized proton-proton at $\sqrt{s}$=200 GeV

4.1 Introduction to Calorimetry

A brief introduction to electromagnetic calorimeters is included to motivate choices made in design and analysis. The discussion is kept brief, since the topic is already well described in other sources. In general these sources fall into two categories:

- A book or review article describing: particle energy loss and electromagnetic showers[66, 67, 68, 69, 70].
- A technical journal describing a study of a specific detector system, material or readout system. This type focuses on real-world applications such as: measurement of the electromagnetic shower shape, distinguishing power between hadronic and electromagnetic showers, and reconstruction of position and/or timing of the incident radiation[63, 62, 71, 72, 73].

The dominant interaction between high energy ($> 20MeV$) photons and electrons with a block of lead is pair-production and bremsstrahlung. In the case of electrons the mean energy loss per unit of material, $\frac{dE}{dX}$, is:

$$-\frac{dE}{dX} = \frac{E}{X_0} \tag{4.1}$$

where X_0 is the radiation length and roughly scales inversely with the atomic number of the medium. In the case of photons, the average intensity of a monochromatic beam drops (to good approximation) like:

$$-\frac{dI}{I} = \frac{dX}{\frac{7}{9}X_0} \tag{4.2}$$

Therefore, the length scale for radiating a photon from an electron is nearly identical to a photon creating an e^+e^- pair. Since the product of either reaction is the reactant for the other, a cascade develops, which is commonly known as an electromagnetic shower. The shower development slows at the critical energy, E_c, where the electron energy losses from bremsstrahlung and ionization are the same. The shower is inherently a stochastic process, but its average properties and mean fluctuations may be studied. The shower depth, X, the distance the shower penetrates the material, grows logarithmically with the incident energy, E:

$$X = X_0 \frac{ln(E_0/E_C)}{ln2} \tag{4.3}$$

The spread of the shower in the transverse direction is described by the "shower shape". After dividing by the incident energy, the shower shape of high energy particles is independent of the magnitude of the incoming energy to a good approximation. The exact shape is the result of a set of complicated processes in the medium, and is typically determined empirically. The Moliere radius, R_M, is defined as the radius

of a cylinder which contains 90% of the shower's energy. This allows for easy comparison between different materials or detector systems.

Finally, the stage is set to measure the position, timing and energy of incoming radiation. They are reconstructed by implanting in the material a mechanism to measure either the multiplicity or path length of the electrons. Two schemes are currently in use in particle physics:

- Sampling calorimeters stack layers of absorber (such as lead) and charge sensitive detectors (such as scintillators). The former drives the shower and latter counts the electrons. The PHENIX PbSc calorimeter falls under this category.

- Homogeneous calorimeters use a single dense material to handle both catalyzing and measuring the shower. Light is typically produced either with Cerenkov radiation or scintillation. The PHENIX PbGl calorimeter falls under this category.

There are several strategies for measuring the position of the incident particle. A popular method and the one most used at PHENIX is to divide the detection area into a grid of regular spaced cells of size comparable to the Moliere radius[4]. On average the electromagnetic shower spreads over a 3x3 grid of towers. Using the measured energy within each tower and the known shower shapes, the position and energy of the particle are reconstructed. Lastly, the shower develops in a calorimeter quickly. By using a suitable readout scheme two important quantities may be generated. The first is the arrival time of the particle, which is useful for rejecting slower moving background particles. Second, a discriminator threshold may be set to generate a fast trigger decision flagging a large energy deposit.

Backgrounds in electromagnetic calorimeters may be caused by a variety of sources. Above a threshold energy of ∼500 MeV, backgrounds in general are heavily suppressed. Heavy charged particles deposit energy through ionization losses governed by the Bethe-Bloch formula. In 20 radiation lengths of lead, the energy deposit is O(100) MeV. Hadrons may also interact strongly with nuclei in the medium leading to a hadronic shower, which is subject to much greater fluctuations than an electromagnetic shower. However, the mean free path for hadrons, λ_I, in dense medium are typically an order of magnitude larger than the radiation length. (For the $PbWO_4$ crystals of the MPC: X_0=0.89 cm, λ_I=22.4 cm and the tower is 18 cm long.). Therefore, in most cases the hadronic shower may start in an electromagnetic calorimeter but it is unlikely to develop into more than two or three generations before the calorimeter ends.

[4]The other major type of calorimeter division scheme uses projective readout where cells follow lines of constant angle from the collision point

4.2 Design

4.2.1 Location

The beampipe runs through two small holes (45 cm diameter, 43 cm deep) in the muon piston. They are both located 200 cm from the interaction point. The muon piston holes' position in PHENIX is shown in figure 4.1 and photographs of each hole are shown in figure 4.2. By virtue of their location within a magnet system, the holes are filled with a several hundred gauss magnetic field (figure 4.3) and are well shielded from beam related backgrounds moving from the MuID towards the interaction point. In the longitudinal direction the muon pistons are 387.4 cm (220 X_0, 23.1 λ_I) in the north and 256.9 cm (146.2 X_0, 15.3 λ_I) in the south. For all their similarity, the holes are differentiated by several features related to the beampipe.

The South muon arm weighs ∼350 tons and rolls ∼1.5 m from its running position against the Central Magnet towards the Muon Identifier. However, the beampipe is stationary. Therefore, the hole sees the beampipe move from a 3" diameter to a larger flange, bellows and spreader. The rolling is shown in figure 4.1 and detailed drawings are in B.1. The spreader's diameter is 6 $\frac{1}{2}$" and determines the minimum allowed radius for the South detector.

In contrast to the South, the North muon system is stationary. The transition of beampipes is done in a similar fashion to the South but without a spreader. The lack of a spreader changes the North keep-out zone from 6.5" for the South to 4.62". The beampipe is supported at the North hole by a bulky stand and block which screens a small fraction of the instrumentable volume from incoming photons. The area is removed from analysis. The stand is shown in figure 4.1 and detailed drawings are in B.1.

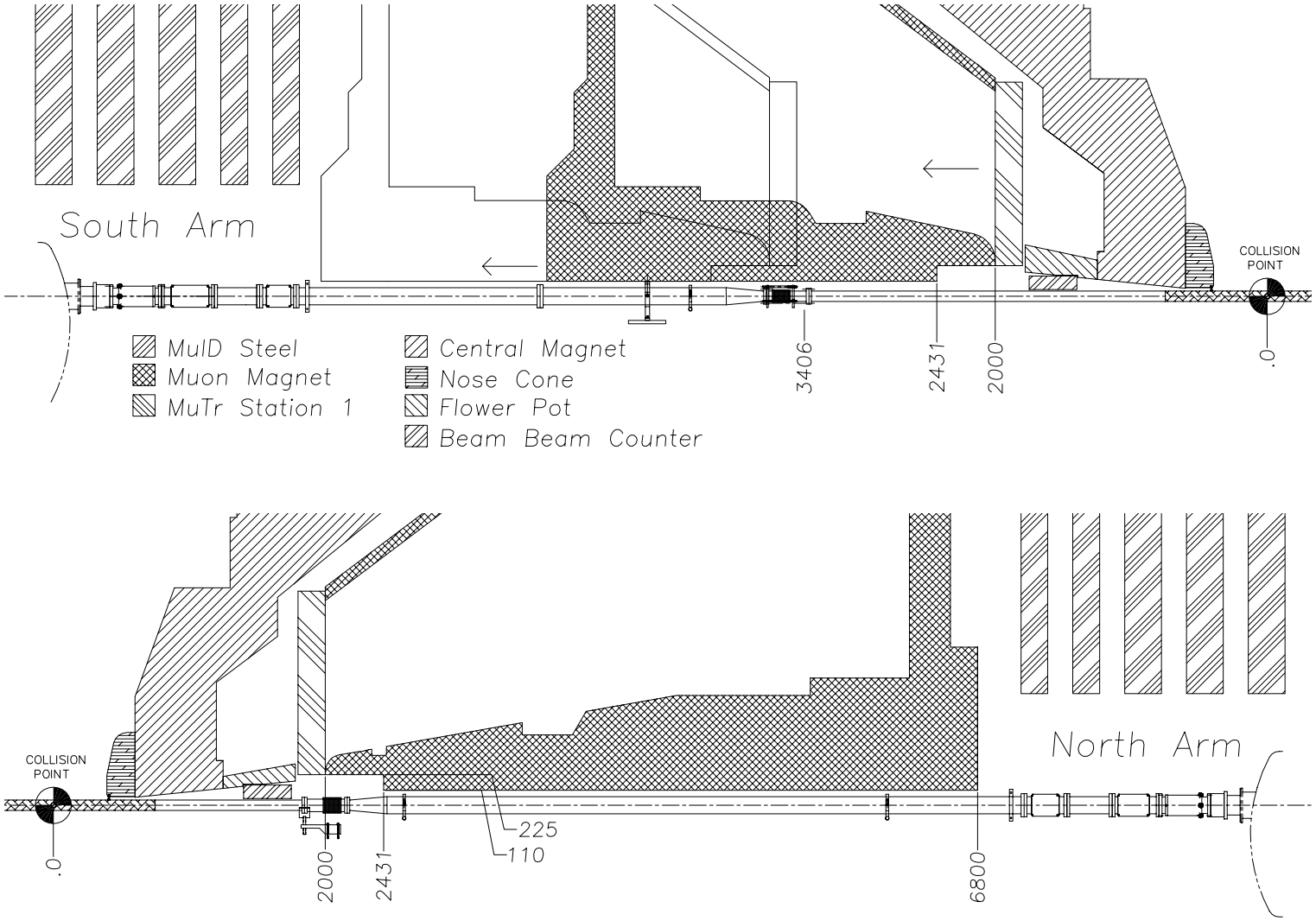

Figure 4.1: Beamline view of PHENIX centering on the South (top) and North (bottom) muon arms around the beampipe area. During shutdowns the South Muon Arm rolls approximately 1.5 meters from its physics running position close to the interaction point to a retracted position. The beampipe is stainless steel with the exception of the hatched area made of Beryllium. The piston hole is located at the upstream end of the muon magnet piston and extends from 2 to 2.431 m parallel to the beam and has a radius of 22.5 cm. The dimensions of the figure are in millimeters.

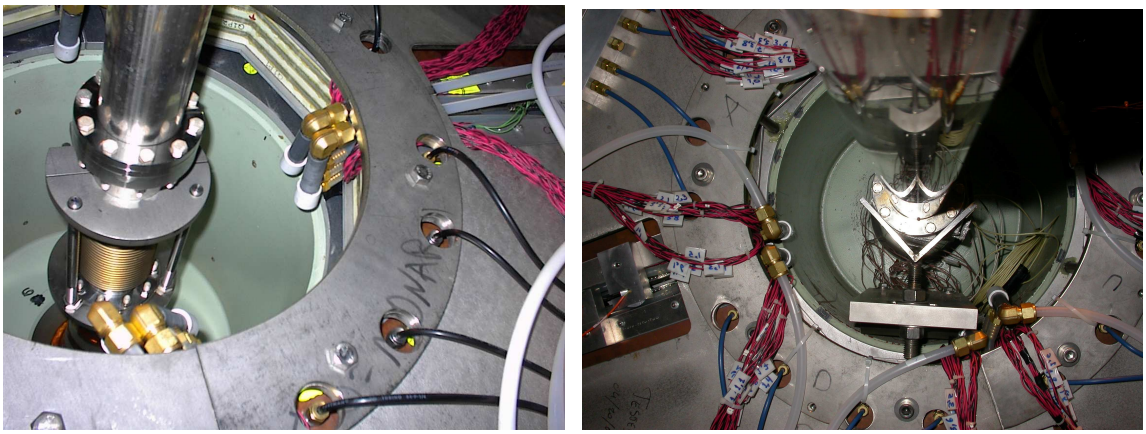

(a) South (b) North

Figure 4.2: The pre-installation muon piston holes

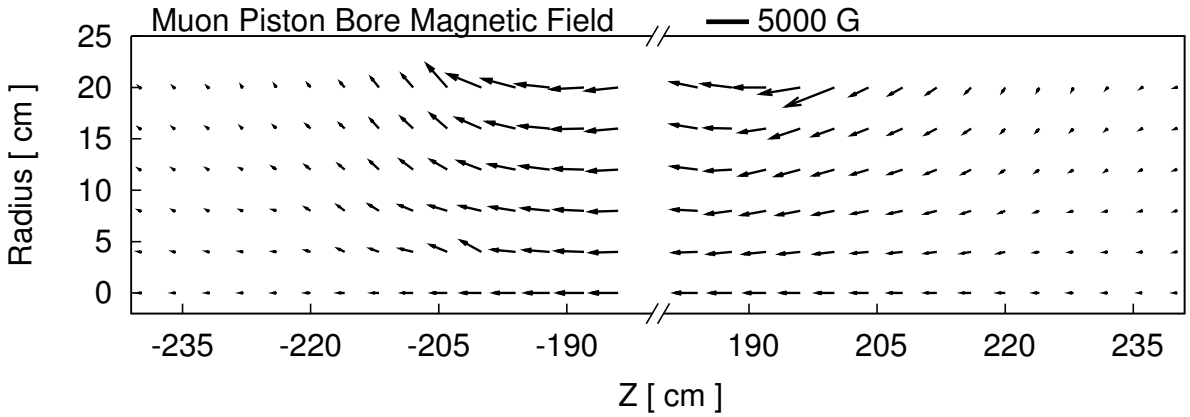

Figure 4.3: Magnetic field of the muon piston holes. The APD/preamps sit at z=±220 cm with the crystal extending to roughly 240 cm. The field is weak (400-500 gauss) inside the hole and increases at the edges to several thousand gauss

4.2.2 Calorimeter Cell

The calorimeter cell consists of two parts: scintillating crystal and avalanche photo-diode. High energy particles produce light in the crystal, and the avalanche photo-diode is used to measure its intensity. The choices of materials and technologies related to the calorimeter cell are explained.

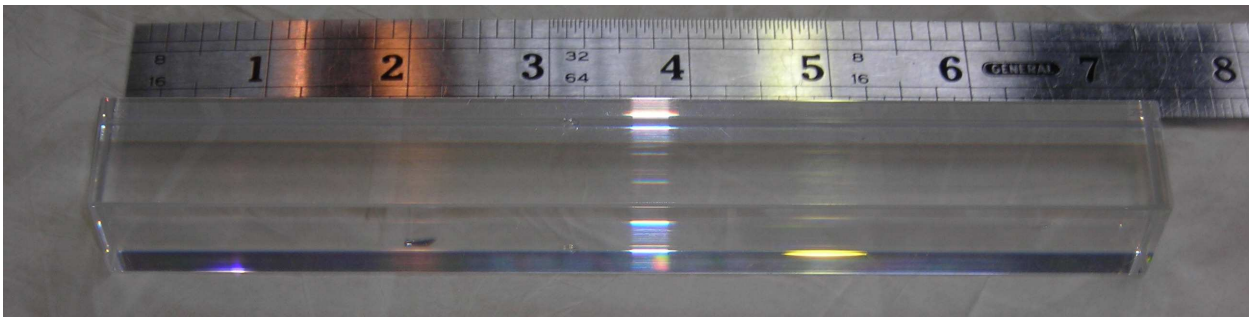

Figure 4.4: The bare $PbWO_4$ crystal

Crystal

The small available space drove the choice to use $PbWO_4$ scintillating crystals. This crystal, originally developed for use in the ALICE and CMS experiments at CERN, has the world's smallest Moliere radius of any known scintillating crystal. Extensive studies have mapped out its: general performance[74, 75, 76], light yield/transmission[74], radiation hardness[74, 77, 78, 79] and temperature stability[74, 79]. Table 4.1 summarizes these properties.

Table 4.1: $PbWO_4$ Properties

Size	2.2 x 2.2 x 18 cm^3
Density	8.28 g/cm^3
Moliere Radius	2.0 cm
Radiation Length	0.89 cm
Interaction Length	22.4 cm
Hardness	4 Moh
Refractive index (λ=632 nm)	2.16
Main emission lines	420, 480-520 nm
Temperature Coefficient	-2%/°C
Radiation Hardness	1000 Gy

Light Collection

Each muon piston hole is embedded in a magnet system and therefore a field, shown in figure 4.3, of several hundred gauss permeates the detector volume. This field drives the choice of light-collection technology. Typically, calorimeters are readout using photomultiplier tubes (PMT). However, unless expensive mesh dynode PMT's are purchased, the magnetic field induces changes in the PMT gain. An alternative, and the one used in the MPC, is the avalanche photodiode (APD), a semiconductor device. Luckily for the project, the ALICE experiment uses Hamamatsu S8664-55 APD's for light-amplification, and quite a bit of that expertise was leveraged. The APD has an active area of 5 x 5 mm^2 and good quantum efficiency ($> 85\%$)

Figure 4.5: The APD/preamp/holder. Left: light collection, right: data and power connection.

around the $PbWO_4$ excitation wavelengths. The APD is soldered directly to a charge sensitive preamplifier and glued to an aluminum holder (figure 4.5). The preamplifiers are designed by Hiroshima University using an earlier Central China Normal University and University of Bergen design for ALICE. Hiroshima University, a collaborator on both PHENIX and ALICE, loaned 250 APD/preamps to the project, and 250 were purchased by Illinois. The holders were built by UIUC and by the UMass-Amherst.

4.2.3 Mechanical Structure

The goal of the mechanical structure is to:

1. Extend the acceptance as much as possible towards the beampipe (high rapidity).
2. Push π^0 and η identification to the highest possible p_T. Therefore, crystals with low Moliere radius and high granularity are needed.

First the major design considerations are reviewed, and then design features are highlighted.

Considerations

Three numbers dictate the design. The beampipe diameter determines the inner diameter of the detector and varies between arms. Therefore, the North detector has an extra inner ring of towers. The piston bore diameter determines the outer diameter of the detector. Its value does not vary between arms and is 45 cm. The third and last number is the height of a fully wrapped crystal: 22.7 mm. With the three numbers set, the design follows practical considerations, some of which were learned through experience. The South arm detector was designed and installed first. Then, in 2006, the North arm was similarly instrumented.

The North design and installation incorporated lessons from the South detector. Finally, in 2008, the South arm was redesigned and installed with a slightly larger acceptance. Engineering drawings of the detector are available in appendices B.2 and B.3.

The detector must be sturdy and made of non-magnetic materials. It must be sturdy to support the heavy crystals, and to protect the beampipe. The choice of construction materials are limited by the hole's location within the muon magnet system whose fields should not be distorted by a new detector. Therefore, the detector must be made of non-magnetic materials. In general, aluminum is used.

Each hole is roughly 15 feet off the experimental floor. The holes are accessed using a two person man-lift. The beampipe is not removed for detector installation. Therefore, each detector is broken into six detector modules: four "L"-shaped modules above and below the beampipe and two "U"-shaped modules to the left and right. The detector shells are installed first, and then the crystals are inserted[5]. A front plate completes the shell to seal and strengthen the detector. The front plate has holes in it to provide access to cables connecting to the APD/preamp.

Design Features

Figure 4.7 shows the design and overall dimension of the South and North detectors. The various components of the detector are labeled in figure 4.6.

Backplate	The plate at the far end of the detector. Holes centered on each crystal are drilled in it to provide access to the optical fibers of the gain monitoring system.
Frontplate	The plate at the open end of the piston hole. Holes centered on each crystal are drilled in it to allow access to each APD and pre-amplifier.
Rib	Solid aluminum pieces which fill the gap between the rectilinear grid of crystals and the curved profile of the skins. The ribs are also important for structural support. There are two ribs in the z coordinate per module.
Fiber Guard	An open box mounted on the back of the detector. It is designed to protect the optical fibers during installation from damage and snagging.
Feedthrough	A narrow pipe extending through the ribs. The optical fiber bundle goes from front to back through it.
Skin	The outermost, curved pieces of aluminum. Made out of 1/16" sheets.
Shell	The detector assembled but without the crystals in it.
Pad	Teflon pads screwed into the ribs. They extend the farthest radially, and make contact with the piston bore. They are designed to be shaved down in case of imperfections in the piston bore.

[5]The original South MPC design used 4 "L"'s and 4 "U"'s, and the modules were installed fully loaded with crystals. The difficulty of manipulating the $\sim$ 40+ pound detector modules motivated the decision to first install empty detector shells and then insert individual crystals. The new way of installing the detector was used in design of the the North detector and in the redesign of the South detector.

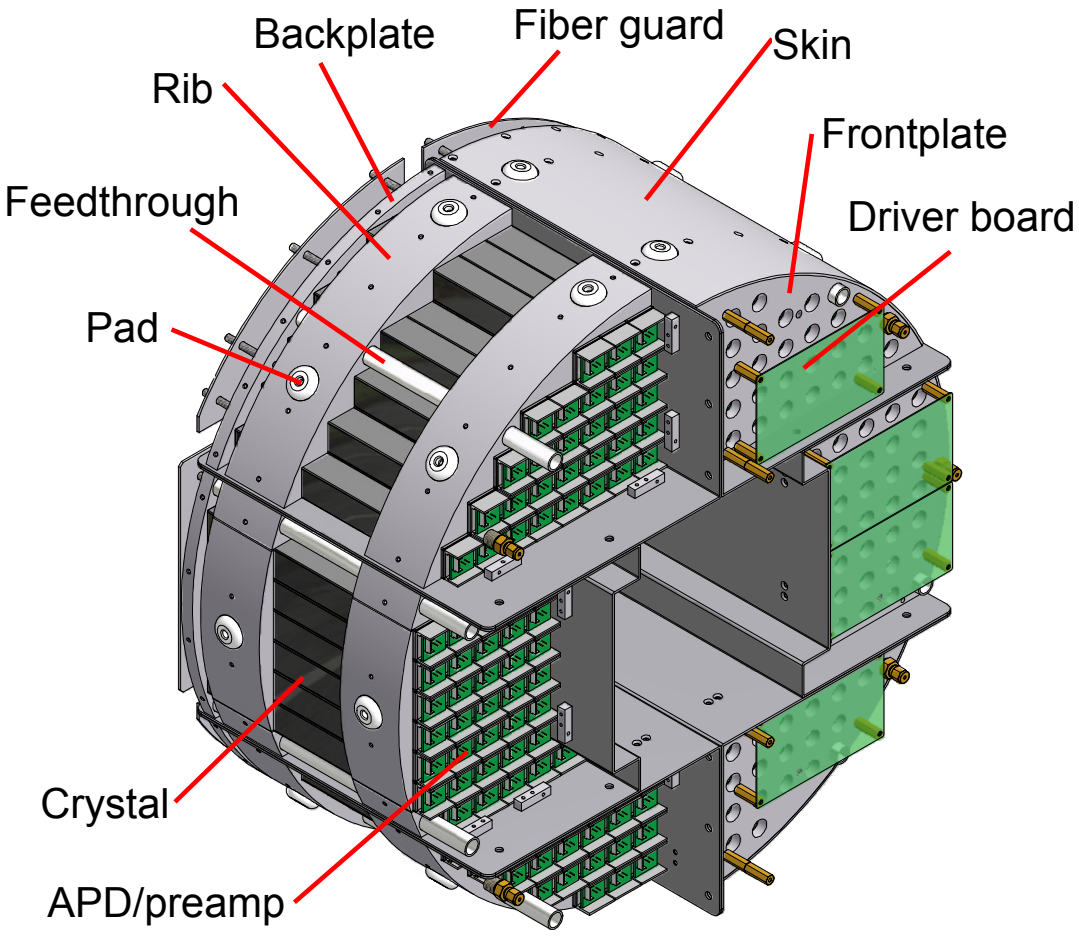

Figure 4.6: AutoCAD model rendering of South MPC with labeled parts.

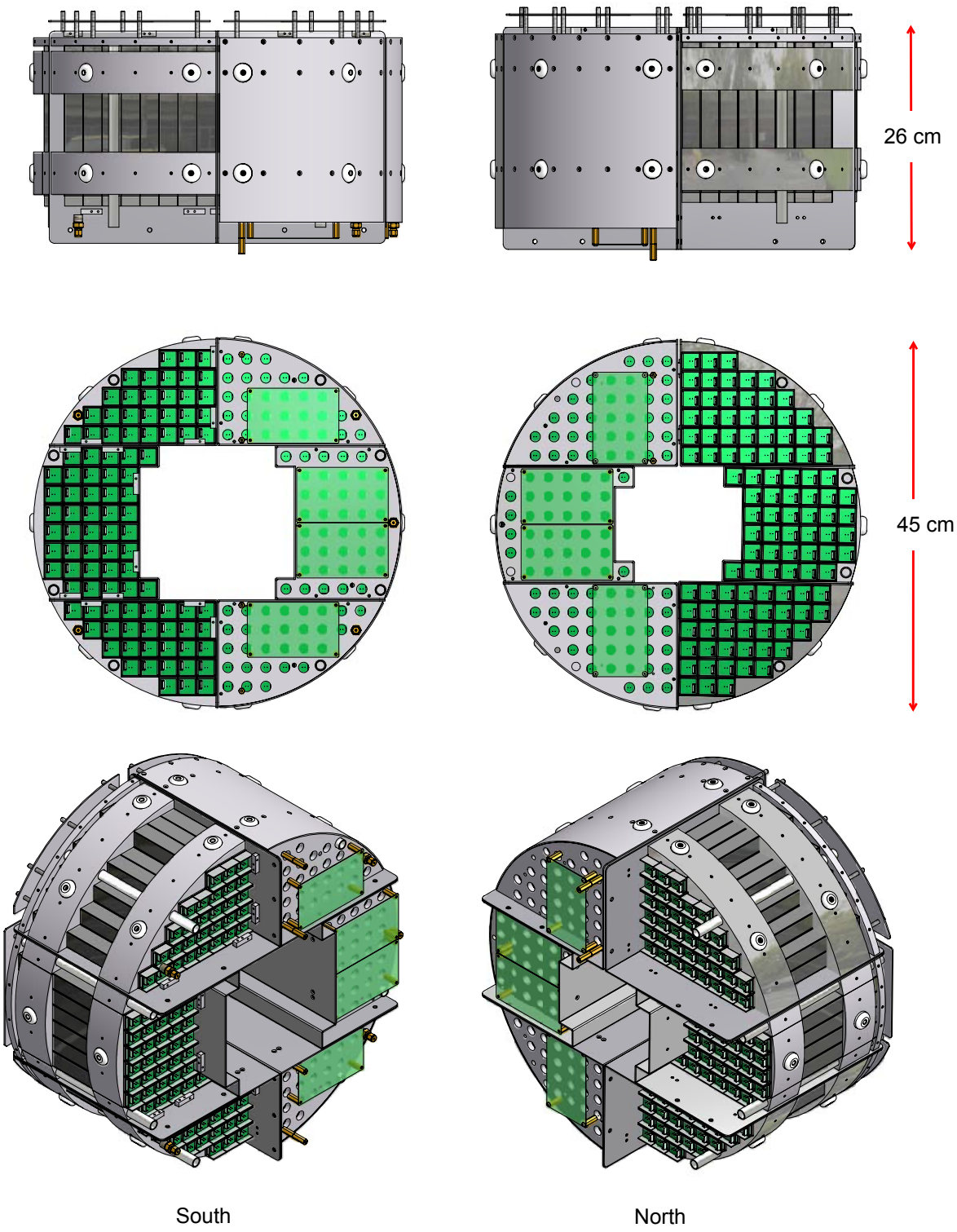

Figure 4.7: AutoCAD model rendering of the South (left) and North (right) MPC's. The bottom panel shows the the front side of the detector which faces the collision point.

Button	Sleeve for the optical fibers which keeps them in place in the back plate.
"U" and "L"	There are six modules per arm: two "U" modules to the left and right of the beampipe and four "L" modules above and below the beampipe. The South (North) "U" module holds 40 (36) crystals. The South (North) "L" module holds 37 (29) towers.
Locking tab	Slots at the back of the detector that lock each module together.
Crystal	A single $PbWO_4$ crystal wrapped in Tyvek, aluminized mylar and Monokote. Details are available in section 4.3.1.

4.2.4 LED Monitoring System

The hardware of the MPC gain monitoring system is described here, and the relative gain calibration analysis is described in section 5.4. Radiation damage, temperature fluctuations or other effects may cause a calorimeter's gain to drift with time. These gain changes are typically tracked by injecting a signal of fixed amplitude at regularly spaced time intervals and tracking the detector response. The design and technology used to construct monitoring systems vary from calorimeter to calorimeter. For example, in PHENIX, the PbSc distributes the light from a high power NdYAG laser to more than 16,000 towers. The laser is synchronized to the PHENIX triggering system such that the laser fires in the RHIC abort gap[6] at a rate of 2 Hz. The MPC makes use of a similar triggering arrangement to fire LED's and collect the data. The MPC monitoring system handles fewer towers than the central arm calorimeter but faces some unique challenges: high radiation environment, temperature fluctuations, and very tight space constraints. Two monitoring systems were designed: the first design was relatively crude but but played an important role for the first two runs, and the second, based on lessons from the first design, uses a more elaborate design and was installed for the 2007/2008 running period. Selected engineering drawings are available in appendix B.4.

System I

The first LED monitoring system which was utilized for the first two runs is based on a system that mounted an LED behind each tower. The design is illustrated in figure 4.8. The system was effective for debugging and checking whether a tower was properly instrumented, but didn't serve as an effective monitor of the tower's gain. The main design flaw of the original system, is that for each tower i the measured output as a function of time, $M_i(t)$, is equal to:

$$M_i(t) = L_i(t) \cdot G_i(t) \tag{4.4}$$

where L_i(t) is the injected light intensity and G_i(t) is the tower gain. G_i(t) and L_i(t) fluctuate independently of each other and so with only one measurement it is difficult to isolate the tower gain.

[6] 10 consecutive empty bunch crossings out of 120.

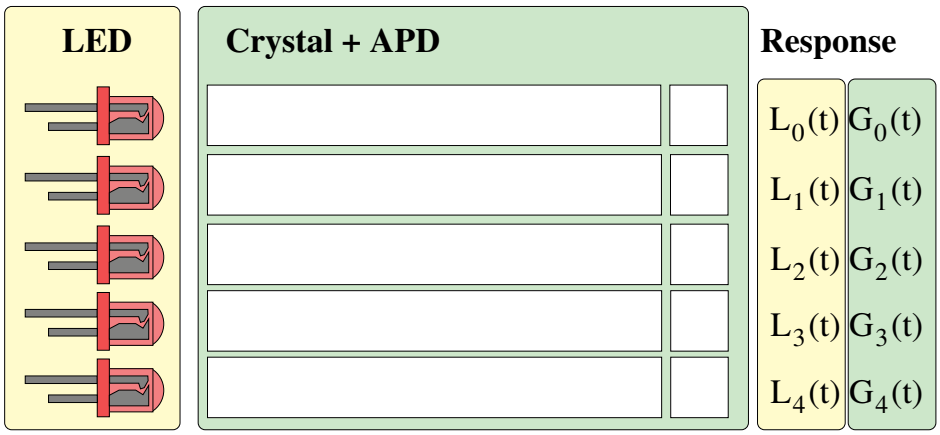

Figure 4.8: Schematic diagram of the first MPC LED monitoring system. Specifics are discussed in the text.

Toyoda Gosei E1L51-3B0A2-02 blue LED's provided light, Its salient features are radiation tolerance, narrow viewing angle and temperature stability. Details on the specific performance characteristics of the LED are available in reference [80].

System II

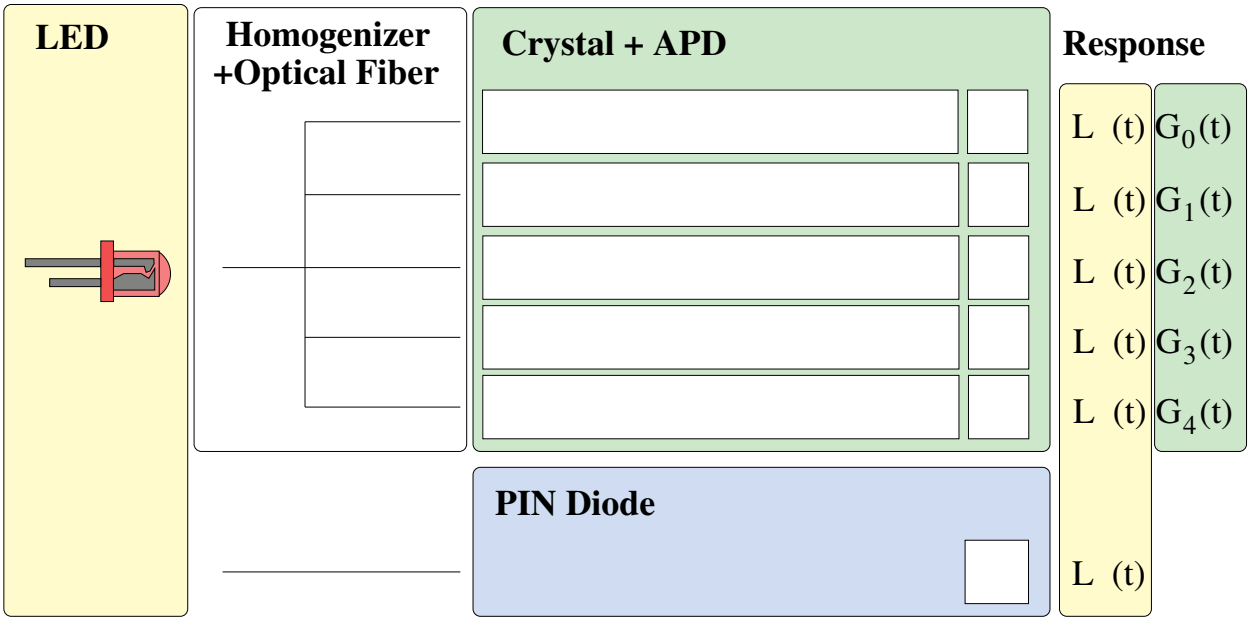

Figure 4.9: Schematic diagram of the second MPC LED monitoring system. Specifics are discussed in the text.

The second and final LED monitoring system was installed after several prototyping rounds done on the test-bench. The triggering system sends a pulse from the rackroom to a custom designed NIM module

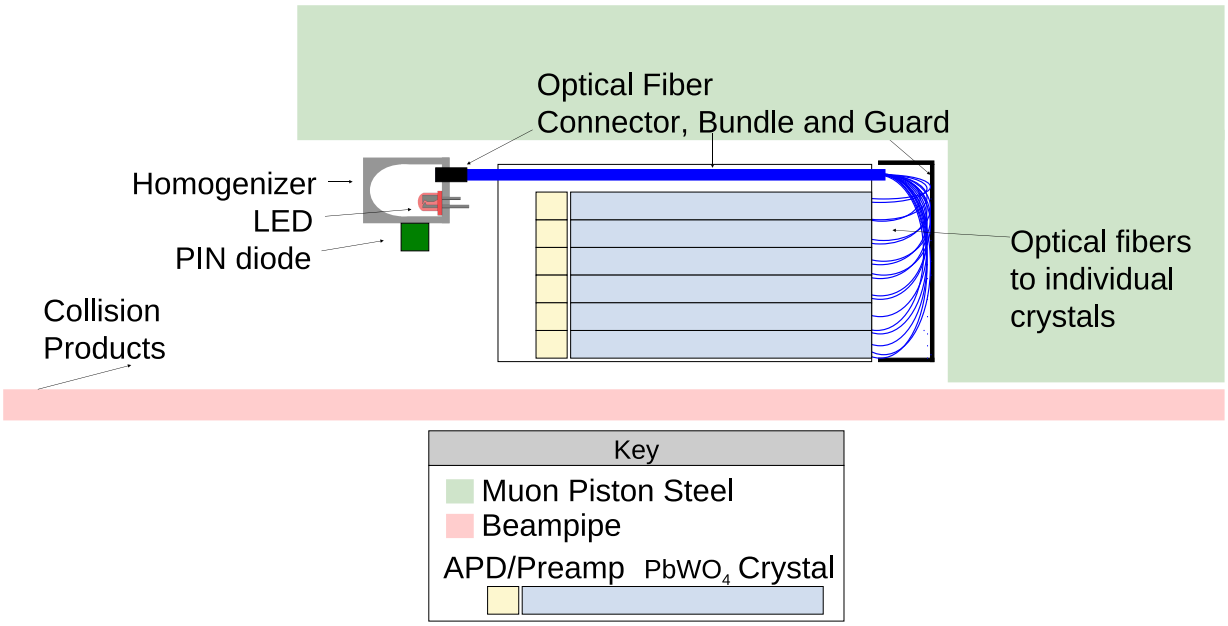

Figure 4.10: Layout of the monitoring system. The light from a single LED is fanned out to many crystals using optical fibers and a hollow box of Teflon, called a homogenizer. The LED intensity is measured using a PIN diode mounted to the side of homogenizer. The optical fiber bundle transverses the entire length of the detector and then splits apart to deliver a pulse to each crystal. An optical fiber guard is mounted to the back of the detector to protect the fibers and prevent tangles during installation.

sitting at the MPC rack in the experimental hall. The module sends out several controllable pulses to LED's mounted in "homogenizers". The homogenizers are mounted on the detector front face. The "homogenizer", shown in figure 4.11, is a hollow Teflon box designed to uniformly distribute the light emitted from a single LED to a bundle of optical fibers. The LED light intensity is monitored by a PIN diode[7] mounted to the side of the homogenizer. Three LED's and the bundle of optical fibers are mounted on a removable lid to the box. Two LED's emit blue light (one primary and the other backup) and the third emits red light. The blue and red colors were picked because any radiation damage in the crystal is expected to affect the colors differently.

The optical fiber strands are joined at one end to form a connector which plugs into the homogenizer lid and left free at the other end to provide light to each tower. The connector is made by inserting fibers in a plastic cylinder[8] and then applying glue. Vacuum forces pull the glue into the connector around the fibers. Every effort was made to ensure that the fibers are parallel to the axis of the cylinder (which ultimately helps to increase the amount of light entering the fiber). Finally, a diamond tipped mill snips off one end of

[7] Hamamatsu S1223-018E: chosen for its radiation hardness and temperature stability. See reference [81] for more information.

[8] Finding the correct inner diameter for the cylinders turned into a fun side-project. The number of optical fibers was fixed, and so was the diameter of an individual fiber but not what their packed diameter plus glue would be. Reference [82] was extremely valuable as it lists the best estimates available for circles stacked within other circles. A fudge factor for the glue was added to the website's values and it turned out to be correct.

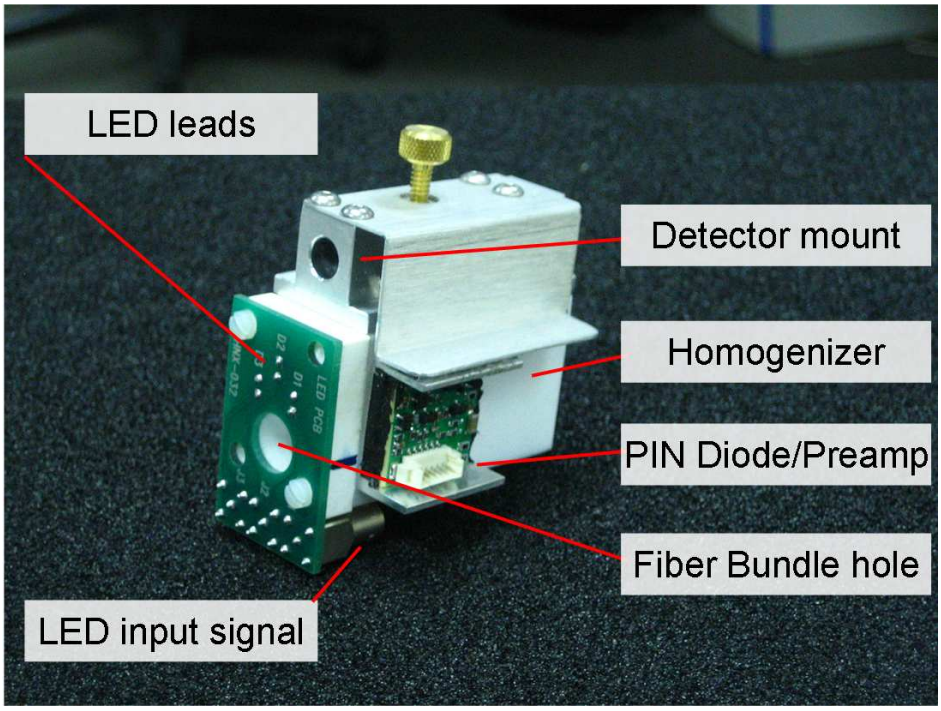

Figure 4.11: Fully assembled homogenizer with highlighted components.

the connector. The diamond tipped mill is crucial to ensure that as much light as possible enters the optical fiber. A rough cut would reduce the amount of light which could make the transition from air with index of refraction 1 and the optical fiber with index of refraction 1.4. Photographs of the fiber bundle at the front and back of the detector are shown in figure 4.12 The optical fiber model which was chosen combines good radiation tolerance, low cost and a small enough allowable bending radius to allow for the 180 degree bend at the far end of the detector. Technical specifications for the fiber are listed in table 4.2.

Table 4.2: Optical Fiber Technical Specifications

Edmund Optics NT02-533	
Core diameter	735.00 μm
Fiber diameter	750 μm
Attenuation	0.15-0.3 dB/m (@600nm)
Core Refractive Index (n1)	1.492
Clad refractive Index (n2)	1.402
Minimum Radius of Bend	25x outer diameter

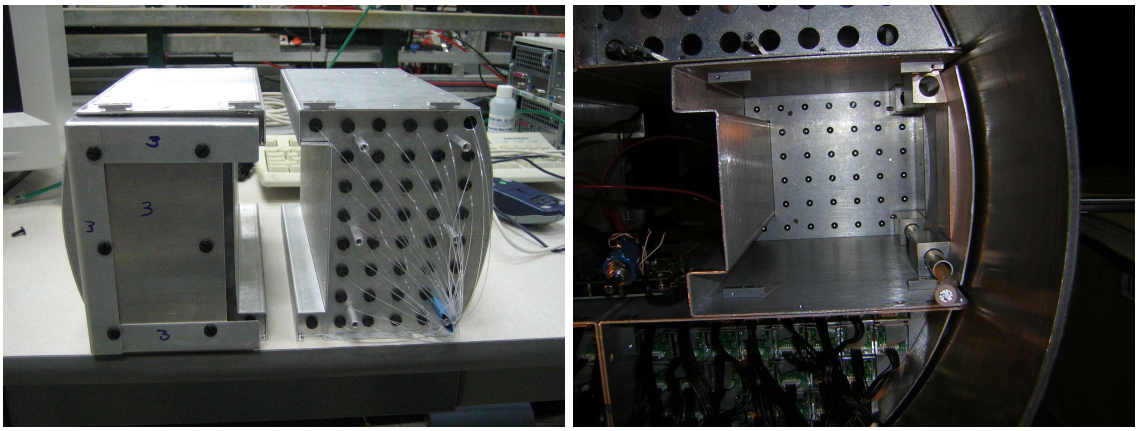

(a) Back view of the monitoring systems and detector with (left) and without (right) the fiber guard in place.

(b) Front view of the optical fiber bundle.

Figure 4.12: Front and back views of the monitoring system's optical fiber bundle.

4.3 Construction

Three construction sessions starting in Fall 2005, Summer 2006 and Summer 2007 were held in the nuclear physics laboratory at UIUC. The major work of each session was $PbWO_4$ crystal preparation, gain testing, and detector shell fitting. Fully assembled and tested detector modules were driven to Brookhaven National Laboratory after each session. In the fall of 2005, a 56 tower prototype was constructed for beam tests at Fermi National Accelerator Laboratory. Details on this beam test are available in section 4.6.1.

4.3.1 Crystal Preparation

The basic unit of the MPC is a $PbWO_4$ crystal glued to an avalanche photodiode with Dow Corning RTV 3145 glue. The glue is chosen for its radiation hardness and its high index of refraction which comes as close as possible to that of the crystal. Two crystal wraps were used: the first for the 2005/2006 run and the second for the 2007/2008 run. The steps described below follow the second, more compact crystal wrap design. An exploded tower assembly is shown in figure 4.13. The crystal is wrapped with Tyvek[9], aluminized mylar and Monokote[10] to increase light yield, ensure light-tightness and minimize light leakage between adjacent crystals. Preparing the crystals for insertion in the detector is a multi-stage, time-consuming process. Contact with hard objects or exposure to oils can easily damage or crack the crystal. Therefore, the entire workarea is covered with foam and all workers must wear gloves. The steps necessary to wrap and clean

[9]Tyvek is a light weight sheet of polyethylene fibers and is highly reflective. It is trademarked by DuPont and the material most FedEx envelopes are made from. The part number is: 5 mil Tyvek 1056D.

[10]Plastic wrap used for making the skin for model airplanes. Coincidentally, its manufacturer is based in Champaign, IL

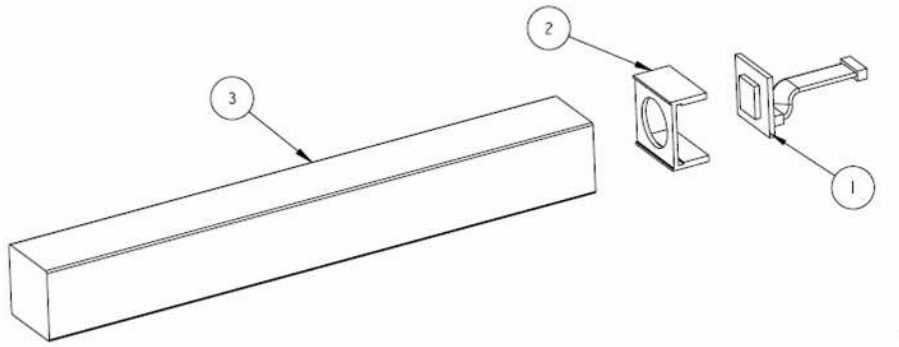

Figure 4.13: MPC Tower Assembly: 1) Crystal, 2) APD Holder, 3) Avalanche Photodiode and preamp

the crystals are summarized and explained in figures 4.14-4.19. A critical number in the preparation of the crystals is the transverse size of a fully wrapped crystal: 22.7 mm. This number was determined by wrapping a small number of crystals, stacking them and measuring the overall height. For the preparation of the crystals it was extremely important to maintain the high-standards of the test-wrapping over a large number of crystals. If the standards for wrapping slip at all in the full scale crystal wrapping, then they will not fit in the mechanical shells.

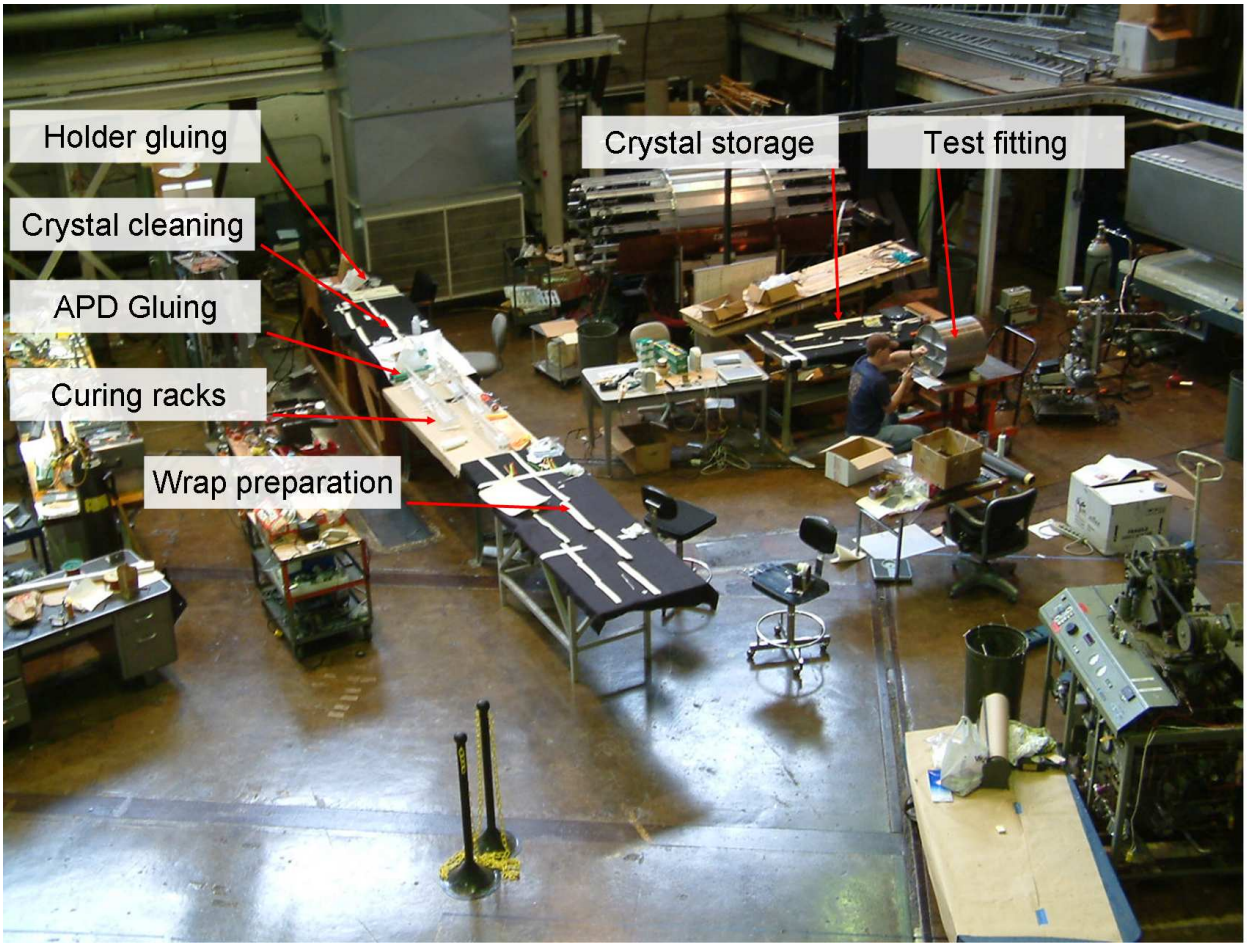

Figure 4.14: Overview photograph of the crystal preparation area.

Figure 4.15: **Crystal inspection**
When the crystals first arrive in Illinois from Russia, they are removed from their shipping crate and inspected for damage. Crystals with non-optimal transparency, chips or scratches are set aside.

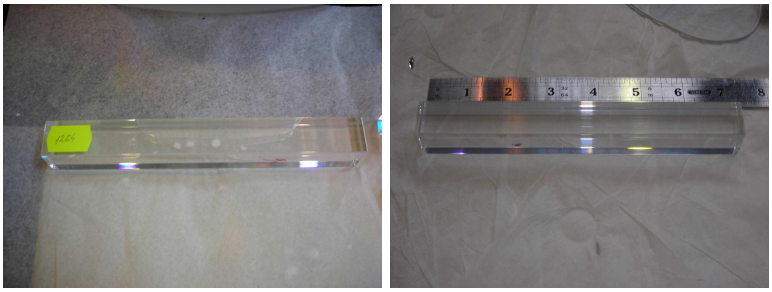

Figure 4.16: **Cleaning**
All crystals arrive with a sticker on them with an identification number and an marker drawn arrow indicating the crystal growth direction. The crystal ID is carefully drawn on the crystal with a diamond tipped scribe. Lastly, the crystal is wiped down with alcohol and kimwipes twice.

Figure 4.17: **Inner Wrap**
Next the crystal is wrapped with a Tyvek wrap. The wrap fits over all six sides of the crystal to trap as much light. To minimize the size of the overall wrap, the sheet is crisply folded. Except for some of the wrap ingredients which were cut by hand in 2006, all the wrap templates were cut by the CAD Cut Company (More information is available in reference [83]). They used computerized knife cutting for our orders, but greater precision is possible with laser cutting.

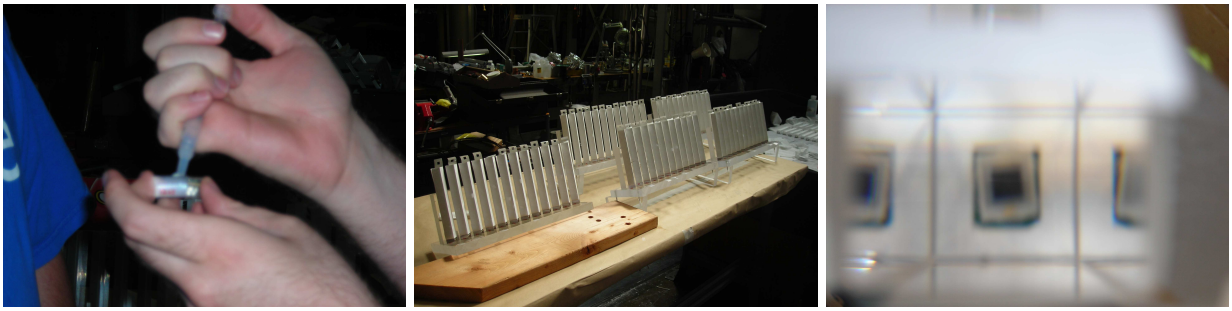

(a) Applying RTV to the APD

(b) Fully-loaded curing racks

(c) View from the top of the crystal viewing the APD

Figure 4.18: **Gluing**
In separate steps, the APD/preamp's are soldered to each other, and are then glued to the APD holder using a UV-curing glue and a UV gun. Then, the APD is glued to the crystal using RTV. The gluing required finesse. The amount of glue had to be sufficient to cover the APD active area completely, but not much more or light would be lost. Best results came from filling a syringe with RTV and replacing the needle with a snipped plastic cap. The glue requires a 48 hour cure time. Air bubbles, which lead to lost light, developed as the glue cured and the process would have to be repeated, often several times. The number of curing racks (5) each with a capacity of twelve crystals, limited the maximum assembly line throughput to sixty crystals per day.

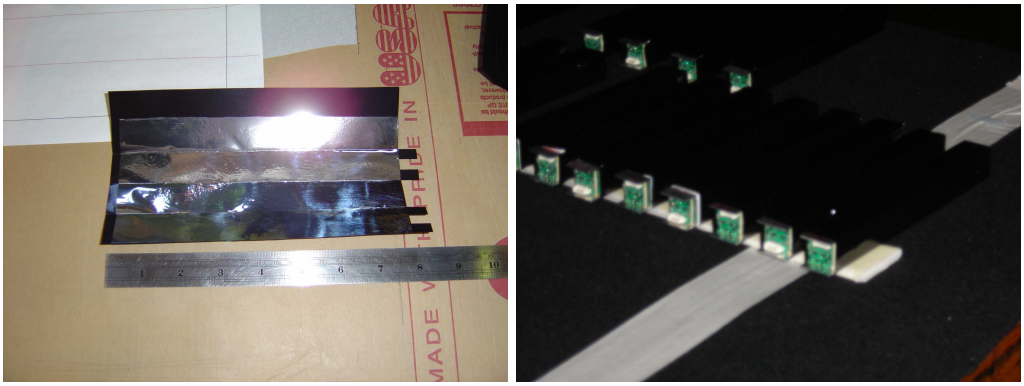

(a) Outer wrap before final ironing

(b) Fully prepared crystals waiting for gain testing.

Figure 4.19: **Outer Wrap**
After the curing is complete, the crystals are wrapped a second time with multi-component wrap. This second wrap has an inner layer of aluminized mylar and and an outer layer of Monokote. The two are pre-cut and ironed together. The combined sheet is crisply folded, molded around a dummy crystal, and ironed to form a sleeve. The sleeves are then slipped over the crystals and ironed a final time.

4.3.2 Crystal Gains

Each APD's gain is determined by exposing each crystal/APD/preamp to a "standard candle". The "standard candle" is a LED mounted to a Lucite block in a light-tight box whose driving pulse was kept constant. In turn, each crystal is exposed to the LED. The reverse bias of each APD is increased until the APD signal exceeds a given threshold. The system is illustrated in figure 4.3.2. The resulting gains are found to agree

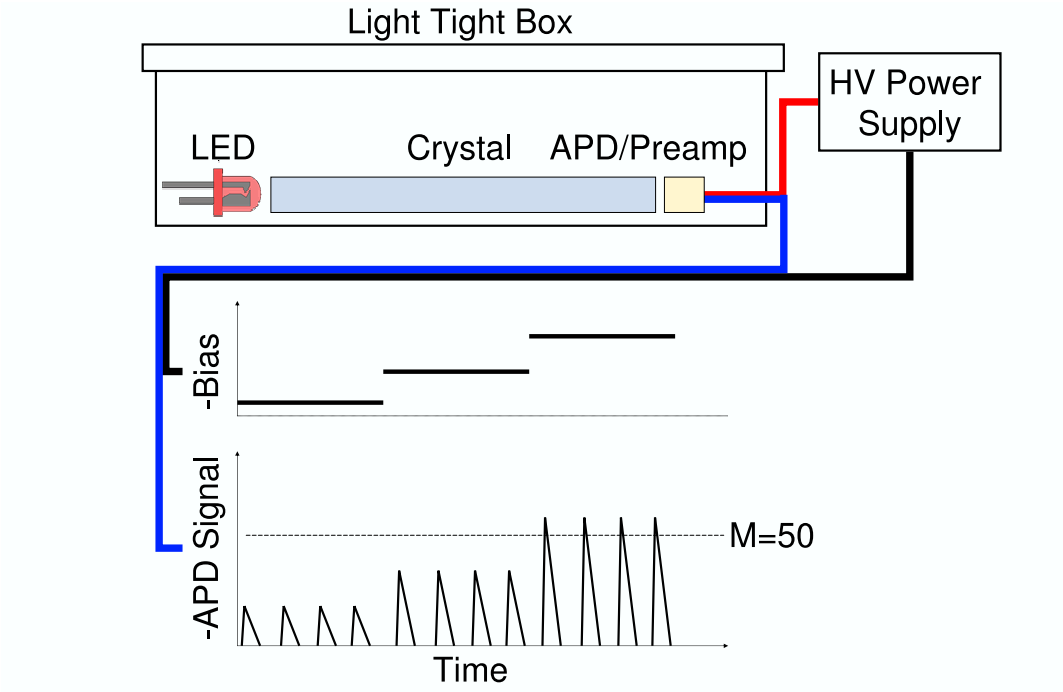

Figure 4.20: Diagram of the APD gain determination. The crystal gain reverse bias is varied until the output pulse amplitude met a gain of 50. The operation is repeated for each crystal. Typical reverse bias voltages range from 350 to 425 Volts.

well with data-sheets provided by Hamamatsu for each APD.

4.3.3 Survey of Mechanical Tolerances

The detector shells were prepared by several machine shops based around Champaign, IL[84, 85]. Before shipping the shells to Brookhaven the detector was assembled to verify that all the components fit together properly. The workmanship was high quality, but the test fitting exposed several areas where adjustments were needed. The test fitting was composed of two parts:

1. **Muon piston bore** A mock up cylinder was prepared by the PHENIX technical support group at BNL with the same dimensions as the muon piston bore and shipped to UIUC. The detector shells were

assembled inside this test cylinder to verify that shells would fit into the bore and leave enough clearance around the RHIC beampipe. The shells needed minor adjustments – mainly to ease installation.

2. **Crystal stack** The crystals were stacked in the shells. In several locations the detector "ribs" needed a few mil removed to allow all the crystals to be comfortably inserted.

Pictures of the test fitting are available in 4.21. In each preparation period the process of fitting and

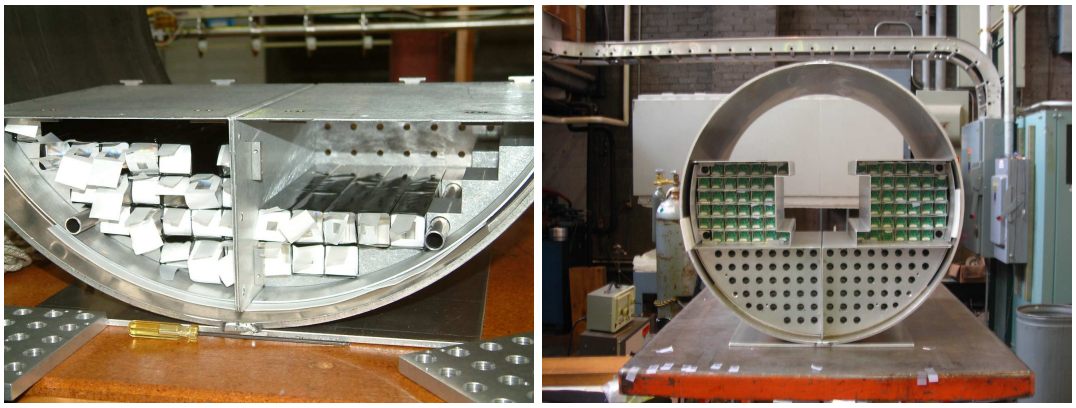

(a) Crystal stack in two "L" sections

(b) Partial detector stack in mock-up muon magnet hole

Figure 4.21: Photographs of the muon piston bore test fitting.

modifying was repeated several times. The process was sped up considerably by the close proximity of the machine shop and the support from two mechanical technicians from the nuclear physics laboratory.

4.4 Readout

An overview of the MPC electronics are shown in figure 4.22 For cost and time efficiency it was decided to utilize existing components of front end electronics. For the readout of the $PbWO_4$ scintillation light, an avalanche photodiode (APD) - pre-amplifier package developed for the ALICE experiment was used and for the back-end digitization and triggering, the standard PHENIX central arm calorimeter boards were used. Two pieces of custom electronics bridge the gap between them: the driver board and the receiver card[11]. An ADAM control module is mounted to the MPC electronics rack for bias voltage control and temperature monitoring.

[11] Stephen Boose and Salvatore Polizzo of the Brookhaven Physics Department designed both boards.

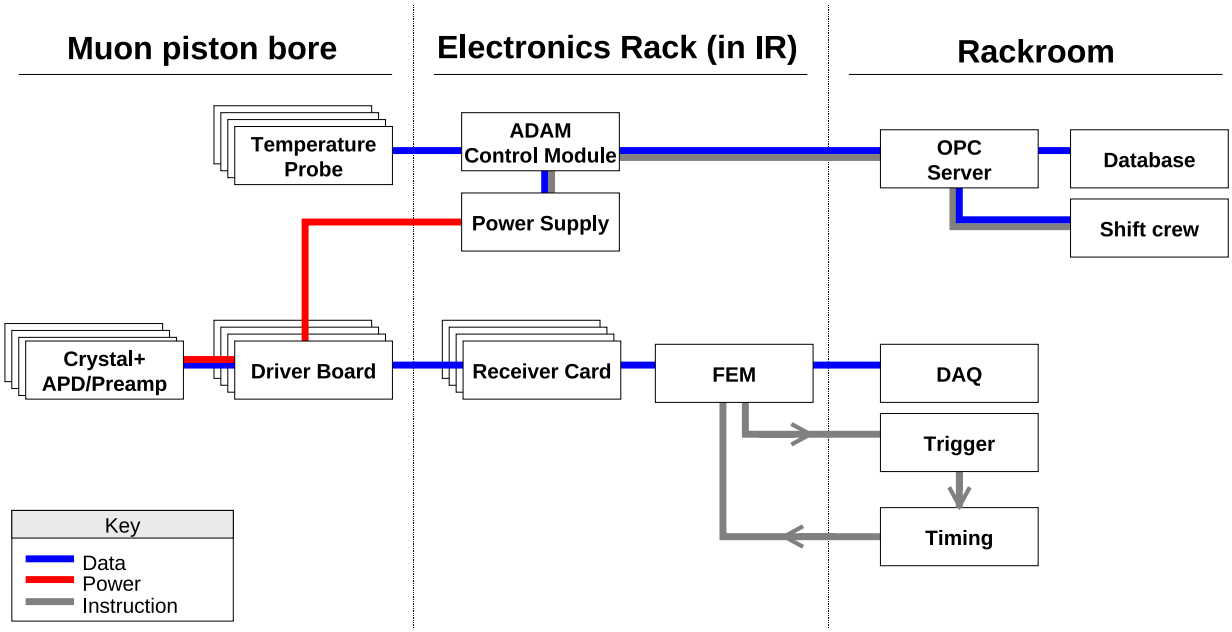

Figure 4.22: Overview of the electronics. See text for details of each component.

4.4.1 Driver Board

The driver board, shown in figure 4.23, supplies power to and reads signals from up to 24 APD/preamps. The boards are mounted to the front plate of the MPC inside the muon piston bore. The driver board is powered by an eight pin cable which includes several low voltages and two levels of high voltage. Connection to the preamps are done with short six-conductor Molex cables. The bias voltage delivered to each preamp is tunable using potentiometers. This set of potentiometers, one for each channel, allow an arbitrary bias to be selected between the two levels of high voltage delivered to the driver board. The potentiometers are controlled by small screws, i.e. they are set before installation and cannot be remotely tuned. The voltages delivered to each APD/preamp are set using the gains determined using the "standard candle" method described in section 4.3.2. The driver board's other function is to handle readout of the preamps. In contrast to the central arm calorimeter and the PHOS electromagnetic calorimeter of ALICE, it is not possible to position the digitization electronics close the towers of the MPC. The signal must be driven approximately 10 meters to an electronics rack in as noise-free way as possible. Therefore, the preamp signals are amplified by a factor of four and are sent differentially over twisted pair cables to the electronics rack. The receiver board subtracts the positive and negative signals from one another; removing, at first order, any noise induced on the line.

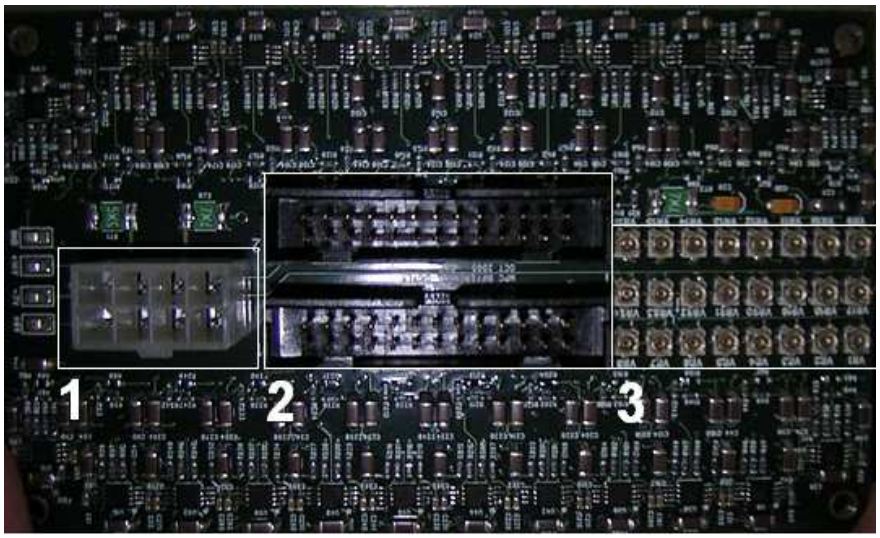

Figure 4.23: Driver board, 1) eight pin power cable delivering low voltage and two levels of high voltage. These voltages power the driver board and are passed to the APD's 2) twisted pair cable for data out, 3) individual potentiometers used to select an intermediate bias voltage between the two levels of high voltage. Connection to the individual towers are made on the reverse side of the board.

4.4.2 Receiver Board

The central arm calorimeter FEE is designed to accept fast analog signals from photomultiplier tubes[61]. The receiver board converts the differential signal sent from the driver board to a signal that matches the input specifications for the front end electronics of the PHENIX central arm. The board is a piece of custom electronics and which sits in a single width NIM module frame.

4.4.3 Front End Electronics

Analog signals, passed from the receiver board, are digitized and used to form a fast trigger signal in the front end electronics (FEE). The MPC FEE is made up of spare boards from the Central Arm Calorimeter. Four front end modules (FEM) make up the FEE: two for the south and two for the north. Each FEM can read the signals from 144 towers. The board configuration can be remotely controlled using `ARCNET`, the slow control and monitoring system for PHENIX FEM's. The basic features of digitization and triggering are described, but for more information see [61].

Digitization

Each FEM is composed of six Application-Specific Integrated Circuits (ASIC) cards which provide 12 bit analog to digital conversion of both the timing and pulse heights from 24 towers. The voltage waveform from a given tower is sampled once per RHIC clock (10 MHz) and stored in an Analog Memory Unit (AMU). In

addition, a waveform amplified by a factor of sixteen is also stored in a separate AMU cell. The amplified waveform gives us better sensitivity to low-energy pulses in the calorimeter. In addition to the low and high gain waveform, the timing information of the pulse is measured by ramping a voltage at the start of each clock tick and only stopping the charging if the input pulse exceeds a given discriminator threshold[12]. The time charge is also stored in the AMU cell. There is a ring buffer of 64 AMU cells which means that at any given moment the data from the present event and the previous 63 events is stored in the AMU buffer. The relatively expensive operation of digitizing the data is only done if the FEM receives a signal to digitize the data and transmit it to the DCM. If the trigger signal is not received, the charge stored in the AMU cells is discarded. Therefore, the trigger decision must be made before 64 clock ticks pass when the AMU ring cell starts overwriting the information stored from the previous cycle. An important component in the design of PHENIX is an agreement amongst all subsystems that their buffer be at least 4 μs (40 clock ticks) deep. Or, in other words, the PHENIX triggering system must decide whether to collect data from a given event within that time period.

The request to digitize data is issued by the trigger generated by GL1. However, the request to digitize and readout comes from the Master Timing Module which is distributed to the Granule Timing Modules and from there to the FEM's. When the request is received by the FEM, the current event's data is digitized as well as the wave form data from the event four clock ticks before the trigger. Including information from previous events measures a pedestal. This pedestal is different from the usual pedestal. The separation in time between events is a random variable. In some cases, the pulse from a previous event does not fully dissipate before an event of interest. Therefore, the waveform from a previous event is measured and then used to subtract it from the present event to find the true charge in a particular tower in a given event.

Trigger

Triggering is handled in the FEM by dividing the 144 channels into a 12 by 12 grid and forming analog sums of charge in blocks of 2x2 and 4x4. The details of the summing operation are elaborated upon in figure 4.24. There is one threshold for the 2x2 sums and three for the 4x4 sums: commonly refereed to as MPC_2x2, MPC_4x4A, MPC_4x4B and MPC_4x4C[13]. If the FEE's sole purpose were to digitize the tower signals, then the towers could be plugged into the FEE arbitrarily. However, the summing operations performed in the trigger complicate the channel input assignments since the sums are performed in a fixed order based on the input signals. Therefore, there is an 18x18 tower grid for each arm and electronics which form sums in a 12x12 grid. The simplest and first proposed implementation split the 18x18 grid into four quadrants

[12]The FEM supports both constant fraction and leading edge type discriminations.
[13]The central arm practice of ordering the trigger thresholds from lowest to highest as: C, A, B is continued in the MPC.

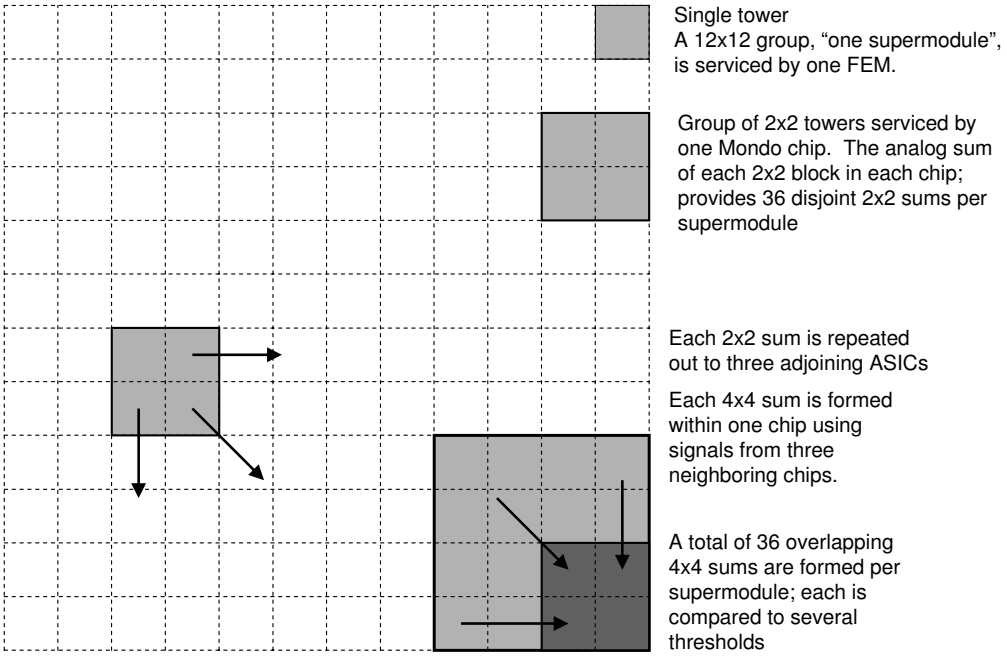

Figure 4.24: Diagram of ERT trigger setup. Taken from [61] and lightly modified.

serviced by four FEM's per arm. However, a creative alternative[14] requires only two FEM's per arm. The division scheme assigns one FEM to the inner 12x12 grid and another to cover the four outer flaps each of which is roughly 10x3. The division is illustrated in figure 4.25 [15].

Each FEM produces the four fast trigger signals (MPC_2x2, MPC_4x4A, MPC_4x4B and MPC_4x4C). Each arm has two FEM's, so the signals from the same arm are immediately OR'd using a NIM logic module at the MPC rack in the interaction region. Four signals per MPC are sent to the first level trigger crate. Most trigger input in PHENIX is sent to trigger-processors (LL1). The LL1 generate trigger primitives and send them to the central trigger crate. Alternatively, it is possible to input trigger primitives as TTL pulses to the so-called Reduced Bit Input Board (RBIB). The RBIB board sits in the central trigger crate and makes primitives available on the backplane for the central trigger processors. The MPC trigger primitives consist of five bits where each bit is the OR between north and south MPC trigger signals for the 2x2, 4x4A and 4x4C signals; and the arm-separated signals for the 4x4B trigger. The triggering system is described in detail in reference [86].

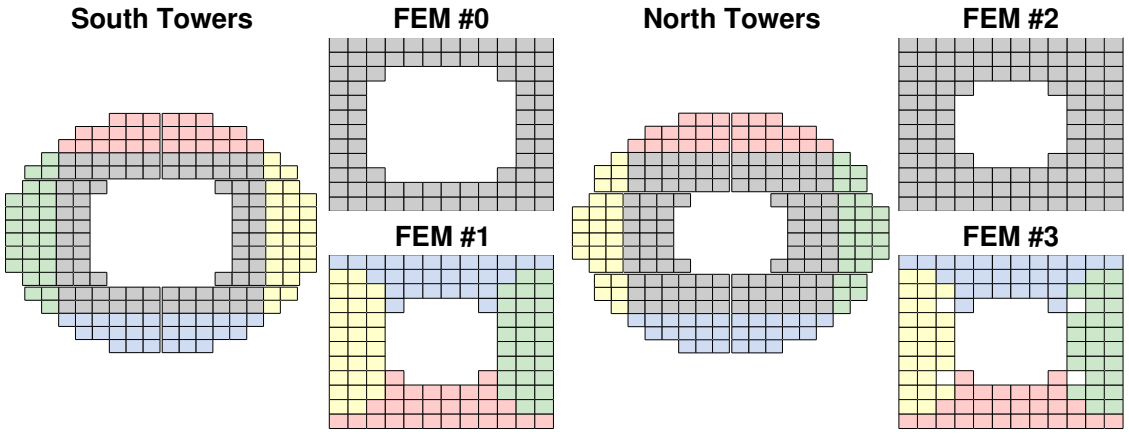

(a) South (b) North

Figure 4.25: Each figure shows the mapping between physical space (left) and the electronics space (right). Signals from the inner 12x12 grid are handled by one FEM and the remaining signals are handled by another FEM. The colors show how the different blocks of towers map from physical to electronics space.

[14] Proposed by Terry Awes of Oak Ridge National Laboratory.

[15] Notice that the inner block of each FEM is left unused. This is in contrast to the central arm calorimeter where every channel of the FEM is used. This difference allowed us to boards of overall good quality, but with a bad tower or two in the middle.

Raw Data

The data taken by the MPC is synchronized with the rest of PHENIX which makes correlation analyses possible. From any given event the MPC data available to the analyzer is:

- The five trigger bits: 2x2, 4x4A, 4x4C, 4x4B North, 4x4B South.
- The AMU cell number (which of the 64 cells was used to store the waveform data).
- For each tower: the raw timing information (TDC, 12 bits), the pedestal information for the charge measurement: high gain pre, low gain pre (12 bits) and the raw charge information for both gains (12 bits).

Where the post and pre refer to the event of interest and the event four clock ticks before the event of interest.

4.5 Integration

4.5.1 Slow Control

Slow control is done using a commercially available ADAM controller module which sits in the MPC rack. The controller: sets and monitors the MPC high voltages, reads out temperature probes mounted in and around the MPC, and controls the power to the entire MPC rack. In the rare case where a component of the rack (for example the FEM to `ARCNET` instructions) fails to respond, the ADAM controller can be used to power the rack on and off to reset all of the electronics.

Communication between the ADAM controller and its control/readback server, called the OPC server, is done over an RS-485 line. The server automatically logs the temperatures and high voltages values in a MySQL database, and provides the shift crew with a graphical interface.

The MPC rack is wired with heat activated fire alarm wire which cuts power to the rack in the case of a trip. In addition, the PHENIX experimental area/hall is rigged with smoke sensors.

4.5.2 Online Monitoring

The MPC online monitoring displays output from the LED monitoring system, and raw ADC and TDC distributions from both minimum bias and MPC triggered events. The monitoring system is designed to detect hardware failures as well as operational issues. In addition, the output is automatically archived which enables the on-call expert to easily check for trends or problems with the data.

4.5.3 Online Calibration

The MPC LED monitoring system analysis is run in the online calibration framework (described in section 3.5). The full analysis is described in section 5.4. The software automatically enters the data into a database and writes various summary files for further analysis.

4.6 Reconstruction

The reconstruction procedure converts the energies measured in an array of towers to photon and electron impact positions. It is summarized as follows:

1. **Domain finding:** Finds all towers above a 10 MeV noise threshold, and group them into clusters of adjacent towers.

2. **Peak finding:** Finds all the towers in the domain with energy greater than 100 MeV, and are not next to another tower meeting the threshold. It is possible that one domain contains multiple peaks.

3. **Fitting:** Fits the measured distribution of energy between towers to the electromagnetic shower shape (see next section). The electromagnetic shape is determined from simulation, but it agrees to simulation well. The shower shape is defined both by a central value and the variance around the central point. The resulting χ^2 value parametrizes the "electromagnetness" of the shower.

More details of the clustering algorithm can be found in the documentation for the Central Arm Calorimeter (reference [87]). Our procedure is based on the central arm code, and only lightly modified. The most significant change is that showers near the edge of the detector leak a portion of their energy outside of the instrumented volume. Clusters with reconstructed positions near the edge of the detector are corrected for this leakage using parameters extracted from simulations. The analyses of this thesis avoid the uncertainties introduced by the leakage correction by restraining the allowed cluster radii to less than 18 cm. This leaves approximately one tower unit of buffer between the cluster position and the edge of the detector. An important input to the clustering algorithm is the shower shape whose extraction is presented next.

4.6.1 Beam Test

Setup

A beam test is a controlled experiment where identified charged particles of known momentum and tracks are fired at a detector whose response is measured. Our beam test provided us with several critical measurements:

- Energy linearity: Confirming that the detector's output pulse height's are linear with the injected energy.
- Energy resolution.
- Electromagnetic shower shapes (explained in 4.1).

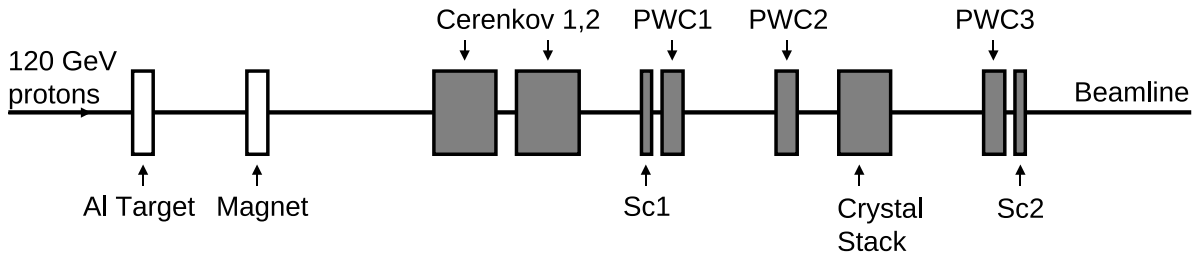

Figure 4.26: Diagram of FNAL MTBF beamline. 120 GeV protons from the Main Injector hit an aluminum target, producing charged particles. A magnet selects the particles of a given momentum, and their particle ID is found using a pair of threshold Cerenkov counters. The particle tracks are found using a set of three proportional wire chambers (PWC1, PWC2, PWC3). Events are triggered using coincidences between a pair of scintillators (Sc1, Sc2) on either side of a crystal stack.

The beam test setup consisted of an eight by seven crystal stack and a light-tight box. They were prepared and taken to the Meson Test Beam Facility (MTBF) at Fermi National Accelerator Laboratory (FNAL) for a test beam. The test beam was a secondary beam from 120 GeV protons of the Main Injector on an aluminum target. Charged particles of a given momentum were selected by magnets whose aperture allowed only a narrow range of momentum. The charged particles were characterized using: a pair of threshold Cerenkov counters for particle identification; two pairs of scintillator paddles for triggering; three sets of proportional wire chambers for straight line tracking. The beam came in four second spills every two minutes with a spot size of approximately four centimeters. Data was taken at six beam energies: 4, 8, 16, 33, 66, 120 (proton only) GeV, and with either a Cerenkov coincidence for an electron sample or without one for a hadron sample. A figure of the beamline is shown in figure 4.26 and more details on the facility are available in reference [88]. The test-setup is shown in figure 4.27. The crystal stack was mounted on a table capable of moving in both axes perpendicular to the beamline. Using the table the detector was scanned through the beam. The pre-amplifier and crystal response are sensitive to temperature so the temperature was before and after each exposure to beam.

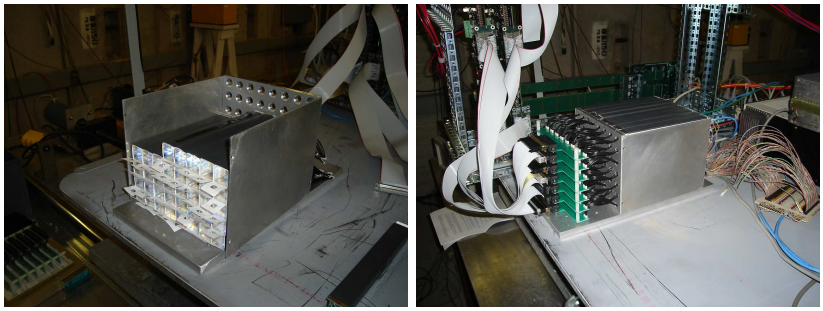

(a) Loading the eight by seven crystal stack

(b) Crystal stack without cover exposing the Molex readout cables

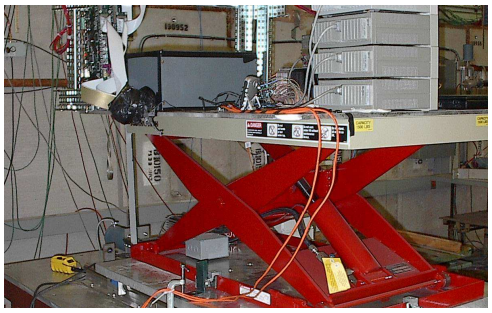

(c) Test beam stack (gray with black trim) on x-y scannable test stand between exposures

Figure 4.27: Photographs of the test beam setup in various stages of readiness.

Energy Linearity and Resolution

The detector's linear response to energy was verified by collecting data at several different energy settings with the electron Cerenkov trigger coincidence. The distribution of reconstructed cluster energies are shown from each beam energy setting in figure 4.28(a). There is a sharp peak in reconstructed energy at the incident beam momenta corresponding to electrons. The distribution is fit with a first degree polynomial and a Gaussian. The resulting Gaussian peak positions are plotted versus the beam energy in figure 4.28(b). The figure shows that, as expected, the response is linear with the energy of the beam. If there were a non-linear response, it would complicate the detector reconstruction algorithm. The Gaussian peak widths divided by the beam energy are plotted against the beam energy in figure 4.28(c). The energy resolution of a calorimeter is discussed in greater detail in section 5.5.2 and in reference [69]. The energy resolution is found to be $\sigma(E)/E = 14\%/\sqrt{E} + 3\%$.

Electromagnetic Shower Shape

The electromagnetic shower shape is extracted by combining the deposited energies in each tower and the incident electron's position. The shape is extracted by filling a two dimensional histogram with axes: deposited energy in a tower divided by the incident electron energy and distance from tower center to incident electron position. The electron position is known both from an outside source (the tracking chambers shown in figure 4.6.1) and from the reconstructed positions measured by the calorimeter. The shower-shape using both position measurements are shown in figure 4.29 and are essentially equivalent. Not shown in the figure are the fluctuations in the deposited energy which are important when forming the χ^2 values mentioned in the previous section.

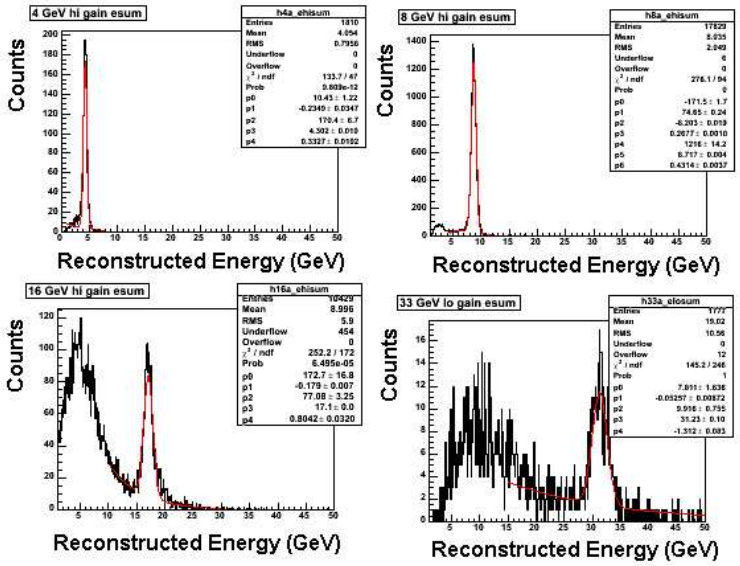

(a) The energy distribution from reconstructed clusters at beam energies of 4, 8, 16 and 33 GeV, and first degree polynomial + Gaussian fits.

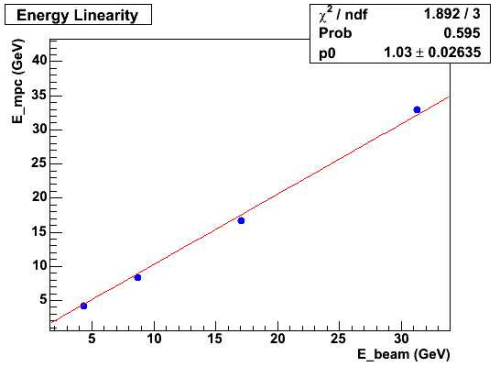

(b) The Gaussian peak positions plotted against the beam energy, and fit with a straight line.

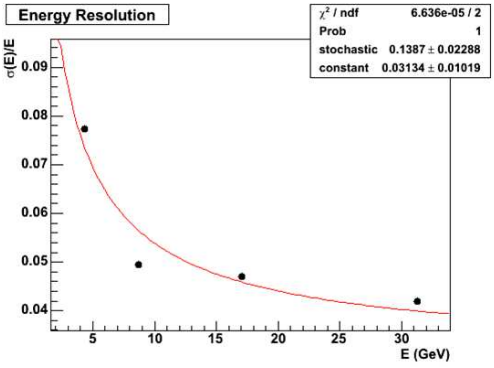

(c) The Gaussian peak widths divided by beam energy plotted against the beam energy, and fit with: $a/\sqrt{(E)} + b$.

Figure 4.28: Results from the energy linearity and resolution analysis.

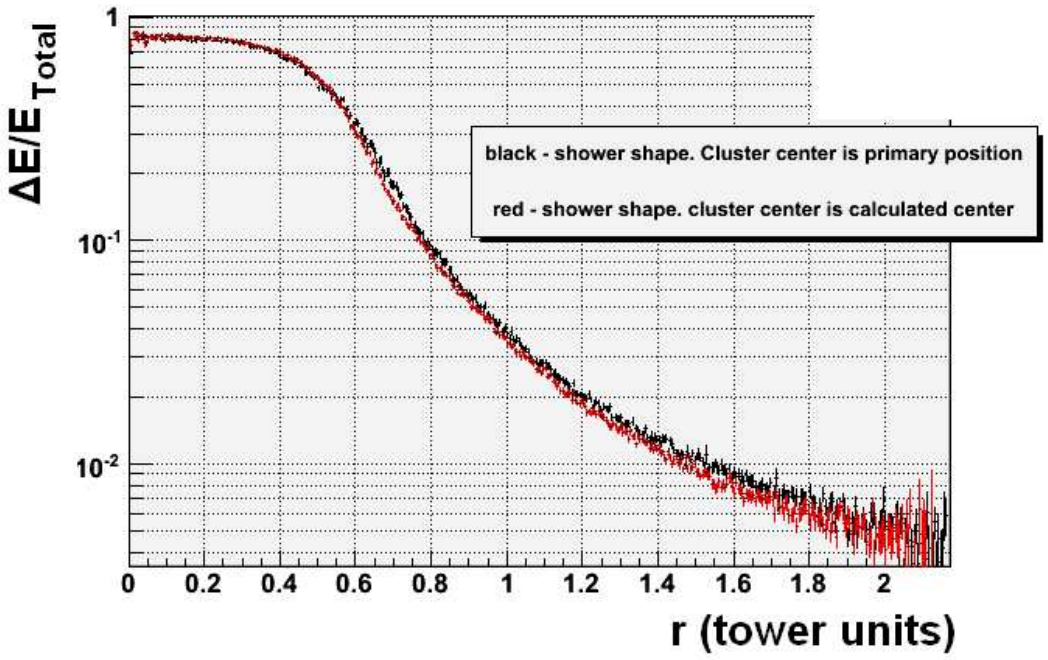

Figure 4.29: The electromagnetic shower-shape of electrons measured using electron positions reconstructed with the tracking chambers and with the calorimeter itself.

4.7 Summary

This chapter has reviewed all steps in the creation of the Muon Piston Calorimeter forward electromagnetic calorimeters. The results are illustrated in figure 4.30.

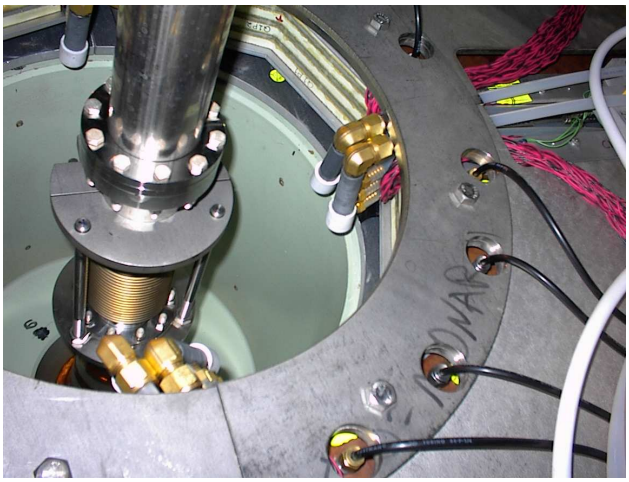

(a) South piston hole before installation.

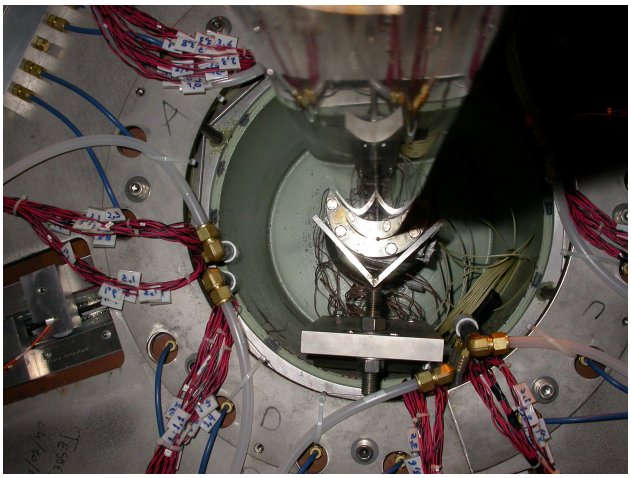

(b) North piston hole before installation.

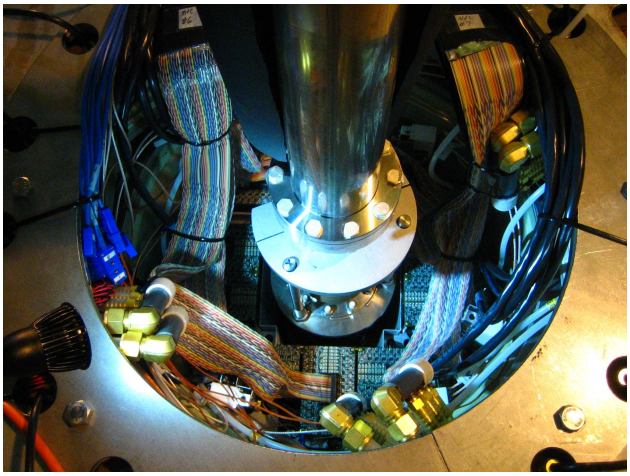

(c) South piston hole after installation.

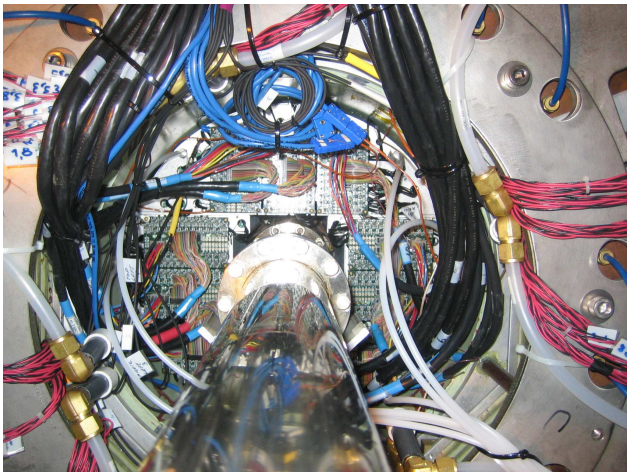

(d) North piston hole after installation.

Figure 4.30: Photographs of the muon piston holes before and after the Muon Piston Calorimeter Upgrade.

Chapter 5

Muon Piston Calorimeter Energy Calibration

5.1 Overview

The output of the MPC front end electronics consists of digital charge and time information that needs to be translated into energy and time. The energy calibration is done with an analysis of the energy deposited by minimum ionizing particles, an inverse slope analysis, and with an LED-based monitoring system. The invariant mass peaks from π^0 and η mesons are used to confirm the detector's energy calibration and stability. They are also compared to simulation and shown to agree well.

For each event and each tower, the uncalibrated energy is converted to energy as:

$$E_i = G_i(t_0) \cdot R_i(t) \cdot ADC_i \tag{5.1}$$

where:

- i stands for a given tower.
- E is the calibrated energy deposited in a tower.
- $G_i(t_0)$ is the tower's absolute gain defined for one reference time, t_0.
- $R_i(t)$ is a relative gain between a reference run and all other times. The smallest time interval used in analysis is one run.
- ADC_i is defined as:

$$ADC = ADC_{post} - ADC_{pre} - (ADC_{post,pedestal} - ADC_{pre,pedestal}) \tag{5.2}$$

The determination of these calibrations factors is explained in this chapter.. The overall calibration scheme is shown in figure 5.1. An important point to remember is that while the MPC shares many similarities to the central arm electromagnetic calorimeter, its location is very different. Experience and assumptions

from the central arm calorimeter may not transfer well to the forward region. For example, different from a calorimeter a mid-rapidity: Energy $\neq p_T$, or energy $\neq$ C p_T. The correct relation at forward rapidity is: energy = C(η) p$_T$. C(η) changes by roughly a factor of 3 between the inner and outer edges of the detector. The calibration consists of four main pieces:

1. Calibration of the ADC and TDC integrated in the EMC front end electronics (FEE).

2. Determination of the absolute energy scale (G$_i(t_0)$). $G_i(t_0)$ is determined for each tower and each fill using the energy deposit from minimum ionizing particles (MIP). The statistical uncertainty for each tower and fill is $\sim$10%. If a MIP fit fails, the gain is estimated using an inverse slope method.

3. $R_i(t)$ is measured using an LED-based monitoring system. In contrast to the MIP calibration, the statistical uncertainty for a given tower and run is approximately 2%.

4. Confirmation of the absolute and relative calibrations is done in three steps using the physics observables: clusters and pairs of clusters.

   (a) Identification of mis-calibrated towers (warnmap). This is done by generating a list of badly calibrated towers based on a plot of the number of tower hits versus the tower radial distance from the beampipe. The outliers are found using an LTS regression fit.

   (b) Monitoring of detector stability. Two photon invariant mass peaks are fit to extract the π^0 and η peak positions as a function of time and to check that they are constant.

   (c) Comparison of the π^0 and η peak properties between data and Monte-Carlo simulations.

5.2 Front End Electronics Calibration

The Front end electronics (FEE) calibration consists of three steps:

- Determining the ADC's pre and post pedestals.
- Finding the high to low gain conversion factors.
- ADC and TDC overflow determination

5.2.1 Pedestals for the ADC Pre and Post Readout

A tower's raw uncalibrated energy is determined by subtracting two digital charges from the same channel but from different times. The pre-charge is measured from an event four clock ticks before the post-charge.

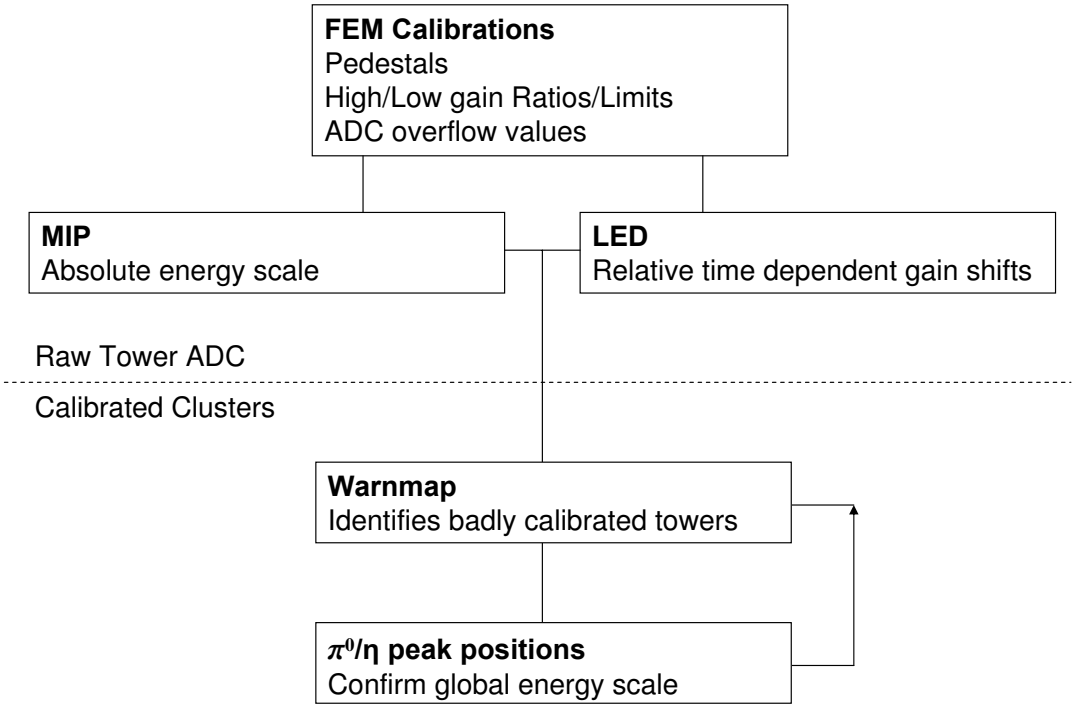

Figure 5.1: Outline of the MPC energy calibration procedure.

The post-charge is the charge from the triggered event. Two charges rather than one are measured in case the tower's charge is not fully dissipated from a previous event. The motivation and digitization chain are more fully described in section 4.4.3.

The pedestals are stable over the course of an entire run (e.g. Run-8). They are found from collecting data while the detector is ready for physics data but there is no beam in the ring, and with a noise trigger.

5.2.2 High to Low Gain Conversion Factors

Two ADC values are available for a given tower and event. The first is called low gain ADC and the second high gain ADC. The conversion from high to low gain is done with a tower dependent relative gain factor, C_i:

$$ADC_{low,i} = C_i \cdot ADC_{high,i} \tag{5.3}$$

Determining C_i is first step in the calibration. The second goal is to determine the end point of the dynamic range of the high gain ADC. Both parameters are illustrated in figure 5.2. The high to low gain conversion

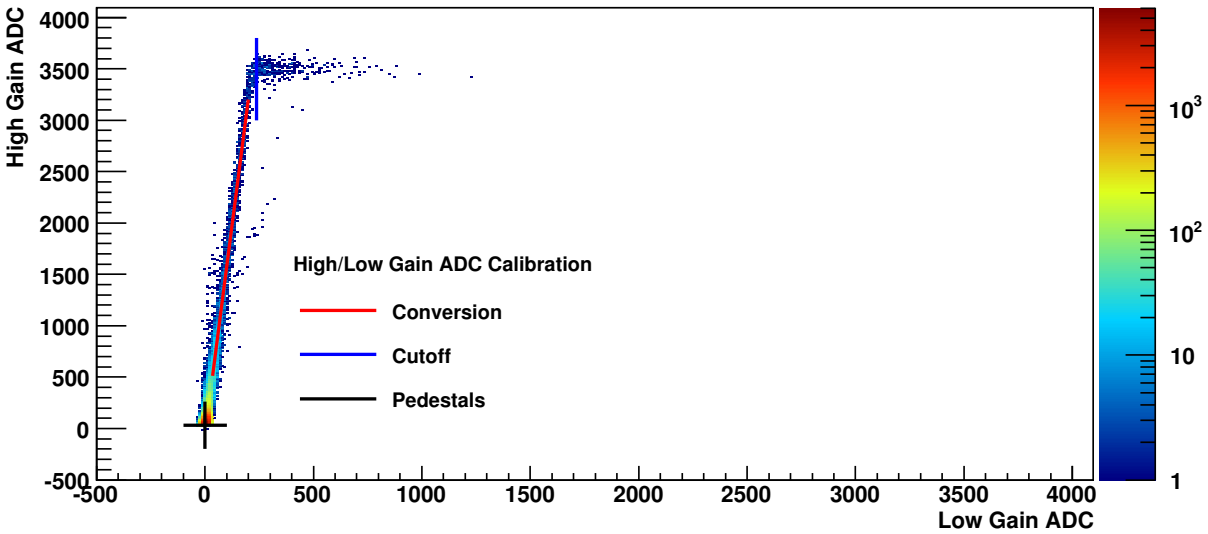

Figure 5.2: High to low gain correlation plot. Line overlays correspond to the pedestals (black) which have already been subtracted, the conversion between high and low gain (red) and the high gain cutoff value (blue).

factors are found by generating a correlation plot between the high gain ADC and the low gain ADC. The high to low gain conversion is found by fitting the correlation plot between 0 and the high gain cutoff value with a straight line. The line's slope is the conversion factor. The expected value is about 16.

5.2.3 ADC and TDC Overflow Determination

The last FEE calibration determines the low gain ADC overflow value and the TDC timeout value. For the 2008 data collection period they are determined in different ways, but the goal is the same: determine the point at which the histogram of the ADC or the TDC counts spike at high values. The discussion provides some detail for the TDC overflow values. A similar procedure is used to find the ADC overflows in section 8.1.1. First, for each tower TDC time histograms are generated. The histograms are generated from the Minimum Bias and MPC triggered datasets separately. For each tower's histogram, the content of each bin above a TDC value of 2000 is inspected. If the bin content exceeds 1% of the total histogram population, the bin is an overflow bin candidate. Next, the integral of the histogram contents several bins beyond the candidate to the end of the histogram is formed. If integral stays below 10% of the total histogram's population, then the candidate bin is accepted as the TDC overflow bin. Figure 5.3 shows an example output plot from the procedure. The overflow values are summarized in figure 5.4.

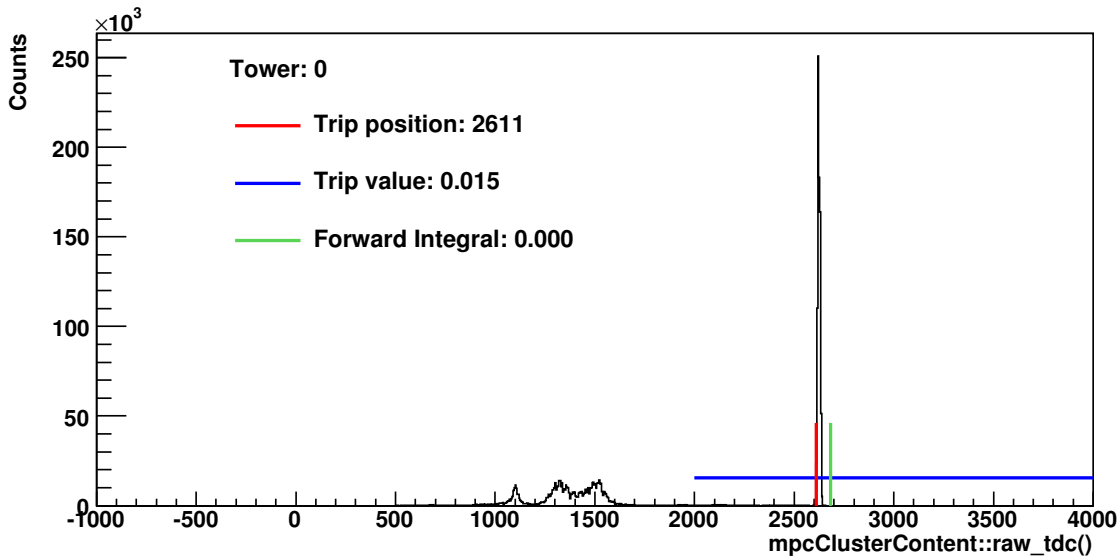

Figure 5.3: Tower 0, Trigger: MPC, TDC time spectra. Line overlays correspond to the algorithms chosen timeout value (red), 1% threshold point (blue). No entries are found in the histogram bins above bin 2700 which is marked by the green line.

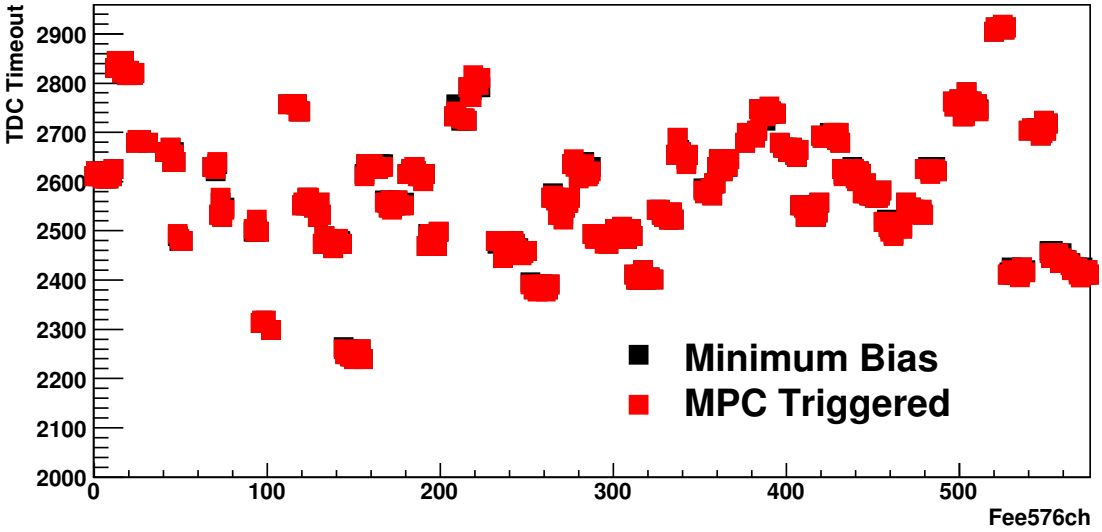

Figure 5.4: Vertical axis: TDC timeout points. Horizontal axis: tower number. MPC South towers are from bins 0 to 287. MPC North towers are bins 288 to 575. The values are shown to agree between the minimum bias and MPC triggered datasets.

5.3 Absolute Energy Scale Calibration

5.3.1 Description

The absolute energy scale is determined by finding the position of minimum ionizing particle peaks in histograms of energy deposited in MPC towers. The position is expected at 234 MeV. The method was originally developed for a two day run at $\sqrt{s} = 62GeV$ with $p^{\uparrow}p$ in 2006[27]. The method was further refined for run08 but its essential elements remain unchanged. If a peak position is not found, then an inverse slope method is used to determine a tower's gain.

5.3.2 Minimum Ionizing Particle Energy Deposits

The distribution of MIP energy deposit is studied by generating histograms of high gain ADC response for each tower and each fill. Cuts, designed to enhance the yield of charged tracks, are applied to each histogram. Two variables are used to enhance the MIP signal:

1. High energy bit sum – number of active towers surrounding a given tower. Maximum is nine. Electromagnetic showers are expected to have a high bit sum while MIP's should have low bit sums. See figure 1 for an illustration. The definition of a "hit" MPC tower is greater than zero counts high gain ADC value.

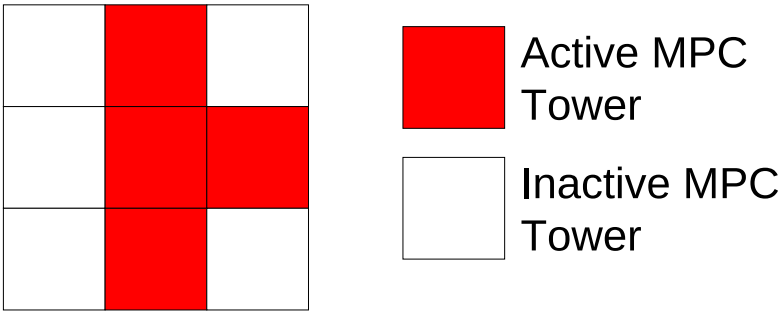

Figure 5.5: Illustration of the high energy bitsum. The bitsum for the central tower is 4

2. dR – distance from the nearest active BBC detector element to a track drawn from the MPC tower to the collision point. An active BBC detector element is defined as an element with both its TDC values less than 2700 counts. See figure 5.6 for an illustration.

For each tower, a two dimensional grid of histograms is generated by cutting against the dR and bitsum variables independently. The grid of histograms is searched from most selective to least selective cut for a good MIP peak fit, and the search is stopped as soon as one is found. The function used to fit the MIP energy deposit is a power law plus a Gaussian. Good fits are defined using the following criteria:

1. Number of counts within the fit-range > 100
2. $\chi^2_{reduced} < 10$
3. Minimum ionizing particle peak fit amplitude > 0
4. $11 <$ Minimum ionizing particle peak position < 40
5. Minimum ionizing particle peak width < 11

The number of MPC towers is only 416, so visual inspection of the fitting has been carried out. In some cases the definition of a good fit is adjusted. An example peak is shown in figure 5.7

5.3.3 Inverse Slopes Method

The MIP analysis works well to determine the gain of towers. However, in some towers the MIP fit consistently fails for all fills. In these cases the inverse slope analysis is used. The inverse slope analysis fits makes use of the fact that a tower's energy spectra, S(E), can for sufficiently large energies be parametrized by:

$$S(E) = a \cdot E^b \tag{5.4}$$

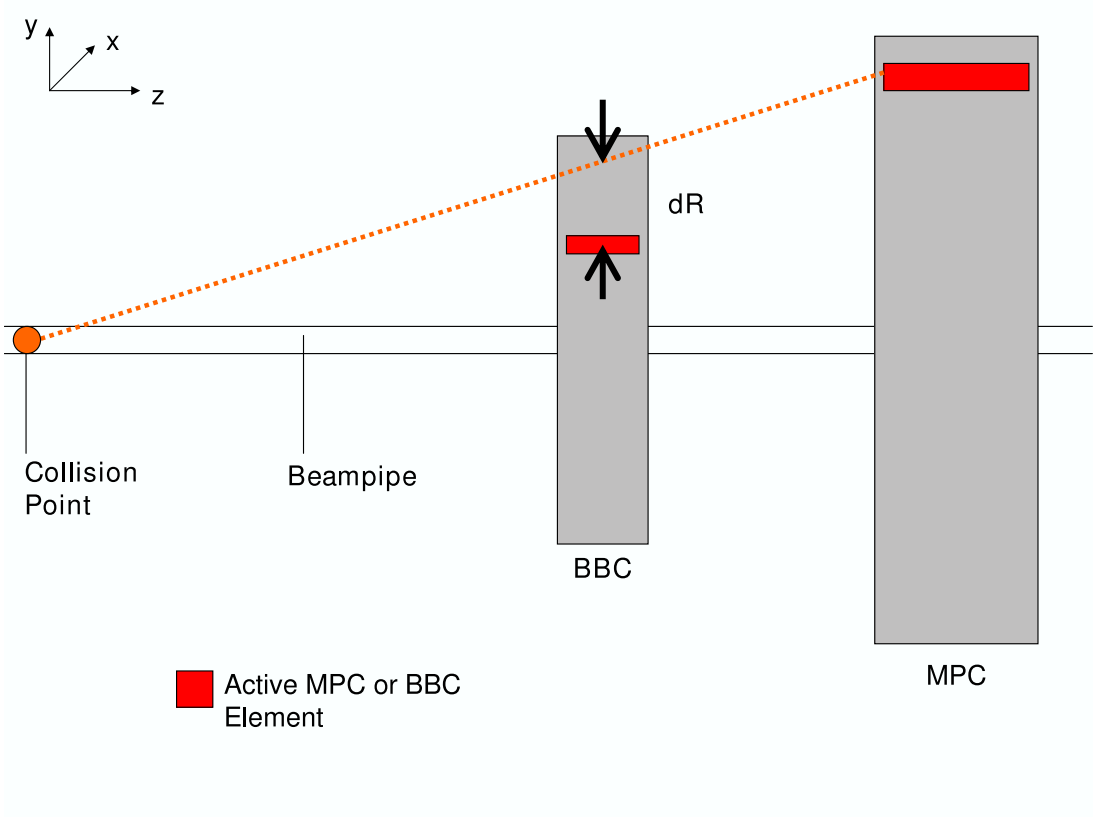

Figure 5.6: Illustration of the dR variable.

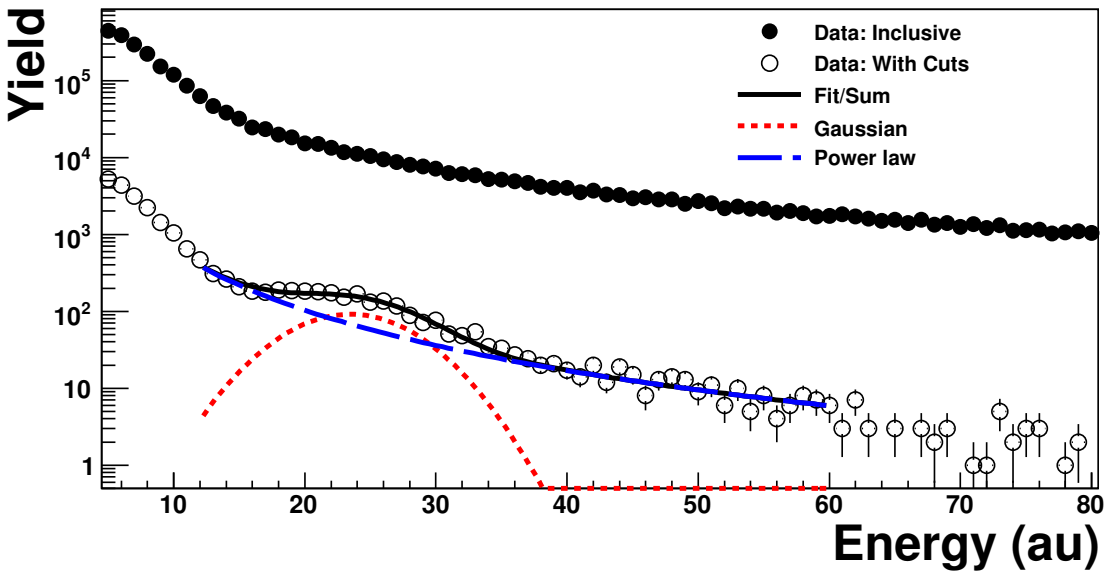

Figure 5.7: Example MIP peak from tower 270 and fill 9919. The filled points are the inclusive spectrum and the open points are after applying the coincidence cut with the BBC and the bitsum cut.

where the parameters b characterize the gain of a particular tower. An example fit is shown in figure 5.8. The major drawback of the procedure is that the extracted gain parameter is only relative. To determine

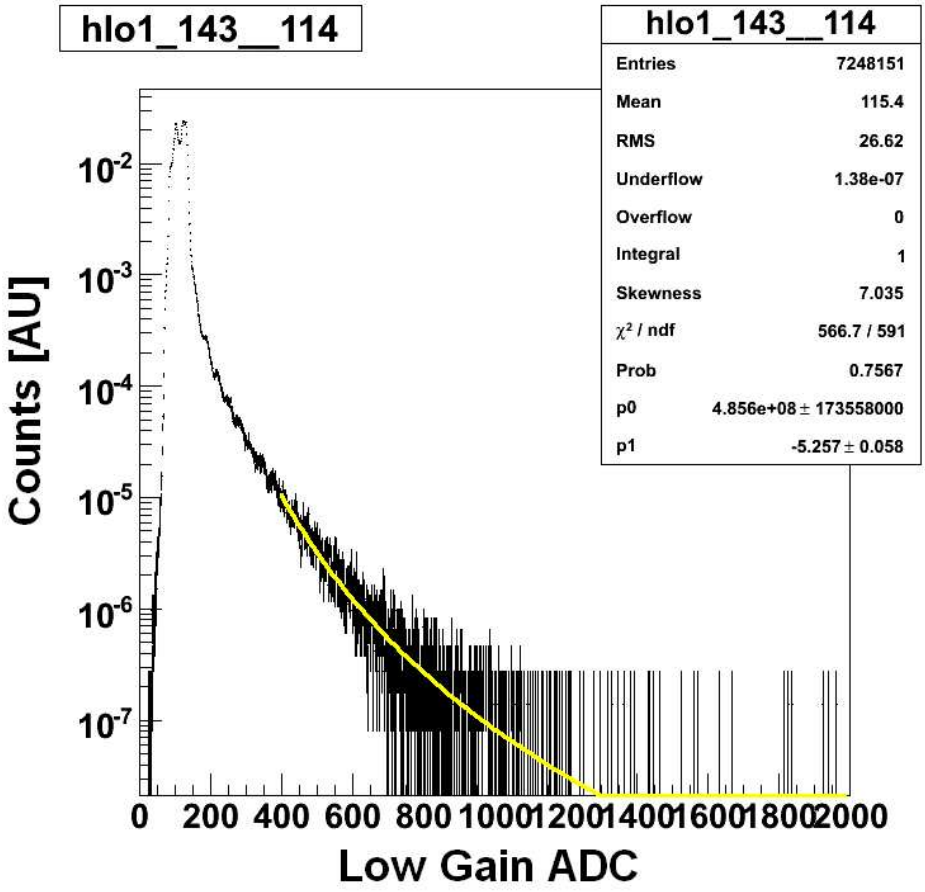

Figure 5.8: Example for an inverse slope fit with $S(E) = aE^{-b}$ from tower 143.

the constant of proportionality between the relative gain and the absolute gain, the correlation between the inverse slope analysis (parameter b) and the MIP peak position is used. Then, this correlation is used to estimate the MIP value of a tower with only the inverse slope. The correlation plot is shown in figure 5.9. The inverse slope values are affected by the pseudorapidity of the tower. Therefore, the correlations are binned in tower radius.

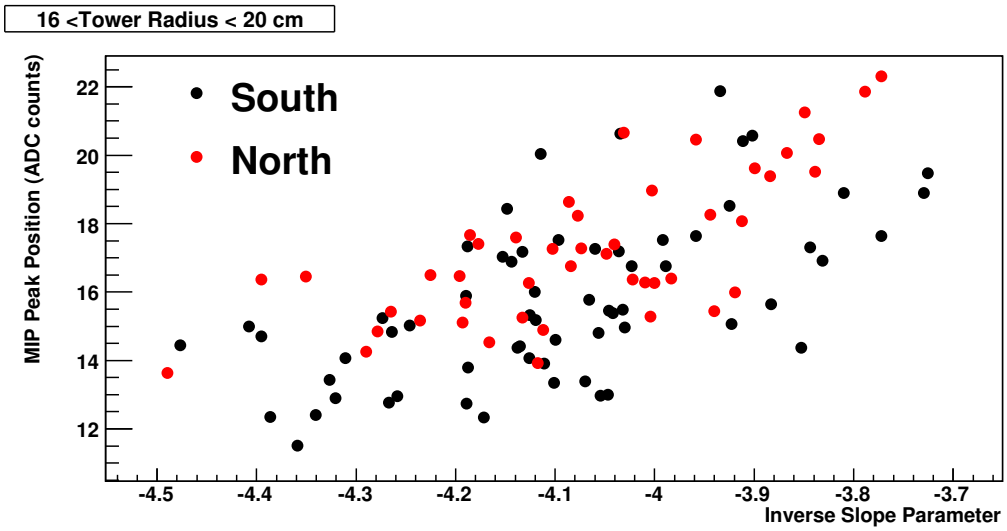

Figure 5.9: Correlation between the inverse slope parameter and the minimum ionizing particle peak position. Each point corresponds to a single tower's inverse slope and MIP position averaged over all of Run-8. The correlation plot is separated by arm, and is consistent between them.

5.4 Relative Gain Changes

5.4.1 Description

There are two major effects which cause the gain to change with time. The first is temperature. During steady-state running the temperature is essentially constant, but when the current in the muon magnets is shut off (i.e. for an access day) the temperature of the muon magnets and the MPC drop rapidly. After the magnets are turned back on, the whole apparatus warms up over a period of days to weeks. Both the light-yield of the $PbWO_4$ crystals and the gain of the avalanche photo-diodes (APD) change with temperature. For the APD the temperature coefficient has been measured to be -2%/° Celsius change in the gain [89]. The second major time-dependent effect is related to radiation damage. With increasing time into the run the amplitude of the MPC tower's response to LED light pulses decays. However, once the run is over the LED signals gradually return to their previous values [89][1]. Both effects are shown in figure 5.10. The full details of the MPC LED monitoring system are given in the PHENIX technical note [89]. The LED system appears to track the MPC gain quite well; applying an LED-based gain correction removes time-dependent shifts in the π^0 and η peak positions. However, the LED system should not in general be trusted blindly. The MPC LED system injects light at one end of the crystal and is collected at the other end using an APD. Therefore:

[1]This can be explained by radiation induced crystal defects which reduce the mean free path of light anneal with a long time constant

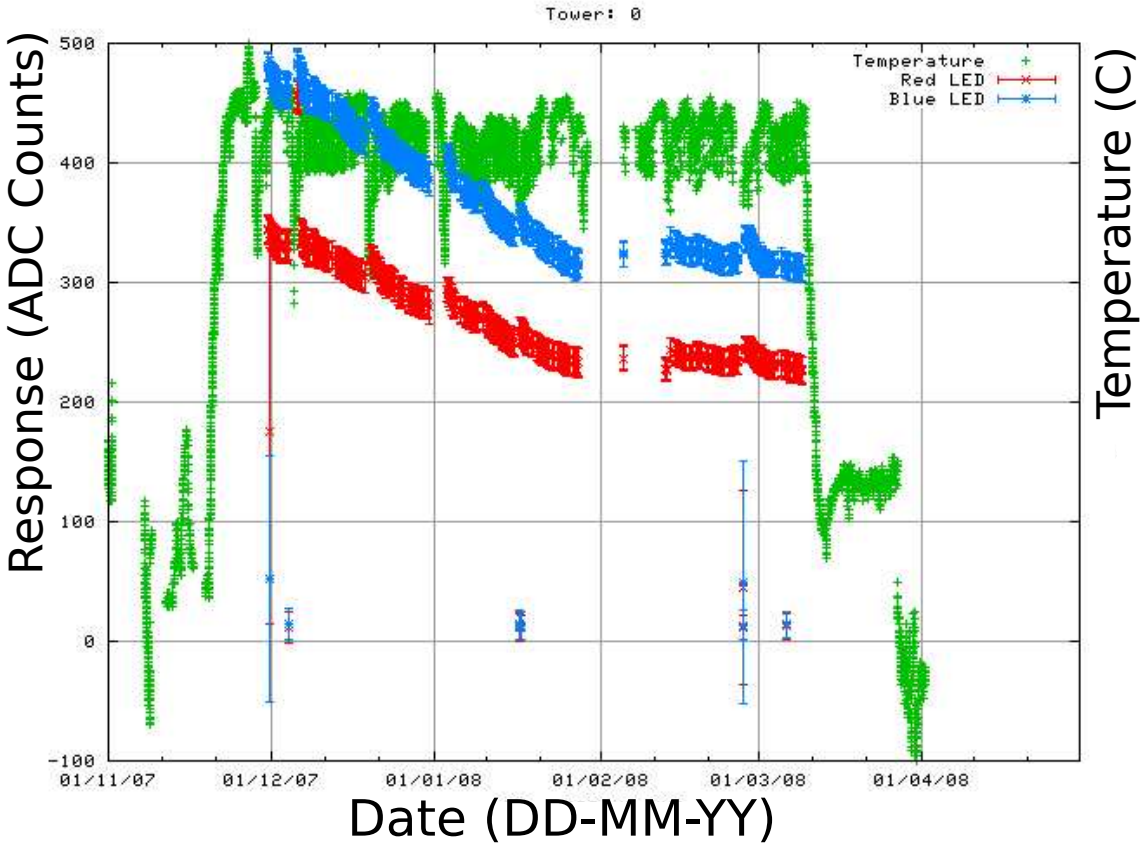

Figure 5.10: The raw ADC response for tower 0 for red and blue LED light shown in red and blue and the temperature of the MPC (green) plotted against time. The full-scale time window corresponds to the entire 2008 run (dA+pp). There is a large drop in gain over the run which suggests radiation damage and also spikes in increased gain caused by temperature drops in the muon magnet system. The muon magnet currents are not shown on the plot, but the periods of decreased temperature correspond to access days.

1. The scintillation light-yield of the crystal is not probed. Any effects related to loss of light yield over time cannot be detected by an LED-based system. Potential effects are temperature and radiation damage.

2. The LED light propagates the entire length of the crystal while the scintillation light from electromagnetic showers is generated randomly and according to the energy deposit within the calorimeter cell.

For all periods of data-taking, the LED system flashes the towers a rate of 2 Hz. For each run and each tower, a histogram is generated of the low gain ADC counts. An example plot is shown in figure 5.11. The LED response for an individual tower and an individual run is taken as the mean of the distribution, $\langle ADC \rangle_{LED}$. The relative change of the LED response between runs represents the chain in gain and can be used to correct for time-dependent gain variations.

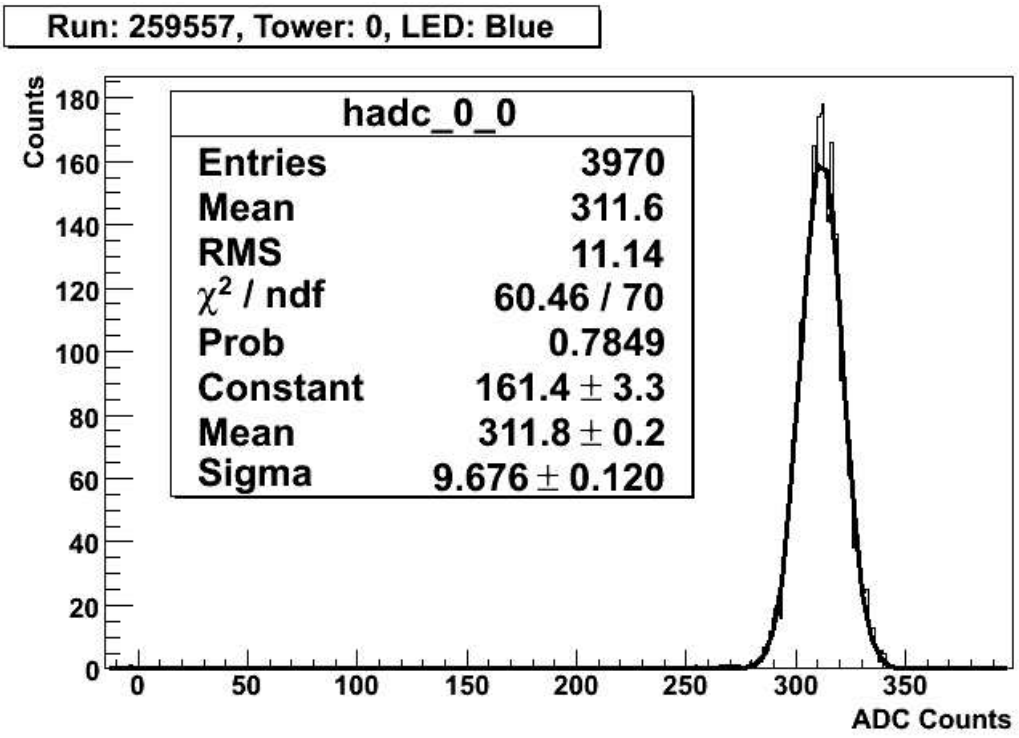

Figure 5.11: Vertical axis: Counts, Horizontal axis: ADC counts from LED-triggered events from run number 259557 and tower 0.

5.4.2 Implementation

The MPC LED calibration is implemented in the PHENIX online calibration system. Histograms and text files are automatically generated. In addition, the results of the calibration are automatically stored

in the PHENIX calibrations database. The stability of the detector within a given run is checked by calculating sub-run averages of the LED response and calculating the χ^2/NDF value of the sub-run means to the mean over the entire run. The detector is shown to be stable within a run. The LED analysis is carried out separately for the red and blue LED light. Four values are stored from the LED analysis in the PHENIX database: $\langle ADC \rangle_{Blue}$, $\langle ADC \rangle_{Red}$ and the LED response normalized to the output of a reference pin diode that monitors the stability of the LED over time ($\langle ADC_{Blue}/ADC_{Pindiode,Blue} \rangle$ and $\langle ADC_{Red}/ADC_{Pindiode,Red} \rangle$). analysis. None of the four values is directly used in analysis. Instead, a smoothing algorithm is used to determine smoothed relative gain corrections with respect to a master reference run. The smoothed relative gain correction values are entered into the database.

5.5 π^0 and η two-photon peaks

This section's goal is to confirm the calibrations performed with the minimum ionizing peaks and the LED-based monitoring system. The first two sub-sections discuss general properties of the detector which are important to understanding aspects of its performance. The remaining sub-sections provide data and comparison between data and Monte-Carlo. Comparison to Monte-Carlo is based only on Minimum Bias triggered data to avoid effects from the trigger event selection which has yet to be properly implemented in the simulations.

5.5.1 Minimum Reconstructible Mass

For the following discussion it is assumed that a photon pair of invariant mass $m_{\gamma\gamma}$ is generated at the collision point distance z away from the surface of the MPC. The photons hit the MPC surface at (x_i, y_i) and deposit energy E_i. The clustering algorithm has a minimum cluster separation distance beyond which it cannot separate clusters. This distance is approximately 2.6 cm (the tower size is 2.2 cm). This minimum cluster separation sets a minimum opening angle on the cluster pairs, and therefore an energy dependent minimum reconstructible mass according to the formula:

$$m^2_{\gamma\gamma} = 2E_1E_2(1 - cos(\theta)) \tag{5.5}$$

where θ is the opening angle between the clusters. The expression can be written in terms of the pair energy $E_{pair} = E_1 + E_2$

$$m^2_{\gamma\gamma} = \frac{1}{2}E^2_{pair}(1 - \gamma^2)(1 - cos(\theta)) \tag{5.6}$$

where the energy asymmetry between the photons, γ is defined as:

$$\gamma = |\frac{E_1 - E_2}{E_1 + E_2}| \tag{5.7}$$

After inserting the minimum reconstructible opening angle, θ_{min}, corresponding to 2.6 cm, an energy asymmetry of 0.6 (maximum allowed γ in a typical analysis[2]) and a pair energy of 15 GeV, the resulting minimum mass is 71 MeV. See figure 5.12 for a plot of the minimum mass plotted against energy. This effect reduces

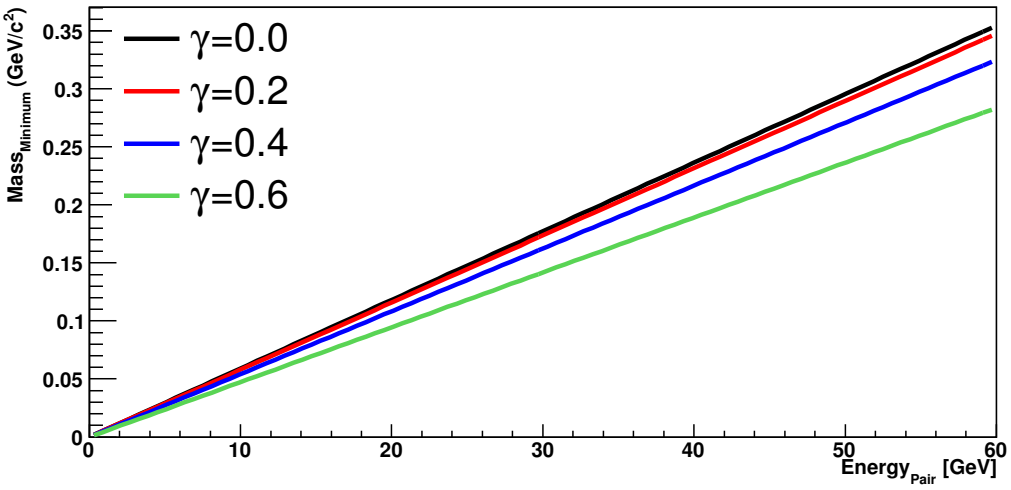

Figure 5.12: Vertical axis: minimum pair mass, Horizontal axis: Pair energy. Different curves are for different energy asymmetry cuts. Note: the figure assumes the collision z-vertex is at zero. Some spread is possible as the collision moves either nearer or further from the detector.

counts at the low mass side of the invariant mass distribution, $m_{\gamma\gamma}$, for photon pairs in an energy dependent way, and leads to a π^0 peak position which shifts up as a function of pair energy. Despite this cutoff at low mass, the π^0 and η meson mass distribution peaks retain a Gaussian-like shape due to detector resolution effects and the fact that the z-vertex distribution is quite broad. Collisions occurring either nearer or farther away from the detectors shift the minimum reconstructible mass to either larger or smaller values than the ones shown in figure 5.12.

5.5.2 Energy and Mass Resolution

The energy resolution of a calorimeter is typically parametrized as:

$$\frac{\delta(E)}{E} = \frac{a}{\sqrt{E}} \oplus \frac{b}{E} \oplus c \tag{5.8}$$

[2]This cut helps to increase the signal to noise ratio of the π^0 and η meson peaks

where the three terms: a, b, c are called: stochastic, noise and constant; and $\oplus$ indicates a quadratic sum. For an extended discussion of each term please see reference [69]. It is important to note that the energy and mass fractional resolutions are not the same. If the energy resolution of clusters 1 and 2 are uncorrelated[3], then the fractional mass resolution is[4]:

$$\frac{\delta m}{m} = \frac{1}{2}\left(\frac{\delta E_1}{E_1} \oplus \frac{\delta E_2}{E_2} \oplus \frac{\delta\theta}{tan(\frac{\theta}{2})}\right) \tag{5.9}$$

$\delta\theta$ can be approximated in terms of the cluster position resolution, δx and the z-vertex position resolution δz as:

$$\theta^2 \approx \frac{(x_1 - x_2)^2 + (y_1 - y_2)^2}{z^2} \tag{5.10}$$

with its resolution

$$\delta\theta \approx \frac{\sqrt{2}\delta x \oplus \theta\delta z}{z} \tag{5.11}$$

Using typical values (2 cm z-vertex resolution, 2 mm cluster position resolution, 8 cm cluster separation) in equation 5.11 gives the angular resolution as: 7.37 $\oplus$ 1.89 hundredths of a degree. Using this value for the invariant mass resolution in equation 5.9 it can be shown that the angular resolution contributes about 3.5% to the total mass width. $\delta\theta$ is roughly proportional to $1/\Delta r$, where Δr is the distance between the clusters. Therefore, the fractional mass resolution will degrade at high energies. This is contrary to naive expectations, based on the energy dependence of the energy resolution, that calorimeter performance increases with energy.

Using equation 5.8 in equation 5.9 gives:

$$\frac{\delta(m)}{m} = \frac{1}{2}\sqrt{a^2\left(\frac{1}{E_1} + \frac{1}{E_2}\right) + b^2\left(\frac{1}{E_1^2} + \frac{1}{E_2^2}\right) + 2c^2 + \frac{2\delta\theta}{tan(\theta/2)}} \tag{5.12}$$

which can be expressed in terms of the pair energy and asymmetry:

$$\frac{\delta(m)}{m} = a\frac{1}{\sqrt{1-\gamma^2}}\frac{1}{\sqrt{E_{pair}}} \oplus b\sqrt{\frac{1+\gamma^2}{2}}\frac{1}{1-\gamma^2}\frac{1}{E_{pair}} \oplus c\frac{1}{\sqrt{2}} \oplus \frac{\delta\theta}{2\,tan(\frac{\theta}{2})} \tag{5.13}$$

Combining equation 5.13 and plots of the fractional mass resolution shown in section 5.5.5, allows an estimation of the energy resolution. The η meson is used and not the π^0 to reduce effects from two-photon merging.

[3]Not the case in the event of common mode noise.
[4]The line width is omitted since it is $\sim$1 keV.

5.5.3 Identification of Mis-Calibrated Towers

In the central arm calorimeter bad towers are identified by looping over all clusters meeting a minimum energy threshold, finding each cluster's central tower and counting the number of times each tower is hit. The hits are expected to be distributed evenly between all towers in the central arm[5]. Towers with too few or too many counts relative to the other towers in the EMC are placed in a "warnmap".

A similar procedure is carried out in the MPC, but the MPC has the complication that hits are not expected to be distributed amongst all towers evenly. There are a number of competing effects which determine the hit distributions. The input flux of particles is determined using the η dependence of the cross-sections. However, each tower integrates over this distribution according to their span in $\Delta\phi$ and $\Delta\eta$. Towers closer to the beampipe have a larger span than towers farther out from the beampipe. To generate a warnmap: all towers meeting an energy threshold are counted in minimum bias data, then the yields are normalized by the number of analyzed triggers, and finally the normalized yields are plotted against the tower radius. The correlation plot is fit with a first degree polynomial using an LTS regression to remove outliers from the fit. Hot and cold towers are defined as lying beyond 3.2 sigma of the central fit value. A plot of the normalized yield for high energy clusters is shown in figure 5.13. The approximate location of each bad tower is shown in figure 5.14.

[5]There is a trivial modification between the PbSc and PbGl since the PbSc towers are larger in $d\eta \times d\phi$ space than the PbGl towers.

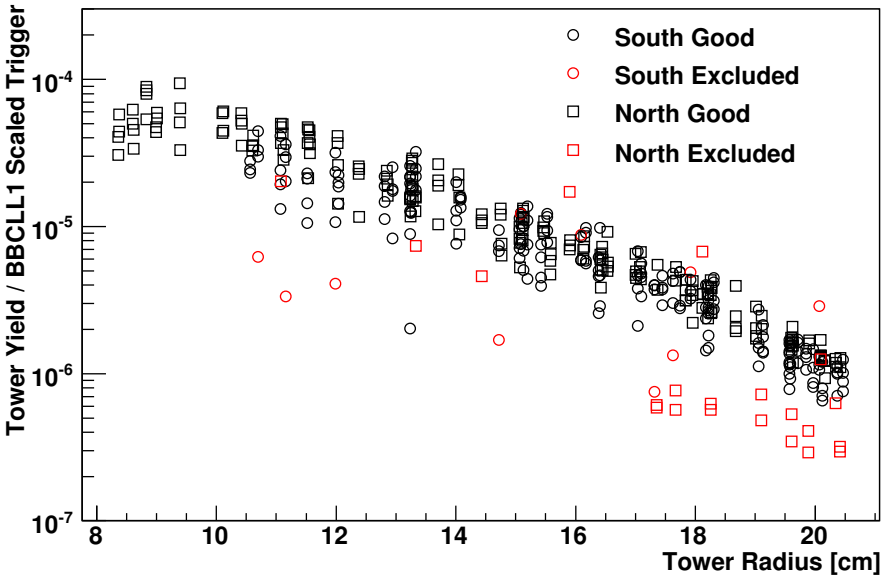

Figure 5.13: Vertical axis: ratio of cluster yields over the number of events for $E_{Cluster} > 20$ GeV. Both are taken from minimum bias data. Horizontal axis: Tower radial position from beampipe center [cm]. Excluded towers are shown in red while good towers are in black.

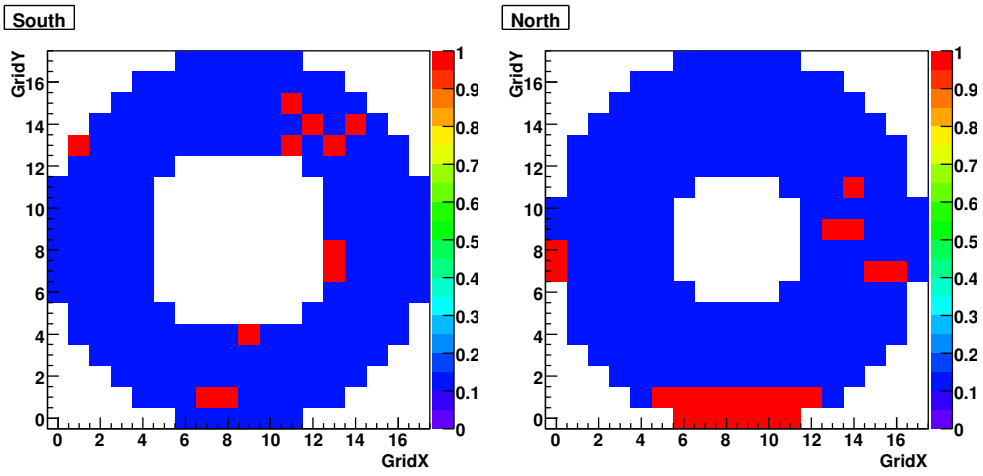

Figure 5.14: The MPC South and North warnmaps. The towers that fail the calibration quality assurance test are in red. Each tower is placed at its approximate position in a horizontal and vertical grid.

5.5.4 π^0 and η Identification

Two photon invariant mass peaks are formed from the minimum bias and MPC triggered datasets. Events are required to have a z-vertex between z = ± 30 cm. The following cuts are imposed on clusters:

- **Photonic cluster** Electromagnetic fit quality $\chi^2_{reduced}$ <2.5.
- **Minimum energy** Energy >2 (GeV).
- **Warnmap veto** towers flagged as either hot or cold are removed from analysis. In addition, towers downstream of the beampipe support in the north arm are removed from analysis.
- **Radius cut** The reconstructed clusters are required to have a radial position between 13 and 18 cm from the center of the beampipe.

The cuts for cluster pairs are:

- **Pair separation** clusters must be separated by more than 2.6 cm.
- **Same arm** clusters must be from the same arm.
- **Energy asymmetry** must be less than 0.6.
- **TDC Timeout** The TDC of the cluster's central tower must be less than the TDC timeout value. The determination of the TDC count timeout values are described in section 5.2.3.

Combining pairs of particles from the same events produces a distribution called the foreground. The foreground counts are broken into three types of contributions:

1. Clusters-pairs from photons from the decay π^0's and η mesons. Determining the yield and invariant mass shape properties is the goal of the calibration.
2. Combinatorial background: Often an event will include multiple π^0's, or a π^0 and a single photon from another source. Since all possible combinations of pairs are generated, photons without a common parent hadron are paired. A technique called event mixing is used to determine the shape of the combinatorial background. This is done by determining the invariant mass of photon pairs from different events. Selecting events from different events guarantees that there is no correlation between the photons. Specifics of the event-mixing method are elaborated upon in the text.
3. Correlated jet background: The event-mixing technique rarely removes all the background under the π^0 and η meson peak. The residual background is referred to as a correlated jet background. This

type of background cannot be removed by the simple event-mixing previously described, but it can be quantified by fitting the mass distribution around the meson peak and it can be reproduced using Monte-Carlo.

The event-mixing implementation of this thesis forms a pool of clusters and their associated vertices. Once the pool is filled, the clusters are randomly combined with the restriction that the z-vertex difference between the pairs is less than 2 cm. The randomly combined clusters are used to fill an invariant mass distribution. The background mass distribution is normalized to the foreground mass distribution in the window between 0.3 (0.7) to 1.0 GeV/c^2 for the π^0 (η). The $M_{\gamma\gamma}$ distributions and fits to the η meson peak are shown in figure 5.15 for the 30-40 GeV pair energy interval. The properties of the π^0 peaks are provided in figure 5.24 and for the η in 5.16. By virtue of the larger opening angle, the η peak properties are relatively stable versus energy.

5.5.5 Fractional Mass Resolutions from Data

The fractional mass resolutions for the η are shown in figure 5.17 for both the Minimum bias and MPC triggered datasets. Both sets of mass resolutions are flat and around $\sim$6%. The energy asymmetry does not affect the mass resolutions. Therefore, at these energies the angular resolution and constant terms dominate equation 5.13. If the angular resolution term is set to $\sim$3.5% (explained in section 5.5.2), then the remaining width must originate from the constant term. Therefore, the energy resolution's constant term is approximately 6.9%[6].

5.5.6 Gain Stability

To check the stability of the gain, peaks are extracted in the same fashion as shown in figure 5.15 on a fill-by-fill basis. The extracted peak positions are shown in figure 5.18.

5.5.7 Comparison to Monte-Carlo

If only a single energy bin is used, then an infinite set of (a,b,c) would be able to match the measured mass resolution. Therefore, the peak widths are extracted as a function of the pair energy with the goal to pick the cluster energy resolution which best matches data. The π^0 and η meson peak positions as reconstructed by our detector are not required to sit at the PDG value. Acceptance and reconstruction effects can shift

[6]The total and angular fractional **mass** resolutions are approximately 6% and 3.5%, respectively. Therefore, the remaining noise is: $\sqrt{6\%^2 - 3.5\%^2}$. Then, factor of $\sqrt{2}$ from formula 5.13 is needed to get the **energy** resolution term.

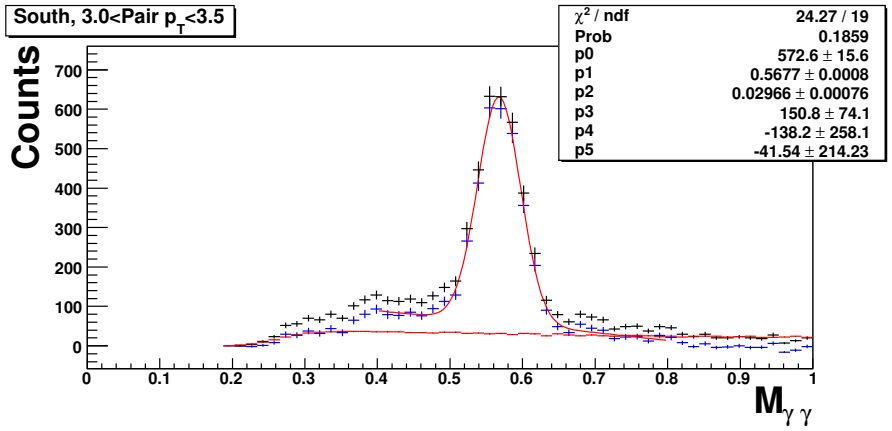

(a) South Arm

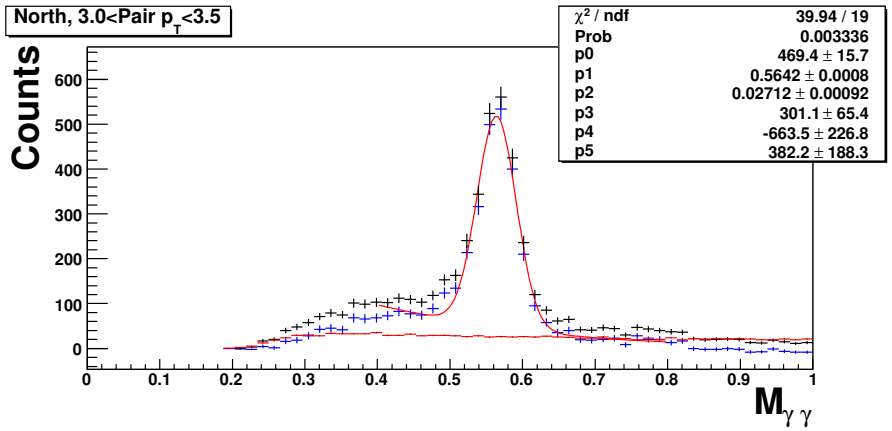

(b) North Arm

Figure 5.15: Vertical axis: Counts, Horizontal axis: $M_{\gamma\gamma}$ for cluster pairs with p_T between 3.0 and 3.5 GeV/c. Foreground (black), scaled mixed (red) and subtracted (blue) distributions are shown. The subtracted distribution is fit to a Gaussian distribution (parameters 0, 1 and 2) plus a second degree polynomial (parameters 3, 4 and 5). The mixed event distribution is normalized to the foreground distribution in the mass window 0.7 to 1.0 GeV/c^2. The plots show a clear η peak. The counts outside the η mass range not subtracted by event mixing originate from a correlated jet-background which cannot be duplicated by event-mixing. It has been studied and duplicated in Monte-Carlo.

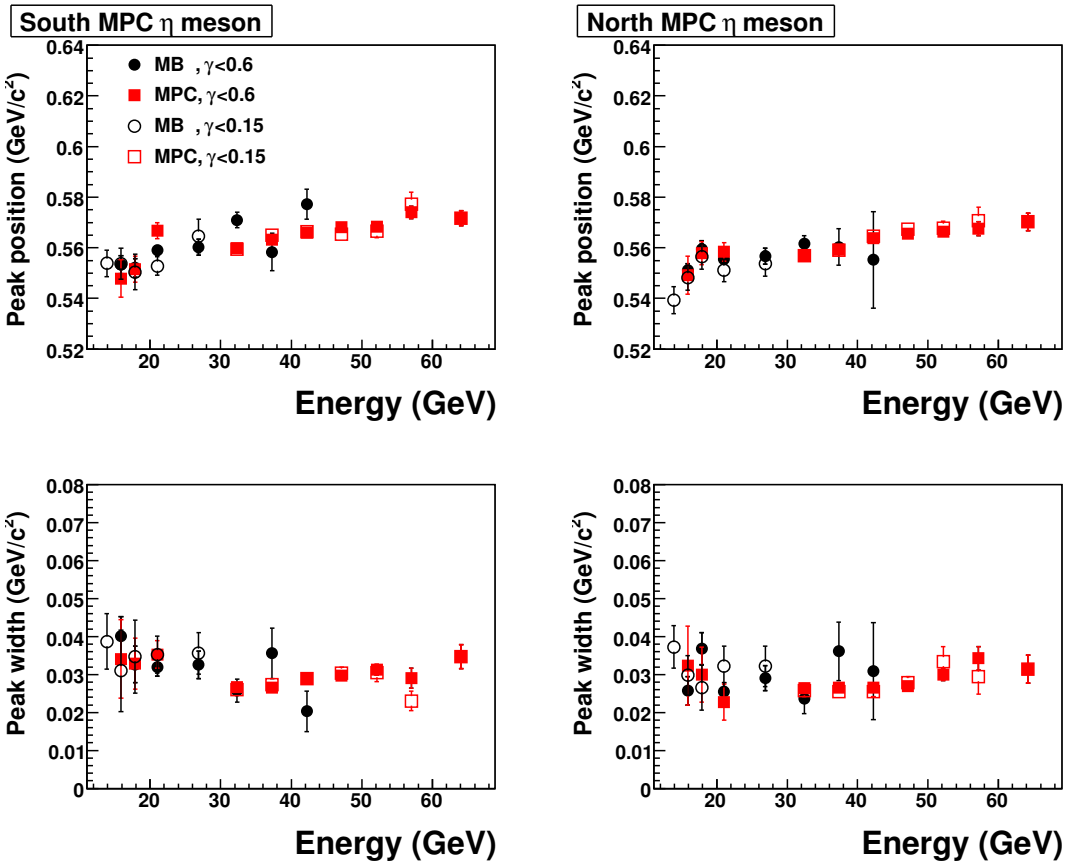

Figure 5.16: The peak positions and peak widths of the η meson invariant mass distributions extracted in bins of energy. Points are plotted at the mean energy in each bin. Points for energy less than or greater than 30 GeV are from minimum bias and MPC triggered data respectively. Open (closed) points are generated with pairs with energy asymmetry less than 0.15 (0.6).

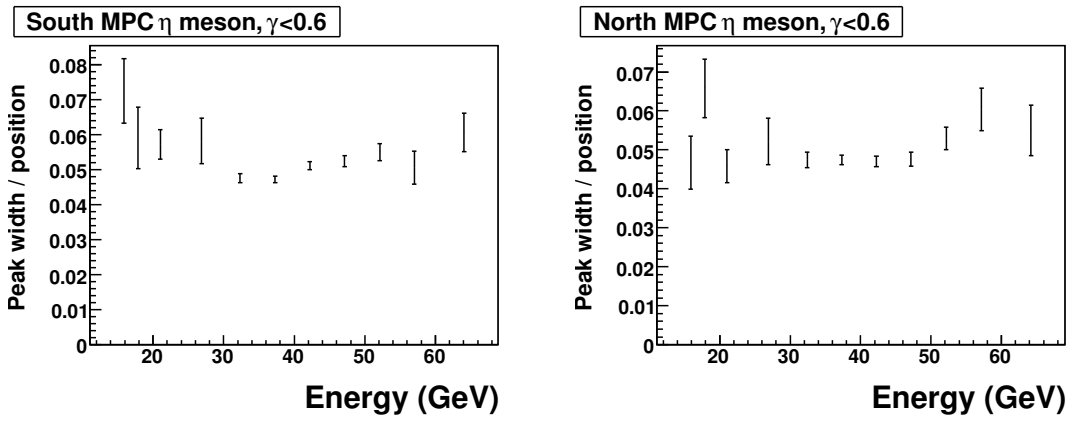

(a) Energy asymmetry < 0.6

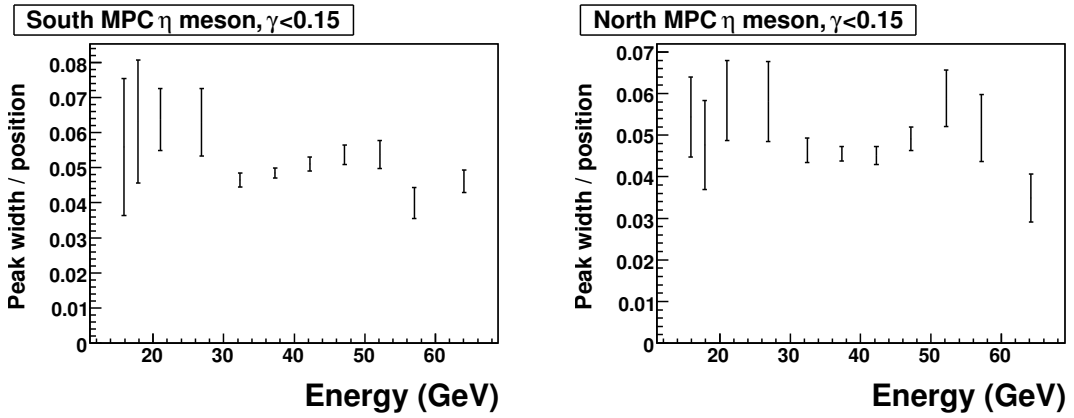

(b) Energy asymmetry < 0.15

Figure 5.17: The peak widths divided by peak positions of the η meson invariant mass distributions extracted in bins of energy from both the Minimum Bias and MPC triggered datasets. Points are plotted at the mean energy in each bin. The top plots are for a pair energy asymmetry, α, less than 0.6. The bottom plots are for α <0.15. The fractional mass resolution does not depend strongly on the energy asymmetry, indicating that the constant term dominates the invariant mass resolution, see equation 5.13

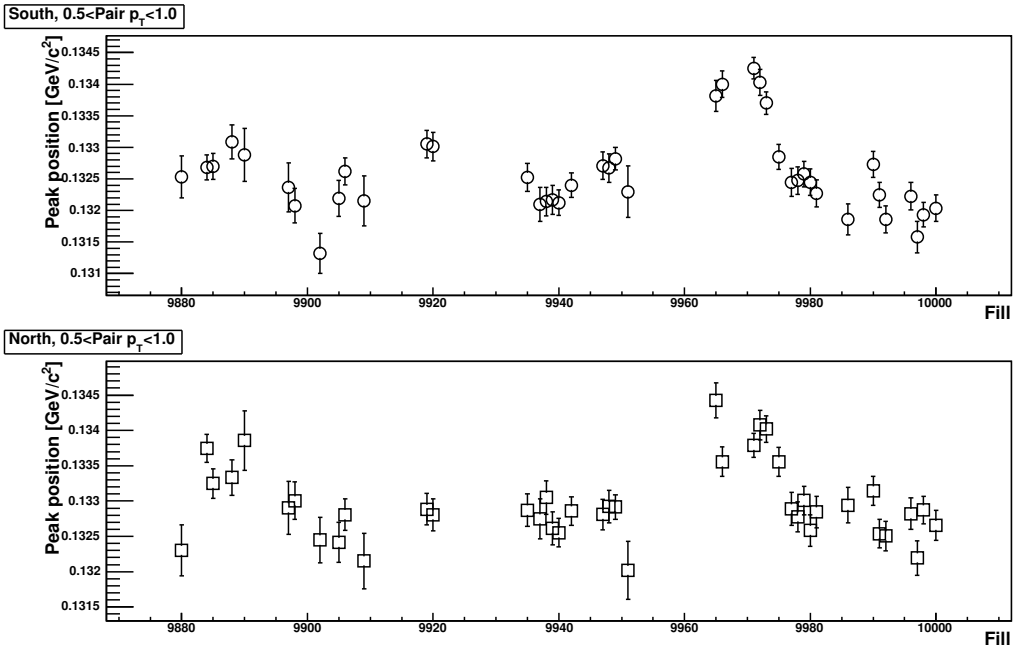

Figure 5.18: Vertical axis: π^0 peak position for cluster pairs with p_T between 0.5 and 1.0 GeV/c, Horizontal axis: fill number. Top: South arm, Bottom: North arm.

the peak value away from the expected location. For example, in the PHENIX central arms the π^0 peak is expected to change with p_T [90].

The simulation is done in two steps. The goal of the first step is to find the correct set of noise terms which describe the MPC data. This effect of mis-calibration and noise is studied by comparing the mass peak widths from data to simulations using different levels of noise, introduced at the tower level. The second step is to compare the absolute peak position between data and simulation.

The simulated dataset is described in detail in section 8.3. Simulated $p+p$ collisions are generated using an event generator called Pythia. The products from the collision are propagated through a simulation of PHENIX implemented in GEANT3 and the detector-response in simulation leads to realistic Monte-Carlo DST's. For the MPC, the DST's contain **raw tower** information only. Calibrated towers and clusters are produced only as part of the high level DST based analysis. This provides the flexibility to introduce and study noise and mis-calibrations at the tower level. By default, the simulation code uses perfect tower gains and 75 MeV electronics noise. Comparison to data is based on Minimum Bias triggered data.

The peak values and widths for π^0 and η mesons were extracted in a 10x10 grid of different constant and noise energy resolution terms. The constant term was varied between 0 and 18% in steps of 2%. The electronics noise was set 75 MeV, and with the following levels added in quadrature 0, 25, 50, 75, 100, 125, 150, 200, 300 and 400 MeV.

Meson	**Trigger**	**Energy** (GeV)
π^0	Minimum bias	9 - 11
π^0	Minimum bias	11 - 13
π^0	Minimum bias	13 - 15
π^0	Minimum bias	15 - 17
π^0	Minimum bias	17 - 19
η	MPC	15 - 17
η	MPC	17 - 19
η	MPC	19 - 25
η	MPC	25 - 30
η	MPC	30 - 35
η	MPC	35 - 40

Table 5.1: Mesons and associated energy ranges for which a comparison of invariant mass spectra between data and Monte-Carlo has been carried out.

The same reconstruction, analysis, and peak extraction code described in 5.5.4 was used for the simulated data. Comparison between simulation and data is done using bins of π^0 and η energy. The two photons from the decay of π^0's merge into a single cluster for energies above 20 GeV. Therefore, at low energies the π^0 is used and at high energies the η meson is used in the comparison between data and simulation. The list of energies and mesons to be compared are listed in table 5.1.

The mass distributions for π^0 and η as a function of trigger, energy and p_T are available in reference [91], as an example, some mass distributions from data and from simulation are provided in figure 5.19.

The data may have a global scale offset from the true calibrations. Therefore, any potential scale factors are divided out by using the meson peak width divided by the position in the data-Monte-Carlo comparison. This ratio will be denoted as $\lambda = width/peak$. Simulations for 100 different noise settings are shown in figures 5.20 and 5.21 for the south and north arms respectively.

To choose the optimal combination of constant and noise energy resolution parameters, the χ^2 value between data and simulation for each combination of noise is calculated. Results are shown in figures 5.22 and 5.23 respectively. Three χ^2 values are presented for each noise setting: π^0 alone, η alone and for both.

Th lowest χ^2 results from using 8% as the constant term, and 75$\oplus$50MeV noise as the noise term. The constant term agrees with the earlier determination of section 5.5.5.

The peak properties for the π^0 and η are shown in figure 5.24. As a result of the comparison between simulation and data, the energy calibration for the North detector is shifted up by 3% relative to the MIP analysis. The South detector's gains were not adjusted. Figure 5.24 shows the peak position, peak widths and ratio λ as a function of energy using the final calibrations, including the 3% adjustment in the North MPC. There is a 2% difference between the π^0 and η peak positions for data and Monte-Carlo. The difference is present in both arms. This difference is assigned as a systematic uncertainty for the global energy scale.

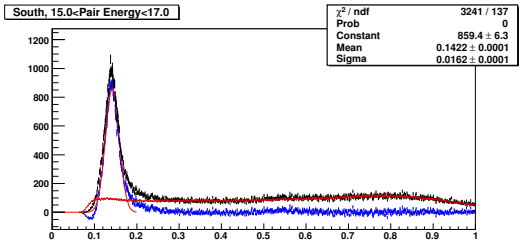

(a) Data, minimum bias triggered

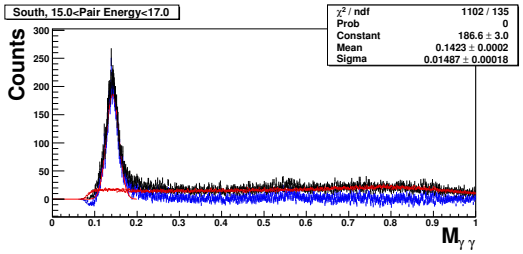

(b) Simulation, 0% constant term, 0 GeV noise

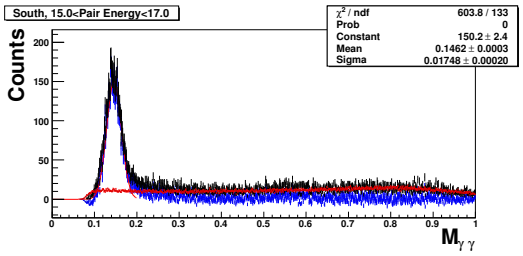

(c) Simulation, 10% constant term, 0.075 GeV noise

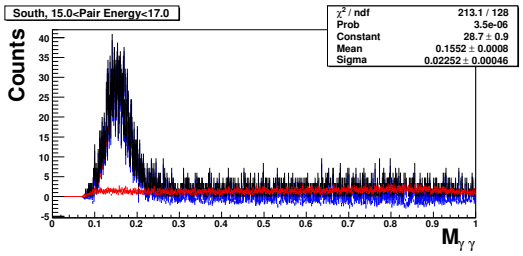

(d) Simulation, 20% constant term, 0.400 GeV noise

Figure 5.19: $M_{\gamma\gamma}$ distributions for the MPC from data and simulation. Arm: South, 15<Energy<17 GeV. Each plot shows the foreground (black), mixed event (red) and subtracted (blue) mass distribution.

5.6 Summary

The energy resolution is estimated to have an 8% constant term and 90 MeV of noise. The global energy uncertainty is 2%.

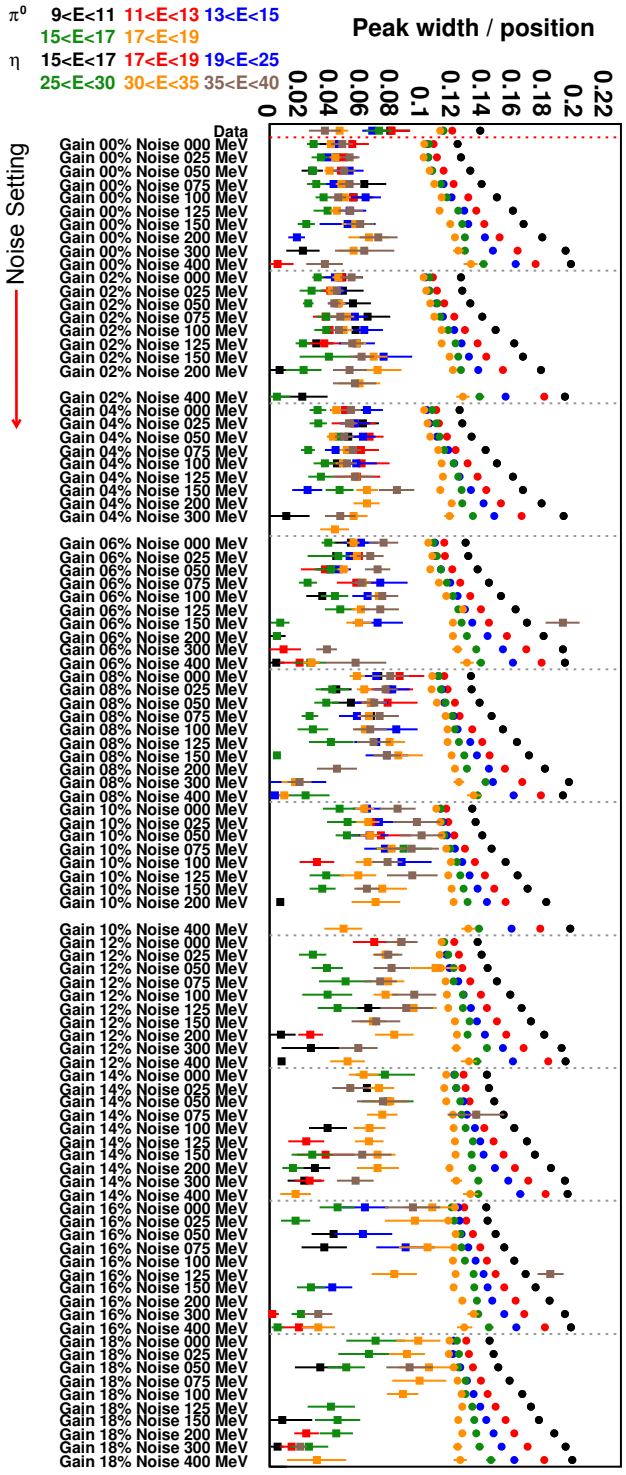

Figure 5.20: Scan of $\lambda = Peakwidth/Peakposition$ for different noise levels in the MPC South Monte-Carlo simulations. The analysis is carried out for the π^0 and η invariant mass distributions. A comparison to data is used to determine the noise level. The color coding indicates the π^0 and η energy bins. Squares are for the η, circles are for the π^0.

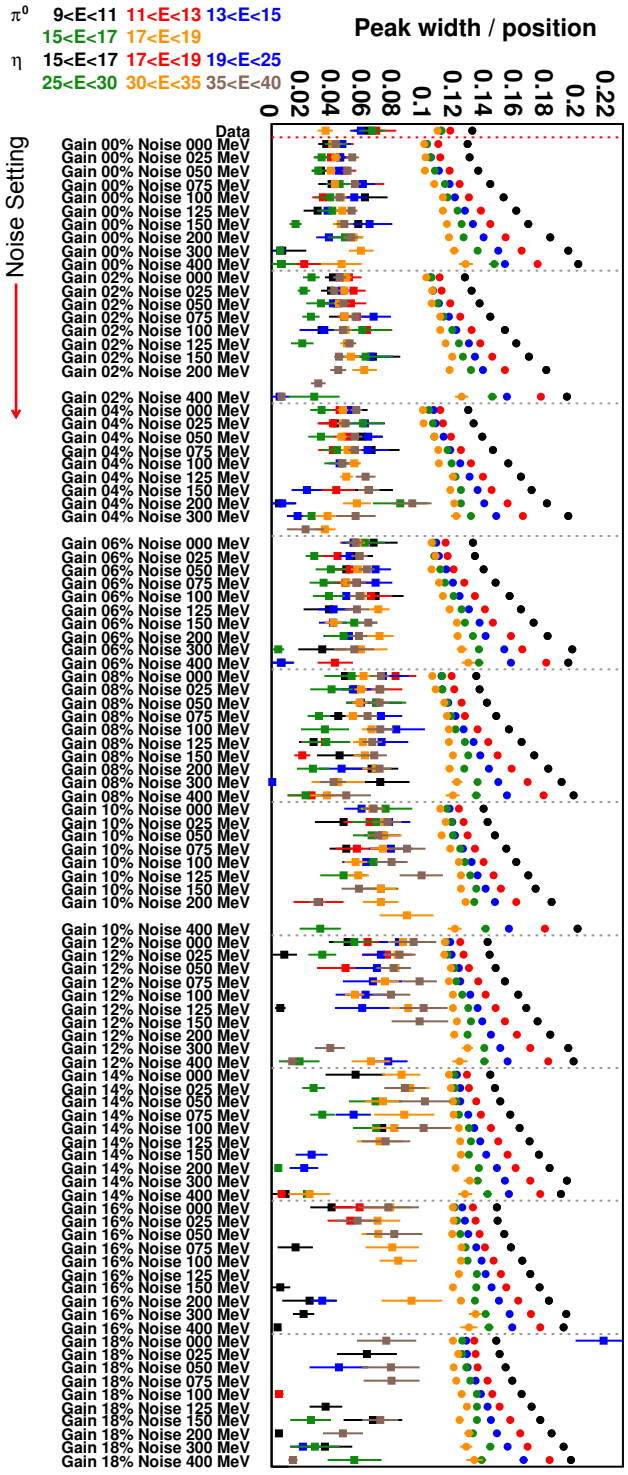

Figure 5.21: Scan of $\lambda = Peakwidth/Peakposition$ for different noise levels in the MPC North Monte-Carlo simulations. The analysis is carried out for the π^0 and η invariant mass distributions. A comparison to data is used to determine the noise level. The color coding indicates the π^0 and η energy bins. Squares are for the η, circles are for the π^0.

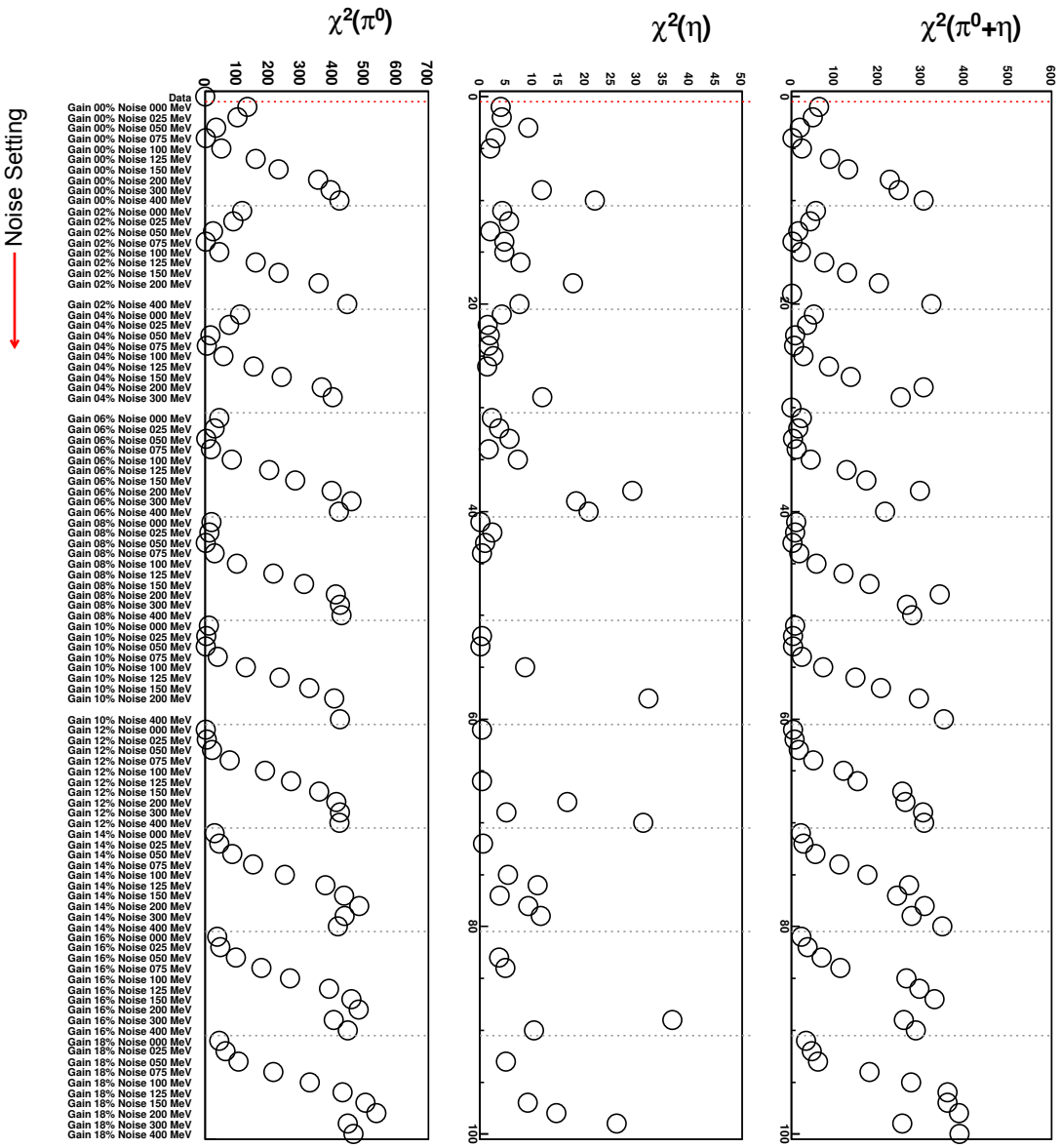

Figure 5.22: The reduced χ^2 values of the difference between the data and simulation for $\lambda = peakwidth/peakposition$. Five kinematic bins are used for the π^0 and six for the η. The reduced χ^2 values are presented separately for the π^0 (left), η (middle) and the sum (right). Values are shown from the South MPC.

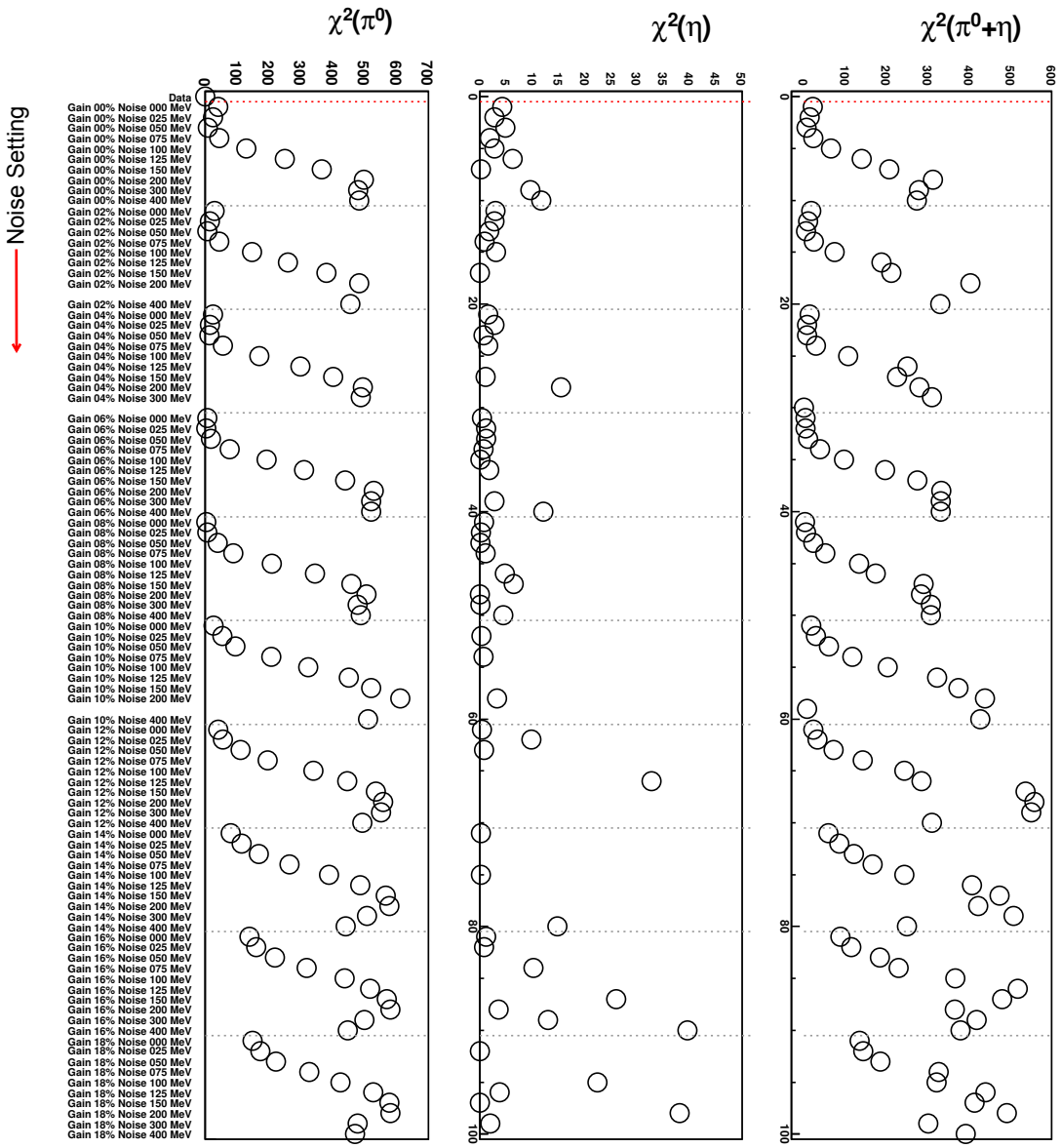

Figure 5.23: The reduced χ^2 values of the difference between the data and simulation for $\lambda = peakwidth/peakposition$. Five kinematic bins are used for the π^0 and six for the η. The reduced χ^2 values are presented separately for the π^0 (left), η (middle) and the sum (right). Values are shown from the North MPC.

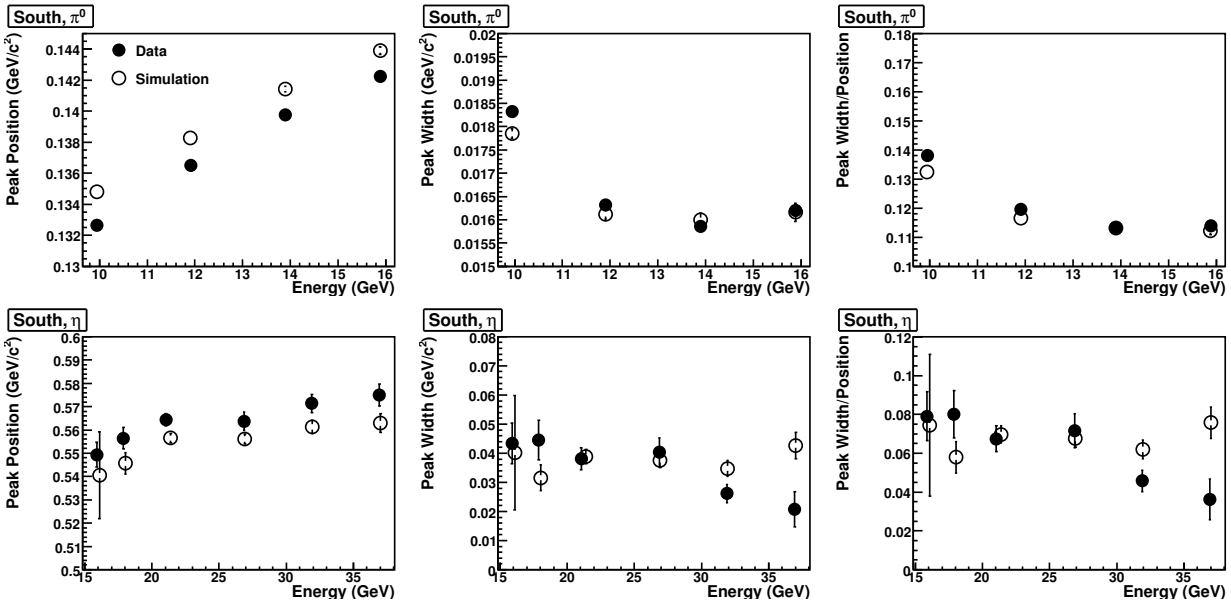

(a) South

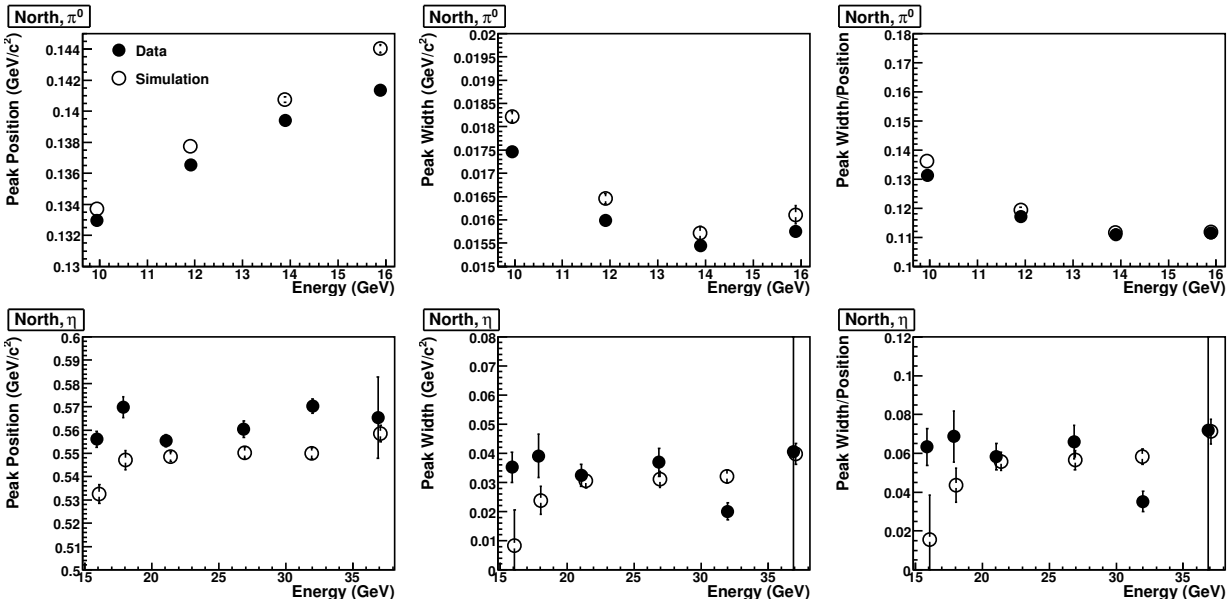

(b) North

Figure 5.24: Comparison between Minimum Bias triggered data and simulation for the peak properties of the π^0 and η meson. In the simulation the energy resolution of the MPC's is smeared with an 8% constant term and 90 MeV of noise.

Chapter 6

Estimators for A_N

This chapter reviews various estimators for A_N and then presents some alternate estimators to use in the limit of low fill-to-fill statistics. The alternate estimators are not used for the physics analysis, but are shown to be unbiased and are used as a cross-check.

6.1 Formulae for Calculating A_N

A_N is the azimuthal modulation of the inclusive cross-section for the production of hadrons in the collision of a transversely polarized beam and an unpolarized target. The cross-section can be written as:

$$\frac{d\sigma}{d\Omega}(\phi) = \left(\frac{d\sigma}{d\Omega}\right)_0 (1 + A_N \, P_y \, cos(\phi)) \tag{6.1}$$

where $\left(\frac{d\sigma}{d\Omega}\right)_0$ is the total unpolarized cross-section, A_N is the analyzing power, P_y is the beam polarization along the arbitrarily chosen y-axis, and ϕ is the angle of the final state hadron with respect to $\hat{y}$.

The number of particles striking the detector is given by:

$$N(\phi) = \mathcal{L} \, a(\phi) \left(\frac{d\sigma}{d\Omega}\right)_0 (1 + A_N \, P_y \, cos(\phi)) \tag{6.2}$$

where $\mathcal{L}$ is the integrated luminosity and $a(\phi)$ is an acceptance/efficiency function. This note treats the simple case where A_N does not depend on ϕ. However, the impact of an azimuthal dependence of the acceptance will be studied. References [92, 93] give a discussion of the general case.

6.1.1 Naive Formula

The Gedanken A_N measurement scatters an unpolarized beam off a polarized target, and then counts the number of particles emitted either to the right or left of the plane formed by the beam polarization and the

beam momentum. The asymmetry is calculated as

$$A_N(\phi) = \frac{\epsilon(\phi)}{P_y} \tag{6.3}$$

$$\epsilon_N(\phi) = \frac{N^\uparrow(\phi) - N^\uparrow(\phi+\pi)}{N^\uparrow(\phi) - N^\uparrow(\phi+\pi)} \tag{6.4}$$

where where P_y is the beam polarization, $\epsilon_N(\phi)$ is the raw asymmetry, and $N^\uparrow(\phi, \phi+\pi)$ are the counts to the left or right of the target. All final state particles from the final state of a given type are summed over. Gaussian error propagation gives the error for the raw asymmetry as:

$$\sigma^2(\epsilon_N(\phi)) = \frac{4N^\uparrow(\phi)N^\uparrow(\phi+\pi)}{(N^\uparrow(\phi) + N^\uparrow(\phi+\pi))^3} \tag{6.5}$$

using:

$$4N^\uparrow(\phi)N^\uparrow(\phi+\pi) = (N^\uparrow(\phi) + N^\uparrow(\phi+\pi))^2(1 - \epsilon_N(\phi)^2) \tag{6.6}$$

The error for the raw asymmetry can be written as:

$$\sigma^2(\epsilon_N(\phi)) = \frac{1 - \epsilon_N^2(\phi)}{N^\uparrow(\phi) + N^\uparrow(\phi+\pi)} \tag{6.7}$$

which shows that the error bar of the asymmetry has a weak dependence on the asymmetry value. For small asymmetries this term can be essentially ignored. The limits of the method can be shown by inserting equation 6.2 into equation 6.4, showing the dependence on the acceptance function $a(\phi)$.

$$\epsilon_N(\phi) = \frac{\mathcal{L}^\uparrow a^\uparrow(\phi)(1 + A_N\, P_y\, cos(\phi)) - \mathcal{L}^\uparrow a^\uparrow(\phi+\phi)(1 + A_N\, P_y\, cos(\phi+\pi))}{\mathcal{L}^\uparrow a^\uparrow(\phi)(1 + A_N\, P_y\, cos(\phi)) + \mathcal{L}^\uparrow a^\uparrow(\phi+\phi)(1 + A_N\, P_y\, cos(\phi+\pi))} \tag{6.8}$$

Dividing out the $\mathcal{L}^\uparrow$ and rearranging terms gives:

$$\epsilon_N(\phi) = \frac{(a^\uparrow(\phi) - a^\uparrow(\phi+\pi)) + A_N P_y cos(\phi)(a^\uparrow(\phi) + a^\uparrow(\phi))}{(a^\uparrow(\phi) + a^\uparrow(\phi+\pi)) + A_N P_y cos(\phi)(a^\uparrow(\phi) - a^\uparrow(\phi))} \tag{6.9}$$

Therefore, this simple formulation of the asymmetry only works in the limit of: $a(\phi) - a(\phi+\pi) \to 0$. Proving this relation or extracting the acceptance factors requires detailed studies with potentially large systematic errors. Fortunately, there are other possibilities which are explained in the next two sections.

6.1.2 Luminosity Formula

One of the advantages of RHIC is that the spin can be chosen either up or down with respect to a given axis. Therefore, the left-right asymmetry between different detector parts or angles can be replaced by a luminosity asymmetry between the count rates for collisions with different spin orientations. The luminosity asymmetry is given as:

$$\epsilon_N^{lumi}(\phi) = \frac{N^{\uparrow}(\phi) - RN^{\downarrow}(\phi)}{N^{\uparrow}(\phi) + RN^{\downarrow}(\phi)} \tag{6.10}$$

where $R = \mathcal{L}^{\uparrow}/\mathcal{L}^{\downarrow}$ is the relative luminosity between bunch crossings with spin up and spin down bunches. As an example: the $N^{\uparrow,\downarrow}(\phi, \phi+\pi)$ are measured using the MPC, and the R value is calculated using the BBC. The error can be shown to be equal to:

$$\sigma^2(\epsilon_N^{lumi}(\phi)) = \frac{4}{(N^{\uparrow}(\phi) + RN^{\downarrow}(\phi))^4} \frac{1}{(N^{\uparrow}(\phi)N^{\downarrow}(\phi)R)^2} \left[\left(\frac{\delta N^{\uparrow}(\phi)}{N^{\uparrow}(\phi)} \right)^2 + \left(\frac{\delta N^{\downarrow}(\phi)}{N^{\downarrow}(\phi)} \right)^2 + \left(\frac{\delta R}{R} \right)^2 \right] \tag{6.11}$$

The relative luminosity in past PHENIX measurements has been determined using the BBC's and the fractional error of R has been vanishingly small compared to the experimental yields. Therefore, the $\delta R/R$ term was dropped. If the error on the yields is assigned to be $\sqrt{N}$ the formula for the error reduces to:

$$\sigma^2(\epsilon^{lumi}) = \frac{1-\epsilon^2}{(N_L + RN_R)^2}(N_L + N_R)R \tag{6.12}$$

which has similar components to equation 6.7 and also reduces to it in the limit of $R = 1$.

Inserting equation 6.2 into equation 6.10 gives:

$$\epsilon_N^{lumi}(\phi) = \frac{\mathcal{L}^{\uparrow}\, a^{\uparrow}(\phi)\,(1 + A_N\, P_y\, cos(\phi)) - R\mathcal{L}^{\downarrow}\, a^{\downarrow}(\phi)\,(1 - A_N\, P_y\, cos(\phi))}{\mathcal{L}^{\uparrow}\, a^{\uparrow}(\phi)\,(1 + A_N\, P_y\, cos(\phi)) + R\mathcal{L}^{\downarrow}\, a^{\downarrow}(\phi)\,(1 - A_N\, P_y\, cos(\phi))} \tag{6.13}$$

Assuming a perfect determination of R, yields:

$$\epsilon_N(\phi) = \frac{(a^{\uparrow}(\phi) - a^{\downarrow}(\phi)) + (a^{\uparrow}(\phi) + a^{\downarrow}(\phi))A_N P_y cos(\phi)}{(a^{\uparrow}(\phi) + a^{\downarrow}(\phi)) + (a^{\uparrow}(\phi) - a^{\downarrow}(\phi))A_N P_y cos(\phi)} \tag{6.14}$$

At RHIC, the spin flips on a timescale of 106 nanoseconds and therefore it would be surprising if the $a^{\uparrow}$ and $a^{\downarrow}$ factors differed[1]. Under the assumption that the two efficiencies are the same, the expression reduces to:

$$\epsilon_N(\phi) = A_N P_y cos(\phi) \tag{6.15}$$

[1]The EMC electronics have a well-known effect where different trigger circuits are used for even and odd crossings leading to slightly different turn-on curves. Therefore, analysis should be split between even and odd crossings to avoid the introduction of a systematic bias between different count rates.

Therefore, the major assumption of the luminosity asymmetry is that the the relative luminosity between up and down polarization states (R) factor is determined perfectly.

6.1.3 Square Root Formula

The square root formula is the most trusted formula for estimating A_N since it eliminates both luminosity and acceptance effects.

$$\epsilon^{sqrt}(\phi) = \frac{\sqrt{N^{\uparrow}(\phi)N^{\downarrow}(\phi+\pi)} - \sqrt{N^{\uparrow}(\phi+\pi)N^{\downarrow}(\phi)}}{\sqrt{N^{\uparrow}(\phi)N^{\downarrow}(\phi+\pi)} + \sqrt{N^{\uparrow}(\phi+\pi)N^{\downarrow}(\phi)}} \tag{6.16}$$

$$\sigma^2(\epsilon(\phi)) = \frac{1}{16}(1-\epsilon^2)^2\left[\frac{1}{N^{\uparrow}(\phi)} + \frac{1}{N^{\uparrow}(\phi+\pi)} + \frac{1}{N^{\downarrow}(\phi)} + \frac{1}{N^{\downarrow}(\phi+\pi)}\right] \tag{6.17}$$

Inserting equation 6.2 gives:

$$\begin{aligned}
\epsilon_N \quad = \quad & \\
& \left\{\sqrt{\mathcal{L}^{\uparrow}a^{\uparrow}(\phi)(1+A_N\,P_y\,cos(\phi))\mathcal{L}^{\downarrow}a^{\downarrow}(\phi+\pi)(1-A_N\,P_y\,cos(\phi+\pi))} - \right. \\
& \left.\sqrt{\mathcal{L}^{\downarrow}a^{\downarrow}(\phi)(1-A_N\,P_y\,cos(\phi))\mathcal{L}^{\uparrow}a^{\uparrow}(\phi+\pi)(1+A_N\,P_y\,cos(\phi+\pi))}\right\}/ \\
& \left\{\sqrt{\mathcal{L}^{\uparrow}a^{\uparrow}(\phi)(1+A_N\,P_y\,cos(\phi))\mathcal{L}^{\downarrow}a^{\downarrow}(\phi+\pi)(1-A_N\,P_y\,cos(\phi+\pi))} + \right. \\
& \left.\sqrt{\mathcal{L}^{\downarrow}a^{\downarrow}(\phi)(1-A_N\,P_y\,cos(\phi))\mathcal{L}^{\uparrow}a^{\uparrow}(\phi+\pi)(1+A_N\,P_y\,cos(\phi+\pi))}\right\}
\end{aligned}$$

Using the same assumption that $a^{\uparrow}(\phi) = a^{\downarrow}(\phi)$ can be used to examine the luminosity asymmetry, a common factor of $\mathcal{L}^{\uparrow}\mathcal{L}^{\downarrow}a(\phi)a(\phi+\pi)$ can be extracted from each term in the numerator and the denominator leaving:

$$\epsilon_N(\phi) = A_N P_y cos(\phi) \tag{6.18}$$

6.1.4 Geometric Weighting

The formulae reviewed in sections 6.1.1, 6.1.2 and 6.1.3 calculate A_N in an infinitely thin slice of ϕ. In practice some finite bin width in ϕ must be used. The most extreme binning is to define two azimuthal bins: left and right. In this case, a geometric scaling factor must be introduced to account for the azimuthal distribution of particles around the spin vector. For example, if the experiment consists of two narrow spectrometers on either side of a beam line which use equation 6.16 to measure $\epsilon = 0.1 \pm 0.1$, the physics asymmetry depends greatly on the orientation of the spectrometer relative to the polarization direction. The

derivation of the weighting procedure follows from equation 6.15 and is:

$$A_N = \frac{\epsilon}{P_y \langle |cos(\phi)| \rangle} \tag{6.19}$$

where the $\langle |cos(\phi)| \rangle$ term accounts for the fact that each particle occurs at a different angle ϕ with respect to the polarization direction.

An alternate approach is to bin the yields and calculate the asymmetries in bins of the azimuthal angle, and then fit the asymmetry versus the azimuthal angle.

6.2 Square Root Formula in the Limit of Low Statistics

This section examines the square root asymmetry formula (equation: 6.16) in the limit of low-statistics. A simple Monte-Carlo was constructed using a fixed polarization and then varying both the yields used to calculate the asymmetry and the input asymmetry. The yields are distributed between up and down polarization states with equal probability and the azimuthal bin, ϕ or $\phi+\pi$ (i.e. Left or Right), is determined randomly by the input asymmetry. There are obvious limitations to the square root formula in the limit of low counts. For example: if the total number of particles is four, most of the possible combinations of yields result in $\epsilon_{sqrt} = 0/0$. For this Monte-Carlo study these asymmetry values are rejected. For the physics analyses of the next few chapters, the analyses do not start if the number of input particles is less than 30 counts. The probability of failure drops as the yield increases. However, for moderate yield a similar problem remains. Only a finite set of discrete values for ϵ_{sqrt} can be generated and therefore the statistical uncertainty is not estimated correctly. This is shown in figure 6.1 for 12 input particles. The transition between the low-statistics region and the higher statistics region is shown in figure 6.2. If the overall yield is greater than thirty counts, the square root formula is safe to use[2].

6.3 Averaging Over Fills

To measure A_N, the yields $N_L^{\uparrow}, N_L^{\downarrow}, N_R^{\uparrow}$ and $N_R^{\downarrow}$ are determined over many fills. Each fill has a unique polarization value which needs to be properly accounted for when taking the mean over all fills/runs.

[2]This assumes that the acceptance between left and right is the same.

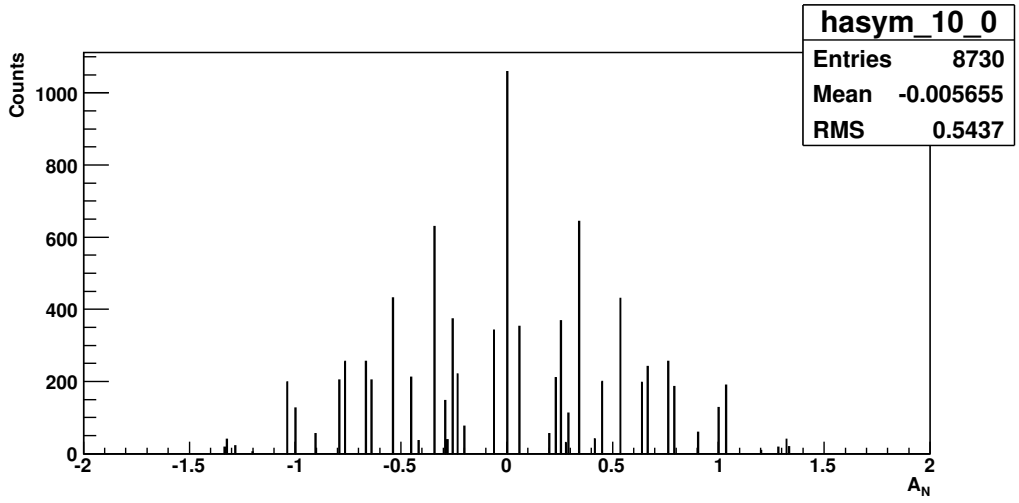

Figure 6.1: Output asymmetry A_N from the square root formula. The input asymmetry is 0, the polarization P_y is set to 50%. Twelve particles are generated and sorted by spin and ϕ as described in the text.

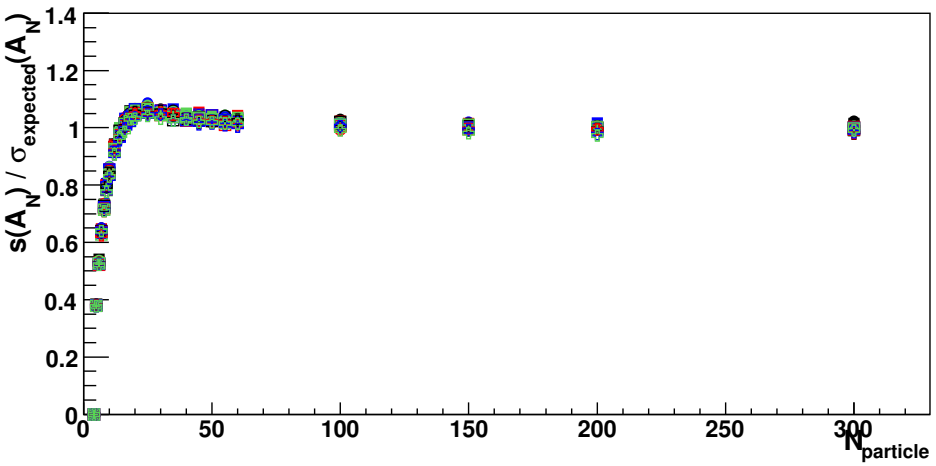

Figure 6.2: Horizontal axis: number of particles participating in asymmetry calculation, Vertical axis: Root variance of the asymmetry distribution divided by the expected asymmetry error bar ($\frac{1}{P\sqrt{N}}$). Polarization is 50%. The different marker colors and styles are the injected asymmetry between 0 and 40% in steps of 2%. For each $N_{particle}$, 10,000 samples of $N_{particle}$ are generated.

6.3.1 Traditional Averaging

The commonly accepted method for doing the averaging over runs is to use $(P, N_{L,R}^{\uparrow,\downarrow})_i$ to calculate $(A_N, \delta A_N)_i$, where i is a fill index. Then, the average over fills is taken as:

$$A_N = \frac{\sum_{i=Fill} A_{N,i}/\delta A_{N,i}^2}{\sum_{i=Fill} \delta 1/A_{N,i}^2} \tag{6.20}$$

To illustrate the limit for low statistics, the error for the naive asymmetry is used assuming that errors are simply $1/(P_y\sqrt{N})$:

$$A_N = \frac{\sum_{i=Fill} \frac{1}{P_i} \frac{N_i^{\uparrow}(\phi) - R_i N_i^{\downarrow}(\phi)}{N_i^{\uparrow}(\phi) + R_i N_i^{\downarrow}(\phi)} P_i^2 (N_i^{\uparrow}(\phi) + R_i N_i^{\downarrow}(\phi))}{\sum_{i=Fill} P_i^2 (N_i^{\uparrow}(\phi) + R_i N_i^{\downarrow}(\phi))} \tag{6.21}$$

$$A_N = \frac{\sum_{i=Fill} P_i (N_i^{\uparrow}(\phi) - R_i N_i^{\downarrow}(\phi))}{\sum_{i=Fill} P_i^2 (N_i^{\uparrow}(\phi) + R_i N_i^{\downarrow}(\phi))} \tag{6.22}$$

$$A_N = \frac{\sum_{Fill} P_i (N_i^{\uparrow}(\phi) - R_i N_i^{\downarrow}(\phi))}{\sum_{Fill} P_i^2 (N_i^{\uparrow}(\phi) + R_i N_i^{\downarrow}(\phi))} \tag{6.23}$$

The method breaks down if the number of total counts in a given fill are too small to use Gaussian error propagation. For this reason a cut on the total number of counts of 30 or more is imposed in the analysis of physics data. Since there are many fills within a given data-sample, the method can significantly reduce the statistics in kinematic bins with small cross sections.

6.3.2 Alternate Averaging Methods

Three proposed alternative methods for averaging over fills were investigated. First, three variables need to be defined:

The sum of the spin dependent yields

$$N^{simple} = \sum_{Fill} N_{Fill} \tag{6.24}$$

The polarization weighted sum of the yields

$$N^{pol} = \sum_{Fill} P_{Fill} N_{Fill} \tag{6.25}$$

The inverse polarization weighted sum of the yields

$$N^{hybrid} = \sum_{Fill} N_{Fill}/P_{Fill} \tag{6.26}$$

The three asymmetry calculations are:

$$A_N^{simple} = \frac{1}{\langle P \rangle_L} \frac{\sqrt{N_L^{\uparrow,simple} N_R^{\downarrow,simple}} - \sqrt{N_R^{\uparrow,simple} N_L^{\downarrow,simple}}}{\sqrt{N_L^{\uparrow,simple} N_R^{\downarrow,simple}} + \sqrt{N_R^{\uparrow,simple} N_L^{\downarrow,simple}}} \tag{6.27}$$

$$A_N^{pol} = \frac{1}{\langle P \rangle_L} \frac{\sqrt{N_L^{\uparrow,pol} N_R^{\downarrow,pol}} - \sqrt{N_R^{\uparrow,pol} N_L^{\downarrow,pol}}}{\sqrt{N_L^{\uparrow,pol} N_R^{\downarrow,pol}} + \sqrt{N_R^{\uparrow,pol} N_L^{\downarrow,pol}}} \tag{6.28}$$

$$A_N^{hybrid} = \frac{\sqrt{N_L^{\uparrow,hybrid} N_R^{\downarrow,hybrid}} - \sqrt{N_R^{\uparrow,hybrid} N_L^{\downarrow,hybrid}}}{\sqrt{N_L^{\uparrow,simple} N_R^{\downarrow,simple}} + \sqrt{N_R^{\uparrow,simple} N_L^{\downarrow,simple}}} \tag{6.29}$$

where $\langle P \rangle_L$ is the luminosity weighted polarization:

$$\langle P \rangle_L = \sum_{Fill} \mathcal{L}_{Fill} P_{Fill} / \sum_{Fill} \mathcal{L}_{Fill} \tag{6.30}$$

The resulting yields are then used in equation 6.16 (square root formula) for evaluation of the asymmetry values. The error bars are assigned as:

$$\delta A_N = \frac{1}{\sqrt{N} \langle P \rangle_L} \tag{6.31}$$

6.3.3 Toy Monte-Carlo

A simple Monte-Carlo was constructed to evaluate the four methods of averaging over fill numbers. The Monte-Carlo has a fixed number of particles (10,000) which are distributed across 40 sub-samples (approximate number of fills in this analysis). The yields are distributed to each sub-sample in three ways: either flatly (i.e. equal luminosity between each fill), according to a Gaussian with μ/σ=5; and assigning each sub-sample's luminosity a random value between 0 and 1. The distribution of fractional luminosities is shown in figure 6.3. In addition, each sub-sample is assigned a polarization which is assigned using four probability distributions: fixed value, Gaussian with mean 55%, even distribution between 0 and a 55%, and a sawtooth distribution with maximum of 55%. The polarization profiles are shown in figure 6.4. Within each sub-sample, each count is randomly assigned a spin direction (up or down) and then assigned left or right according to an input A_N value. The study is repeated thousands of times for each combination of polarization and luminosity distribution combination, and input A_N value, and then compared to the input A_N value. An example plot from the analysis is shown in figure 6.5.

The different asymmetry algorithms are tested for bias by comparing the reconstructed asymmetries with the input asymmetries. This is done by subtracting the mean reconstructed asymmetry and the input

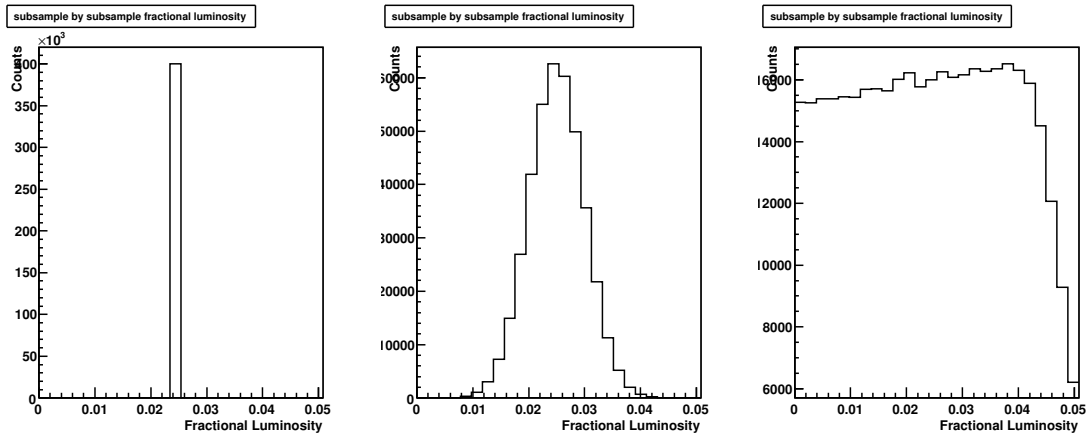

Figure 6.3: Distribution of fractional luminosities between sub-samples for the three luminosity distributions used: equal luminosity between all sub-samples (left), a Gaussian distributed luminosity between sub-samples (middle). The parent Gaussian distribution has μ/σ=5 and assigning the luminosity a random value between 0 and 1 (right).

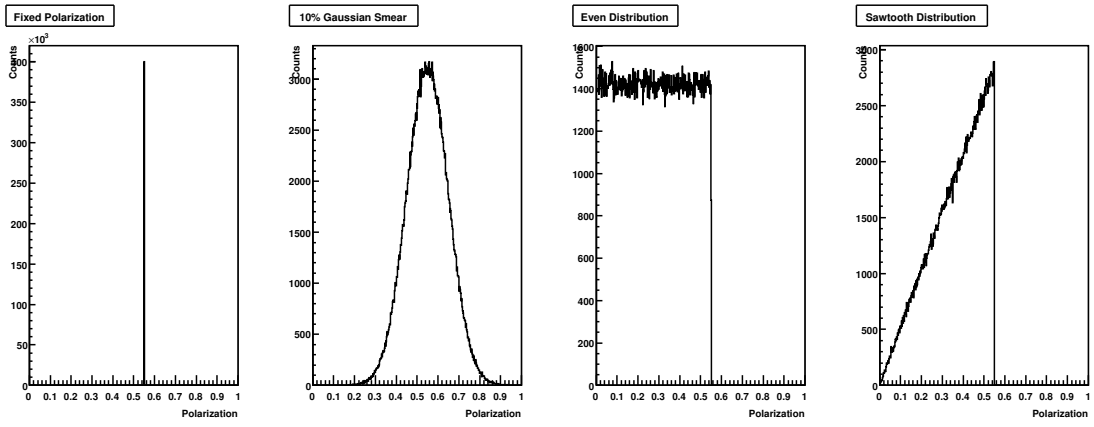

Figure 6.4: Distribution of polarization values for the four distributions investigated in the study. From left to right: equal polarization for all sub-samples, Gaussian distributed polarization, even distribution of polarization, saw-tooth distribution of polarization.

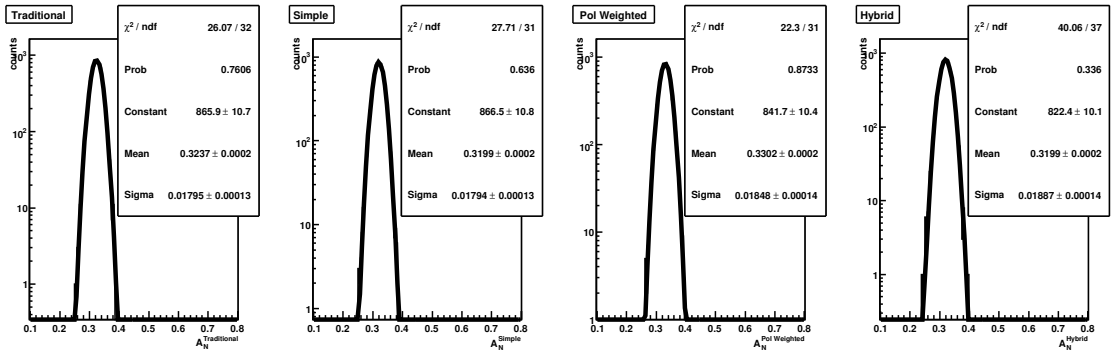

Figure 6.5: Histograms of 10,000 reconstructed A_N's using (from left to right) the traditional method of averaging over fill, A_N^{simple}, A_N^{pol}, and A_N^{hybrid}. In this example: the luminosity and polarization were smeared by a Gaussian; the input asymmetry was 32%; the polarization was 55%; and the total number of counts was 10,000. A bias towards higher asymmetries is seen in A_N^{pol}.

asymmetry. The error on the difference is taken as the $\sqrt{Var(A_N^{reconstructed})/N_{repetition}}$. In addition to a bias test, it is also checked that the reconstructed asymmetries follow the expected statistical distribution around the input asymmetry. The reconstructed asymmetries are expected to fluctuate like: $1/(\langle P\rangle \cdot \sqrt{Nparticle})$. This is checked by plotting the square root of the reconstructed asymmetry's variance. Figures 6.6-6.8 show results.

Figure 6.6(a) shows that there is a small bias in the traditional method toward higher asymmetries. Similarly, figures 6.6(b) together show that non-uniform polarization values introduce a bias toward higher asymmetry values in the polarization weighted yield method. With this particular set of smearing parameters, the bias is 10% toward higher asymmetry values. Figures 6.6(c) and 6.6(d) indicate that the luminosity smearing does not introduce a bias in any of the three new methods for averaging over fill. Therefore, the luminosity is held fixed, and the four polarization smearing methods are compared in figure 6.7.

For completeness the effects of the luminosity distributions on the reconstructed asymmetries are shown in figure 6.7.

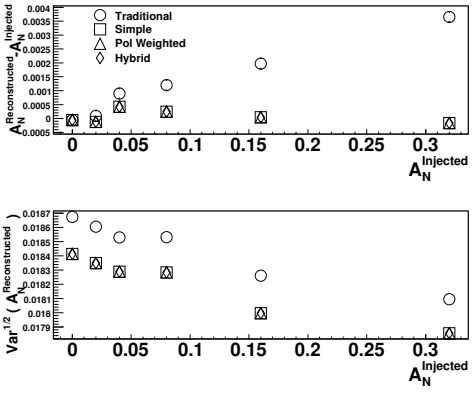

(a) No polarization or luminosity smearing

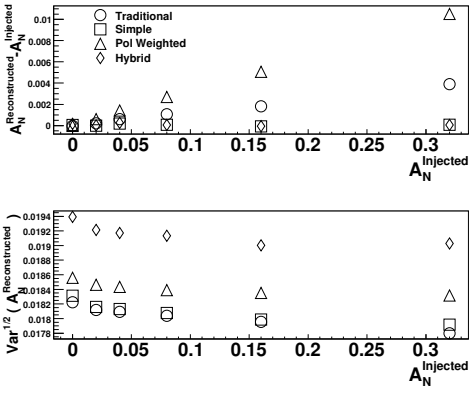

(b) 10% absolute value Gaussian polarization smearing and no luminosity smearing

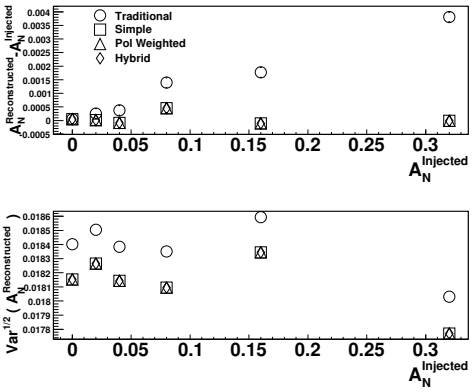

(c) No polarization smearing and Gaussian luminosity smearing

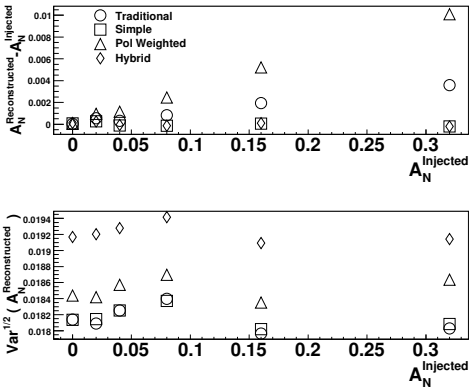

(d) 10% absolute value Gaussian polarization and luminosity smearing

Figure 6.6: The results from 10,000 sets of Monte-Carlo asymmetries compared to the input asymmetry. The polarization is set to 55% and 10k particles are shared across 40 sub-samples. Smearing to the polarization and luminosity are described in the text. Horizontal axis: input asymmetry, Vertical axis: reconstructed asymmetry - input asymmetry.

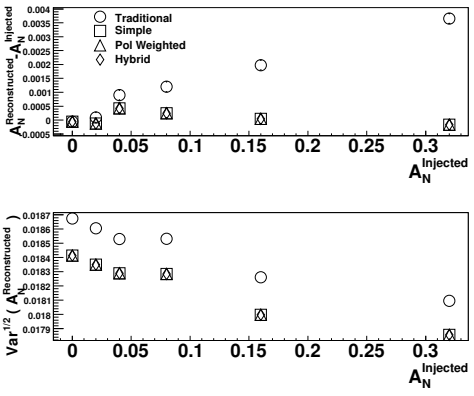

(a) No polarization smearing

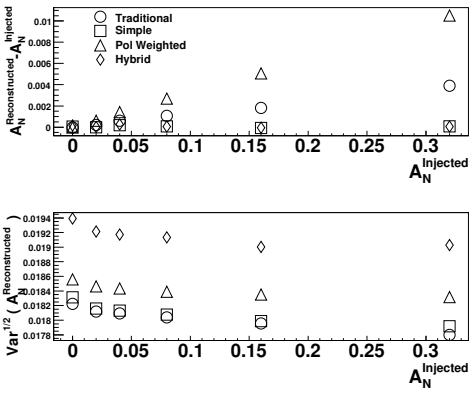

(b) 10% absolute value Gaussian polarization smearing

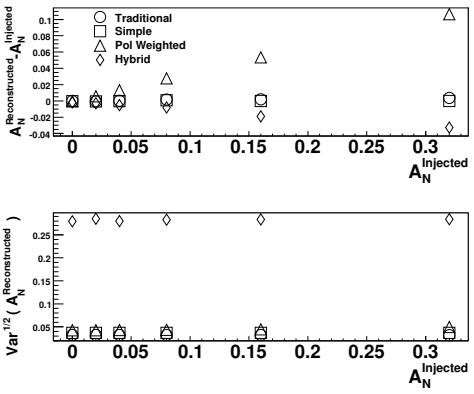

(c) Even distribution of polarization from 0 to 55%

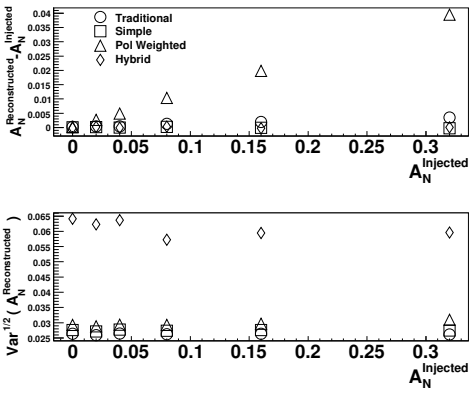

(d) Saw-tooth polarization distribution from 0 to 55%

Figure 6.7: The results from 10,000 sets of Monte-Carlo asymmetries compared to the input asymmetry. 10k particles are shared across 40 sub-samples. Smearing is applied to each sub-sample's polarization value taking it away from 55% polarization, but the luminosity is distributed equally between sub-samples. Horizontal axis: input asymmetry, Vertical axis: reconstructed asymmetry - input asymmetry.

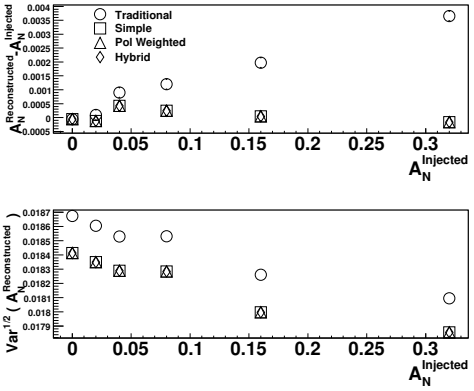

(a) No luminosity smearing

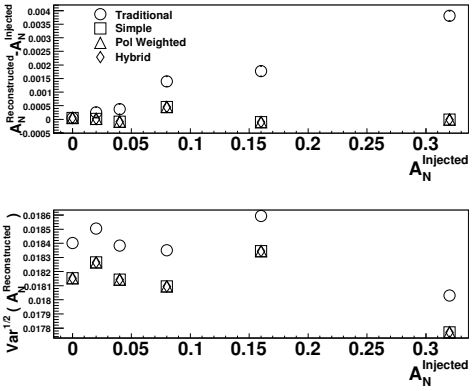

(b) Gaussian luminosity smearing

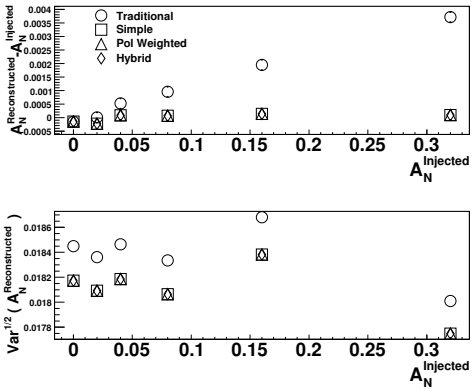

(c) Luminosity sub-sample luminosities set between 0 and 1

Figure 6.8: The results from 10,000 sets of Monte-Carlo asymmetries compared to the input asymmetry. 10k particles are shared across 40 sub-samples. Smearing is not applied to each sub-sample's polarization value of 55%, but the luminosity is smeared according to the sub-figure descriptions. Horizontal axis: input asymmetry, Vertical axis: reconstructed asymmetry - input asymmetry.

6.3.4 Conclusion

The conclusion of the study for averaging over fills is that using a simple sum of the spin-dependent yields (equation 6.24) is an unbiased estimator of the asymmetries. It is important to note that the proof outlined in this section assumes that the detector acceptance does not change with time.

6.4 Common Cross-Checks

Several statistical tools are employed repeatedly throughout the thesis. The tools are briefly introduced here. Results will be given in the analysis chapters.

6.4.1 Combining Results From Sub-Sets of Data

The MPC and EMC A_N analyses of chapters 8 and 9 both utilize a set of electronics with independent trigger thresholds for even and odd crossings. To avoid complications from different trigger thresholds, the analysis of asymmetries is done separately for even and odd crossings. Asymmetries are also generated by combining yields from bunch crossings to polarize either the Blue or Yellow beams while keeping the other beam unpolarized. This generates two additional sets of asymmetries.

Therefore, the data sample is split into four sub-samples of roughly equal weight. Before statistically combining the answers, the answers are checked for consistency within statistical fluctuations. For example, if the Blue beam polarization was wrong, there would be a non-statistical discrepancy to the Yellow beam (assuming non-zero asymmetries). The first cross-check compares the results between even and odd crossings for each beam separately. After combining the asymmetries by even and odd, the results are compared between the Blue and Yellow beams. Two measures of consistency are defined. Both are based on a t value defined as:

$$t = \frac{A_a - A_b}{\sqrt{\delta A_a^2 + \delta A_b^2}} \tag{6.32}$$

where asymmetries A_a and A_b with errors δA_a and δA_b stand for the same physical measurement but taken from two sub-samples: a and b. The t value is the distance from zero of the difference between the two samples measured in units of the statistical error bars. The natural values of the asymmetries should not depend on which beam is polarized, or which set of crossings is used. Therefore, the theoretical value of the t value is 0. The zero hypothesis can be tested with a simple χ^2 test:

$$\chi^2 = \sum_{i=0}^{N} t_i^2 \tag{6.33}$$

where the sum is over (for example) N t_i values from N p_T bins. The zero hypothesis is tested, so the number of degrees of freedom is N. There are no free parameters! The χ^2 test is a good test, but since it squares the t value it is blind to skew. For example, this χ^2 test would not return anything unusual if all the values from one sub-sample were larger than the other. To test for this type of bias, another test is needed:

$$\langle t \rangle = \frac{1}{N} \sum_{i}^{N} t_i \tag{6.34}$$

The distribution of the t-values should follow the Student's distribution.

6.4.2 Bunch Shuffling

Bunch shuffling is a technique used in asymmetry analyses to check for false asymmetries. The analysis is repeated exactly as in the physics analysis, but each fill's spin patterns are randomly assigned. There are 4 possible spin orientations ($\uparrow\uparrow$, $\uparrow\downarrow$, $\downarrow\uparrow$, $\downarrow\downarrow$), ~100 bunches per fill and ~40 fills in Run-8, so there are approximately $4^{40 \cdot 100}$ possible combinations of spin dependent yields. Three statistical tests are placed on the spin shuffled asymmetry results. The first and second are that the distribution of the shuffled asymmetry values should be symmetric about zero and distributed with variance equal to the statistical error of the physics asymmetry. In practice, this is checked by filling a histogram with: $\frac{A_N^{shuffle}}{\delta A_N^{physics}}$. Consistency to zero is checked by taking the mean of the distribution with error bar assigned as the variance of the distribution / $\sqrt{N_{shuffle}}$, where $N_{shuffle}$ is the number of times the analysis is repeated with random spin patterns. The third check fills a histogram of the χ^2 values from the fit of shuffled asymmetries over fill numbers. The distribution of χ^2 is then compared to the distribution of the same name. The checks are performed on the raw asymmetries, i.e. separated by beam, even-odd bunch crossing, etc. which leads to hundreds of output plots. A sample plot is shown in figure 6.9.

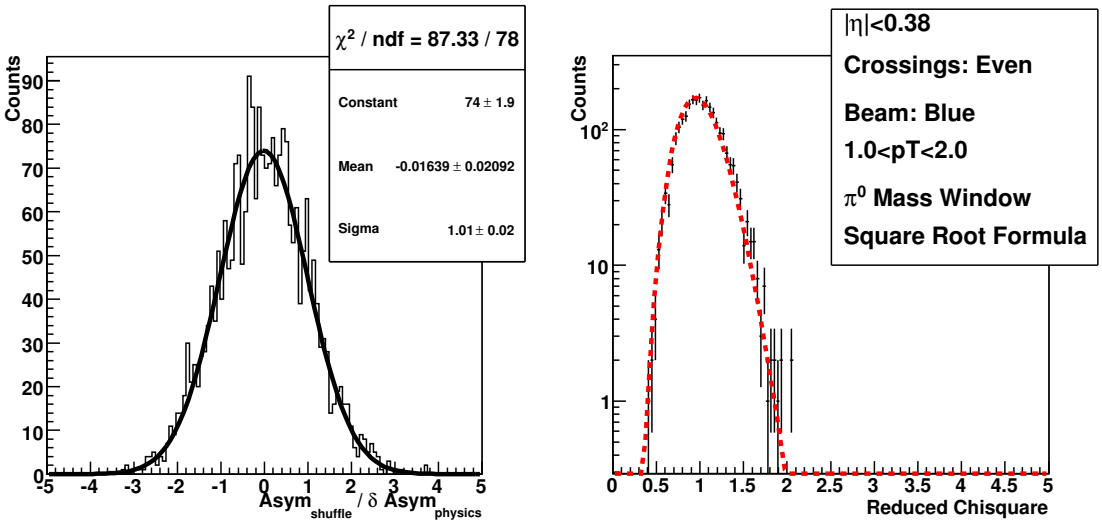

Figure 6.9: Right: histogram of $A_N^{shuffle}/\delta A_N^{physics}$. The distribution is fit with a Gaussian. Both the width and central value are consistent with the expectation of 1 and 0, respectively. Left: reduced χ^2 distribution from each shuffle's fit over fill to a constant of $A_N^{shuffle}$ values from each fill. The dotted red line shows the expected distribution.

Chapter 7

Local Polarimeter Analysis

The official RHIC beam polarization amplitude is determined using the CNI and HJet polarimeters. However, both these polarimeters are located near the 12 o'clock position in the RHIC beam tunnel and are separated from the PHENIX interaction point by a kilometer. Between the two points the beam polarization direction evolves. Therefore, a polarimeter is built into the PHENIX experiment to verify both the polarization magnitude and direction. It is called the local polarimeter. It does this by measuring the left-right single transverse spin asymmetry in the production of very forward neutrons. Asymmetries in forward neutron production was originally discovered at the RHIC-IP12 experiment [55]. We use the ZDC and SMD, whose hardware is described in section 2.2.3, to reconstruct the neutron hit positions and then the asymmetries.

This chapter is divided into three sections:

- Short summary of the first near real-time local polarimeter analysis performed during Run-8.
- In depth summary of the offline analysis which revealed flaws in the real-time analysis.

7.1 Real-time Analysis

A local polarimeter analysis was run in real time during the 2008 data collection period to provide feedback to the Collider Accelerator Department on the polarization performance. The logistically challenging measurement was done in near real time in the counting house by passing over the 700 MB/s raw data stream in near real time as it waited for transfer to RCF for archiving. The results were used to provide feedback to the RHIC accelerator physicists. After the analysis was completed, a channel mapping problem was discovered in the north arm SMD. A comparison between the neutron asymmetry from the south ZDC/SMD and the polarization determined by the CNI polarimeter is shown in figure 7.1.

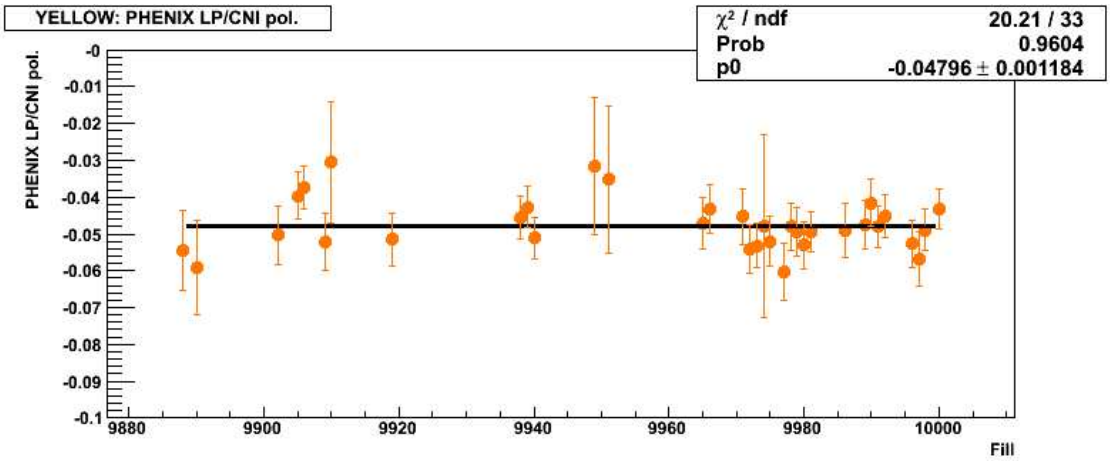

Figure 7.1: Vertical axis: Ratio between the neutron raw asymmetry value and the CNI-determined polarization values from Run-8. Horizontal axis: fill number. The ratio is fit with a constant which shows that the yellow beam's polarization delivered to PHENIX was stable over Run-8.

7.2 Offline Analysis

7.2.1 Detector QA

ZDC and SMD calibration constants are assumed to be constant from the previous RHIC run. However, there is a known problem with the channel mapping which is detected by inspecting scintillator by scintillator luminosity asymmetries in the SMD. Hit slats are determined by an energy cut in the ZDC and a charge threshold determined scintillator to scintillator. Figure 7.2 shows a summary of the asymmetries averaged over all the RHIC fills.

7.2.2 Neutron Reconstruction

Using the channel ordering determined from the previous section the neutron hit position is reconstructed using the following formula for the SMD scintillator slats in x and y:

$$X = A\frac{\sum_i G_i(ADC_i - Ped_i)i}{\sum_i G_i(ADC_i - Ped_i)} + B \tag{7.1}$$

where ADC_i is the scintillator raw ADC, Ped_i is the tower's pedestal [1] and G_i is the tower's gain. A and B are geometric mapping factors which depend on the North or South and are different for the x and y coordinates. G, A and B are constants. Neutrons are selected by requiring that the SMD multiplicity in both the x and y direction is greater than 1, and a high energy deposit in the ZDC.

[1] Determined by visual inspection of each tower's ADC spectra

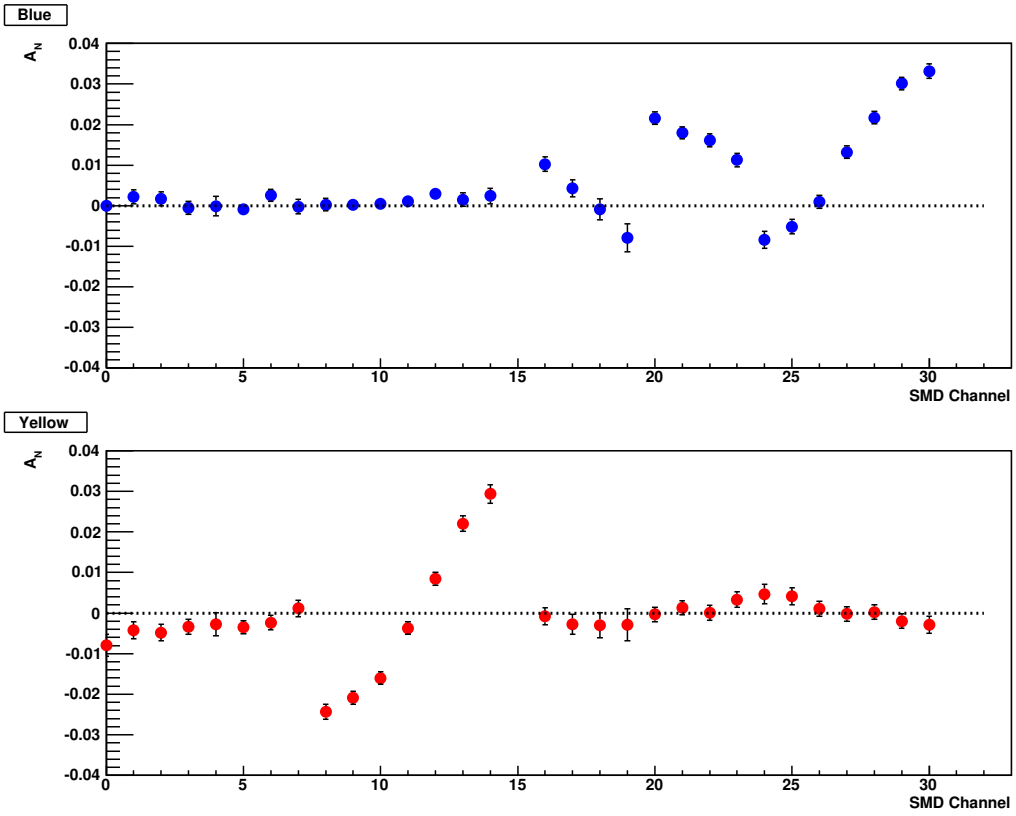

Figure 7.2: Vertical axis: A_N. Horizontal axis: SMD channel number. Top: Blue beam, Bottom: Yellow beam. Channels 0-7, 8-14, 16-23 and 24-30 give the South Y, South X, North Y, and North X coordinates respectively. The figure clearly shows that the channels giving the y-coordinate in the north are mis-mapped, and that there is a significant polarization component in the radial direction.

7.2.3 Asymmetry Analysis

Neutron asymmetries are formed using the spin-dependent yield of neutrons with radial positions between 3 and 5 cm from the beam position center. Asymmetries are calculated using the square root and luminosity formulas (defined in section 6.1) on a fill-by-fill basis. The raw asymmetry ϵ is then divided by the polarization on a fill by fill basis. For each azimuthal bin, the asymmetries are averaged over fill number and then fit with an azimuthal modulation. The results are shown in figures: 7.3 and 7.4.

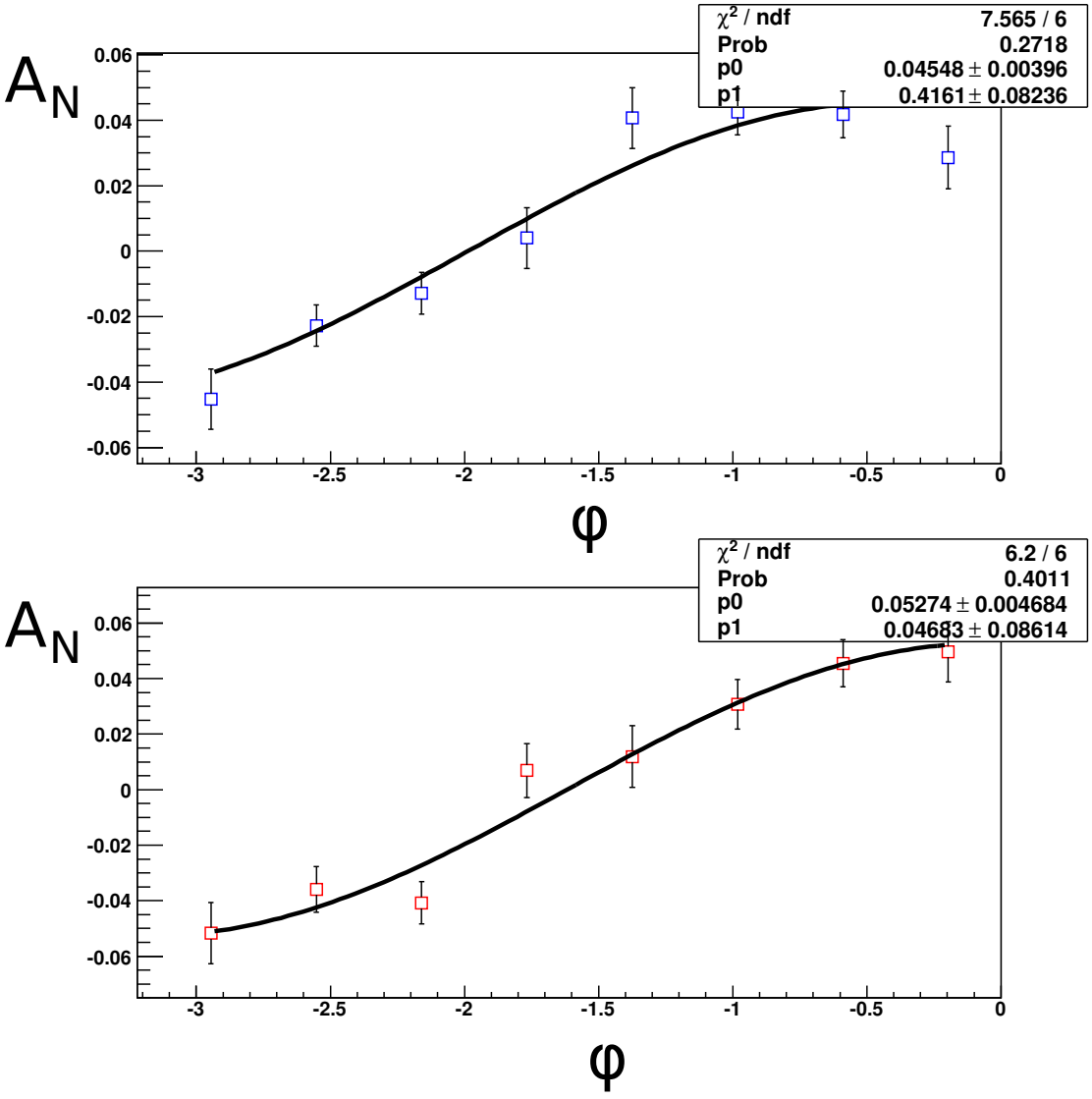

Figure 7.3: Horizontal axis: ϕ. Vertical axis: A_N magnitude (phase) on left (right). Blue top, Yellow bottom. Forward asymmetries only. The square root formula is used.

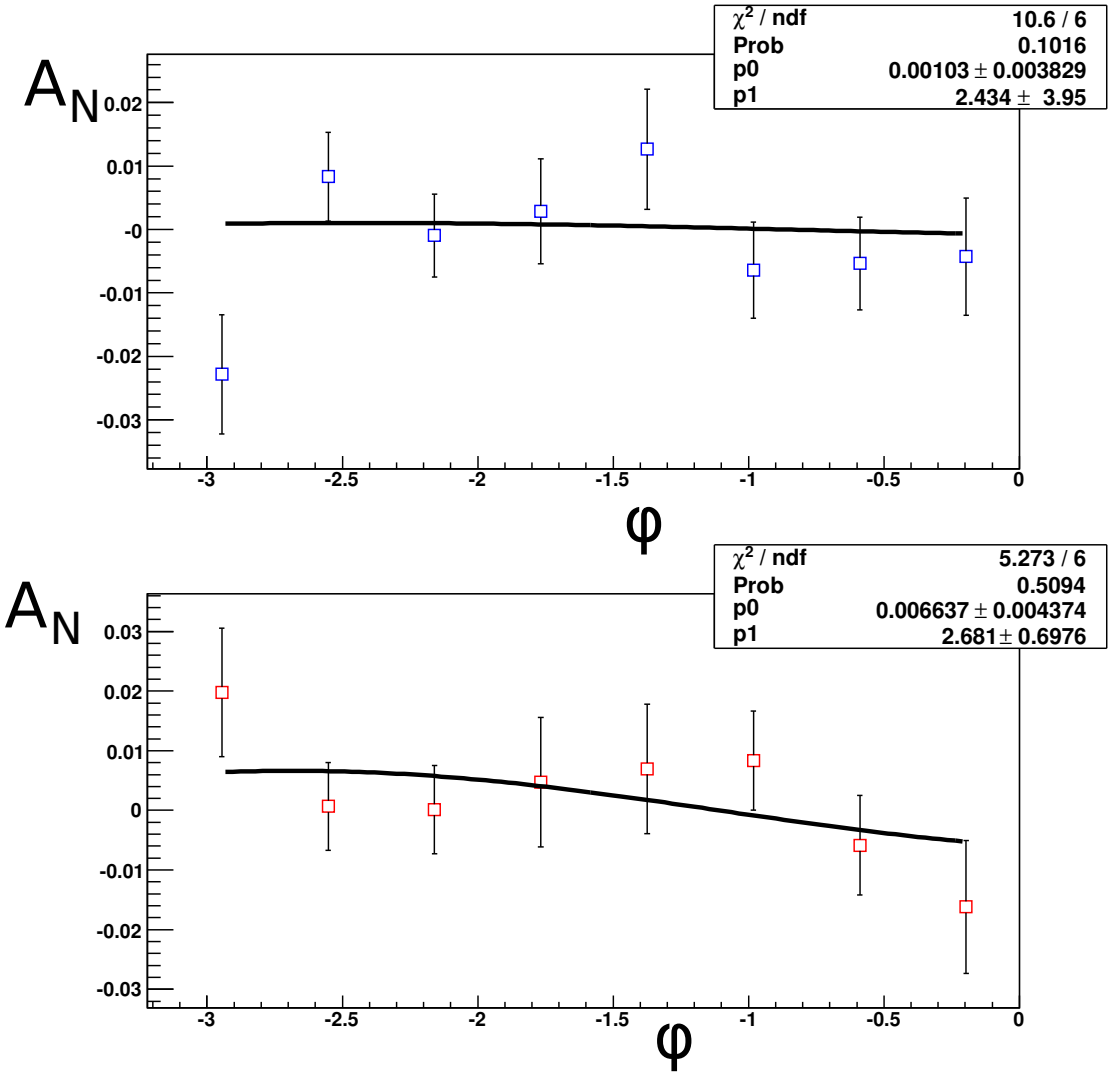

Figure 7.4: Horizontal axis: ϕ. Vertical axis: A_N magnitude (phase) on left (right). Blue top, Yellow bottom. Backward asymmetries only. The square root formula is used.

7.2.4 Local Polarimeter Results for Run-8

The polarization angle from this analysis is 0.43 ± 0.066 radians from the vertical direction for the blue beam. The yellow beam is consistent with a vertically polarized beam. After this study was completed, an more precise analysis was performed with greater precision on the phase. This study is available in reference [94]. The blue beam phase from this analysis is: 0.242 ± 0.030 (statistical) +0.111 -0.069 (systematic) radians from vertical. The yellow beam phase determined in the same analysis is: 0.031 ± 0.048 (statistical) +0.091 -0.114 (systematic). These values are used in chapters 8 and 9 for the determination of left-right asymmetries.

Chapter 8

Forward Rapidity MPC $A_N^{Cluster}$ Analysis

One of the main goals of constructing the MPC is to measure the forward single spin asymmetries of π^0's and η mesons at high x_F. For π^0's with energy below about 20 GeV the MPC is able to cleanly resolve the decay to two photons. However, above that energy the impact position separation is comparable to the tower size and both photons are reconstructed as a single "merged" energy cluster. At $\sqrt{s}$=62 GeV, this means the maximum x_F is approximately 0.65, but at $\sqrt{s}$=200 GeV it is only 0.2. The most interesting A_N results from past experiments have exhibited rising asymmetries with x_F starting at around 0.3. Therefore, in order to probe the non-zero high x_F region, π^0's reconstructed with two photons can be used at $\sqrt{s}$=62 GeV but π^0's with two merged photon clusters, which are susceptible to backgrounds, must be used at $\sqrt{s}$=200 GeV. This chapter presents the asymmetries for inclusive clusters in the MPC at $\sqrt{s}$=200 GeV and an estimate using Monte-Carlo of their decomposition into contributions from π^0's, η's, direct photons and other sources. The calibrations used for extraction of the asymmetries are improved versions from the ones presented in chapter 5.

The asymmetry analysis is split in two parts:

- Detector quality assurance checks. These are checks beyond the calibrations discussed in chapter 5.
- Discussion of the analysis procedure and presentation of the final results. In addition, important consistency checks are discussed.

The cluster decomposition is also split into two parts:

- Description of the simulation setup and cross-checks that the simulation accurately models the detector.
- Results of the decomposition analysis. This work was done primarily by my colleague, Anselm Vossen. Some of the text is taken from our joint analysis note[95].

8.1 Detector QA

Before calculating asymmetries using the MPC, a series of detector checks are performed. The asymmetry analysis presented here is the first analysis performed on a data-sample taken at $\sqrt{s}$=200 GeV with the MPC. It is also the first analysis based on an MPC data-sample collected over a long period of time. Therefore, many of the detector checks are performed for the first time for this analysis. Only the most significant checks are described here. Reference [96] includes many more checks.

The section is divided as follows:

1. Description of the tower-by-tower dynamic range.
2. Differences between data-samples collected with different triggers and features of the MPC triggered data-sample.
3. Cross-check that the detector is stable during the high luminosity running of RHIC.
4. Definition of criteria for a good data run.

8.1.1 Tower-by-Tower Dynamic Range

In Run-8, the dynamic range for individual MPC **towers** varies from 25 and 50 GeV. However, in this analysis the maximum **cluster** energy extends to 72 GeV. Therefore, high energy clusters striking the center of a crystal front face deposit most of their energy in the crystal and are expected to saturate the ADC value of the cluster's central tower. Clusters with impact positions closer to the edge between two crystals are not expected to saturate the ADC since, in the extreme case, the shower energy distributes equally across four towers. This section provides details of a simple calibration procedure to identify the ADC overflow value for each tower. The discussion assumes the reader has read section 4.4.3. The concept of the overflow does not apply to the difference between post and pre. It applies to the low (and high) gain post ADC response. If the low gain post ADC response is found to exceed the overflow value for the tower, then the corresponding cluster is removed from analysis.

Overflow Estimation

The analysis to find the overflow value is quite simple:

1. A finely binned histogram of the low gain post value is generated for each tower. At the same time a pre_ADC histogram is generated which will be used to subtract a pedestal and determine the dynamic range of the tower.

2. Run over the histograms tower-by-tower to find the overflow point. The overflow point algorithm is quite simple: starting at low ADC values, the bins are iterated over. For each bin the summed counts 15 bins below and 15 bins above the current bin are found until the forward over backward ratio exceeds 2.5. The choice of ratio limit and scanning window were largely arbitrary but were settled upon after a few earlier choices stumbled on tower-dependent features in the distributions.

The overflow values are plotted against tower number with removal of towers from my warnmap and non-instrumented towers in figure 8.1.

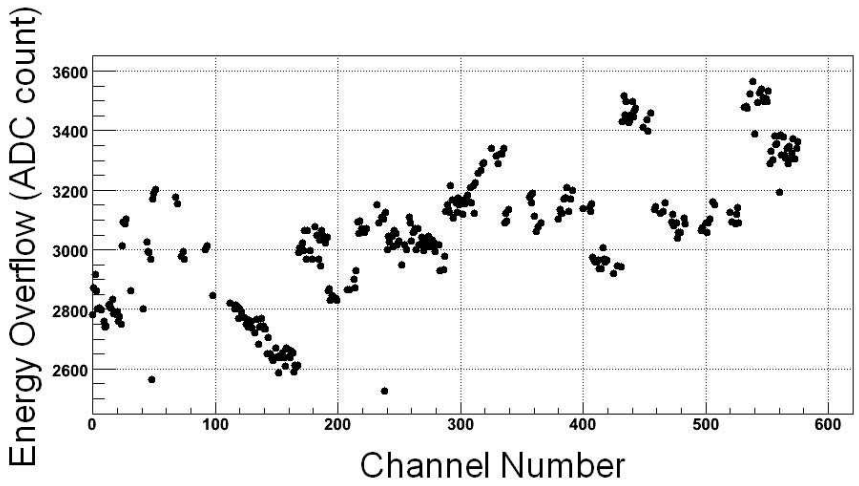

Figure 8.1: Vertical axis: Overflow values for the low gain ADC post response for MPC_4x4(A|B) triggered events, Horizontal axis: tower identifier. South towers range from 0 to 287, and north towers range from 288 to 575. Note that 416 out of 576 total channels are instrumented.

To translate the overflow values from low gain post ADC response to tower energy, the pedestals are subtracted and the difference is multiplied by the tower gain. The overflow value in units of GeV is shown in figure figure 8.2.

Effect of Overflow Veto on Cluster Spectra

The cluster energy spectra with and without the ADC overflow veto are shown in figure 8.3 for the North and South arms. The percentage of clusters passing the overflow veto is shown in 8.4.

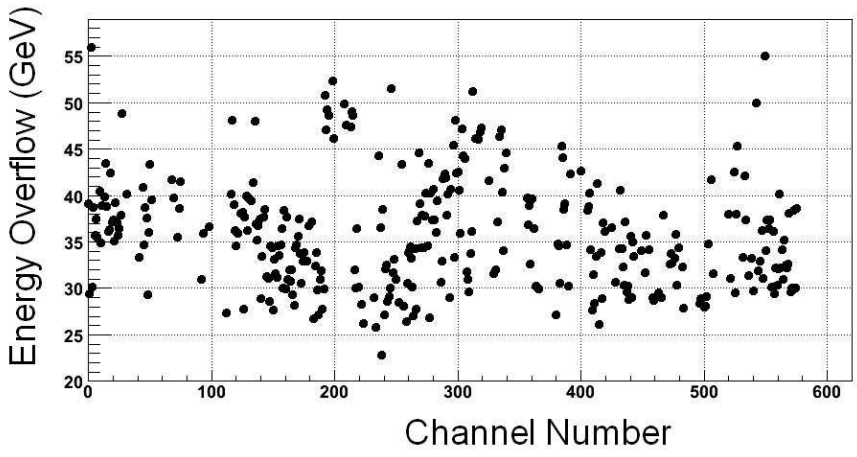

Figure 8.2: Vertical axis: Tower overflow points after the energy calibration. Horizontal axis: tower identifier. South towers range from 0 to 287, and north towers range from 288 to 575.

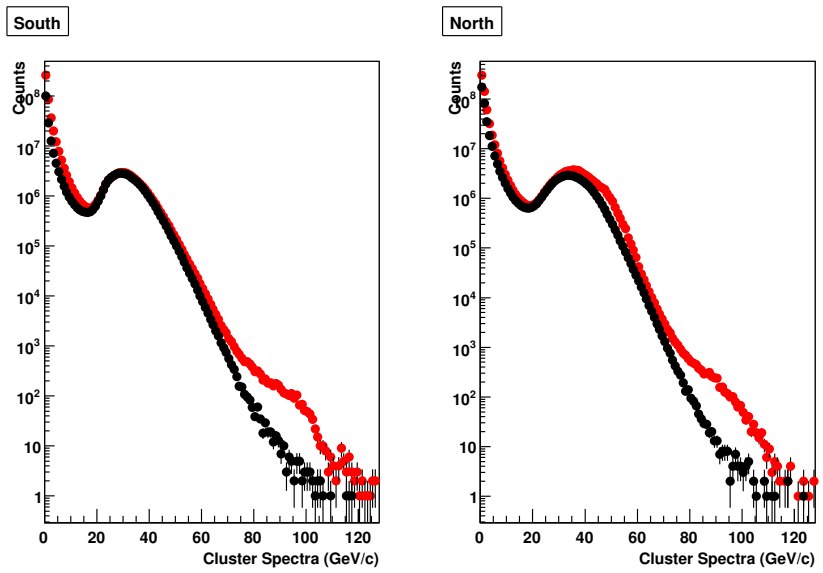

Figure 8.3: Vertical axis: Counts, Horizontal axis: Cluster p_Z in GeV/c. The spectra are compared for MPC_4x4B triggered data between inclusive clusters (red), and clusters with the MPC_4x4B trigger bit check on the corresponding arm and an ADC overflow veto (black).

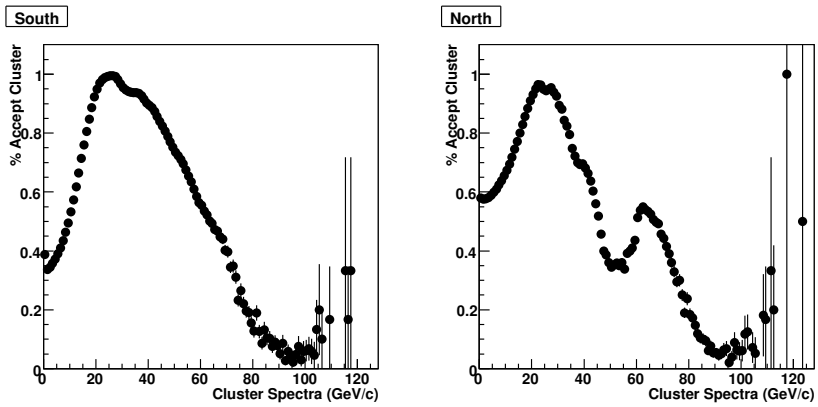

Figure 8.4: Vertical axis: Percentage of clusters passing overflow veto cut and MPC_4x4B trigger bit check, Horizontal axis: cluster energy. The trigger bit lookup rejects clusters and lowers the probability of acceptance at low momenta.

8.1.2 Trigger

Each MPC arm's trigger is formed using two central arm EMC FEM's. A long-standing effect in the central arm triggered data is the so-called "even-odd effect" which is caused by separate trigger circuits for even and odd bunch crossings. Similar to the central arm, significant differences between the cluster spectra from even and odd crossings are found for both the MPC triggers, but not in the minimum bias dataset. Therefore, this analysis is done separately for even and odd crossings. The impact of the effect on the asymmetries is evaluated in subsequent sections. The triggering system is described in detail in section 4.4.3. First, the best trigger for extraction of high energy cluster asymmetries is determined, next the even-odd effect is quantified, and finally a reconstruction problem in the triggered dataset is explained.

Choice of Trigger

To collect the largest possible data-sample, the best choice of trigger would be the MPC_4x4(A|B). However, the cluster energy spectra collected using this trigger may be biased from events when the trigger occurs on one MPC arm and clusters are collected from other arm. To avoid this problem, a trigger match is performed. It is only possible lookup the trigger bit by arm and only for the MPC_4x4B trigger[1]. The issue of trigger bias could be avoided by choosing the minimum bias trigger. However, as figure 8.5 shows, for $E_{Cluster} \geq 20GeV$ the triggered dataset is far larger than the minimum bias data set. The analysis only includes clusters with energy greater than 25 GeV.

Even-Odd Bunch Crossing Effect

Figure 8.6 illustrates the even-odd triggering effect using the ratio of energy spectra from even and odd crossings after the warnmap cut (described in section 5.5.3) and the good run list selection (described in section 8.1.4) have been applied. The effect is caused by slightly different energy threshold turn-on curves between two sets of trigger electronics circuits. As a consequence, all analysis is performed separately for two data samples corresponding to the even and odd bunch crossings. The two sets of asymmetries are compared for consistency and then combined using a weighted statistical mean.

Z-Vertex Reconstruction in Triggered Dataset

The z-vertex is reconstructed using the BBC. The MPC trigger does not included a coincidence with the BBC-based minimum bias trigger. Therefore, a z-vertex selection is not included in the trigger decision.

[1] details of the MPC triggering system are available in section 4.4.3.

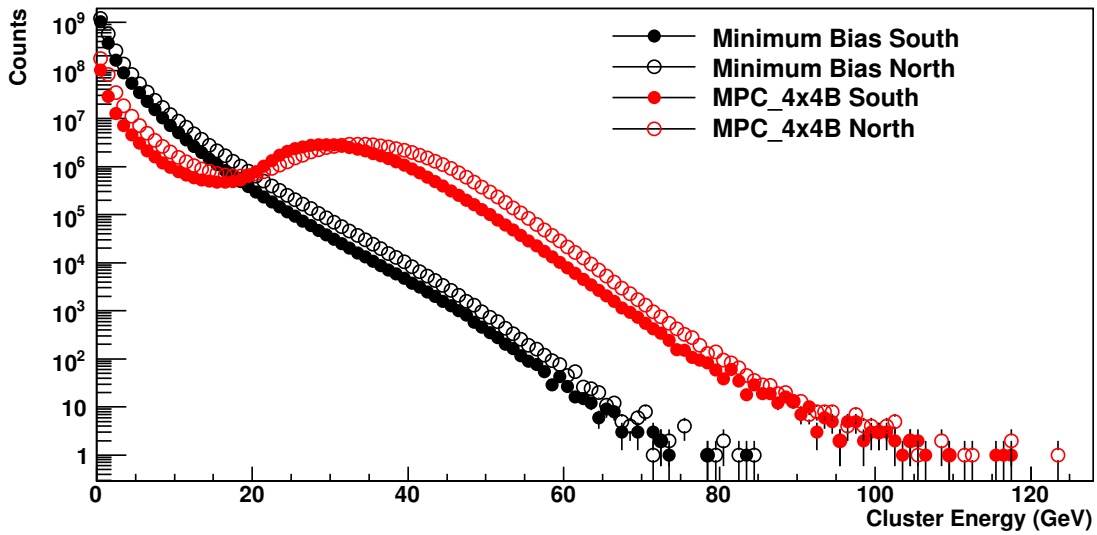

Figure 8.5: Vertical axis: Counts, Horizontal axis: Cluster energy [GeV]. Comparison between cluster yields for the minimum bias dataset and the data-sample acquired with the MPC_4x4B trigger.

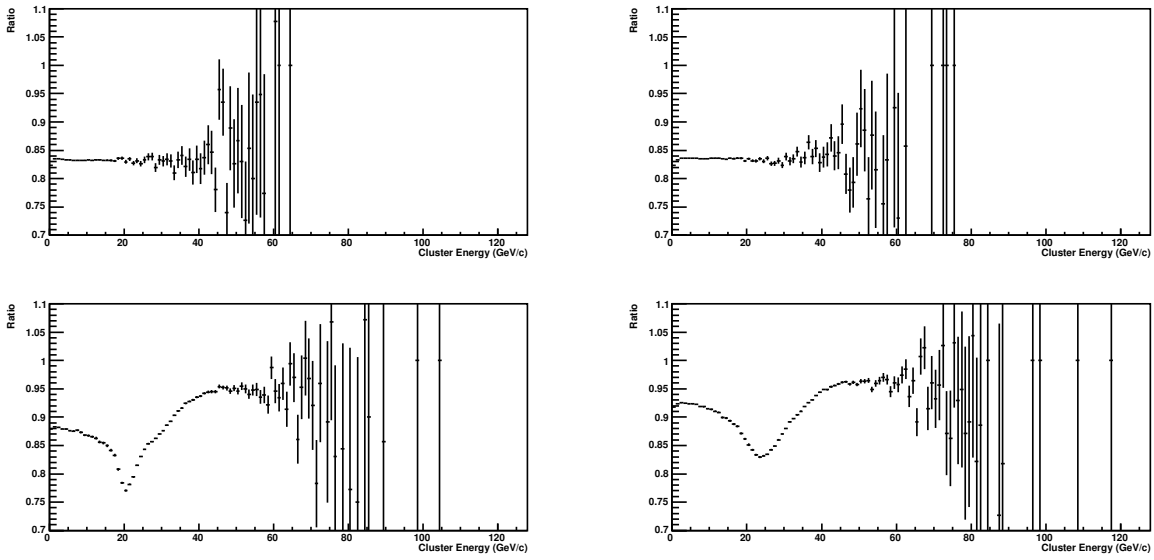

Figure 8.6: Vertical axis: ratio of energy cluster spectra for even and odd bunch crossings. No cluster cuts have been applied. Top: minimum bias triggered data, Bottom: MPC_4x4B triggered data, Left: South MPC, Right: North MPC.

The z-vertex distribution for the MPC_4x4B and for the minimum bias triggered data are shown in figure 8.7.

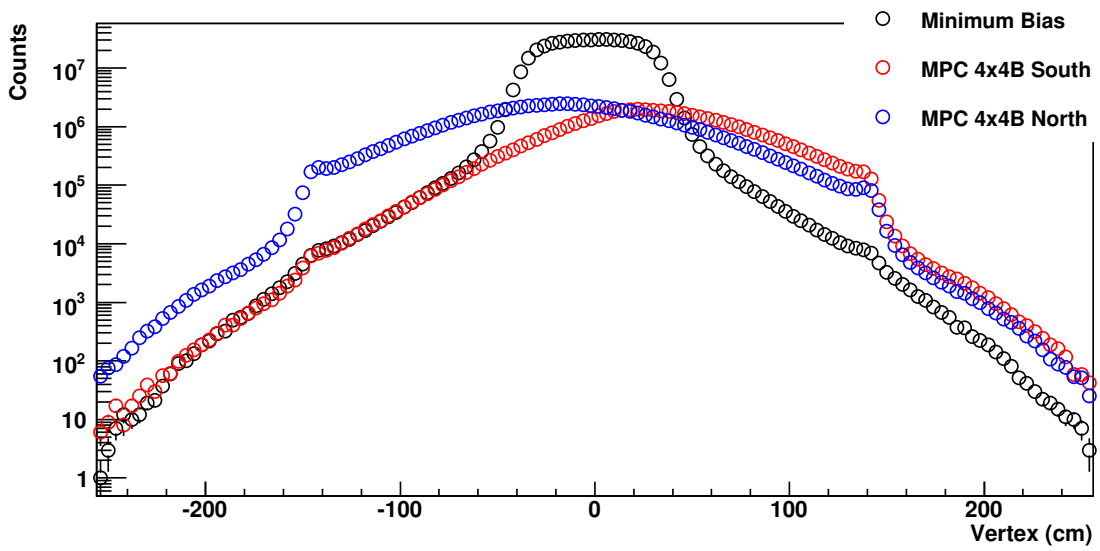

Figure 8.7: Vertical axis: counts. Horizontal axis: Z-Vertex (cm). Z-Vertex distributions for data-samples obtained with the minimum bias trigger and the MPC_4x4B energy threshold trigger. The BBC's are located at ± 140 cm and the MPC's at ± 220 cm.

In the case of the minimum bias data set nearly all the events return a valid z-vertex, but in the case of MPC triggered data approximately 25% of the events do not include a well reconstructed z-vertex position[2]. Figure 8.8 shows the percentage of events with a non-reconstructible z-vertex from triggered data. Events beyond a z-vertex of ± 70 cm do not enter the analysis.

[2]The BBC z-vertex position reconstruction is done by taking the time difference between the South and North BBC detectors. The MPC trigger does not include a coincidence with the BBC, so not all of events include a coincidence between the two BBC arms.

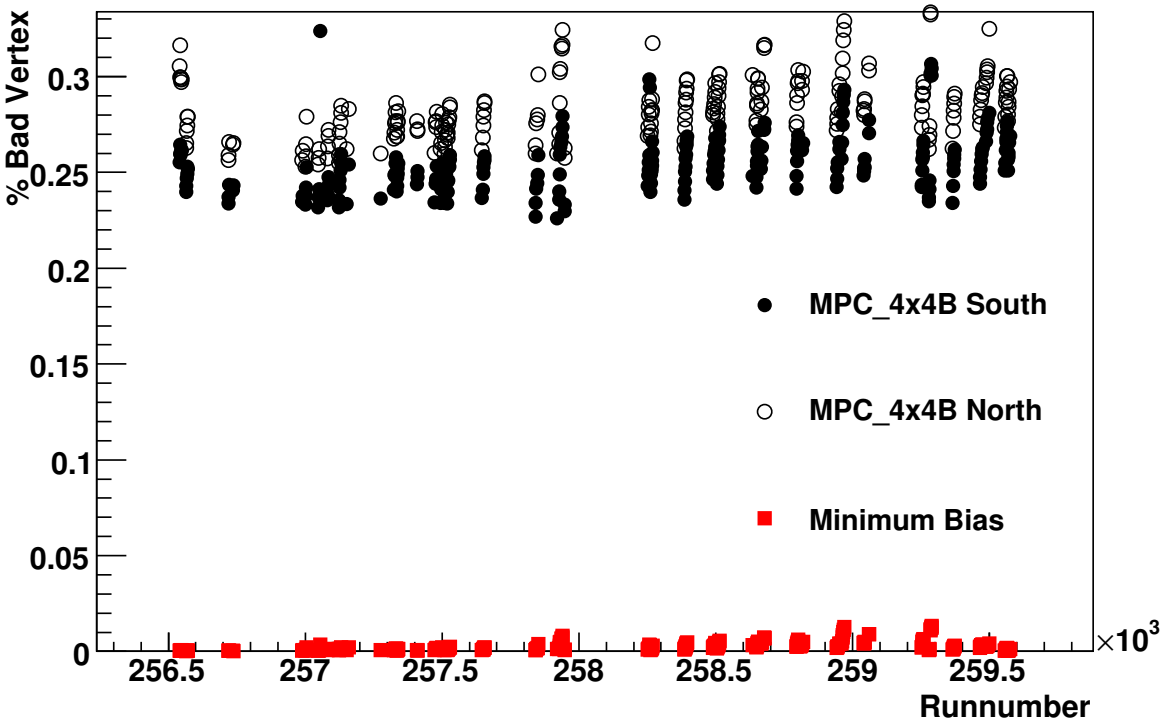

Figure 8.8: Vertical axis: Percentage of triggered events with unreconstructed vertices. Horizontal axis: run.

8.1.3 Rate Correlation

This section presents the correlation between the RHIC luminosity and the normalized yield of clusters meeting an energy threshold in the MPC. This correlation serves as a consistency check to exclude possible saturation effects at high rates. The normalized yield is the yield of clusters divided by the number of events. The normalized yield should be independent of the RHIC luminosity. The cluster yields are determined by counting clusters with longitudinal momenta between 20 and 30 GeV after the warnmap cut and ADC overflow veto. The normalized yield is plotted against the luminosity in figure 8.9. Luminosity is estimated using the number of live BBCLL1 triggers divided by the number of live Clock triggers[3].

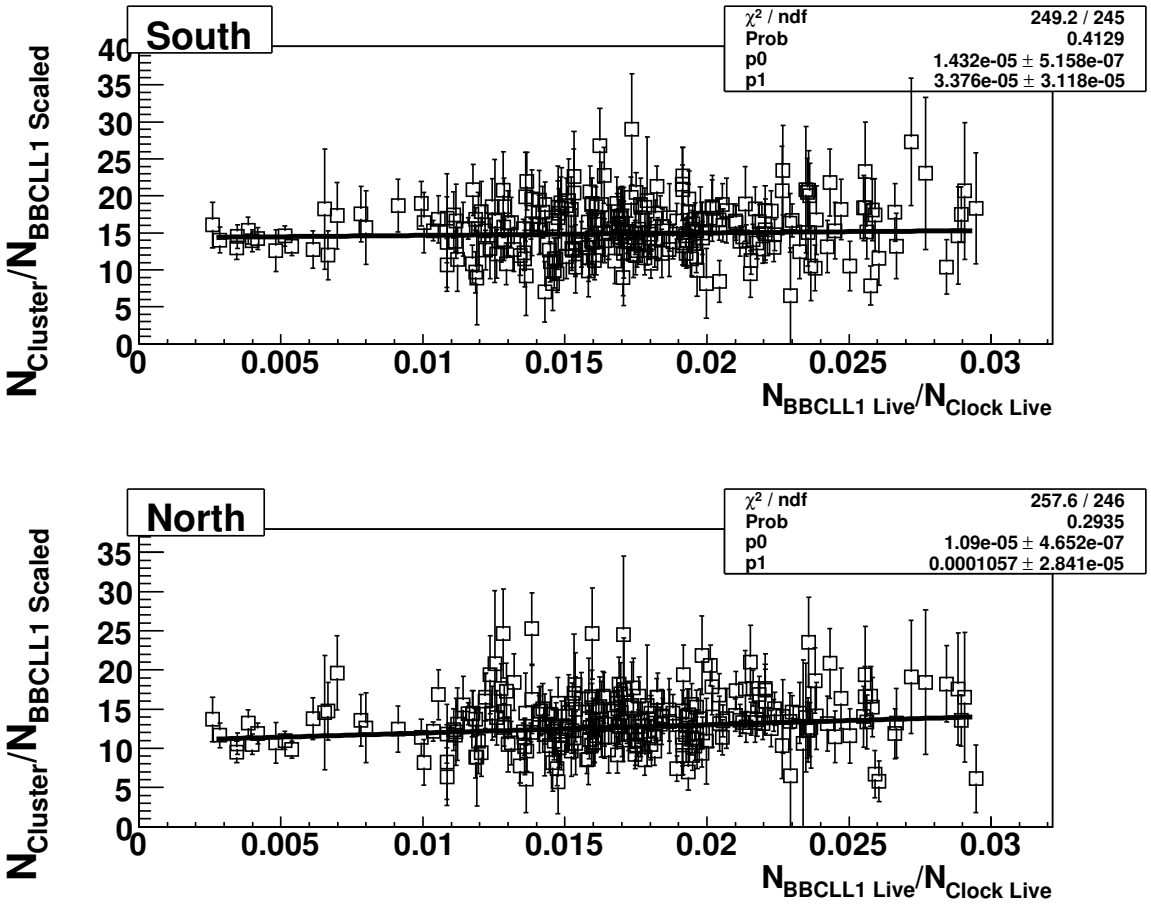

Figure 8.9: Vertical axis: Yield of clusters divided by number of triggers (both taken from Minimum Bias triggered events), Horizontal axis: Luminosity. Top panel: South MPC, Bottom panel: North MPC. The cluster energy window is $20 < p_z < 30$ GeV/c. The absolute difference in normalized yield between North and South is expected since the North has an extra ring of towers at high pseudorapidity. Figure 5.13 shows that for towers at the same radius, the normalized yields are the same.

[3]The PHENIX database has a problem with integer overflows, and its values cannot be trusted for high rate triggers like the ones used. Therefore, the number of live triggers is estimated using the number of scaled triggers multiplied by the corresponding scale down factor.

8.1.4 Run Selection

Runs are rejected for a variety of criteria. The following section defines the run selection cuts.

Spin Database Check

1. **Spin Database:** The following runs have no information in the spin database[4]:

   Run Number=256724 257502 257517 257644 257649 258663 258808 258950 259050 259572

2. **No polarization measurement** Fill 9947 does not have a blue beam polarization measurement. For ease of analysis the entire fill is rejected:

   Run Number=257792 257793 257794 257797 257798 257799 257802 257803

3. **Non-vertical polarization** Some runs at the beginning of the 2008 $p+p$ run were radially polarized:

   Run Number=256450 256451 256452 256454

High Voltage

Occasionally the PHENIX data taking shift crew forgets to turn on the MPC high voltage at the beginning of a store. This is checked by calculating the yield of clusters meeting a 20 GeV energy threshold requirement and the warnmap veto per minimum bias trigger. The resulting ratios are shown in figure 8.10. The following runs have been removed:

Run Number=258249 258250 259276 259277

The difference in the normalized yields between the North and South detector arms is expected and shown in figure 8.10. The North and South arms have different acceptances and the plot is not corrected for the effect. Figure 5.13 shows the normalized yield plotted against the tower radius and also shows good agreement of the yields between arms.

8.2 Analysis

Left/right asymmetries are extracted separately for even and odd crossings, separately for the blue and yellow beams and separately for the South and North MPC arms. The results are appropriately combined and are checked for consistency within statistical uncertainties. This section presents a summary of the analysis and its cross checks. The PHENIX analysis note in reference [96] includes an extensive set of cross-checks: detailed acceptance comparisons between the South and North arms, tables of results for each

[4]The spin database centralizes all spin information for each fill including: the spin pattern, the polarization values, the GL1-1P scalers, and other more technical quantities.

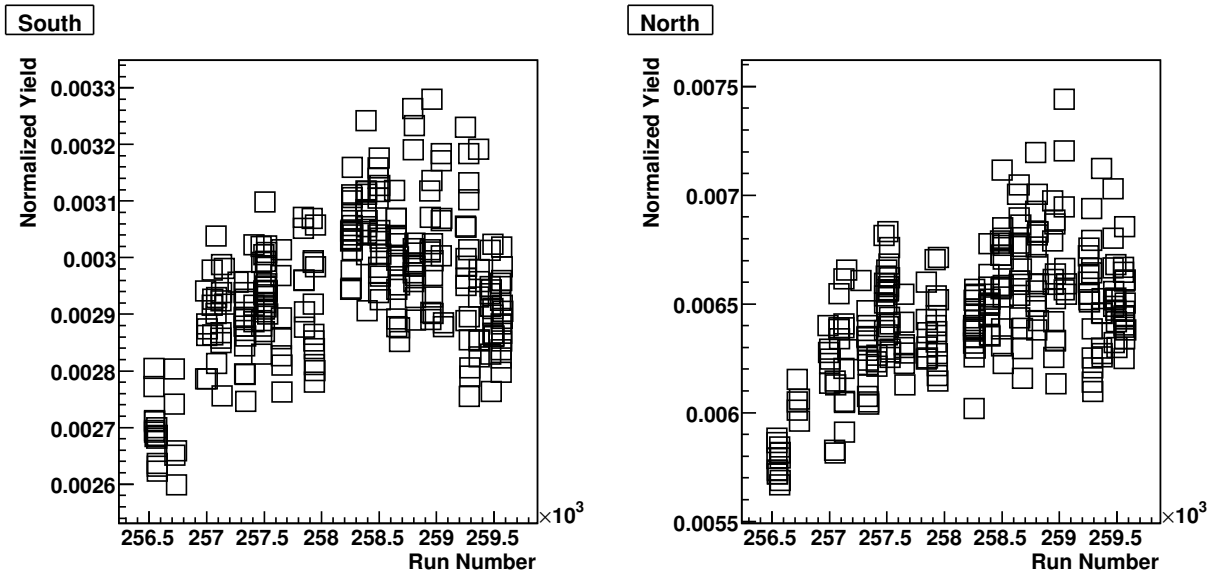

Figure 8.10: Vertical axis: Yield of clusters divided by the number of minimum bias events analyzed. Horizontal axis: run number. The ratio is used to detect operator errors in turning on the MPC high voltage.

sub-sample, comparison plots between the sub-samples, comparison between five different A_N estimators, bunch-shuffling, and separated analysis between the four spin patterns and statistical comparison between each result. With the exception of the one test shown in section 8.2.2, all results behave as expected.

8.2.1 Asymmetry Calculation

Kinematic Binning

The inclusive yield of clusters is shown in figure 8.11. The spin-dependent yields are extracted and used to calculate asymmetries using four sets of kinematic binning schemes. The cluster yields are extracted in:

- A grid of p_z, p_T. This binning is shown in table 8.1. Except for the last two p_z bins, the binning is taken from a publication of $A_N^{\pi^0}$ from the STAR collaboration[28]. The asymmetries are denoted: $A_N(x_F, p_T)$. For the measurements of this thesis, $x_F = 2p_Z/\sqrt{s} = p_Z/100$.

- Bins of p_z above and below a pseudorapidity cut of η=3.5. The p_z bins are identical to the p_z binning used in the previous selection. The asymmetries are denoted $A_N(x_F, \eta)$.

- Bins of p_T for clusters with $|p_Z| > 40$ GeV/c. The binning is shown in table 8.2. The asymmetries are denoted $A_N(p_T)$.

$p_Z^{low} - p_Z^{high}$	p_T bin					
25-30	0.5-1.1	1.1-1.4	1.4-1.9	1.9-2.4	2.4-3.2	3.2-6.0
30-35	0.5-1.2	1.2-1.7	1.7-2.2	2.2-2.7	2.7-3.4	3.4-6.0
35-40	0.5-1.5	1.5-1.9	1.9-2.4	2.4-3.0	3.0-3.6	3.6-6.0
40-47	0.5-1.7	1.7-2.2	2.2-2.7	2.7-3.3	3.3-3.8	3.8-6.0
47-60	0.5-2.0	2.0-2.3	2.3-2.9	2.9-3.4	3.4-4.0	4.0-6.0
60-72	0.5-2.2	2.2-2.7	2.7-3.3	3.3-4.0	4.0-4.4	4.4-6.0
72-85	0.5-2.6	2.6-3.5	3.5-4.2	4.2-5.0	5.5-5.5	5.5-6.0

Table 8.1: p_z, p_T kinematic binning used to determine spin-dependent yields and extract single transverse spin asymmetries

- A single bin for $|p_Z| > 30$ GeV/c and p_T >1.2 GeV/c. This bin is used as a check of the PHENIX local polarimeter and not for physics analysis.

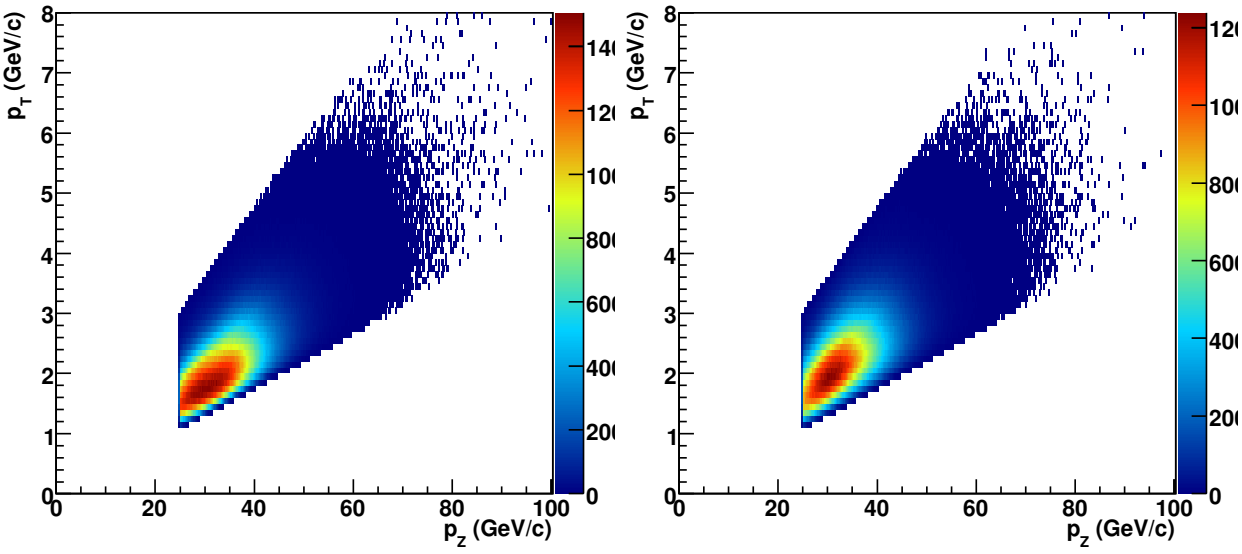

Figure 8.11: Cluster p_z and p_T distributions of clusters in the MPC.

Cluster Cuts

- Tower containing the cluster center not in the warnmap. The warnmap is shown in figure 5.14.
- Cluster distance from the beam axis, $R_{Cluster}$, between 13 and 18 cm. This is a fiducial cut to ensure that the MPC North and South have similar acceptance for particles and for energy deposited in the MPC.
- Time of flight value is less than the overflow value and within a wide window around the photon time of flight.

p_T^{low}	p_T^{high}
1.0	1.5
1.5	2.0
2.0	2.5
2.5	3.0
3.0	3.5
3.5	4.0
4.0	5.0
5.0	8.0

Table 8.2: p_T kinematic binning used to determine spin-dependent yields and extract single transverse spin asymmetries

- ADC overflow veto. Determination of the overflow is described in section 8.1.1. The overflow veto is not applied for the highest bin in p_T for the $|x_F|$ >0.4 p_T binned asymmetries. This leads to an underestimation of the bin's $\langle p_T \rangle$, but increases the statistics in the bin significantly.

Figures 8.12-8.14 show the mean kinematic variables for each of the three sets of kinematic binning. Two plots are shown: one without radius cuts on the clusters and the other requiring radii between 13 and 18 cm. The restriction on the radius improves the agreement between the North and South acceptances. Statistical error bars for the average kinematics are assigned as the variance of either p_Z or p_T divided by $\sqrt{N_{counts}}$.

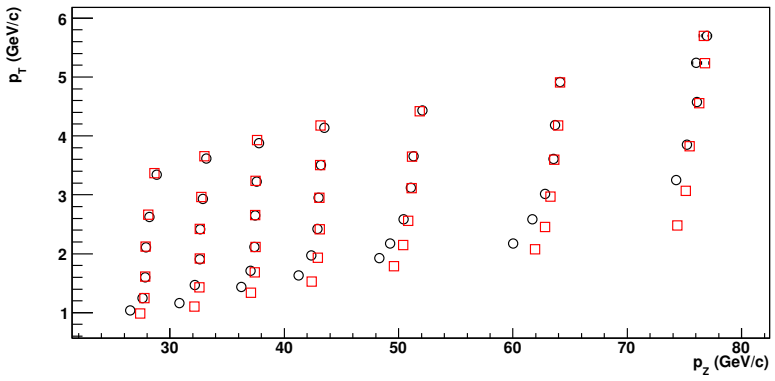

(a) Unrestricted Cluster Radius

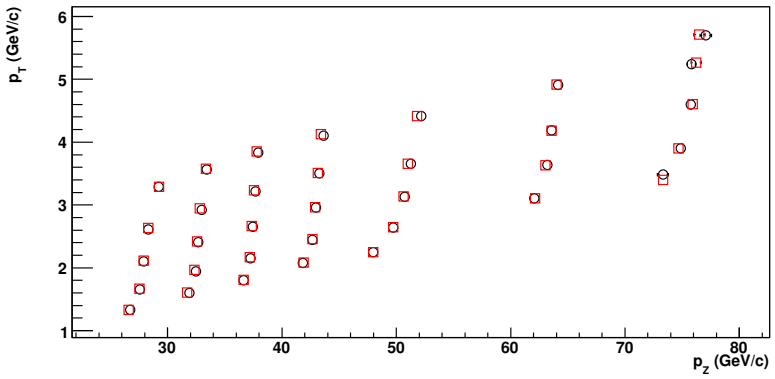

(b) 13< $R_{cluster}$ <18 cm

Figure 8.12: Comparison of the underlying mean kinematic variables from the $A_N(x_F, p_T)$ asymmetry analysis. Black points: South, Red points: North MPC. The p_T and p_z kinematic bins are shown in table 8.1.

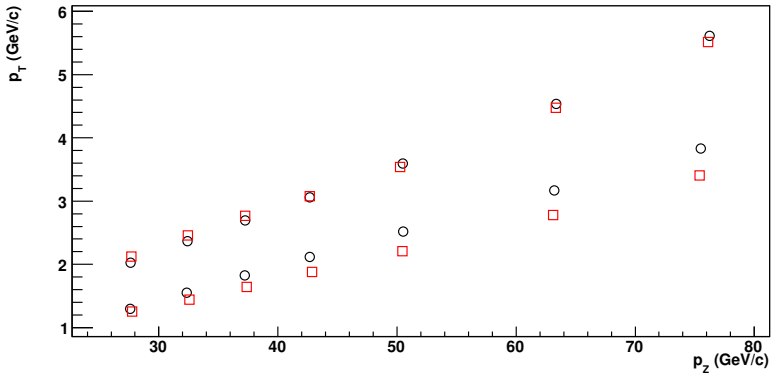

(a) Unrestricted Cluster Radius

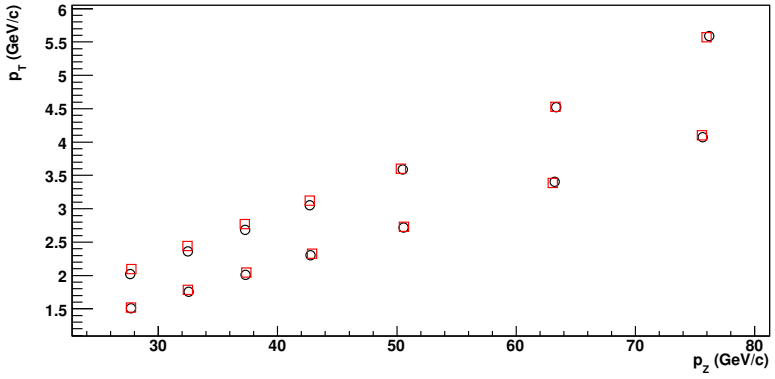

(b) 13< $R_{cluster}$ <18 cm

Figure 8.13: Comparison of the underlying mean kinematic variables from the $A_N(x_F, \eta)$ asymmetry analysis. Black points: South, Red points: North MPC. The p_z kinematic bins are shown in table 8.1.

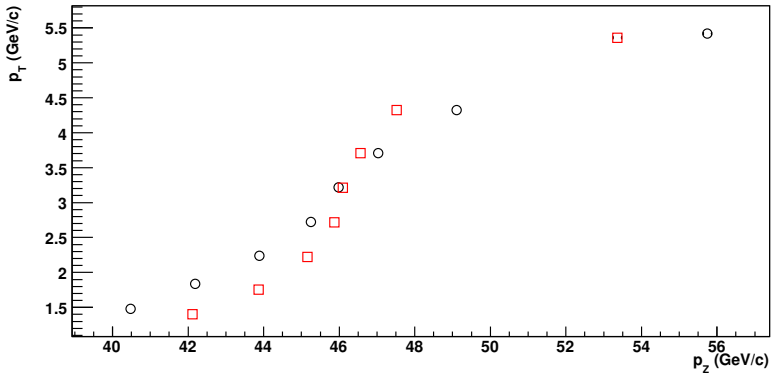

(a) Unrestricted Cluster Radius

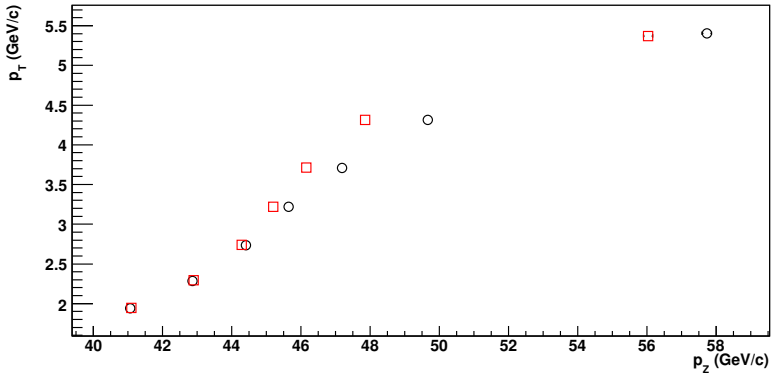

(b) 13< $R_{cluster}$ <18 cm

Figure 8.14: Comparison of the underlying mean kinematic variables in the p_T from the $A_N(p_T)$ asymmetry analysis. Black points: South, Red points: North MPC. The p_T bins are shown in table 8.2.

Without the cluster radial cut balancing the North and South MPC acceptance, significant differences in the mean kinematic variables are observed. After introducing the cut, the mean kinematics are very similar. Therefore, the asymmetries are expected to agree between the North and South MPC detector arms.

Verification of the Polarization Direction

The ZDC/SMD Local Polarimeter analysis (which is documented in chapter 7) determines the polarization directions to be vertical for the Yellow beam and 0.24 radians from the vertical direction for the Blue beam. The MPC cluster asymmetry can perform a consistency check to the polarization direction obtained from the ZDC/SMD. Asymmetries are determined in the MPC by accumulating as much statistics as possible on a fill by fill basis with a broad kinematic cut of: p_Z >30 GeV/c, p_T >1.2 GeV/c. The asymmetries are determined in bins of azimuthal angle for each fill, then the asymmetries are averaged over fill, plotted against the azimuthal angle and fit. The fit function is p0*cos(ϕ+p1). The ϕ angle is the angle with respect to the polarization direction determined by the ZDC/SMD local polarimeter analysis. The p0 parameter is the magnitude of the asymmetry. The p1 parameter estimates the proton polarization direction. Since the ϕ angle is rotated out of the PHENIX coordinate system and into the coordinate system with respect to the polarization direction, the p1 parameter is expected to be statistically consistent with zero. The fits of A_N across the ϕ angle are shown in figures 8.15-8.18. Asymmetries are estimated using both the square root and luminosity formuli (equations 6.10 and 6.16). The figures show that the p1 parameters are consistent with zero, as expected. The MPC cluster determination of the polarization directions agrees with the local polarimeter analysis done with the ZDC/SMD.

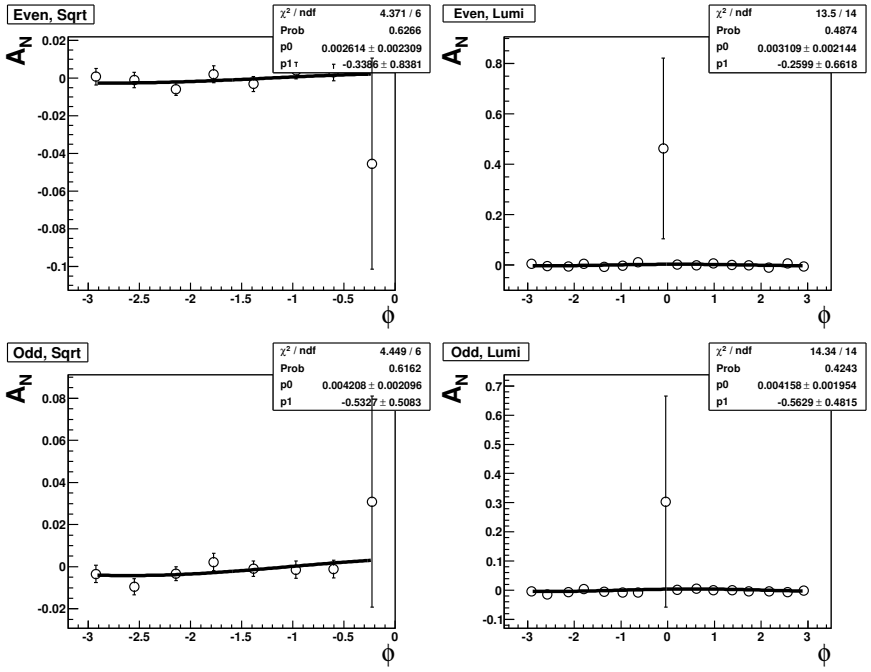

Figure 8.15: Vertical axis: The fill averaged raw asymmetry/Polarization value. Horizontal axis: azimuthal angle with respect to the polarization direction. Beam: Yellow, Arm: North (Backwards). Top: even, Bottom: odd, Left: square root formula, Right: luminosity formula. The two parameters p0 and p1 correspond to a fit of p0*cos(ϕ+p1).

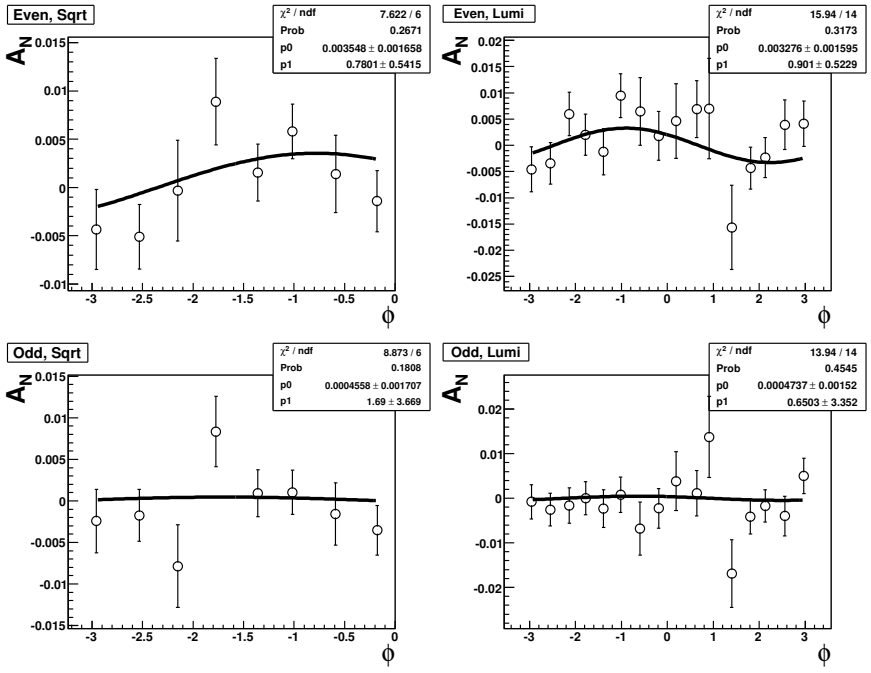

Figure 8.16: Vertical axis: The fill averaged raw asymmetry/Polarization value plotted Horizontal axis: azimuthal angle with respect to the polarization direction. Beam: Blue, Arm: South (Backwards). Top: even, Bottom: odd, Left: square root formula, Right: luminosity formula. The two parameters p0 and p1 correspond to a fit of p0*cos(ϕ+p1).

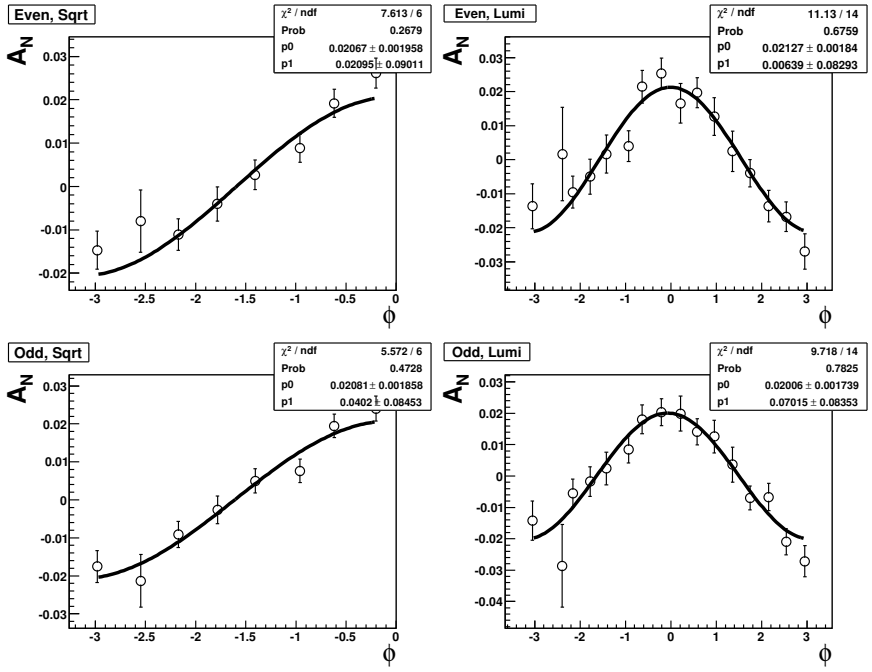

Figure 8.17: Vertical axis: The fill averaged raw asymmetry/Polarization value plotted Horizontal axis: azimuthal angle with respect to the polarization direction. Beam: Blue, Arm: North (Forward). Top: even, Bottom: odd, Left: square root formula, Right: luminosity formula. The two parameters p0 and p1 correspond to a fit of p0*cos(ϕ+p1).

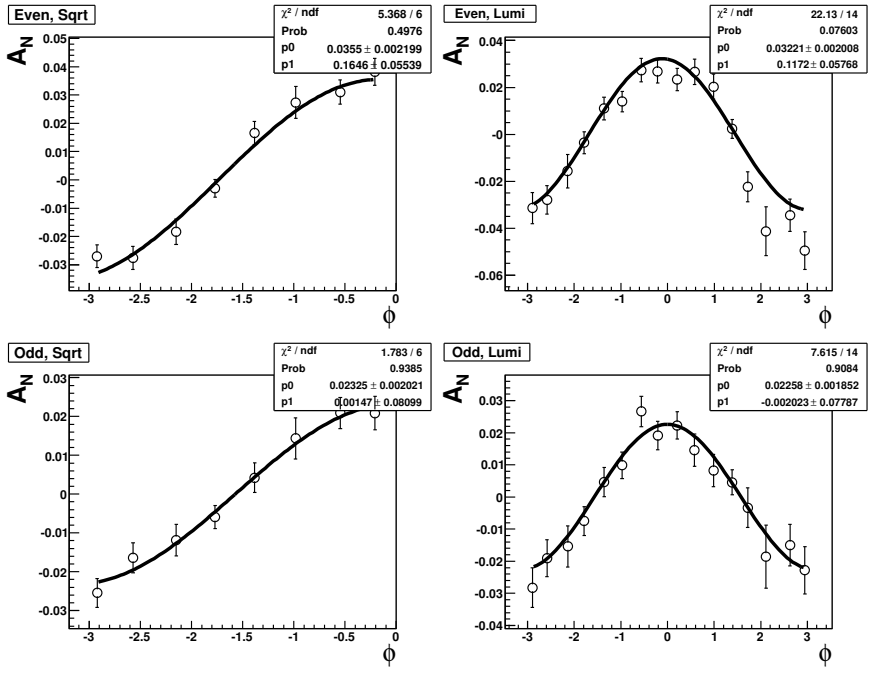

Figure 8.18: Vertical axis: The fill averaged raw asymmetry/Polarization value plotted Horizontal axis: azimuthal angle with respect to the polarization direction. Beam: Yellow, Arm: South (Forward). Top: even, Bottom: odd, Left: square root formula, Right: luminosity formula. The two parameters p0 and p1 correspond to a fit of p0*cos(ϕ+p1).

8.2.2 Final A_N for Electromagnetic Clusters in the MPC

The final cluster asymmetries are estimated using the square root formula in two large azimuthal bins (see equations: 6.16 and 6.19). The results are determined for every fill and within various sub-samples. The sub-samples are checked for consistency in section 8.2.2, the combined asymmetries are presented in section 8.2.2, and finally a comparison to previous results from the STAR collaboration is made.

An important consideration is the issue of background particles, i.e. clusters generated by non-collision related particles such as beam backgrounds. In a two-photon analysis of π^0's, or η mesons, it is possible to estimate the background contamination using the photon pair invariant mass distribution. In the central arm analysis of chapter 9, the meson invariant mass distributions are fit with a Gaussian and a polynomial. In the single cluster analysis of this chapter, that method of background estimation is not possible. However, the clusters are not expected to be sensitive to high levels of background. There are four experimental observations in support of the statement.

First, the MPC is one of the best shielded detectors at RHIC against particles traveling with the incoming beam. The detector is surrounded by the solid iron muon piston. The arrangement of this piston around the calorimeter is shown in section 4.2.1, figure 4.1. Second, the normalized yield of clusters does not significantly vary with the accelerator luminosity. If the detector were sensitive to beam related backgrounds, the yield of high energy clusters would scale with the beam current and not with the luminosity. Third, section 8.4 shows that the π^0 and η meson invariant mass distributions agree with simulations of the detector over a wide range of energy. The simulation does not include beam backgrounds, only particles originating from the collision between protons. Lastly, not all bunch crossings are between two bunches of protons. Some bunch crossings include only one proton bunch or no proton bunches at all. The MPC high-energy trigger rejects crossings without colliding proton bunches by a factor of 10,000 compared to the bunch crossings with two filled proton bunches. This adds further evidence that the detector does not suffer from beam related backgrounds.

Comparison Between Sub-samples

A summary table listing the χ^2 and $\langle t \rangle$ values between the various sub-analyses is available in table 8.3. These statistical tests are discussed in section 6.4. The difference in asymmetries between North and South are not consistent within statistical fluctuations. Point to point each blue and yellow asymmetry agree with each other, but examining the full set of asymmetries shows that on average the yellow asymmetry is approximately a unit of statistical error above the blue asymmetry. Therefore, the systematic errors are assigned to be half a unit of statistical error for each point.

Binning	Even/Odd Blue Beam χ^2/NDF	$\langle t \rangle$	Even/Odd Yellow Beam χ^2/NDF	$\langle t \rangle$	Blue/Yellow[1] χ^2/NDF	$\langle t \rangle$	Blue/Yellow[2] χ^2/NDF	$\langle t \rangle$
			Forward Asymmetry					
x_F, p_T	23 / 29	-0.22	41 / 29	0.66	37 / 29	0.79	29 / 29	0.69
x_F, η	10 / 12	-0.3	18 / 12	0.86	25 / 12	1.1	16 / 12	0.83
$\lvert x_F \rvert > 0.4$, p_T	6.8 / 7	0.19	26 / 7	0.79	10 / 7	0.99	5.4 / 7	0.76
			Backward Asymmetry					
x_F, p_T	33 / 29	-0.11	20 / 29	-0.027	17 / 29	-0.11	17 / 29	-0.11
x_F, η	13 / 12	-0.083	3.5 / 12	0.023	8 / 12	-0.24	7.7 / 12	-0.24
$\lvert x_F \rvert > 0.4$, p_T	14 / 7	-0.25	5.3 / 7	0.29	3.5 / 7	-0.086	3.4 / 7	-0.086

Table 8.3: χ^2 values and $\langle t \rangle$ values between the four sub-analyses. The two statistical tests are defined in the text. The values are for square root asymmetries only.
[1] errors calculated without polarization uncertainties
[2] errors calculated with polarization uncertainties

Final Asymmetries

The final asymmetries are available in tables 8.4-8.6 and in figures 8.19-8.21.

$A_N^{Cluster}(x_F, p_T)$					
$\lvert x_F^{low} - x_F^{high} \rvert$	$p_T^{low} - p_T^{high}$	$\langle x_F \rangle$	$\langle p_T \rangle$	$A_N, x_F > 0$	$A_N, x_F < 0$
0.25 - 0.3	1.1 - 1.4	0.27	1.3	-0.0052 ± 0.008	0.01 ± 0.008
0.25 - 0.3	1.4 - 1.9	0.28	1.7	0.0049 ± 0.0027	-0.004 ± 0.0028
0.25 - 0.3	1.9 - 2.4	0.28	2.1	0.01 ± 0.0029	0.0023 ± 0.0031
0.25 - 0.3	2.4 - 3.2	0.28	2.6	-0.0019 ± 0.0052	-0.0031 ± 0.0058
0.25 - 0.3	3.2 - 6	0.29	3.3	0.038 ± 0.043	-0.081 ± 0.049
0.3 - 0.35	1.2 - 1.7	0.32	1.6	0.012 ± 0.0051	0.0037 ± 0.0049
0.3 - 0.35	1.7 - 2.2	0.32	2	0.01 ± 0.0024	0.0056 ± 0.0025
0.3 - 0.35	2.2 - 2.7	0.33	2.4	0.018 ± 0.0028	0.0044 ± 0.0029
0.3 - 0.35	2.7 - 3.4	0.33	2.9	0.015 ± 0.0046	0.01 ± 0.0049
0.3 - 0.35	3.4 - 6	0.33	3.6	0.039 ± 0.016	0.003 ± 0.017
0.35 - 0.4	1.5 - 1.9	0.37	1.8	0.016 ± 0.0059	0.0018 ± 0.0056
0.35 - 0.4	1.9 - 2.4	0.37	2.2	0.018 ± 0.0028	-0.0035 ± 0.0027
0.35 - 0.4	2.4 - 3	0.37	2.7	0.028 ± 0.003	0.0035 ± 0.003
0.35 - 0.4	3 - 3.6	0.38	3.2	0.03 ± 0.0056	0.01 ± 0.0057
0.35 - 0.4	3.6 - 6	0.38	3.8	0.018 ± 0.013	-0.01 ± 0.013
0.4 - 0.47	1.7 - 2.2	0.42	2.1	0.033 ± 0.0064	-0.00047 ± 0.0061
0.4 - 0.47	2.2 - 2.7	0.43	2.5	0.035 ± 0.0037	0.0019 ± 0.0036
0.4 - 0.47	2.7 - 3.3	0.43	3	0.041 ± 0.0042	1.7e-05 ± 0.0041
0.4 - 0.47	3.3 - 3.8	0.43	3.5	0.051 ± 0.0076	0.01 ± 0.0075
0.4 - 0.47	3.8 - 6	0.44	4.1	0.036 ± 0.012	-0.017 ± 0.013
0.47 - 0.6	2 - 2.3	0.48	2.2	0.056 ± 0.035	0.031 ± 0.033
0.47 - 0.6	2.3 - 2.9	0.5	2.6	0.054 ± 0.0079	-0.0087 ± 0.0075
0.47 - 0.6	2.9 - 3.4	0.51	3.1	0.063 ± 0.0085	-0.012 ± 0.0081
0.47 - 0.6	3.4 - 4	0.51	3.7	0.056 ± 0.011	0.0093 ± 0.01
0.47 - 0.6	4 - 6	0.52	4.4	0.038 ± 0.017	0.012 ± 0.016
0.6 - 0.72	2.7 - 3.3	0.62	3.1	0.14 ± 0.072	-0.1 ± 0.068
0.6 - 0.72	3.3 - 4	0.63	3.6	0.086 ± 0.045	0.068 ± 0.042
0.6 - 0.72	4 - 4.4	0.64	4.2	0.0051 ± 0.098	0.11 ± 0.09
0.6 - 0.72	4.4 - 6	0.64	4.9	0.03 ± 0.071	-0.039 ± 0.067

Table 8.4: Final asymmetry values for the $A_N^{Cluster}(x_F, p_T)$

$A_N^{Cluster}(x_F, \eta)$					
η	$x_F^{low} - x_F^{high}$	$\langle x_F \rangle$	$\langle p_T \rangle$	$A_N, x_F > 0$	$A_N, x_F < 0$
< 3.5	0.25 - 0.25	0.28	2.1	0.006 ± 0.0021	0.00029 ± 0.0022
< 3.5	0.3 - 0.3	0.32	2.4	0.015 ± 0.0019	0.0057 ± 0.002
< 3.5	0.35 - 0.35	0.37	2.7	0.025 ± 0.0023	0.0026 ± 0.0023
< 3.5	0.4 - 0.4	0.43	3.1	0.039 ± 0.0032	0.00051 ± 0.0031
< 3.5	0.47 - 0.47	0.5	3.6	0.056 ± 0.0069	0.0013 ± 0.0066
< 3.5	0.6 - 0.6	0.63	4.5	0.041 ± 0.04	0.0089 ± 0.038
> 3.5	0.25 - 0.25	0.28	1.5	0.0043 ± 0.0035	-0.0026 ± 0.0036
> 3.5	0.3 - 0.3	0.33	1.8	0.012 ± 0.0028	0.0054 ± 0.0028
> 3.5	0.35 - 0.35	0.37	2	0.018 ± 0.0029	-0.0021 ± 0.0028
> 3.5	0.4 - 0.4	0.43	2.3	0.037 ± 0.0035	0.0019 ± 0.0034
> 3.5	0.47 - 0.47	0.51	2.7	0.055 ± 0.0068	-0.0092 ± 0.0065
> 3.5	0.6 - 0.6	0.63	3.4	0.11 ± 0.039	-0.016 ± 0.037

Table 8.5: Final asymmetry values for the $A_N^{Cluster}(x_F, \eta)$

$\|x_F\| > 0.4, A_N^{Cluster}(p_T)$					
$\|x_F\| > 0.4$	$p_T^{low} - p_T^{high}$	$\langle x_F \rangle$	$\langle p_T \rangle$	$A_N, x_F > 0$	$A_N, x_F < 0$
-	1.5 - 2	0.41	1.9	-0.013 ± 0.014	0.0058 ± 0.014
-	2 - 2.5	0.43	2.3	0.038 ± 0.0038	0.0033 ± 0.0037
-	2.5 - 3	0.44	2.7	0.042 ± 0.0036	-0.0029 ± 0.0034
-	3 - 3.5	0.46	3.2	0.052 ± 0.0047	-0.0028 ± 0.0046
-	3.5 - 4	0.47	3.7	0.048 ± 0.0076	0.0068 ± 0.0074
-	4 - 5	0.49	4.3	0.034 ± 0.012	-0.0071 ± 0.011
-	5 - 8	0.56	5.4	0.005 ± 0.018	0.0089 ± 0.021

Table 8.6: Final asymmetry values for the $|x_F| > 0.4, A_N^{Cluster}(p_T)$

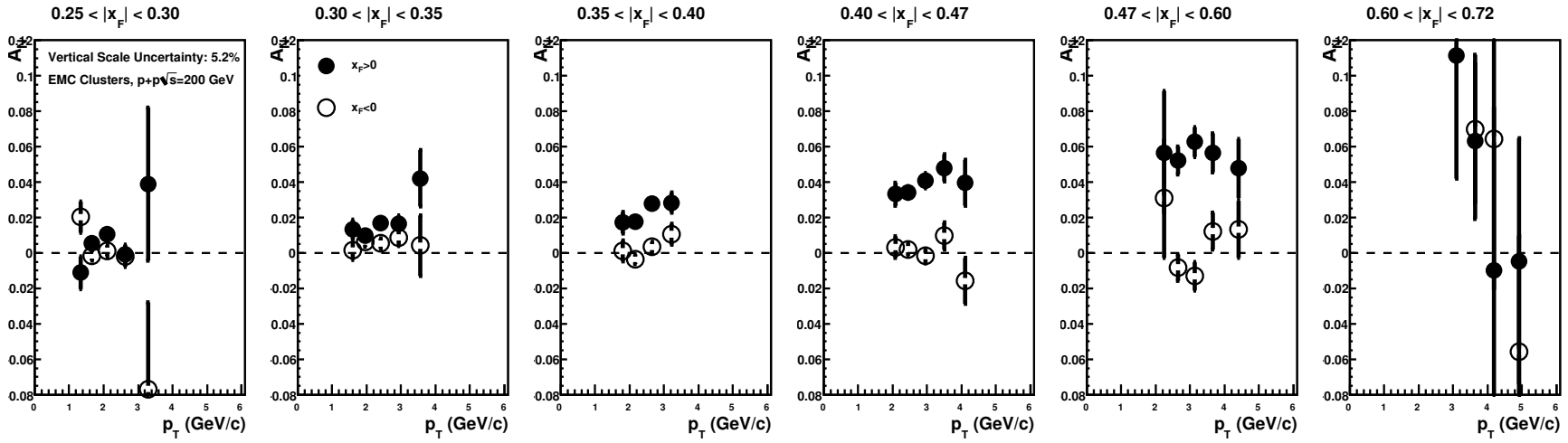

Figure 8.19: Final results for the $A_N(x_F,p_T)$ asymmetry analysis. The closed and open circles are for positive and negative values of x_F.

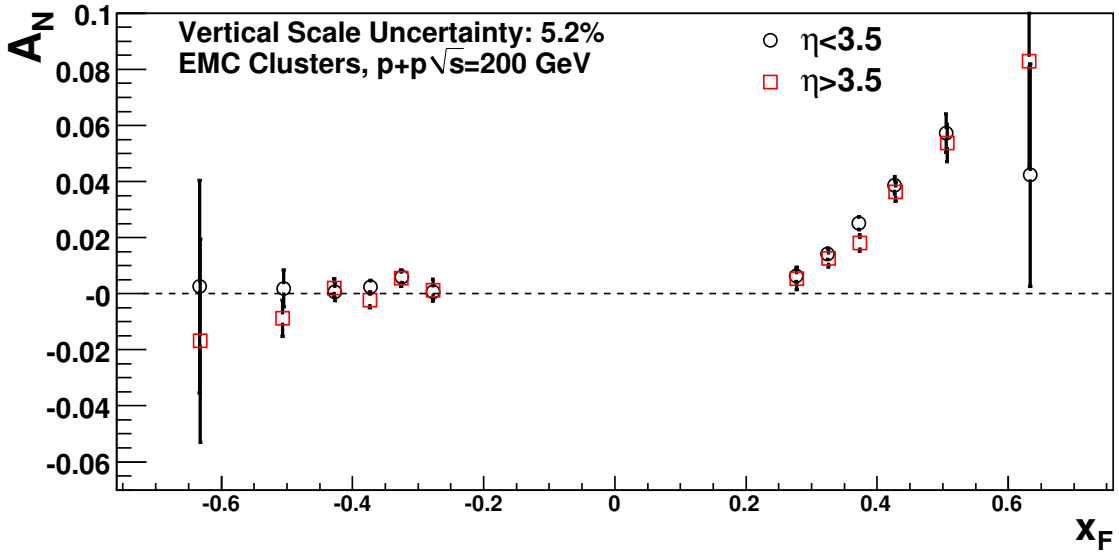

Figure 8.20: Final results for the $A_N(x_F, \eta)$ asymmetry analysis.

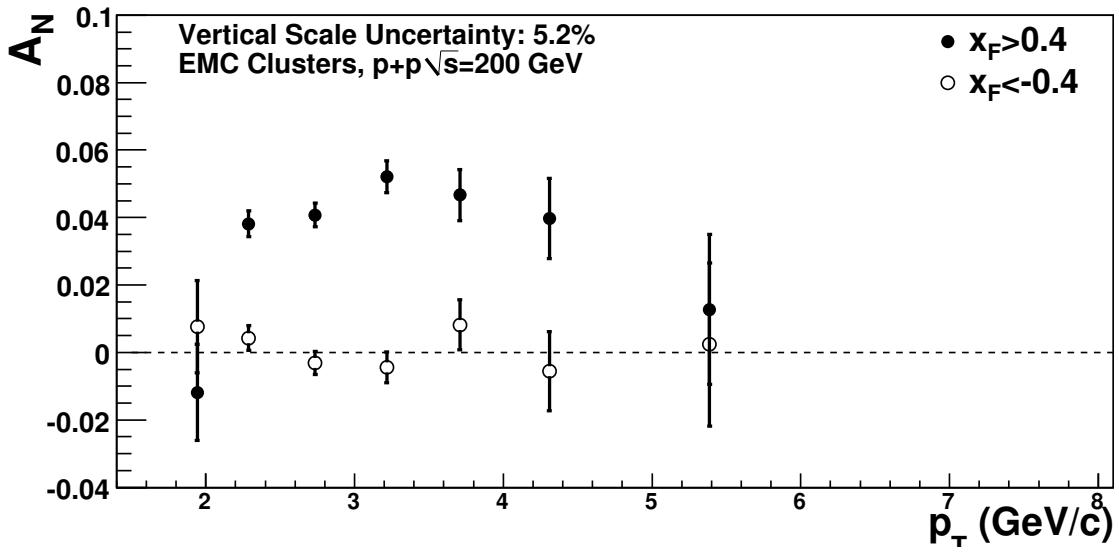

Figure 8.21: Final results for the $A_N(p_T)$ asymmetry binning. The open and closed circles are for positive and negative values of x_F with the restriction that $|x_F|$ >0.4.

8.2.3 Comparison to Previous Results

The MPC $A_N^{Cluster}$ is compared to the previous results from the STAR collaboration in figures 8.22 and 8.23. The direct comparison of the results is of limited significance. The clusters are highly correlated with the π^0, but they are not the same physics object. The STAR π^0's are reconstructed with two-photons and an invariant mass selection. The clusters in this thesis are mainly π^0's but receive contributions from η mesons, direct photons, and other particles. There is also smearing between different kinematic bins. The decomposition and smearing are elaborated upon in sections 8.3 and 8.4.

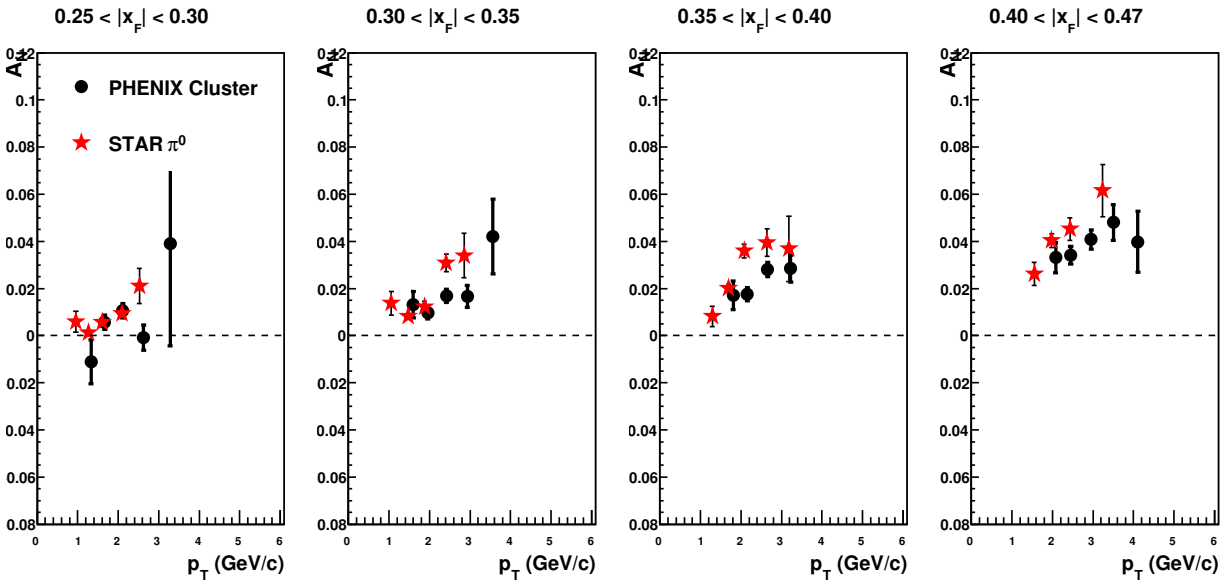

Figure 8.22: Comparison of A_N between the STAR two-photon π^0's and the PHENIX single cluster in bins of x_F and p_T

Despite the difference between the $A_N^{Cluster}$ and the $A_N^{\pi^0}$, qualitative agreement is found. The new cluster measurement pushes the p_T coverage from 3.5 GeV/c to 5.5 GeV/c.

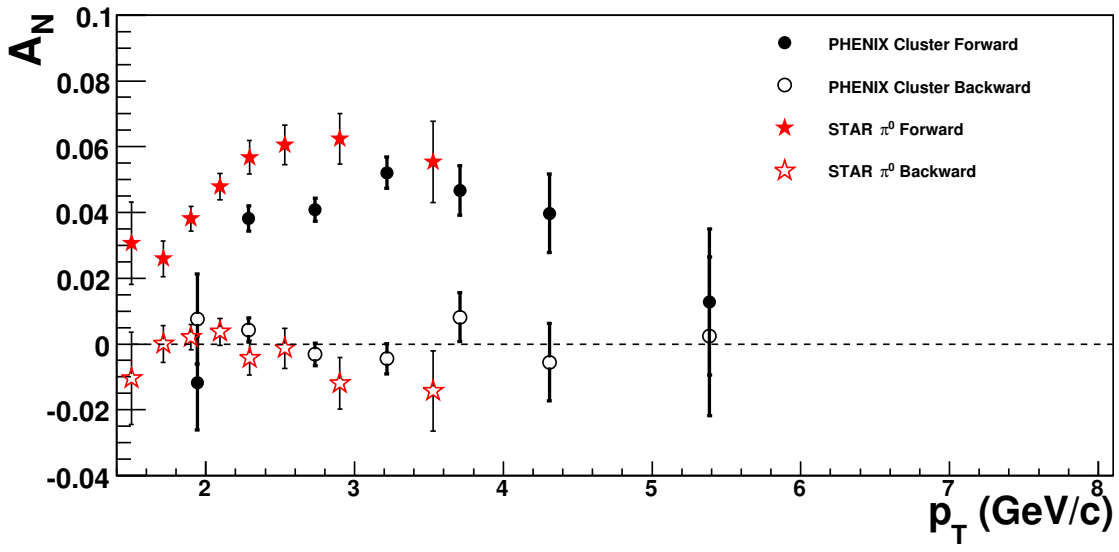

Figure 8.23: Comparison of A_N between the STAR two-photon π^0's and the PHENIX single cluster in bins p_T with an x_F threshold cut of 0.4. The PHENIX data extend the p_T from 3.5 to 5.5 GeV/c.

8.3 Simulated Data

8.3.1 Overview

The cluster decomposition is studied using the following simulation tools:

- Pythia, a Monte-Carlo simulation package which collides protons and produces a list of particle products. The configuration is highly customizable, and many different types of parameters can be adjusted by hand. For example: the parton distribution functions, the sub-processes (quark-gluon, gluon-gluon) can be selectively turned on and off, parameters of the hard scattering can be cut on, etc.

- PISA[5], a GEANT3 based simulation package containing a realistic description of the PHENIX detector. PISA takes the list of particles from Pythia and propagates them through the simulation of PHENIX. For this simulation, only the MPC and BBC detectors were enabled.

- p2DST, a realistic reconstruction chain. This step uses a realistic simulated implementation of the detector response to produce data files. These files can be analyzed as if they were from real collisions, and combined with knowledge of the $p+p$ collision from Pythia. Realistic detector effects are included in the creation of the simulated data files. The most important effect is the MPC energy resolution, and it is documented in section 5.5.

Each step of the simulation is checked against experiment to increase confidence in the cluster decomposition. Section 8.3.2 describes the configuration of Pythia, section 8.3.3 describes the calculation of cross-sections using Pythia, and section 8.3.4 compares cross-sections from the Pythia simulation to all experimental results for cross-sections for $p+p$ at $\sqrt{s}$=200 GeV. A similar benchmarking of PISA and p2DST is shown in section 5.5. In addition, a comparison between the shower shapes extracted from the experimental beam-test (section 4.6.1) and PISA was done but it is not presented in the thesis. Section 8.4 presents the decomposition results from the full simulation chain.

8.3.2 Pythia Configuration

The configuration of Pythia is set to match experimentally determined cross-sections at $\sqrt{s}$=200 GeV. Two basic configuration options are explored: the Pythia tune and which sub-processes to enable. The comparisons between different Pythia tunes are not shown in the thesis. Tune-A[97] is used with a threshold cut on p_T of the hard scattered partons of 2 GeV/c. The sub-process specified is the type of underlying partonic interaction for a given event, e.g. quark-gluon scattering. Multiple sub-processes can be enabled

[5]PHENIX Integrated Simulation Package

Tag	Description	Pythia Sub-process Code	σ [mb]
`hard`	Hard Scattering (quark-gluon, etc.)	11 12 13 28 53 68 96	10
`msel2`	Hard Scattering + Diffractive	`hard` 91 92 93 94 95	51
`dgam`	Direct Photons	14 18 29 114 115	0.00173

Table 8.7: Description of sub-process bundles used for the simulation. TuneA is used along with a cut on the scattered parton's p_T of 2 GeV/c.

Pythia Sub-process Code	Sub-process
11	$q_i q_j \rightarrow q_i q_j$
12	$q_i \bar{q}_i \rightarrow q_k \bar{q}_k$
13	$q_i \bar{q}_i \rightarrow gg$
14	$f_i \bar{f}_i \rightarrow g\gamma$
18	$f_i \bar{f}_i \rightarrow \gamma\gamma$
28	$q_i g \rightarrow q_i g$
29	$f_i g \rightarrow f_i \gamma$
53	$gg \rightarrow q_k \bar{q}_k$
68	$gg \rightarrow gg$
91	elastic scattering
92	single diffraction ($AB \rightarrow XB$)
93	single diffraction ($AB \rightarrow AX$)
94	double diffraction
95	low-$p_\perp$ production
96	semihard QCD $2 \rightarrow 2$
114	$gg \rightarrow \gamma\gamma$
115	$gg \rightarrow g\gamma$

simultaneously. The goal of this study is to select a pythia tune and sub-process bundle which comes as close as possible to the experimentally determined cross-sections. Three sub-process bundles are shown in table 8.7. The meaning of each sub-process code is shown in table 8.3.2 As the table shows, the cross-section for enabling diffractive processes is five times larger than the pure hard-scattering cross-section for certain kinematic cuts[6]. However, diffractive events are not expected to contribute to the high p_T production of π^0's; figure 8.24 confirms this. The figure shows that is safe to ignore diffractive processes in the simulation of $p+p$ collisions since they will not contribute for p_T >2 GeV/c. This speeds up the simulation since the generation and propagation of many uninteresting events are avoided.

8.3.3 Cross-Section Calculation

Twelve cross-sections are extracted from Pythia and compared to various RHIC data. The Pythia cross sections plotted against p_T are calculated as follows:

$$E\frac{d^3\sigma}{dp^3} = \frac{N_{counts}\langle\frac{1}{p_T}\rangle}{2\pi \int \mathcal{L}\Delta p_T \Delta y} \tag{8.1}$$

[6]In the case of the pure hard scattering cross-section, a p_T cut of 2 GeV/c is placed on the scattered partons (CKIN 3 = 2). For the sub-process selection which includes the diffractive processes, this cut is not applied.

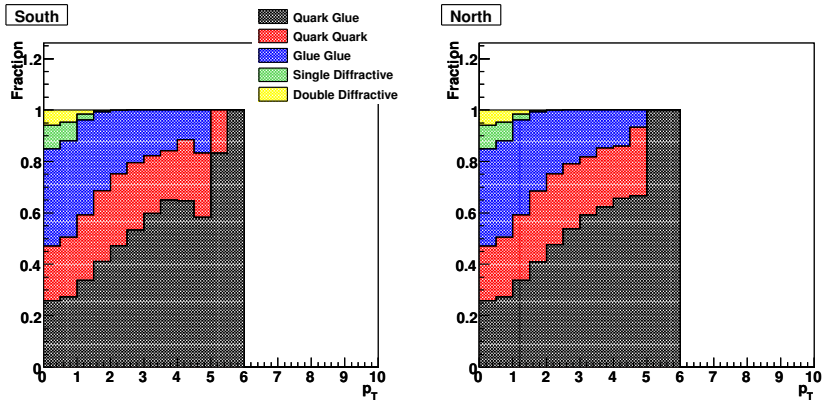

(a) Binning in E^{π^0}

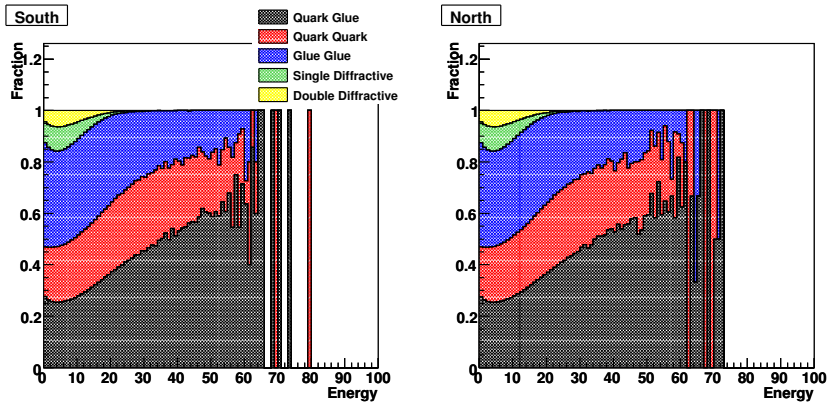

(b) Binning in $p_T^{\pi^0}$

Figure 8.24: Fractional contribution for each sub-process contributing to the π^0 cross-section in the acceptance of each MPC (-3.7< η <-3.1, 3.1< η <3.9). The binning is in p_T and in Energy. Diffractive processes only contribution for $p_T < 2$ GeV/c and $E < 20$ GeV.

Where: $\int \mathcal{L}$ is the integrated luminosity which is calculated as the number of thrown events divided by the cross-section of the selected processes. Δy and Δp_T are the bin widths in pseudorapidity and transverse momentum respectively. The cross-sections binned in energy are calculated as follows:

$$E\frac{d^3\sigma}{dp^3} = \frac{N_{counts}\langle\frac{E}{p_T^2}\rangle}{2\pi\int\mathcal{L}\Delta E\Delta y} \tag{8.2}$$

Where: ΔE is the bin width in energy. The error for the Pythia simulations are statistical only. The experimental error bars are taken as the statistical error bars only and systematic error bars are not included in the comparison.

8.3.4 Cross-section comparisons between Experiment and Pythia

This section compares the cross-sections measured by the PHENIX (π^0 and direct photon at mid-rapidity), STAR (forward π^0) and BRAHMS (forward $\pi^{\pm}$, $K^{\pm}$) collaborations at $\sqrt{s}$=200 GeV. Except for the direct photon, the experimentally determined cross-sections are compared to the `hard` and `msel2` sub-process bundles. References to the experimental papers are given in each sub-section.

PHENIX Central Arm Neutral Pion

The PHENIX collaboration measures the cross-section of neutral pions in a spectrometer and calorimeter located at mid-rapidity. Its acceptance is taken as $-0.35 < \eta < 0.35$. The data is taken from reference [98]. Good agreement between the PHENIX measurement and Monte-Carlo is found.

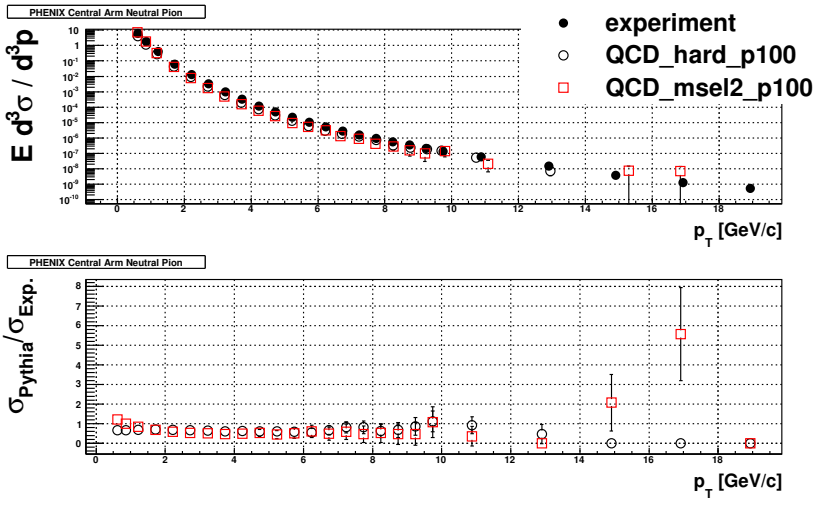

Figure 8.25: Comparison between experimentally determined cross-sections and Pythia. Vertical axis: PHENIX central arm π^0 cross-section, Horizontal axis: p_T.

PHENIX Central Arm Direct Photon

Next, the cross-section for direct photons is compared between the mid-rapidity PHENIX experimental measurement and Pythia. Data are taken from reference [99]. Except for a normalization factor of 0.5, the two agree.

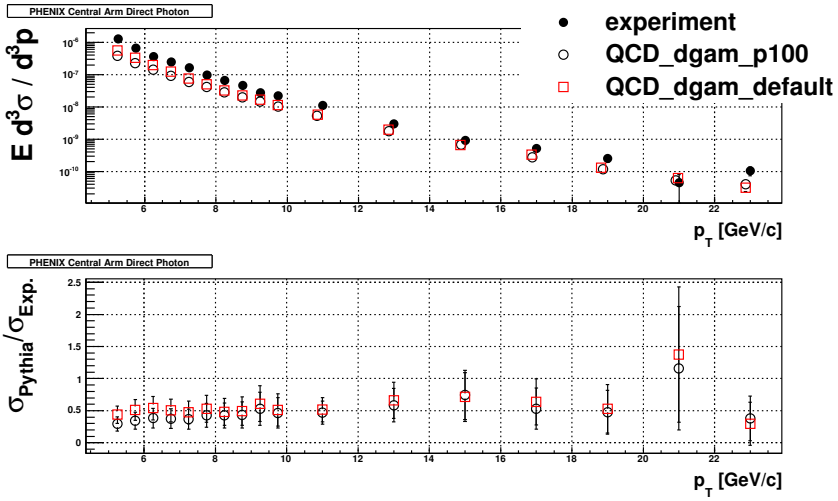

Figure 8.26: Comparison between experimentally determined cross-sections and Pythia. Vertical axis: PHENIX central arm direct photon cross-section, Horizontal axis: p_T

STAR Forward Neutral Pion

The STAR datasets were taken in three ranges of overlapping pseudorapidity by shifting the FPD and PFPD detectors. The results are taken from reference [100]. The Pythia acceptance of each detector/setting are taken from same reference: 3.7< η <-4.15, 3.4< η <4.0, 3.05< η <3.45. At high p_T, the experimental measurement and the Pythia simulation agree. At lower p_T's the agreement is not as good.

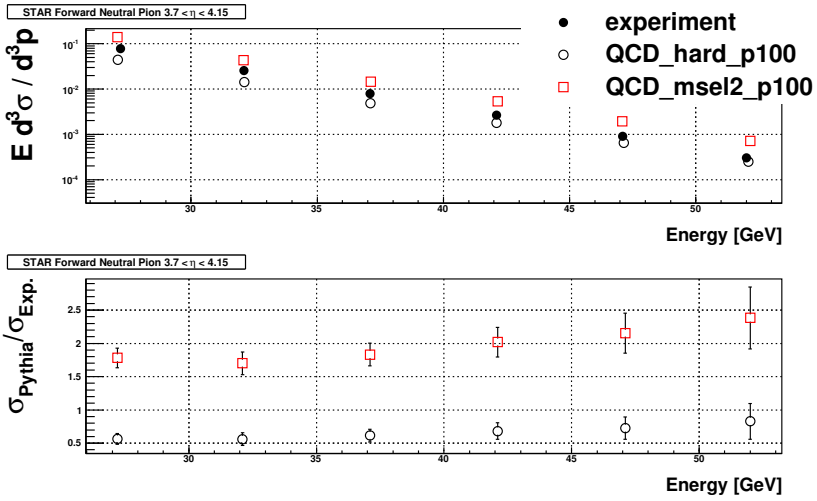

Figure 8.27: Comparison between experimentally determined cross-sections and Pythia. Vertical axis: STAR forward π^0 $3.7 < \eta < 4.15$ cross section, Horizontal axis: Energy.

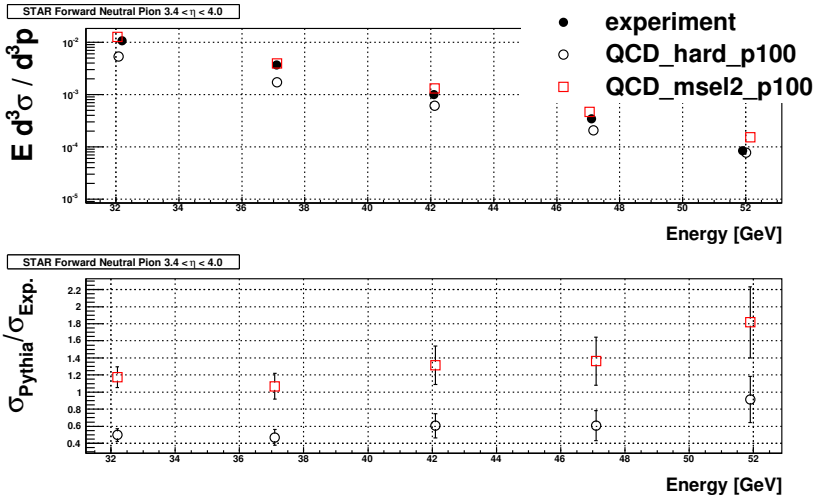

Figure 8.28: Comparison between experimentally determined cross-sections and Pythia. Vertical axis: STAR forward π^0 $3.4 < \eta < 4.0$ cross section, Horizontal axis: Energy.

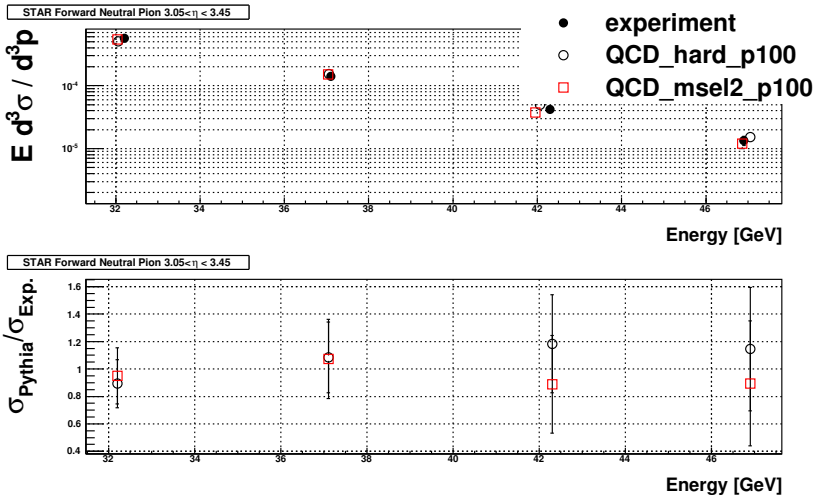

Figure 8.29: Comparison between experimentally determined cross-sections and Pythia. Vertical axis: STAR forward π^0 $3.05 < \eta < 3.45$ cross section, Horizontal axis: Energy.

BRAHMS Forward Charged Hadrons

The BRAHMS collaboration measured the cross-sections for charged pions and kaons in the forward region in two pseudorapidity intervals. Their data is taken from reference [101] and compared to Pythia. The data tables indicate their acceptance as 2.95 and 3.3 with no range for the upper or lower bound of the spectrometer. The Pythia cross-sections are calculated assuming an experimental acceptance of $\pm$ 0.05 in η.

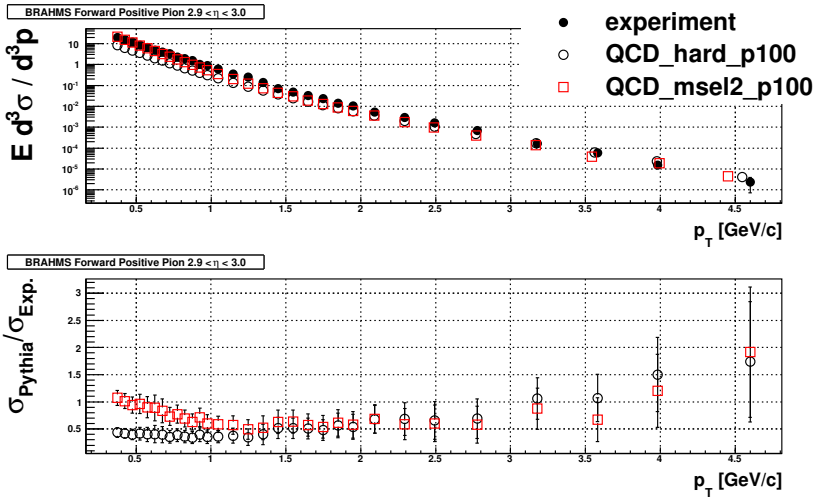

Figure 8.30: Comparison between experimentally determined cross-sections and Pythia. Vertical axis: BRAHMS forward π^+ $\eta = 2.95$ cross section, Horizontal axis: p_T.

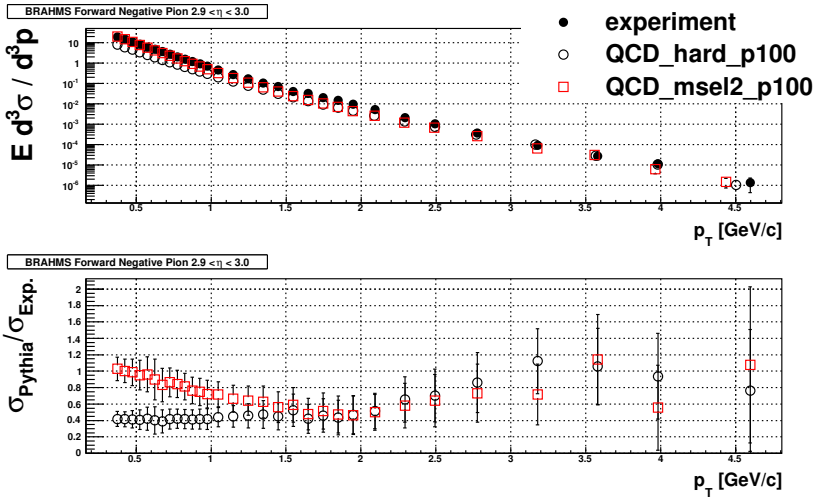

Figure 8.31: Comparison between experimentally determined cross-sections and Pythia. Vertical axis: BRAHMS forward π^- $\eta = 2.95$ cross section, Horizontal axis: p_T.

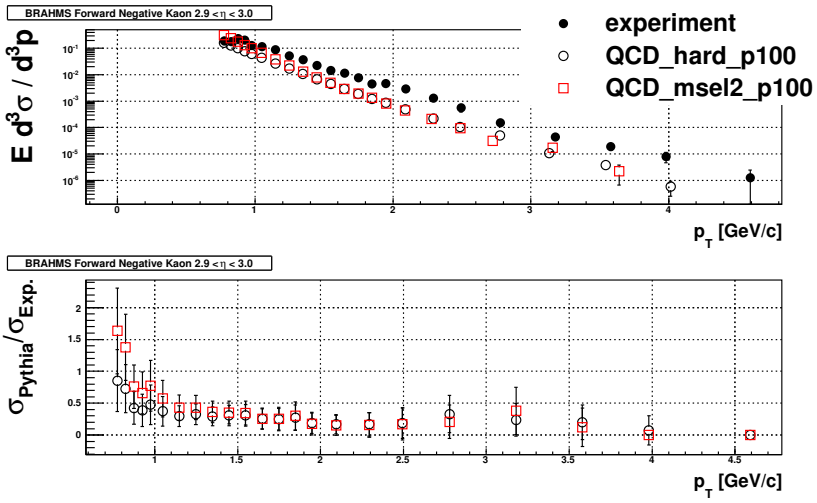

Figure 8.32: Comparison between experimentally determined cross-sections and Pythia. Vertical axis: BRAHMS forward K^+ $\eta = 2.95$ cross section, Horizontal axis: p_T.

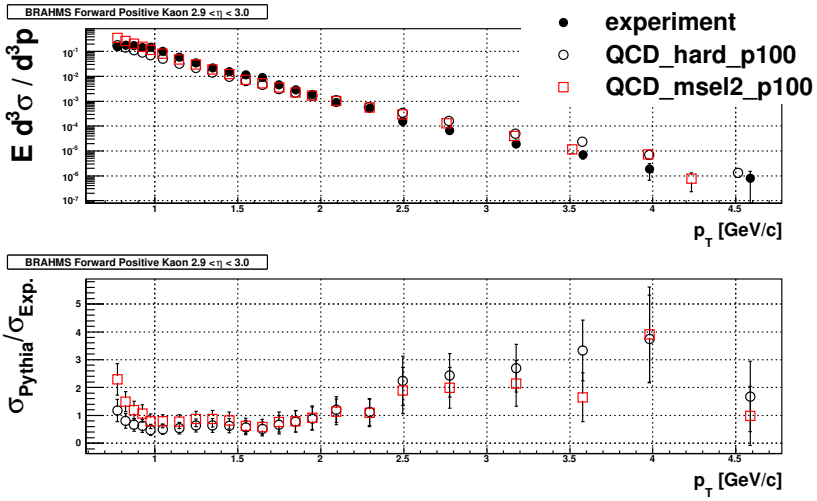

Figure 8.33: Comparison between experimentally determined cross-sections and Pythia. Vertical axis: BRAHMS forward K^- $\eta = 2.95$ cross section, Horizontal axis: p_T.

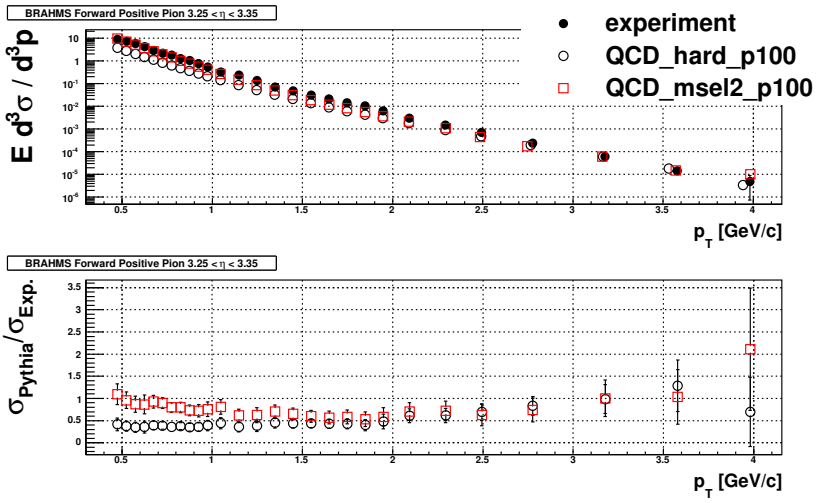

Figure 8.34: Comparison between experimentally determined cross-sections and Pythia. Vertical axis: BRAHMS forward π^+ $\eta = 3.3$ cross section, Horizontal axis: p_T.

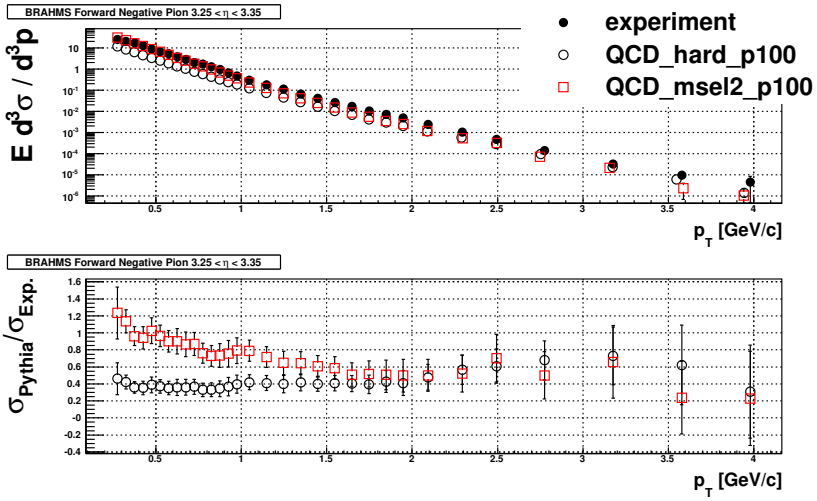

Figure 8.35: Comparison between experimentally determined cross-sections and Pythia. Vertical axis: BRAHMS forward π^- $\eta = 3.3$ cross section, Horizontal axis: p_T.

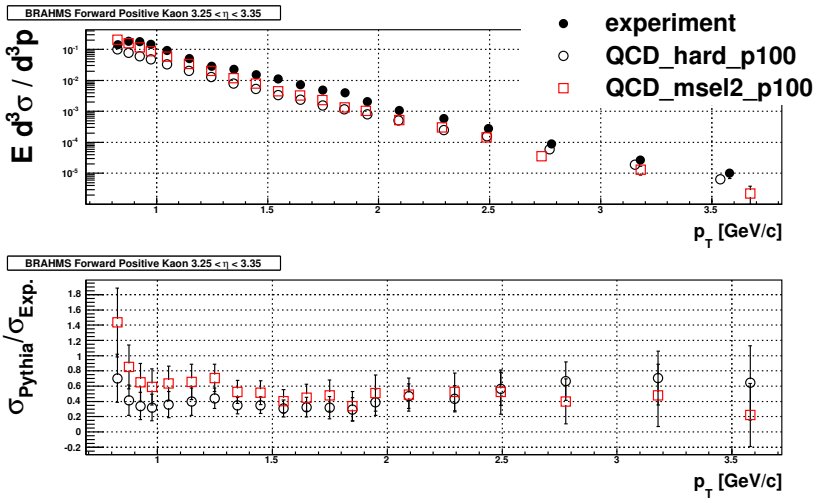

Figure 8.36: Comparison between experimentally determined cross-sections and Pythia. Vertical axis: BRAHMS forward K^+ $\eta = 3.3$ cross section, Horizontal axis: p_T.

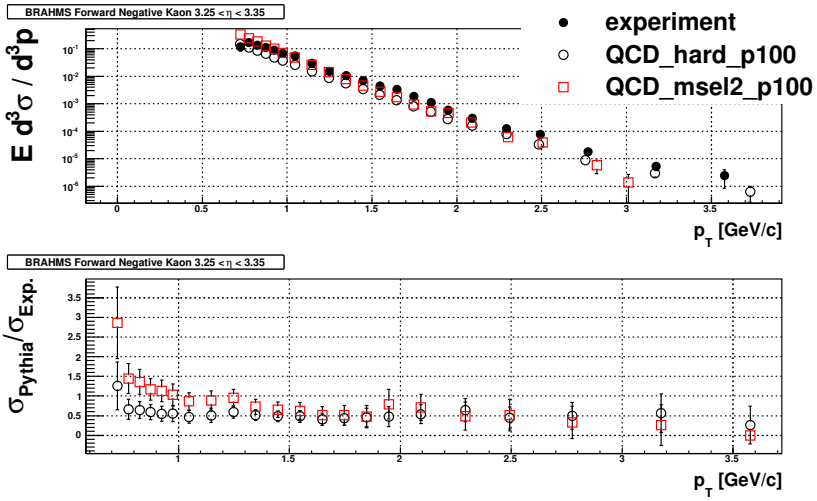

Figure 8.37: Comparison between experimentally determined cross-sections and Pythia. Vertical axis: BRAHMS forward K^- $\eta = 3.3$ cross section, Horizontal axis: p_T.

Summary

The cross-section at high p_T in the forward region is shown to agree between the STAR measurement and the Pythia simulations. In contrast, to match the PHENIX direct photon experimental data, the Pythia cross-section must be multiplied by approximately a factor of two. The next section uses the Pythia simulation as input to decompose the cluster. Since Pythia under-predicts the production of direct photons by a factor of two, the direct photon yields are doubled in the decomposition analysis.

8.3.5 Simulated Detector Response

The detector response was simulated using the PHENIX simulation packages: PISA and p2DST. The events were thrown with a Gaussian z-vertex profile with $\sigma = 50cm$ and a hard cutoff at $\pm$ 70 cm. To save processing time and disk space, only the MPC and BBC's were turned on in the reconstruction. Events were thrown in ten thousand event segments. At this point, the simulation forked into two parts:

1. Using the `hard` sub-process bundle a set of minimum bias $p + p$ files was saved to disk. For each 10 thousand event set, the pythia file (33 MB) and p2DST (144MB) files were saved to disk, but the PISA file was discarded. 5000 files with 10 thousand events per file were generated. The comparison between MPC data and Monte-Carlo shown in section 5.5 uses this dataset in the low energy bins. To push the simulation to higher p_T's more statistics were needed, but this would require too much disk space.

2. The simulation chain of the previous simulation was repeated, but with one additional step. The reconstructed DST's were skimmed for clusters with energy greater than 15 GeV. If the event passed the test, it was written to disk. Slightly less than one billion events corresponding to 0.10 pb^{-1} were generated using the `hard` sub-process bundle. 170 million events were generated corresponding to 93 pb^{-1} were thrown using the `dgam` sub-process bundle.

The final part of the simulation was the implementation of realistic energy resolution to the calorimeter. The determination of the energy resolution is described in section 5.5. It was found to be $8\% \oplus 90$ MeV. This noise is introduced at the tower level and propagated through the clustering and position/energy reconstruction.

8.4 Decomposition Implementation and Results

As a first step, pico DSTs (Root trees) are generated from the simulated data. They contain the global event characteristics like the parent process, and the Bjorken x of the involved partons as well as information on each cluster in the MPC. Here the primary particle initiating the shower, shower shape variables and kinematics of each cluster are tracked. For each of those the real (generated) and the reconstructed values were saved.

8.4.1 Cluster Decomposition Results

The decomposition of clusters for binning in p_T with $x_F > 0.4$ is shown in figure 8.38. The figure shows that the yield of clusters is dominated by π^0's in all p_T bins; that direct photons and η mesons contribute to

the yield; and that charged hadrons contribute a negligible amount. As the p_T increases, the contribution from direct photons increases relative to the π^0 and η meson. The reason for relative increase may be due to a fragmentation function effect. Fragmentation functions are steeply falling functions with the hadron momentum fraction, z. The pi^0 and η mesons are affected by this steeply falling spectra, but the direct photons are not.

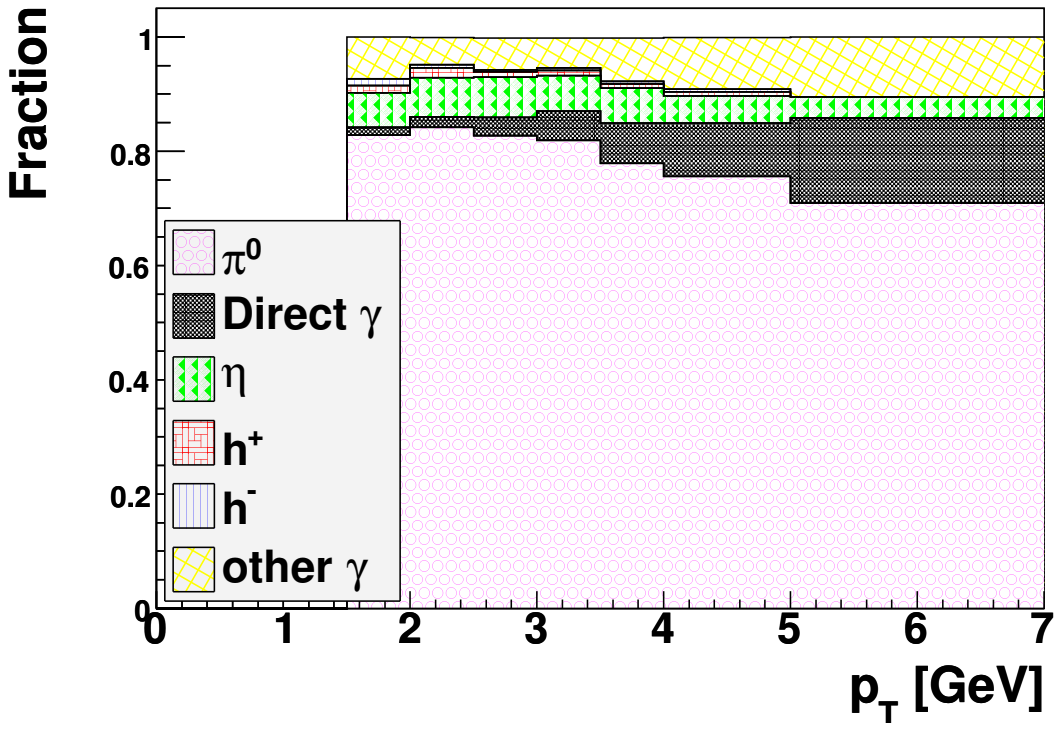

Figure 8.38: Cluster decompositions as a function of reconstructed cluster p_T with an x_F threshold cut of 0.4.

8.4.2 Energy Reconstruction

One important physics question to be answered by the measurement of the cluster asymmetries is if the asymmetries are decreasing at high p_T. For this reason, and of course on a more general level, the energy reconstruction and bin smearing effects are investigated. Figure 8.39 shows the ratio of deposited energy and reconstructed energy over all clusters meeting an energy threshold cut of 25 GeV whose showers were started by π^0's. The distributions look very similar even after splitting the histogram apart by the various kinematic bins used in the $A_N^{Cluster}$ analysis. The reason behind the energy mis-reconstruction is understood. When the clustering includes energy from neighboring clusters, the reconstructed energy is overestimated.

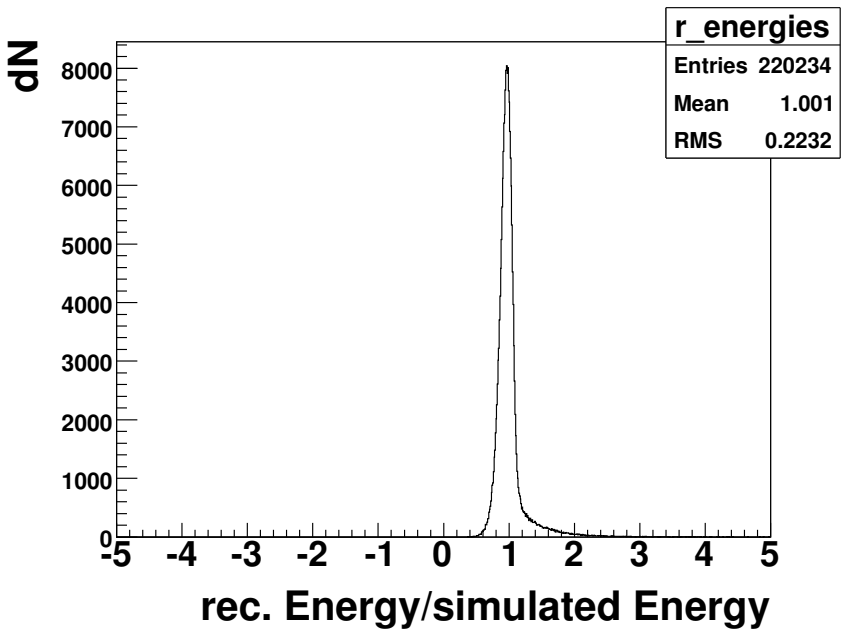

Figure 8.39: Ratio distribution for reconstructed cluster over generated π^0 energy.

8.4.3 Bin Smearing

The shift in the reconstructed energy does not affect the π^0 purity, however it leads to a smearing in the kinematic binning. A cluster that should be in a specific bin, is reconstructed in an incorrect bin. The bin smearing effects are shown for various types of selections and with two different types of normalization. The selections are for generated π^0's and direct photons. Two normalizations are used. The first is the probability of reconstructing the particle in bin r given an incident particle in bin i, i.e. $P(r|i)$[7]. The second normalization flips the probability so that it is $P(i|r)$. Figure 8.40 shows the bin smearing.

The smearing matrices are not used to unsmear the asymmetry results. The most interesting feature of the results is the high p_T behavior. Since the smearing from low to high p_T is small, the essential physics will not be changed in an unfolding.

[7]The method ignores particles which are either not measured or are outside the binning, so the statement is not 100% correct.

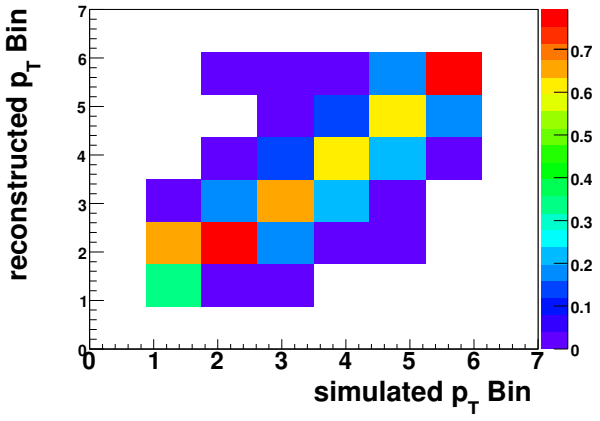

(a) Real axis: π^0's, all reconstructed bins for one real bin adds up to 100%

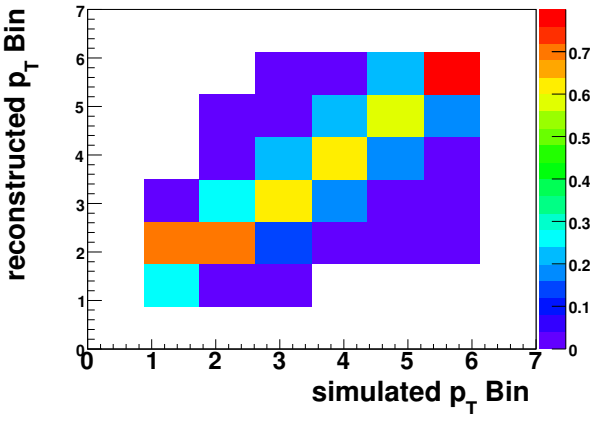

(b) Real axis: Direct-photons, all reconstructed bins for one real bin adds up to 100%

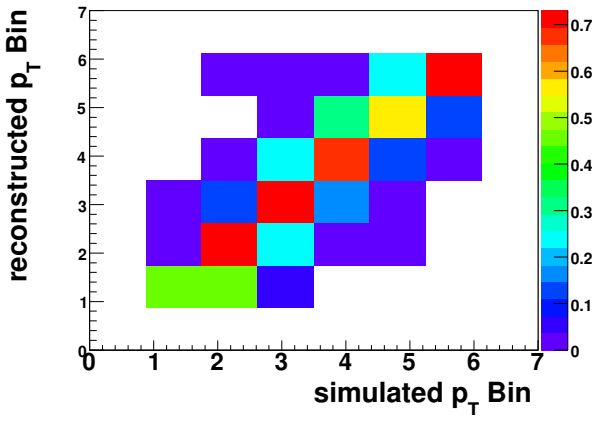

(c) Real axis: π^0's, all real bins for one reconstructed bin adds up to 100%

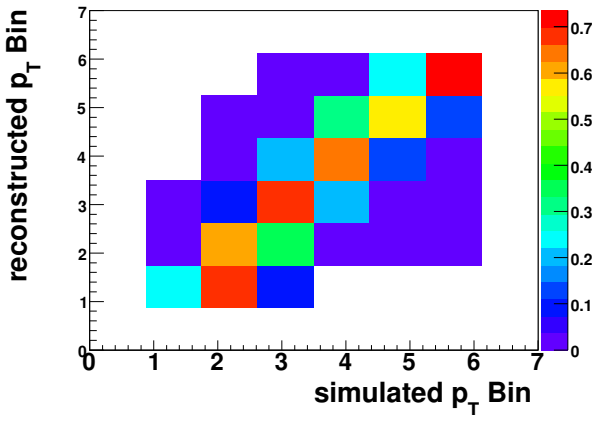

(d) Real axis: Direct-photons, all real bins for one reconstructed bin adds up to 100%

Figure 8.40: p_T bin smearing matrices. Horizontal-axis: the Pythia particle's "real" p_T bin number. Vertical-axis: reconstructed cluster p_T bin number. The bin-numbering is the same as the $A_N^{Cluster}$ (p_T: 1.0, 1.5, 2.0, 2.5, 3.0, 3.5, 4.0, 5.0, 8.0 GeV/c). Left and right correspond to π^0 and direct photons as the parent to the cluster. Top and bottom correspond to the two normalization schemes.

Chapter 9

Mid-rapidity $A_N^{\pi^0}$ and A_N^{η}

This chapter covers the determination of single transverse spin asymmetries of π^0 and η mesons at mid-rapidity using the central arm electromagnetic calorimeter. The single transverse spin asymmetry of π^0's was measured previously with the same detector setup in Run-2. The high luminosity, high polarization and vertically polarized beams from Run-8 used for this analysis deliver a dataset with a figure of merit more than 300 times larger than the Run-2 dataset. Using the new dataset: the measurement of $A_N^{\pi^0}$ is repeated and expanded to higher p_T; for the first time at $\sqrt{s}$=200 GeV A_N^{η} at y≈0 is measured; and to search for non-zero asymmetries pseudorapidity cuts are imposed on both analyses.

The previous study with π^0's was the subject of a leading order Sivers analysis[40] part of which was shown in figure 1.6(b) of the introduction chapter. With the significantly improved error bars, the study can be repeated to further constrain the Sivers function. The η mesons are included in the study because of recent measurements by the STAR collaboration at forward rapidity. Their preliminary results indicate the η meson asymmetry is larger than π^0 asymmetry and approaches one at high x_F[102]. In a more general sense, the partonic composition of the η meson $((u\bar{u}+d\bar{d}+2s\bar{s})/\sqrt{6})$ is different from the π^0 $((u\bar{u}-d\bar{d})/\sqrt{2})$. The inclusion of its asymmetry will strengthen a future global analysis of the proton's transverse spin structure.

The chapter is divided into three sections:

- Detector quality assurance steps. To prepare the asymmetries for publication, both a time of flight and energy calibration are performed. The detector is found to be stable.
- Analysis procedure used in determining the asymmetries, and a summary of the asymmetry results.
- Showing that both the detector performance and extracted asymmetries are consistent with previous work.

9.1 Detector QA

The analysis is based on particle identification cuts originally developed for the measurement of double-longitudinal spin asymmetries and cross-sections [103, 104, 105]. Where possible comparisons to these analyses are provided. Unless otherwise noted, the analysis is done using events selected using a high p_T photon trigger which is described in section 4.4.3.

The quality assurance procedure first eliminates runs which are flagged as bad. Then, using the set of remaining runs, fill by fill and sector by sector energy calibrations are determined from fits to the π^0 invariant mass distributions. The detector stability is verified by examining the π^0 and η invariant mass peak positions as a function of fill over the entire dataset for the triggered data. Finally the peak properties are shown as a function of p_T using the triggered dataset.

9.1.1 Data Selection

1. **Spin Database:** The following runs have no information in the spin database:
   `256724 257502 257517 257644 257649 258663 258808 258950 259050 259572`

2. **No official polarization** Fill 9947 does not have an official blue beam polarization. For ease of analysis the entire fill is rejected:
   `257792 257793 257794 257797 257798 257799 257802 257803`

3. **Non-vertical polarization:** Some runs at the beginning of Run-8 were radially polarized:
   `256450 256451 256452 256454`

4. **One run fills:** After applying the previous cuts, fills 9974 and 9910 consisted of only one run. To ensure good fits for the η mass peak, the corresponding runs were removed from analysis:
   `258634 257275`

9.1.2 Time of Flight Calibration

To extract the true flight time (t_{true}) of a particle from the collision to the calorimeter, two offsets must be subtracted from the measured time of the calorimeter (t_{raw}): a tower-by-tower offset (t_{offset}), and the time of the collision (t_{start}) which is determined using the BBC. t_{true} is calculated as:

$$t_{true} = t_{raw} - t_{offset} - t_{start} \tag{9.1}$$

This t_{offset} value varies tower to tower based on individual cable lengths, on variations in each tower's digitization electronics and on variations in each tower's pulse shape. The offset values are determined by selecting clusters of energy consistent in shape with photons and then filling histograms of the $t_{raw} - t_{start}$ for each tower. The t_{offset} is found by examining each tower's histogram. The procedure is more fully documented in reference [106]. With the exception of a small fraction of towers, the t_{offset} values are confirmed to be stable across all of physics running period. Towers found to be unstable are added a list of mis-calibrated towers.

9.1.3 Energy Calibration

The initial tower energy calibration is done shortly after the physics running period ends. It uses a small subset of runs and an iterative π^0 peak position to determine gain constants for each tower. For a variety of reasons, approximately 30% of the towers in the EMC fail this procedure and are added to a "warnmap", or list of towers not to be used in analysis. After the calibration constants and warnmap are determined, they are used to convert the raw and uncalibrated tower information into a condensed data format based on reconstructed electromagnetic clusters with timing, energy and position information. This condensed format is saved to disk and later analyzed. Because the gain constants are derived from a limited time interval, it is important to verify that the gains do not change with time. The analysis of this section shows that the gains are not constant, and time-dependent relative gain factors are introduced to ensure stability.

Cluster and Pair Cuts

The followings cuts are applied to the event:

1. **Trigger:** The high p_T photon trigger is used to select events[1].
2. **Z-Vertex:** between +/- 30 cm. The z-vertex is found using the beam beam counter.
3. **Crossing:** Any crossings which include an unfilled bunch are removed from analysis.

The following cuts are applied to clusters:

1. **Warnmap:** Tower that contains the cluster center not in warnmap. The warnmap is the superset of the standard warnmap supplied by an expert analysis as part of the base calibration of the EMC and from the ToF calibration described in section 9.1.2.
2. **ToF:** A time of flight cut is applied to clusters of $-5 < ToF < +10$ ns.

[1]For PHENIXians, it is the OR of the ERT4x4A&&BBCLL1 and ERT4x4C&&BBCLL1 triggers.

3. **Minimum cluster energy:** of 200 MeV. This cut removes clusters caused by electronics noise, and improves the purity of the π^0 and η mass peaks.

4. **Shower shape:** An electromagnetic shower-shape cut is applied to clusters to select photons and reject showers initiated by hadrons.

5. **Charged particle veto:** An energy dependent pad chamber station 3 (PC3) matching cut is applied. The PC3 sits immediately in front of the central arm calorimeter and provides charged particle tracking. The angle between the cluster center of gravity and the nearest hit in Pad Chamber 3 is calculated. Charged particles bend in the magnetic field, so the formula for which angles to reject is energy dependent. Very small opening angles were most likely caused by a photon which converted to an electron-positron pair very close to the PC3, and the two electrons likely merged to a single cluster. The large angle difference indicates that no charged tracks were in the vicinity of the electromagnetic cluster. Separate formuli are used in the two types of calorimeter: lead-scintillator and lead-glass.

The following cuts are applied to cluster pairs:

1. **Same arm:** Clusters must both be in either the east or west arm.

2. **Energy asymmetry:** π^0: < 0.8, η: < 0.7.

3. **Active SM trigger bit:** The higher energy cluster in the pair must have fired the trigger which selected the event. It is possible to lookup the trigger bits for a 12 by 12 grid of towers.

An energy non-linearity correction is also applied:

$$E_{pbsc} = \frac{E_{pbsc}}{0.021 + (1 - 0.02E_{pbsc}^{-1})} \tag{9.2}$$

$$E_{pbgl} = \frac{E_{pbgl}}{0.003 + (1 - 0.01E_{pbgl}^{-1})} \tag{9.3}$$

which is derived from test beams.

9.1.4 Time Dependent Gain Factors

A check was performed on the calibrations by forming di-photon invariant mass histograms for each fill and each sector for photon pairs with p_T between 2 and 12 GeV/c. The peaks are fit with a Gaussian plus a third degree polynomial in the mass region of the π^0. There is a small (O(5% shift) but noticeable time dependency to the gain which is balanced out on a fill by fill basis. Figures 9.1 and 9.2 show the peak positions before and after the recalibration is applied.

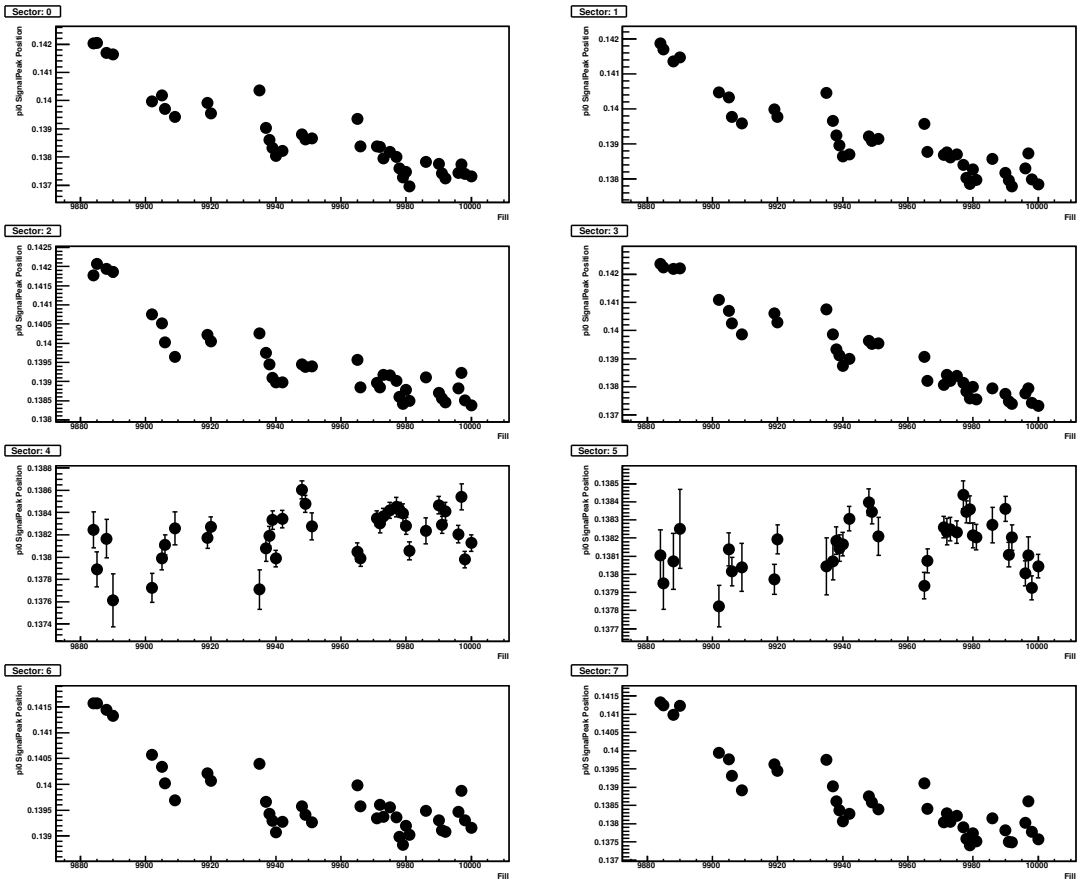

Figure 9.1: Vertical axis: π^0 invariant mass peak positions before the re-calibration. Horizontal axis: fill number (time). The calibration used to generate the plot are the default Run-8 calibrations. Different panels correspond to different sectors in the central arm calorimeter. Sectors four and five are lead glass while the other six are lead scintillator.

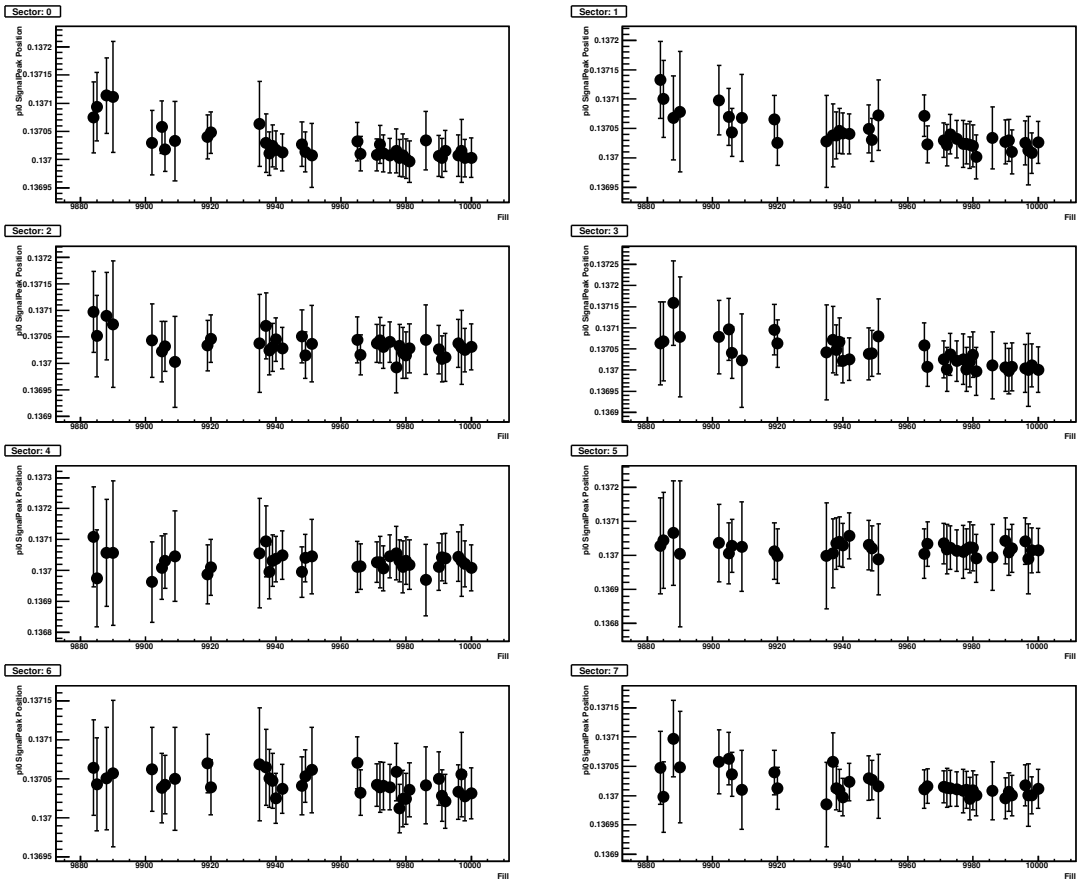

Figure 9.2: Vertical axis: π^0 invariant mass peak positions after re-calibration. Horizontal axis: fill number (time). The calibrations used to generate the plot are the corrected Run-8 calibrations. Different panels correspond to different sectors in the central arm calorimeter. Sectors four and five are lead glass while the other six are lead scintillator.

9.1.5 Peak Position Properties Versus p_T

After the detector has been verified to be stable against time, invariant mass histograms are generated in bins of p_T. Different binning in p_T is used between the π^0 and the η since the π^0 has much higher yields. The fits are separated by even crossings only, odd crossings only and by all crossings and by either the lead scintillator or lead glass detectors. The analysis is separated by even and odd crossings because of two separate trigger circuits used in the front end electronics for even and odd bunch crossings. The same front end electronics are used in the MPC, and are discussed in section 4.4.3. The fits to the meson invariant mass distributions are used to extract: the meson peak positions, the meson peak width and the background contamination under the meson peak (r). A sample plot from the lead glass is shown in figure 9.3. The properties of the peaks do not disagree between the two crossings. Therefore, a single value is used for both sub-analyses.

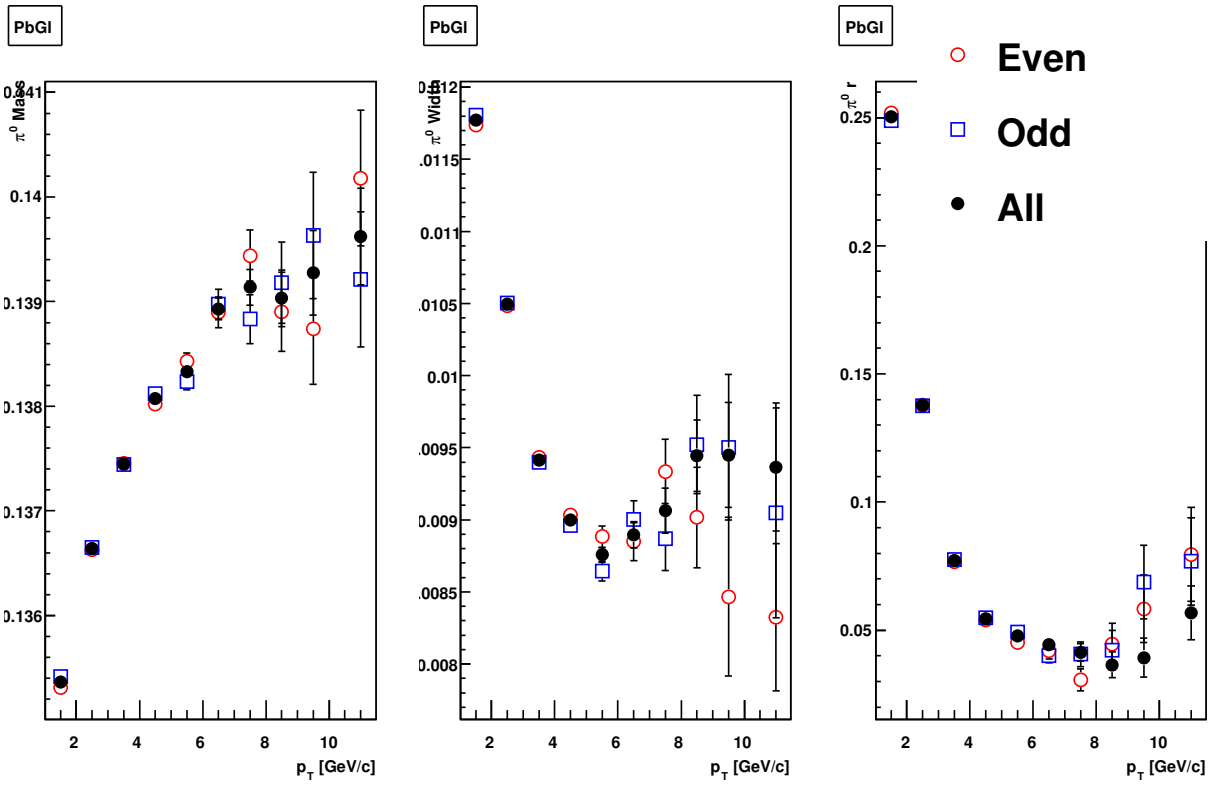

Figure 9.3: π^0 invariant mass properties using the lead glass detector. Horizontal axis: p_T. From left to right the vertical axis is: π^0 invariant mass peak position, π^0 invariant mass peak width, π^0 invariant mass background contamination (r). The different point colors refer to selecting even, odd and all bunch crossing numbers.

9.2 Analysis

9.2.1 Asymmetry Calculation

The central arm left-right asymmetries are calculated using the square root formula and simple left-right yields (defined in equations 6.16 and 6.4). The integral over the hemispheres is motivated by the limited azimuthal angle coverage of the central arm. The asymmetries are also found using the luminosity formula (equation 6.10). Comparison to the luminosity formula is done in reference [107] and the results are consistent.

The counts entering equation 6.19 are selected using two invariant mass windows. Inside the mass windows there are signal counts from either π^0's or η's, and background counts. The analysis measures the signal+background asymmetry, estimates the background asymmetry by measuring the asymmetry outside of the signal mass window, and then subtracts the results to extract a pure signal asymmetry. The subtraction is done as follows:

$$A_N^S = \frac{A_N^{S+B} - rA_N^B}{1-r} \tag{9.4}$$

where S and B stand for Signal and Background, and r indicates the level of background contamination. The background contamination factors are summarized in tables 9.2 and 9.3. For the π^0 the signal (background) region is defined as 112-162 MeV (47-97, 177-227 MeV). For the η the signal (background) is defined as 480-620 MeV (300-400, 700-800) MeV. The various mass windows are binned in p_T according to table 9.1. They asymmetries are also extracted using identical p_T binning with pseudorapidity cuts.

p_T binning			
π^0_{Signal}	$\pi^0_{Background}$	η_{Signal}	$\eta_{Background}$
1-2	1-2	-	-
2-3	2-3	2-3	2-3
3-4	3-4	3-4	3-4
4-5	4-5	4-5	4-5
5-6	5-6	5-6	5-12
6-7	6-12	6-7	5-12
7-8	6-12	7-8	5-12
8-9	6-12	8-12	5-12
9-10	6-12	-	-
10-12	6-12	-	-

Table 9.1: p_T binning used for the extraction of asymmetry values. Due to low statistics in the background region at higher p_T's, a large window is used above 6 and 5 GeV/c for the π^0 and η, respectively.

Separate spin analyses are carried out for the even and odd crossings to avoid potential trigger complications stemming from separate trigger circuits for even and odd crossings. For each kinematic bin, a fill is rejected if the number of counts entering the asymmetry calculation is less than 30. This avoids potential

π^0 Signal					
	PbSc		PbGl		Combined
p_T Bin	r	S+B Counts	r	S+B Counts	r
1-2	0.291±0.000119	2.07e+07	0.25±0.000612	6.68e+05	0.29
2-3	0.138±9.67e-05	1.48e+07	0.138±0.000348	1.14e+06	0.138
3-4	0.0698±0.000147	3.25e+06	0.0772±0.000423	4.32e+05	0.0706
4-5	0.0533±0.000282	6.71e+05	0.0545±0.0007	1.11e+05	0.0535
5-6	0.049±0.000545	1.65e+05	0.0478±0.00127	2.96e+04	0.0488
6-7	0.0525±0.00102	5.01e+04	0.0443±0.00218	9.31e+03	0.0512
7-8	0.0525±0.00172	1.77e+04	0.0413±0.00348	3.42e+03	0.0507
8-9	0.0451±0.00245	7.52e+03	0.0365±0.00508	1.41e+03	0.0437
9-10	0.0384±0.00331	3.5e+03	0.0393±0.00762	676	0.0386
10-12	0.0362±0.00378	2.53e+03	0.0568±0.0105	519	0.0397

Table 9.2: Background contamination values for the PbSc and PbGl.

η Signal					
	PbSc		PbGl		Combined
p_T Bin	r	S+B Counts	r	S+B Counts	r
2-3	0.76±0.000453	3.7e+06	0.744±0.0024	1.29e+05	0.76
3-4	0.569±0.000881	7.33e+05	0.569±0.00303	6.18e+04	0.569
4-5	0.467±0.00175	1.53e+05	0.48±0.00521	1.77e+04	0.469
5-6	0.427±0.00331	3.9e+04	0.452±0.00923	5.3e+03	0.43
6-7	0.405±0.00583	1.19e+04	0.403±0.0149	1.8e+03	0.405
7-8	0.393±0.00944	4.41e+03	0.591±0.0282	742	0.421
8-12	0.417±0.0115	3.13e+03	0.4±0.0264	576	0.414

Table 9.3: Background contamination values for the PbSc and PbGl.

problems in the breakdown of the error calculation in the limit of small statistics.

Relative Luminosity

Relative luminosity is the ratio of beam luminosities after selecting bunch crossings by the spin orientation. It is only relevant to the luminosity formula and not to the square root formula. Nonetheless, it is presented. It is calculated fill to fill using a BBC based trigger which is scaled using the GL1-1P. The relative luminosity values are plotted against fill in figure 9.4.

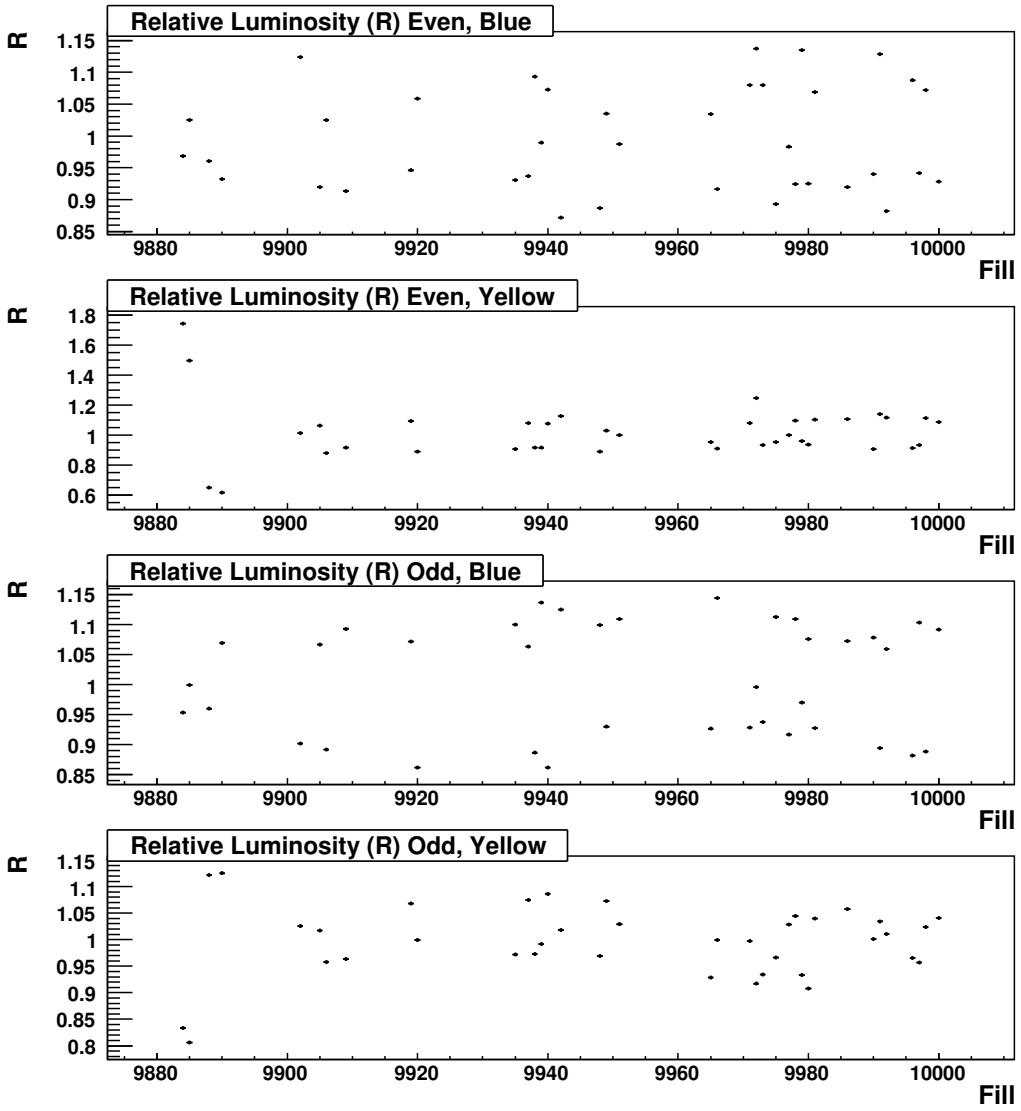

Figure 9.4: Relative luminosity calculated using the BBCLL1 trigger scaled using the GL1-1P (see section 3.4 for information on the scaler)

AN721		This work			
	Inclusive		Inclusive	$\|x_F\| > 0.01$	$\|\eta\| > 0.2$
p_T bin	$k^{\pi^0}_{enhance}$	p_T bin	$k^{\pi^0}_{enhance}$	$k^{\pi^0}_{enhance}$	$k^{\pi^0}_{enhance}$
1.0-1.5	1.05 (1.09)	1.0-2.0	1.066 (1.114)	-	1.044 (1.084)
1.5-2.0	1.04 (1.08)	-	-	-	-
2.0-2.5	1.03 (1.07)	2.0-3.0	1.035 (1.084)	1.005 (1.019)	1.024 (1.062)
2.5-3.0	1.02 (1.06)	-	-	-	-
3.0-3.5	1.01 (1.06)	3.0-4.0	1.014 (1.059)	1.007 (1.036)	1.010 (1.047)
3.5-4.0	1.01 (1.05)	-	-	-	-
4.0-5.0	1.01 (1.07)	4.0-5.0	1.008 (1.05)	1.006 (1.041)	1.006 (1.043)
5.0-6.0	1.01 (1.07)	5.0-6.0	1.006 (1.048)	1.006 (1.034)	1.005 (1.034)
6.0-7.0	1.01 (1.07)	6.0-7.0	1.005 (-)	1.004 (-)	1.004 (-)
7.0-9.0	1.01 (1.08)	7.0-8.0	1.004 (-)	1.003 (-)	1.003 (-)
-	-	8.0-9.0	1.004 (-)	1.005 (-)	1.006 (-)
-	-	9.0-10.0	1.004 (-)	1.005 (-)	1.009 (-)
-	-	10.0-12.0	1.005 (-)	1.003 (-)	1.005 (-)
-	-	6-12	- (1.063)	- (1.068)	- (1.057)

Table 9.4: $k_{enhance}$ factors for the π^0 signal (background) and comparison to previous work. The p_T binning between the two analyses do not match up exactly, but are close enough to compare. AN721 refers to an internal PHENIX analysis note documenting the measurement of $A_{LL}^{\pi^0}$. Note that AN721 lists the $k^2_{enhance}$ values while the comparison is done between $k_{enhance}$.

$k_{enhance}$

The error bars of all asymmetries require adjustment to account for the fact that in some events multiple counts are recorded. Previous $A^{\pi^0}_{LL}$ analyses [103, 108] justify and derive the k-factor which corrects the error bar according to the mean multiplicity. The formula used is:

$$\delta A_N = k_{enhance} \delta A_{N,Poisson} \tag{9.5}$$

where

$$k_{enhance} = \sqrt{\frac{\bar{k^2}}{\bar{k}}} \tag{9.6}$$

The $k_{enhance}$ values are listed in tables 9.4 and 9.5 and compared to a previous analyses. The values are expected to be similar but not identical because of slightly different running conditions, particle identification cuts, etc.

Consistency Check

The χ^2 and $\langle t \rangle$ tests described in section 6.4 are summarized in table 9.6. The bunch shuffling results are all consistent with expectations. An example plot from the bunch shuffling is available in figure 6.9.

AN649		This work			
	Inclusive		Inclusive	$\|x_F\| > 0.01$	$\|\eta\| > 0.2$
p_T bin	$k^{\eta}_{enhance}$	p_T bin	$k^{\eta}_{enhance}$	$k^{\eta}_{enhance}$	$k^{\eta}_{enhance}$
2-3	1.042 (1.052)	2-3	1.050 (1.062)	1.005 (1.007)	1.038 (1.043)
3-4	1.025 (1.032)	3-4	1.031 (1.041)	1.015 (1.022)	1.021 (1.030)
4-5	1.018 (1.026)	4-5	1.022 (1.033)	1.014 (1.024)	1.014 (1.024)
5-6	1.014 (1.023)	5-6	1.018 (-)	1.011 (-)	1.011 (-)
6-7	1.013 (1.020)	6-7	1.014 (-)	1.015 (-)	1.014 (-)
7-9	1.015 (1.020)	7-8	1.013 (-)	1.007 (-)	1.005 (-)
-	-	8-12	1.029 (-)	1.026 (-)	1.018 (-)
-	-	5-12	- (1.056)	- (1.047)	- (1.043)

Table 9.5: $k_{enhance}$ factors for the η signal (background) and comparison to previous work. The p_T binning between the two analyses do not match up exactly, but are close enough to compare. AN649 refers to an internal PHENIX analysis note documenting the measurement of A^{η}_{LL}.

	Even/Odd Blue Beam		Even/Odd Yellow Beam		Blue/Yellow	
Mass selection	χ^2/NDF	$\langle t \rangle$	χ^2/NDF	$\langle t \rangle$	χ^2/NDF	$\langle t \rangle$
Inclusive η selection						
π^0 Signal	6.54 / 10	0.30	3.40 / 10	0.13	7.55 / 10	-0.12
π^0 Background	6.68 / 6	0.18	2.63 / 6	0.27	5.20 / 6	-0.02
η Signal	4.86 / 7	0.81	5.00 / 7	-0.46	6.82 / 7	0.12
η Background	0.81 / 4	-0.26	4.04 / 4	-0.90	5.57 / 4	-0.36
η <-0.2						
π^0 Signal	4.73 / 7	0.10	9.32 / 8	-0.02	7.71 / 7	0.56
π^0 Background	1.60 / 5	-0.18	6.67 / 6	0.38	2.39 / 5	0.02
η Signal	3.02 / 4	-0.39	4.11 / 5	-0.73	2.31 / 5	0.05
η Background	7.48 / 4	-0.61	3.54 / 4	-0.33	3.39 / 4	-0.66
η >0.2						
π^0 Signal	5.90 / 8	0.09	5.80 / 7	0.60	7.28 / 7	-0.66
π^0 Background	6.16 / 6	-0.39	4.49 / 5	-0.10	1.76 / 5	-0.36
η Signal	9.23 / 5	-0.23	8.33 / 4	-0.46	8.19 / 5	-0.45
η Background	4.88 / 4	-0.65	1.42/4	-0.20	3.83 / 4	-0.26

Table 9.6: χ^2 values and $\langle t \rangle$ values between the four sub-analyses. The two statistical tests are defined in the text. The values are for square root asymmetries only.

p_T ($\langle p_T \rangle$) (GeV/c)	Inclusive	$A_N^{\pi^0}$ (10^{-4}) $\eta < -0.2$	$\eta > 0.2$
1.58635	7.5 ± 6.2	16.7 ± 13.9	19.1 ± 13.8
2.4	5.2 ± 5.6	12.0 ± 12.9	20.6 ± 12.9
3.4	3.1 ± 10.3	3.1 ± 24.2	21.3 ± 24.5
4.4	0.3 ± 21.8	-12.8 ± 51.1	40.1 ± 51.4
5.4	2.1 ± 43.4	-150.8 ± 101.9	139.2 ± 102.2
6.4	-63.7 ± 78.6	27.5 ± 191.3	-270.0 ± 189.6
7.4	-70.8 ± 130.8	573.0 ± 323.4	-703.4 ± 323.9
8.4	30.2 ± 200.8	103.0 ± 813.3	-838.7 ± 703.6
9.4	45.7 ± 299.3	-	-
10.8	402.9 ± 363.6	-	-

Table 9.7: Single transverse spin asymmetries for the π^0 binned in p_T and pseudorapidity at mid-rapidity

9.2.2 Final Asymmetries

Final results are shown in figure 9.5 and in tables 9.7 and 9.8. The asymmetry value and statistical error bar are calculated using the square root formula. The systematic error bars are calculated as:

- Upper bound on false asymmetries from bunch shuffling. 2500 bunch shuffles were thrown. The results are consistent with expectations. This sets an upper bound on false asymmetries as $\frac{1}{\sqrt{2500}}\delta A_{sqrt,statistical}$. This systematic uncertainty is assigned to all points.

- Polarization magnitude uncertainty. The total statistical and systematic uncertainty on the polarization magnitude is ($\delta P/P$): 4.2% for the blue beam and 7.2% for the yellow beam.[109]. The combined effect is a 5.2% scale uncertainty on the combined asymmetry. This leads to a scaling of both the asymmetry and its error bar. This is noted in the plot of the asymmetries as text.

- Polarization direction uncertainty. The uncertainties in the polarization direction can be interpreted as an uncertainty on the polarization magnitude. Therefore, the effect is estimated as $cos(\delta\phi_{Polarization})$, which is less than half a percent. Compared to the much larger polarization magnitude uncertainty it is safe to ignore this uncertainty. The polarization direction analysis is discussed in chapter 7.

9.2.3 Comparison to Previous Results

The present analysis is compared to existing π^0 and η analyses. No previous central arm spin analysis has binned in pseudorapidity, so comparison can only be done for inclusive kinematic cuts.

The π^0 analysis is compared to previous PHENIX analyses to verify that the detector performance and analysis are consistent with previous work. The most direct comparison is to reference [29] and its internal PHENIX analysis note AN293[110] which document the measurement of $A_N^{\pi^0}$. However, these references only

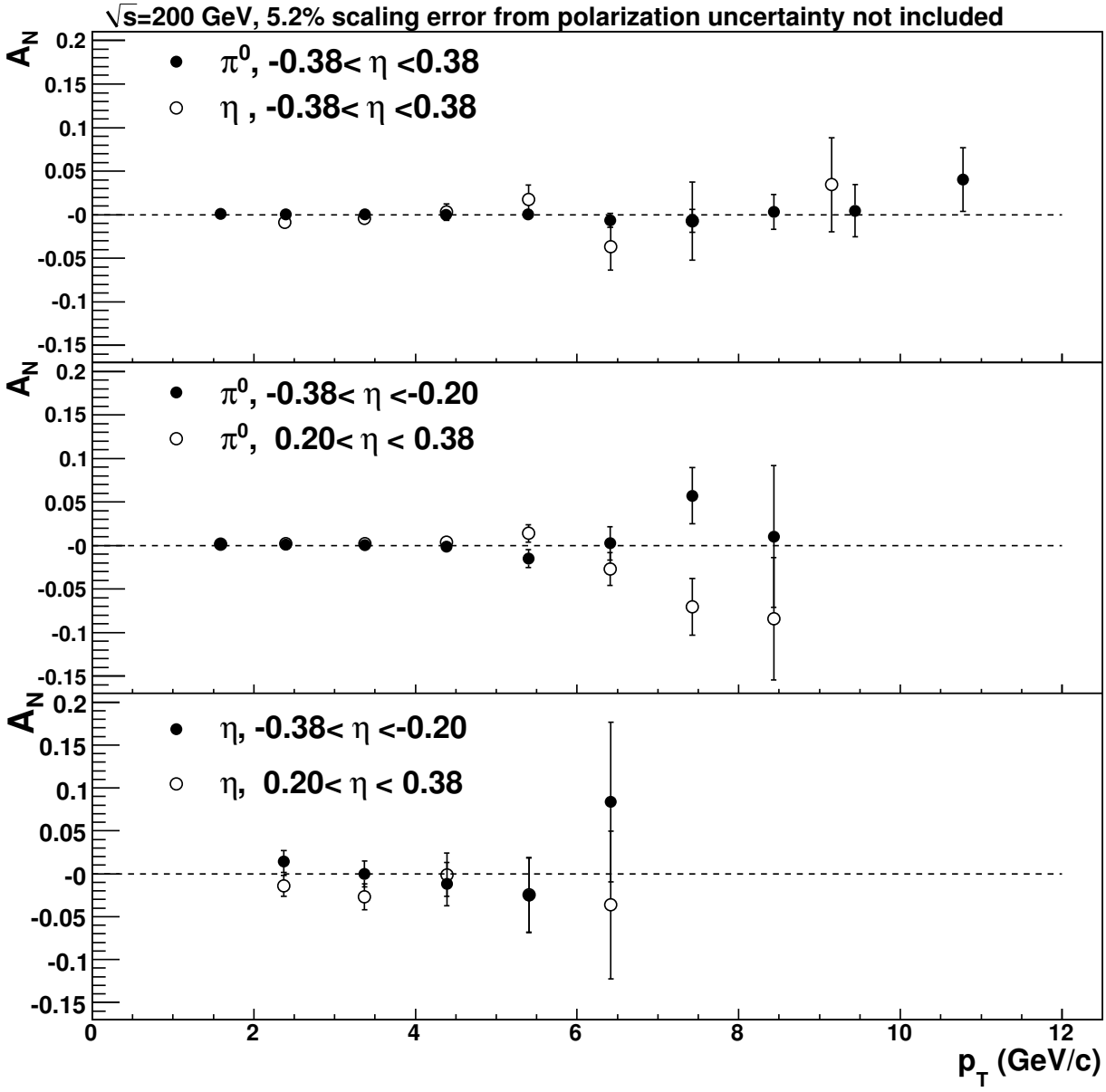

Figure 9.5: Final A^{π^0} and A_N^η values determined using the square root formula. All asymmetries are consistent with zero within statistical uncertainties.

p_T ($\langle p_T \rangle$)		A_N^η (10^{-4})	
(GeV/c)	Inclusive	$\eta < -0.2$	$\eta > 0.2$
2.4	-86.0 ± 48.4	142.9 ± 125.0	-140.9 ± 124.0
3.4	-40.7 ± 55.7	-3.6 ± 149.8	-268.1 ± 149.6
4.4	30.9 ± 94.5	-118.7 ± 252.2	-11.6 ± 252.2
5.4	175.9 ± 165.2	-250.2 ± 435.2	-247.8 ± 434.9
6.4	-368.5 ± 265.1	837.4 ± 929.4	-364.2 ± 860.4
7.4	-73.6 ± 446.6	-	-
9.1	345.0 ± 540.3	-	-

Table 9.8: Single transverse spin asymmetries for the η binned in p_T and pseudorapidity at mid-rapidity

measure the π^0 and only to relatively low p_T. In addition, the previous analysis used the Run-2/ERT2x2 triggered dataset while the present analysis uses the Run-8/ERT4x4(A||C) dataset. Therefore, a comparison with less triggering uncertainty can be done to the more recent π^0 and η A_{LL} analyses. The present work is compared to the Run-6 π^0 publication[98] using its internal PHENIX analysis notes: AN567[103] and AN602[104]. The η double longitudinal asymmetry analysis is not yet published, but comparison is done to its internal note: AN649[105].

$k_{enhance}$

The η $k_{enhance}$ values are taken from its previously mentioned internal PHENIX analysis note. For the π^0, the values are taken from AN567 and not from AN602. The particle identification cuts used between the two analyses are not identical, so exact agreement is not expected. Tables 9.4 and 9.5 list the comparison to previous analyses.

Background Contamination

Comparison is done between previous analyses and the present work for the background contamination factors, r. The contamination factor is determined with the ratio B/(S+B), where B and S stand for background and signal. The values are taken from the internal PHENIX analysis notes AN567 and AN602 for the π^0 and from AN649 for the η. The background contaminations from the present analysis are consistent with past analyses.

Yields

In this section the yields of π^0's are compared to previous analyses. An important point to remember is that the official integrated luminosities for each run do not include analysis dependent bad run lists. Often the integrated luminosity actually used in analysis is quite different. There are no firm numbers for the integrated luminosities sampled by the previous analyses, so the values are estimated and summarized in table 9.11.

The comparison between the yields are done in two ways. Comparison to AN293 is done using the statistical error on the asymmetries, while, for AN602, the yields are used. Assuming polarization of 15%

[2]The standard integrated luminosity for run02 is 0.15 pb^{-1}, but there is no corresponding list of run numbers. There is at least a factor of two difference between the number of runs marked as PHYSICS in the daq database and the run list provided in AN293. The difficulty of comparing Run-2 and Run-8 is compounded by the fact that the $BBCLL1(>0 tubes)$ did not exist in Run-2. Instead, the "$BBCLL1 >= 1(noVertexCut)$" trigger is used to provide a link between the integrated luminosities of Run-2 and Run-8. The summed total number of live triggers for the Run-2 trigger in run02 is: $1.79 \cdot 10^9$. Based on the name, this trigger made no z-vertex cut and the number of triggers can be roughly translated to a ± 30 cm z-vertex cut trigger by dividing its counts by a factor of two.

π^0 r Comparison			
p_T bin	r^{AN567}	r^{AN602}	$r^{Thiswork}$
0.5-0.75	0.814	-	-
0.75-1	0.577	-	-
1-1.5	0.373	0.436	0.29
1.5-2	0.261	0.266	-
2-2.5	0.175	0.158	0.138
2.5-3	0.127	0.100	-
3-3.5	0.102	0.071	0.0706
3.5-4	0.089	0.057	-
4-5	0.084	0.051	0.0535
5-6	0.081	0.048	0.0488
6-7	0.081	0.049	0.0512
7-9	0.079	0.047	-
7-8	-	-	0.0507
8-9	-	-	0.0437
9-10	-	-	0.0386
10-12	-	-	0.0397

Table 9.9: Background contamination value comparison between previous work (AN567 and AN602) and the present analysis. The background contamination values are taken from table 6 of AN567 and table 3 of AN602.

η r Comparison			
p_T bin	r^{AN649}_{even}	r^{AN649}_{odd}	r^{AN864}
2-3	0.777	0.777	0.760
3-4	0.572	0.572	0.569
4-5	0.464	0.472	0.469
5-6	0.426	0.432	0.430
6-7	0.413	0.403	0.405
7-9	0.417	0.406	-
7-8	-	-	0.421
8-12	-	-	0.414

Table 9.10: Background contamination value comparison between previous work (AN649) and the present analysis. The background contamination values are taken from table 2 of AN567.

Analysis	NTrigger_{Live}
AN293[2]	8.95×10^8
AN602	1.23×10^{11}
AN864	9.89×10^{10}

Table 9.11: Number of live $BBCLL1(> 0\,tubes)$ triggers for each π^0 analysis. The number for AN293 is only an estimate. Good run lists for AN293 and AN602 are not exact but are close to the lists used for analysis.

and 46% for Run-2 and Run-8 respectively, the ratio of error bars is expected to be: 32.2. In addition, for the Run-2 analysis, there is uncertainty stemming from the warnmaps used in the analysis and the percentage of the ERT trigger which was active, etc. The factor of 32 is only a rough estimate. The comparison between Run-2 and Run-8 is shown in table 9.12. In contrast to the Run-2 case, comparison to the Run-6 yields is

p_T bin	AN293/Run-2 $A_N^{\pi^0}$	AN864/Run-8 $A_{N,sqrt}^{\pi^0}$	Ratio of errors
1-2	-0.005 ± 0.012	7.49e-04±6.21e-04	19.6
2-3	-0.012 ± 0.020	5.27e-04±5.55e-04	36.0
3-4	-0.016 ± 0.047	3.13e-04±1.03e-03	45.6
4-5	0.052 ± 0.109	4.23e-04±2.18e-03	50.0

Table 9.12: Comparison between the Run-2 and Run-8 analyses

much simpler. The two analyses used the same trigger and similar warnmaps. The present analysis masks 31% of the EMC towers while AN602 masked 24% of the towers. Therefore, the expected yields are expected to differ by a factor of 1.35. The Run-6, Run-8 comparison is shown in table 9.13.

p_T bin	$Yield^{AN602}$	$Yield^{AN864}$	$\frac{Yield^{AN602}}{Yield^{AN864}}$	$\delta A_{N,projection}$	$\delta A_{N,measured}$	$\frac{\delta A_{N,projection}}{\delta A_{N,measured}}$
1-2	4.43 e+7	2.07 e+7	2.14	5.29e-4	6.21e-4	0.851
2-3	2.50 e+7	1.48 e+7	1.69	5.15e-4	5.55e-4	0.927
3-4	5.11 e+6	3.25 e+6	1.57	1.02e-e	1.03e-3	0.990
4-5	1.01 e+6	6.71 e+5	1.51	2.20e-3	2.18e-3	1.01
5-6	2.50 e+5	1.65 e+5	1.51	4.42e-3	4.34e-3	1.08
6-7	7.63 e+4	5.01 e+4	1.52	8.04e-3	7.68e-3	1.05
7-9	3.94 e+4	2.52 e+4	1.56	-	-	-
9-12	9.09 e+3	6.03 e+3	1.51	-	-	-

Table 9.13: Adapted yields from AN602 table 3 and this analysis for mass window 112 to 162 MeV and associated values which are explained in the text.

The fourth column of 9.13 shows the consistency of the yields between the two datasets by forming their ratio. The low p_T yields are not expected to scale like the high p_T yields since the present analysis uses a 200 MeV rather than a 100 MeV minimum photon energy in the PbSc. The fifth column shows the projected error bar of A_N given the run08 yields, a mean polarization of 46% and the signal background ratios given in tables 9.2 and 9.3. The projected error is calculated as: $\delta A_{N,projection} = \frac{1}{0.9P(1-r)\sqrt{2N}}$ The factor of 0.9 approximates the $\langle|cos(\phi)|\rangle$ term and the factor of two is takes into account the fact that a single particle is used in both the blue and yellow beam analyses. The projected error can be compared to the sixth column which shows the measured square root asymmetry error bar. Finally, the ratio of the projected over the measured error bar is shown in the seventh and final column.

Chapter 10

Forward Rapidity MPC $A_{TT}^{DoubleCluster}$

Using data from Semi-Inclusive Deep Inelastic Scattering (SIDIS) and electro-positron experiments, the quark transversity distributions have been extracted[111, 112]. In principle, the known transversity distributions can be used to predict a double transverse spin asymmetry (A_{TT}) in polarized $p+p$ collisions. If the predicted and measured asymmetries were to match, then it would provide one of the first experimental confirmations that the framework of perburbative QCD, factorized cross-sections and universality is applicable to extracting spin dependent distribution functions from $p+p$ collisions. So far, the work in measuring transversity using $p+p$ collisions has concentrated on Drell-Yan production which is a theoretically clean experimental observable[113]. Unfortunately, a Drell-Yan based measurement also requires high integrated luminosity. In addition, RHIC collides protons with protons. Therefore, the anti-quark will be drawn from the sea-quark distribution where transversity is expected to be small. Instead, this chapter measures A_{TT} using coincidence pairs of clusters in the forward region. The coincidences are formed from clusters in the same arm and with clusters in the opposite arm. At high enough p_T, the two are expected to be sensitive to high-x against low-x scattering and to high-x against high-x scattering. For the case of high-x against high-x scattering, the underlying processes are expected to both draw from the valence quark region where the transversity distributions are known to be non-zero. The expected asymmetry will scale roughly like $\delta q(x) \cdot \delta q(x)$ with a dilution from $gluon - gluon$ scattering and by cancellations between the opposite signs of the u and d transversity distributions. At a maximum, the asymmetry is expected to be approximately 2%. At the present time, the available luminosity does not allow the measurement to be extended to high p_T with sufficient statistics. However, an exploratory measurement of A_{TT} in the MPC is carried out with the idea that later RHIC runs will add additional statistics to the analysis.

10.1 Detector QA

The same set of detector and run quality assurance checks are used for the double transverse spin asymmetry as for the single spin asymmetry discussed in chapter 8.

10.2 Analysis

10.2.1 Cluster Cuts

The following four cuts are used on the clusters:

- Energy > 25 GeV. This selects mostly merged π^0's.
- TDC Timeout veto.
- ADC Overflow veto.
- Warnmap veto.

10.2.2 Di-Cluster Correlation Functions

For each event, the clusters that meet all cuts are used to form di-cluster pairs and to study their correlations. The "trigger" cluster is defined as the first cluster in the event to meet the requirements. Typically, the trigger cluster meets a higher p_T cut than the second cluster, called the "associate" cluster, in the event to meet the requirements. For a given trigger cluster, all possible pairs in an event are found. In rare events when two clusters are found, the cluster pairs are iterated over in a grid of p_T threshold cuts for the "trigger" and "associate" clusters. The p_T threshold cuts are : $p_T > 1.0$, $p_T > 1.5$, $p_T > 2.0$, $p_T > 2.5$ and $p_T > 3.0$ GeV/c.

The azimuthal difference (ϕ_1-ϕ_2) distributions between two clusters is shown in figures 10.1, 10.2 and 10.3. Figure 10.1 for two clusters in the South MPC. Figure 10.2 for two clusters in the North MPC. Figure 10.3 for one cluster in the North MPC and the other in the South MPC.

The dip in yield at $\Delta\phi$=0 is due to the fact that there is a minimum distance between neighboring clusters which the clustering algorithm can handle. If two photons are separated by only 1 cm, then they are reconstructed as a single cluster. In general the cluster correlation contains contributions from the same jet clusters at ϕ=0 and from clusters in opposite jets at ϕ=π. The distributions are used to identify azimuthal angle difference cuts to select events with two jets. Cuts at $\Delta\phi \approx \pi$, select di-jet events into the MPC. Therefore, there is a large imbalance in momenta between x_1 and x_2, where $x_1 >> x_2$. This selects quark-gluon scattering as the dominant process.

10.2.3 Final Results

Asymmetries are extracted using the grid of trigger and associate p_T cuts defined in the previous section and the three combinations of cluster arm pairings. The asymmetries are also extracted using an inclusive

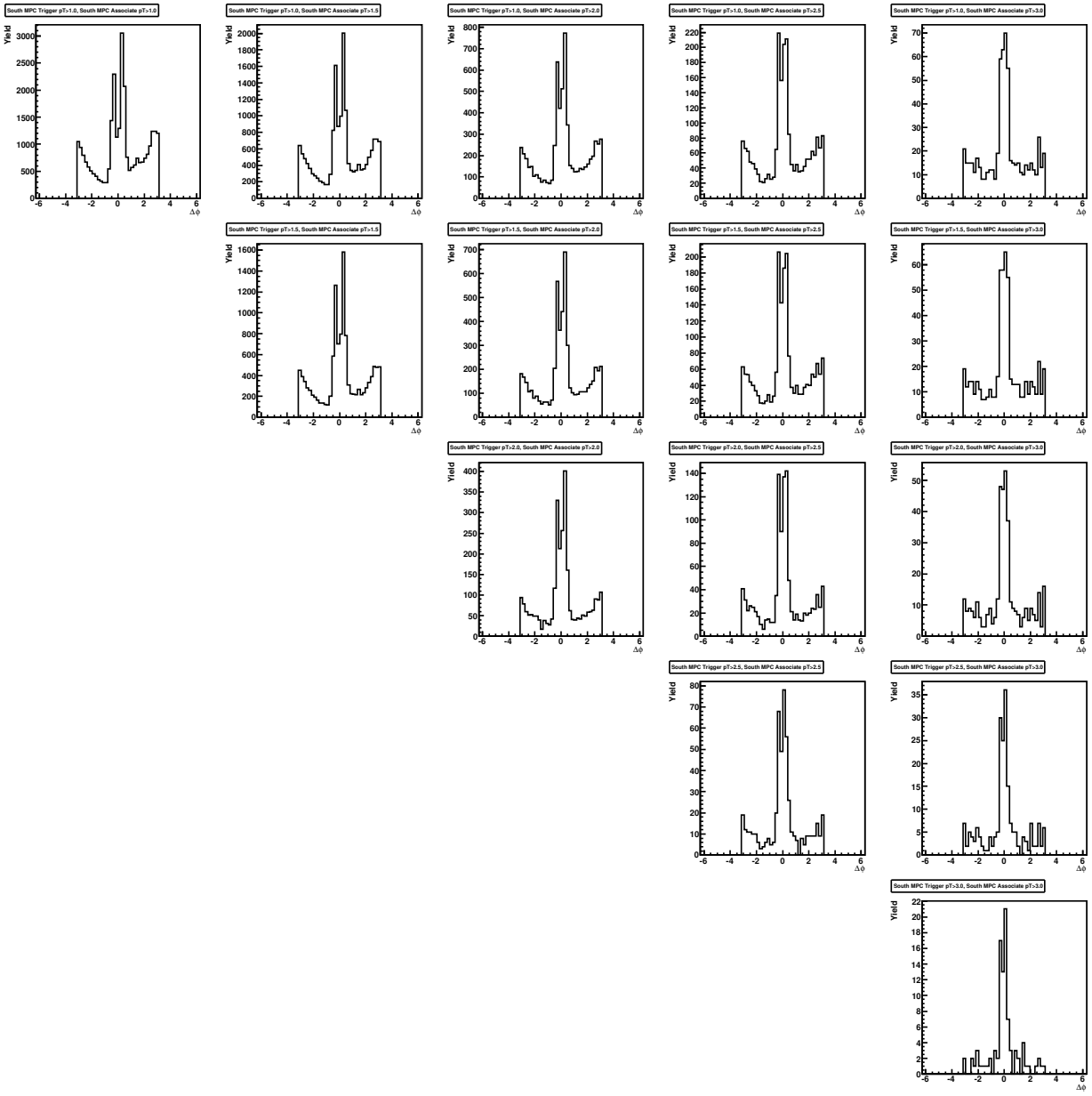

Figure 10.1: Cluster pair azimuthal angle difference distribution between a South MPC Trigger cluster and a South MPC Associate cluster. The correlations are shown for different p_T cuts on the trigger and associate particles.

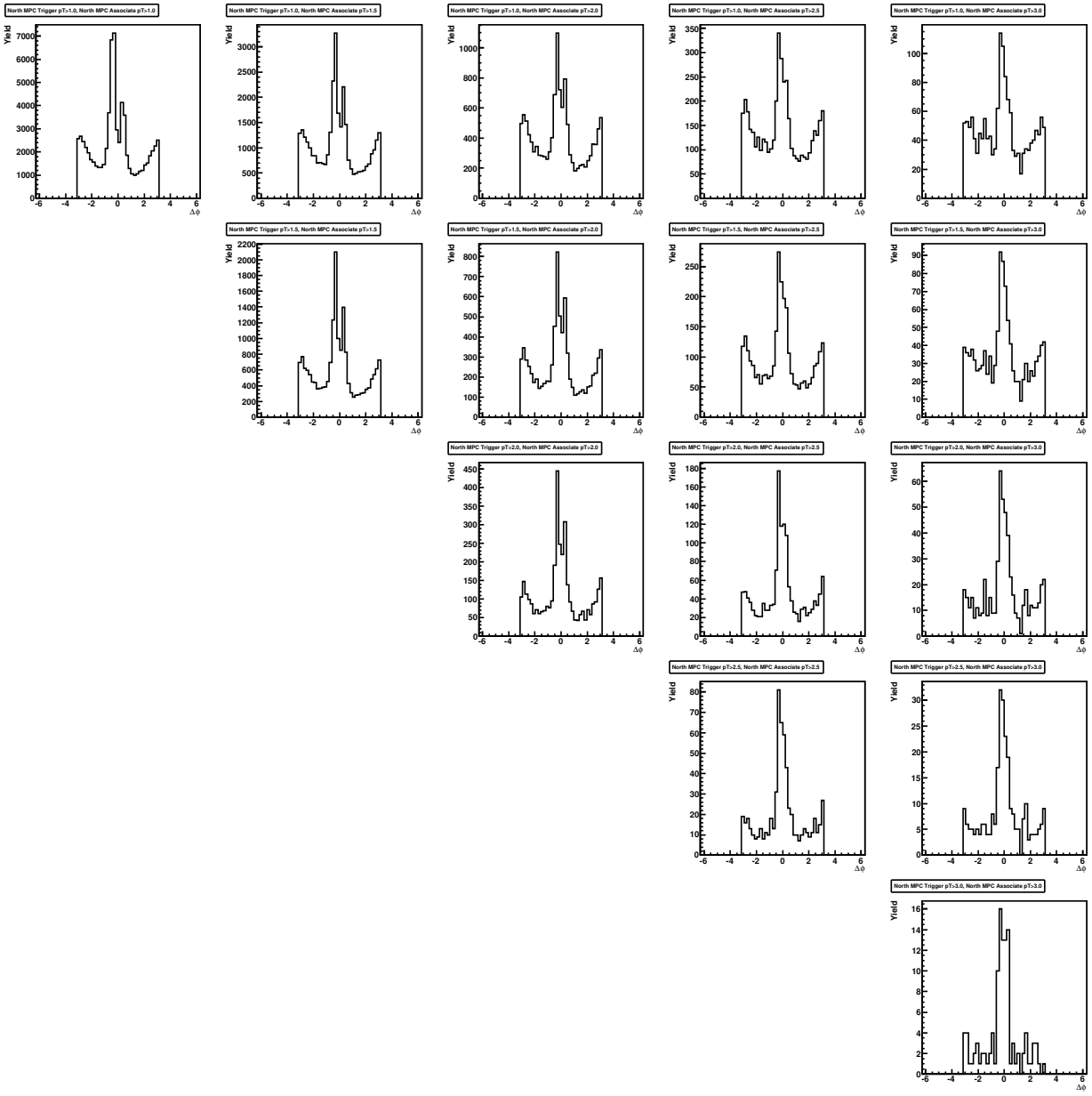

Figure 10.2: Cluster pair azimuthal angle difference distribution between a North MPC Trigger cluster and a North MPC Associate cluster. The correlations are shown for different p_T cuts on the trigger and associate particles.

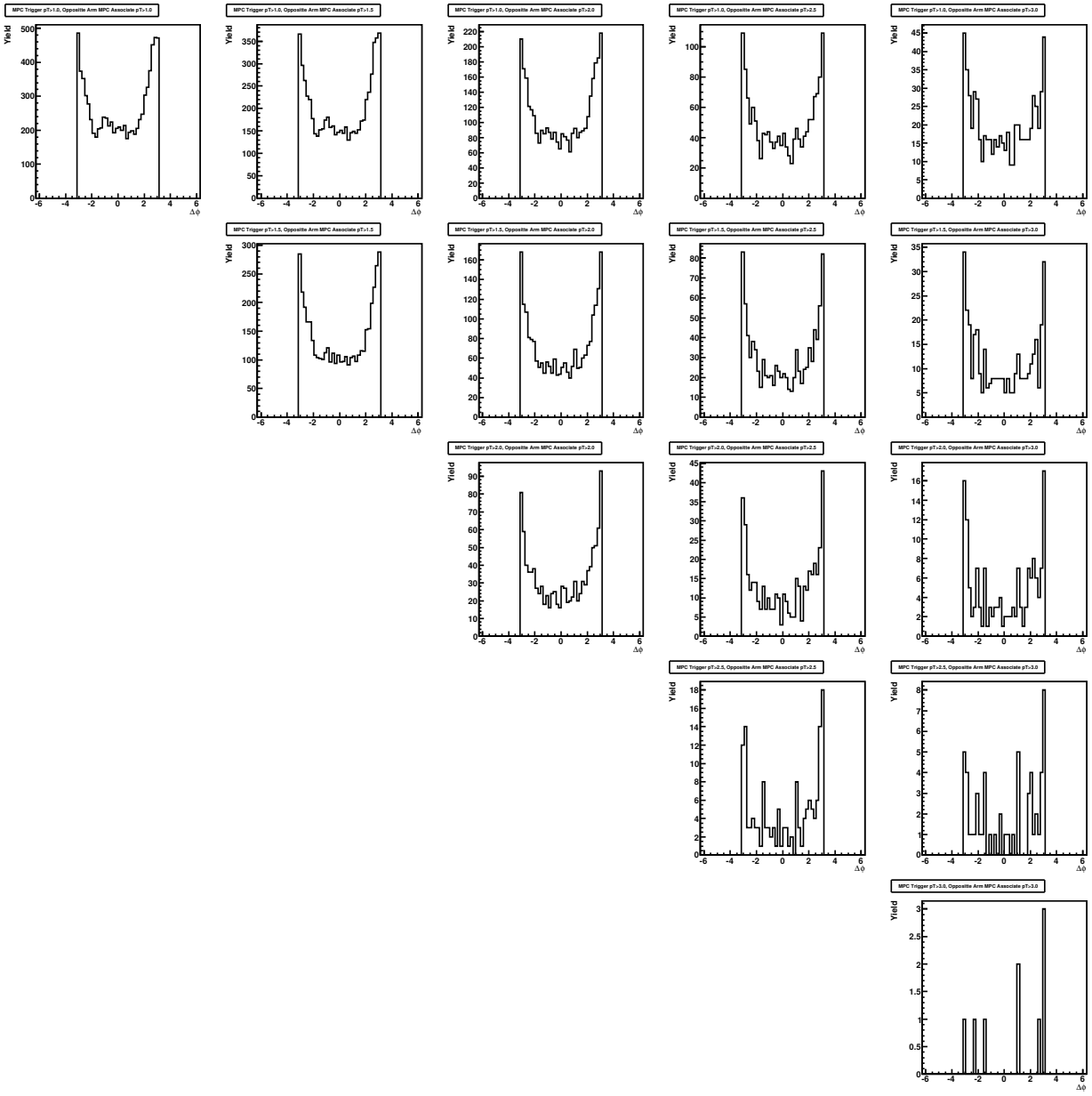

Figure 10.3: Cluster pair azimuthal angle difference distribution between a North or South MPC Trigger cluster and an Associate cluster from the opposite arm. The correlations are shown for different p_T cuts on the trigger and associate particles.

selection of di-clusters and with a two-jet $\Delta\phi$ cut.

The calculation of the double transverse spin asymmetry, A_{TT}, is identical to that of A_{LL}:

$$A_{TT} = \frac{N_{++} - R \cdot N_{+-}}{N_{++} + R \cdot N_{+-}} \tag{10.1}$$

where R is the ratio of luminosities between bunches of like and unlike spin states. The luminosity is estimated using the BBCLL1 GL1-1P scaled trigger. The asymmetries are shown in table 10.2.3

$p_T^{Trigger}$	$p_T^{Associate}$	2South	2South+$\Delta\phi$	2North	2North+$\Delta\phi$	1 Each	1 Each+$\Delta\phi$
1	1	-0.031 ± 0.029	-0.081 ± 0.051	-0.025 ± 0.018	-0.053 ± 0.032	-0.0056 ± 0.05	-0.036 ± 0.074
1	1.5	0.008 ± 0.038	0.0047 ± 0.066	-0.066 ± 0.027	-0.054 ± 0.046	0.002 ± 0.059	-0.015 ± 0.086
1	2	0.046 ± 0.061	0.042 ± 0.11	-0.048 ± 0.044	-0.041 ± 0.075	-0.034 ± 0.081	-0.055 ± 0.12
1	2.5	0.053 ± 0.11	0.085 ± 0.21	-0.042 ± 0.075	0.08 ± 0.13	0.085 ± 0.12	0.2 ± 0.19
1	3	0.12 ± 0.23	0.76 ± 0.98	-0.038 ± 0.13	-0.1 ± 0.27	-0.0017 ± 0.21	-0.11 ± 0.42
1.5	1.5	0.023 ± 0.044	0.021 ± 0.08	-0.068 ± 0.036	-0.058 ± 0.063	0.034 ± 0.071	0.067 ± 0.1
1.5	2	0.04 ± 0.068	-0.015 ± 0.13	-0.033 ± 0.056	-0.014 ± 0.098	0.028 ± 0.1	0.079 ± 0.14
1.5	2.5	0.0056 ± 0.12	0.002 ± 0.23	-0.043 ± 0.091	0.06 ± 0.16	0.25 ± 0.16	0.14 ± 0.26
1.5	3	0.012 ± 0.25	0.59 ± 1	-0.24 ± 0.16	-0.2 ± 0.34	0.27 ± 0.35	0.049 ± 0.72
2	2	0.099 ± 0.095	-0.12 ± 0.19	-0.03 ± 0.084	0.067 ± 0.15	0.057 ± 0.15	0.14 ± 0.23
2	2.5	0.14 ± 0.16	-0.015 ± 0.39	-0.042 ± 0.13	0.088 ± 0.3	0.11 ± 0.28	-0.16 ± 0.55
2	3	-0.14 ± 0.31	-	-0.18 ± 0.23	0.31 ± 1.1	-0.0097 ± 0.75	-
2.5	2.5	0.15 ± 0.25	0.55 ± 1.3	0.017 ± 0.22	-0.48 ± 1.4	-0.59 ± 0.81	-
2.5	3	0.062 ± 0.56	-	-0.52 ± 0.41	-	-	-
3	3	-	-	0.79 ± 1.7	-	-	-

Table 10.1: Double Cluster A_{TT} asymmetry values and statistical errors. 2South, 2North and 1 Each indicate a di-cluster coicidence with no $\Delta\phi$ cut. 2South+$\Delta\phi$, 2North+$\Delta\phi$ and 1 Each+$\Delta\phi$ are the same, but do include the $\Delta\phi$ cut. 2South is two clusters reconstructed in the South arm and 2North is the same, but both reconstructed in the North arm. 1 Each is one cluster reconstructed in the South or North, and the other cluster reconstructed in the opposite arm.

These results are consistent with zero within statistical limits for all combinations or cluster pairs. This is not surprising given the small expected asymmetries and the large error bars, but it is consistent with expectations from the framework of perburbative QCD, factorization and universality.

Chapter 11

Conclusion

The physics reach of the PHENIX detector has been significantly extended by the Muon Piston Calorimeter upgrade. This upgrade is the installation of two electromagnetic calorimeters in the forward region. I have played a leading role in all aspects of the detector from design to data collection and physics analysis.

The calorimeters are used for the analysis of single and double transverse spin asymmetries, A_N and A_{TT}, using an observable - clusters of energy deposits in the MPC - closely linked to neutral pions, but suffering from η meson and direct photon contamination. The single spin asymmetry measurement pushes the measurement of non-zero single spin asymmetries to high p_T in search of the expected $1/p_T$ dependence. The high p_T dependence of A_N is tested with two fits to the asymmetries above a p_T of 3 GeV/c. In both fits, systematic errors are ignored under the assumption that the systematic errors are dominated by scale uncertainties. The first fit checks the consistency of the asymmetries with a constant value. The χ^2/NDF for a fit to a constant is: 7.76 / 3. Therefore, the asymmetries are disfavored at the two sigma level. Future running at RHIC with transversely polarized beams is scheduled for 2012 and 2013. Advances in intensity and polarization are expected to increase the figure of merit for the A_N measurement by roughly a factor of 60. A second fit is carried out following a suggestion by Kang[114] and modified slightly. The motivation is given in his talk and summarized here. In the higher-twist framework, the asymmetries are expected to follow a general pattern of:

$$A_N \approx \frac{\alpha}{p_T} - \frac{\alpha'}{p_T^3} + ... \tag{11.1}$$

Including the two leading terms in the expansion, the asymmetry can be approximated by:

$$A_N \approx \frac{\alpha}{p_T} \frac{1}{1 + \Delta^2/p_T^2} = \alpha \frac{p_T}{p_T^2 + \Delta^2} \tag{11.2}$$

where $\Delta = \alpha'/\alpha$. The form of A_N taken in equation 11.2 is aimed by Kang to provide initial guidance on the form A_N might take in a resummed calculation, including higher orders in the twist expansion. Fitting Kang's function, equation 11.2 multiplied with a scale factor for the MPC asymmetries, does not lead to a good description of the data. However, after including a constant offset of the asymmetry from zero, the

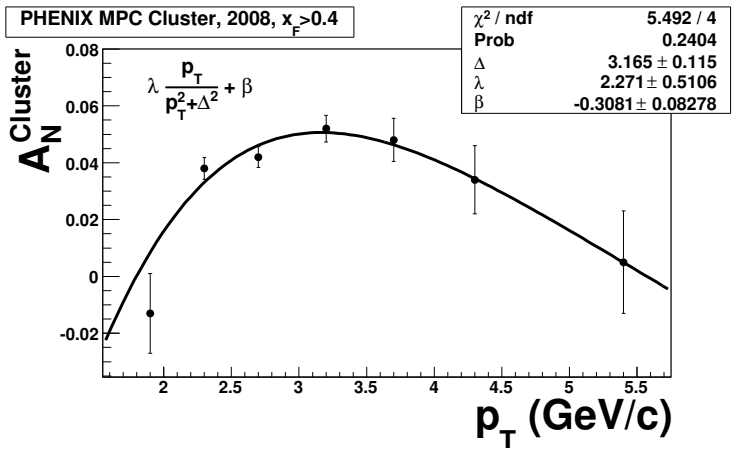

Figure 11.1: MPC cluster single transverse spin asymmetries binned in p_T with an x_F >0.4 threshold cut applied. The fit function is a modified version from Kang[114].

asymmetries are described well. This offset is unphysical (implying a non-zero asymmetry at $p_T = 0$), but is needed for the fit to converge. Despite this limitation, the fit provides a useful parametrization for the asymmetries for $p_T \geq$2 GeV/c. The asymmetries including the fit are shown in figure 11.1.

In addition to the asymmetry measurements with the MPC, the PHENIX central arms were used for asymmetry measurements. Single spin asymmetries for $p^{\uparrow} + p \rightarrow h + X$ at $|\eta|$ <0.35 are reported. The statistical precision compared to the previous PHENIX result[29] is improved by a factor of approximately 30. This analysis repeats and extends the measurement of neutral pions to higher p_T with precision ranging from 6.2 $\cdot 10^{-4}$ to 3.6 $\cdot 10^{-2}$. The asymmetry for η meson is also reported with precision ranging from 4.8 $\cdot 10^{-3}$ to 5.4 $\cdot 10^{-2}$ from low to high p_T. The asymmetries are also measured in the interval 0.2< $|\eta|$ <0.35 for both the π^0 and η meson to probe for non-zero asymmetries. The asymmetries for 0.2$\leq$ $|\eta|$ $\leq$ 0.35 are consistent with zero. The previous PHENIX result was used to impose bounds on the gluon Sivers function[40]. That study can now be repeated in future research using these new precision results to impose further bounds.

Double transverse spin asymmetries are also presented as part of an an exploratory analysis motivated to measuring asymmetries predictable in the framework of perburbative QCD, factorized cross-sections and universality. The transversity distribution has been measured using data from SIDIS and electron-positron annihilation experiments. With improved luminosity and polarization, these double spin asymmetries will become experimentally accessible in proton-proton collisions. At the current level of statistical precision, the $p + p$ data cannot resolve the asymmetry.

11.1 Future Work

At present, proposals for new experiments and theoretical advancements furthering the study of transverse spin physics are proceeding at a rapid pace. Some selected topics are discussed, but it is not an exhaustive review.

- **Jet and Hadron A_N:** The current measurements of single transverse asymmetries in proton-proton collisions are done using $p^{\uparrow} + p \rightarrow h$ where h is a final state hadron. The non-zero hadron asymmetries can be generated by multiple sources elaborated upon in the introduction. If the final state hadron is substituted for a jet, the Collins effect (which relies upon a fragmentation function analyzer to generate the asymmetry) cannot contribute to the jet asymmetry. At PHENIX, the measurement of forward jets does not appear possible. However, proposals to install a hadronic calorimeter at the STAR detector, behind the existing forward electromagnetic calorimeter, are currently under consideration.

- **Drell-Yan Production:** One of the azimuthal modulations in the factorized cross-section for Drell-Yan production in $p^{\uparrow} + p$ is sensitive to Sivers function. It has been shown that in the framework of perburbative QCD and factorization the asymmetry's sign is expected to flip between the Sivers function extracted in Drell-Yan and in semi-inclusive deep inelastic scattering (SIDIS) experiments. This sign change and other transverse spin effects (not discussed in this thesis) are the focus of multiple proposed or approved experiments at Fermilab[115], GSI[116], J-PARC[117], Protvino[118], JINR[119], CERN[120] and RHIC[121, 122, 123]. In addition, the sign change may also be measured using proton spin correlations in direct-photon and jet production. However, recent simulation studies have shown this to be an experimentally challenging channel at PHENIX.

- **Jefferson Laboratory 12 GeV Upgrade:** A parallel and complementary experimental program to the the $p^{\uparrow} + p$ experiments discussed in this thesis, is SIDIS at CERN, DESY and Jefferson Laboratory. The high-luminosity electron beams of the CEBAF accelerator at Jefferson Laboratory are currently being upgraded from 6 GeV to 12 GeV. Several experiments measuring transverse momentum dependent observables are planned.

- **Electron Ion Collider:** The existing and soon-to-be existing polarized SIDIS experiments use a lepton beam and a polarized hadronic fixed target. The proposed Electron Ion Collider (EIC) project plans to collide, for the first time, beams of polarized electrons and polarized light ions. This experimental facility will continue and extend the existing measurements to higher values of center of mass energies and higher Q^2, where effects from sub-leading twist and target mass corrections are suppressed.

- **Fragmentation Functions:** Fragmentation functions (FF) play an important role in the determination of polarized distribution functions. The FF's are often required as analyzers to a theoretical extraction of the polarized distributions. FF's can be extracted from $p + p$ collisions, SIDIS and $e^+ + e^-$ annihilation. The BELLE experiment at the $e^+ + e^-$ KEK B-factory has already measured the charged pion spin-dependent Collins fragmentation function[33] and Interference fragmentation functions[124]. In the case of the published Collins asymmetries, the results have already been used as part of an extraction of the transversity distribution[111, 112]. There are many possibilities for future measurements at BELLE. Present theoretical work with transverse momentum dependent fragmentation functions assume a Gaussian shape for the p_T relative to the jet-axis. At BELLE the dataset is large enough to explicitly measure the p_T dependence of both the Collins polarized fragmentation function and the unpolarized fragmentation function. In addition, the existing measurements of the the Collins and Interference fragmentation functions with pions may be extended to neutral pions, η mesons and charged hadrons to better understand measurements from $p + p$ and SIDIS.

Appendix A

MPC

A.1 Channel Maps

The MPC channel mapping relating the tower identifier (fee576ch) to the physical position is shown in figure A.1.

A.2 Confirmation of Channel Mapping

Each tower is assigned a physical location in the reconstruction code. While the cables connecting each tower to its channel in the front end electronics are carefully checked for consistency, it is reassuring to check that the channel mapping is correct using data. The data method exploits energy deposition pattern from electromagnetic showers. If a photon deposits a large energy in a tower j, the electromagnetic shower will spread to its neighbors, depositing energy in them as well. Therefore, the analysis measures the conditional probability $P(i|j)$ for a tower i containing an energy deposit of 3 GeV or more, given that tower j has an energy deposit of 10 GeV or more. If towers i and j are neighbors the conditional probability will be high, and if they are not neighbors it will be low. For each tower, j, a plot is generated with the conditional probabilities for all other towers. The plot is drawn in the grid space of the previous section to clearly illustrate the effect. Two example plots are shown in figure A.2.

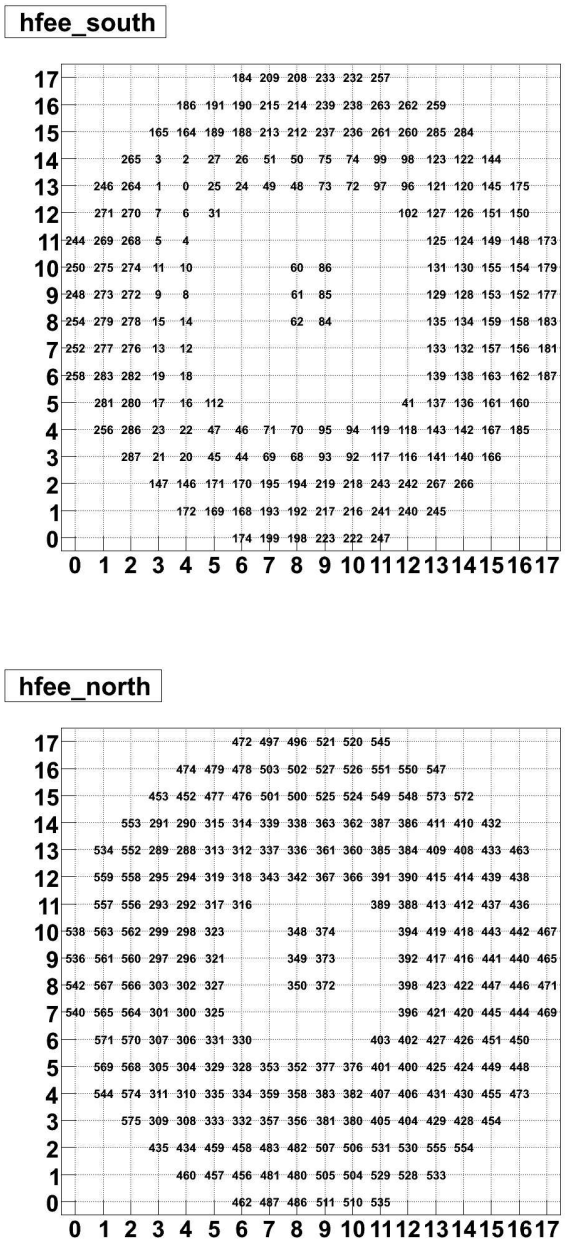

Figure A.1: The MPC towers arranged in a rectilinear grid. In reality, there are small shifts away from the grid. The number at the center of each square is the tower identifier, called "Fee576ch". Towers in the center of the detector are PIN diode channels, and are are arranged in their order from top to bottom of the detector.

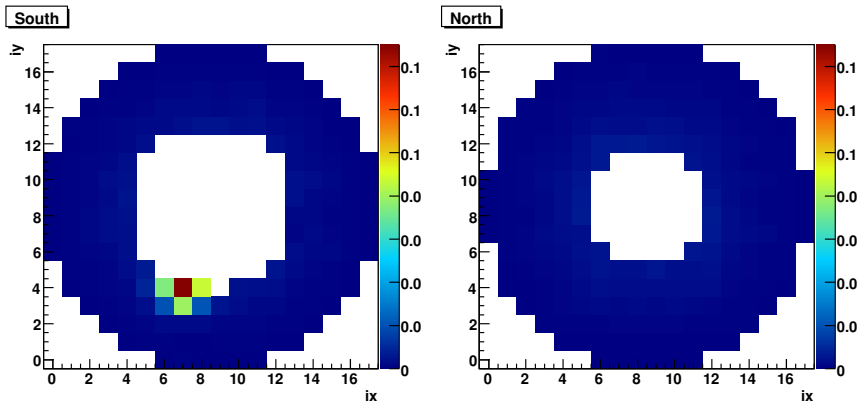

(a) Tower j is located in the South Arm (ix,iy)=(7,4)

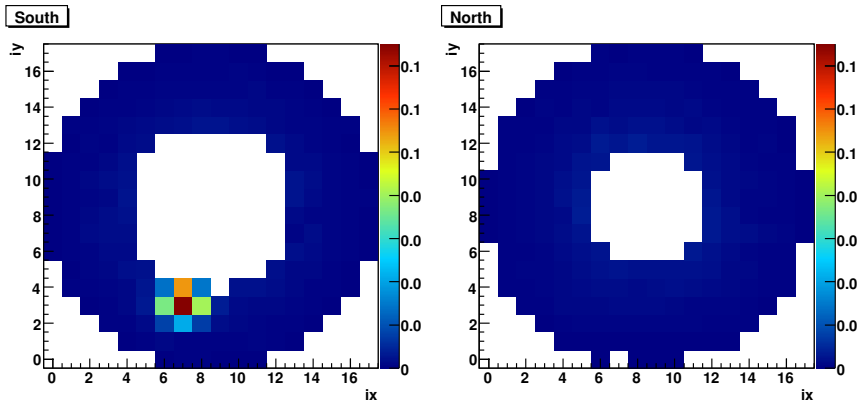

(b) Tower j is located in the South Arm (ix,iy)=(7,3)

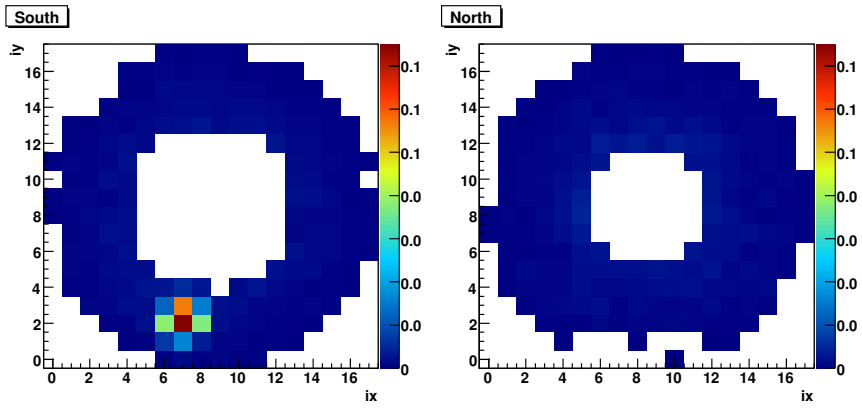

(c) Tower j is located in the South Arm (ix,iy)=(7,2)

Figure A.2: Z-axis: Conditional probabilities, $P(i|j)$, for tower i to contain more than 3 GeV given that tower j contains more than 10 GeV. Three sample towers are used for tower j. The fullscale of the z-axis goes to one since $P(j|j) \equiv 1$, but it is set to 15% to better see the neighboring tower's conditional probabilities.

Appendix B

Selected Engineering Drawings

B.1 Beampipe and Related Hardware

Richard Ruggiero, Donald Lynch and the Brookhaven Collider Accelerator Department maintain the archive of beampipe drawings. It is important to realize that the beampipe was replaced during the shutdown of summer 2010. All drawings are of the first beampipe assembly. The drawings are drawn from reference [125].

B.1.1 Overview

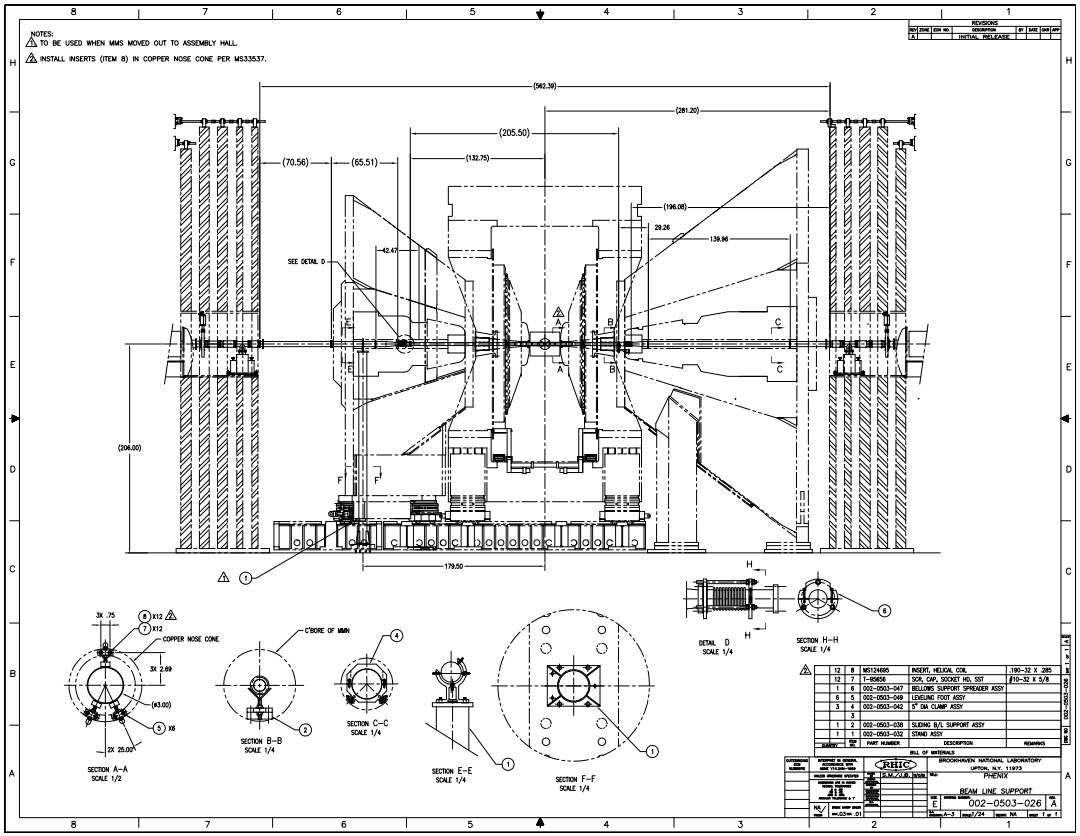

Figure B.1: Overview of the beampipe in PHENIX. Some components are in place for only a single muon arm and should be ignored.

B.1.2 South Flange, Bellows and Spreader

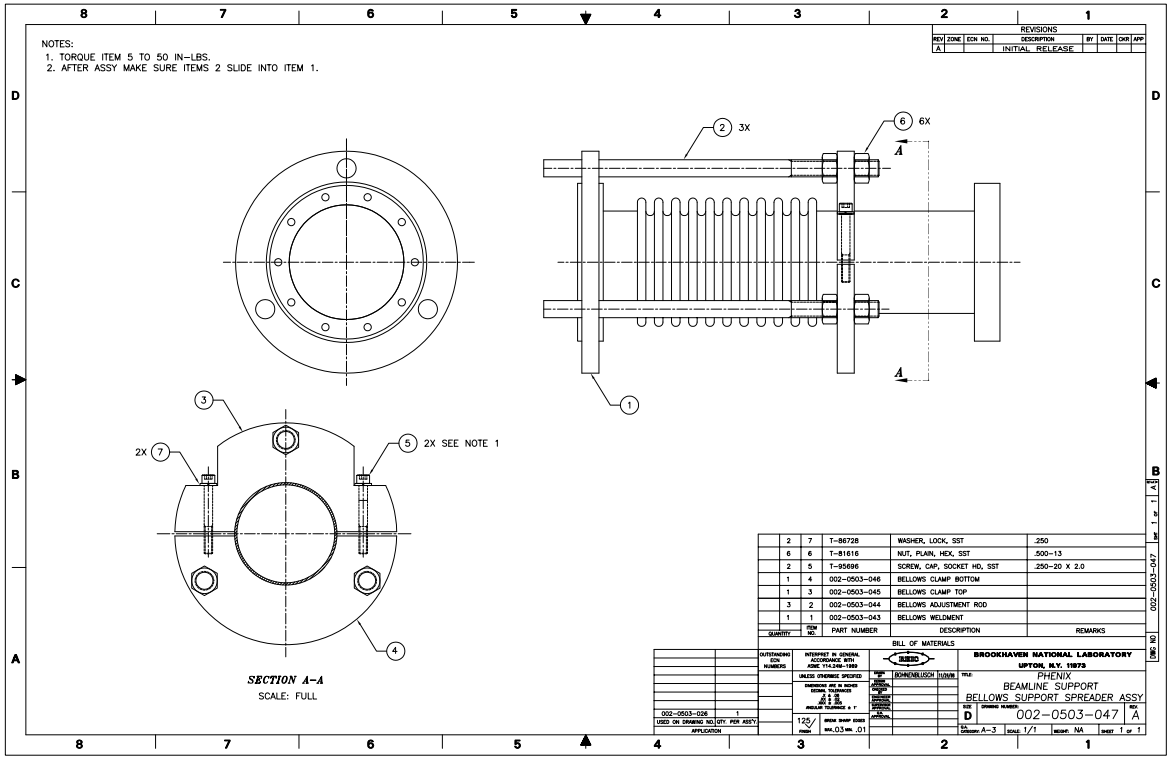

Figure B.2: Overall assembly of the flange, bellows and spreader on the South beampipe. The two spreader plates determine the south keep-out radius.

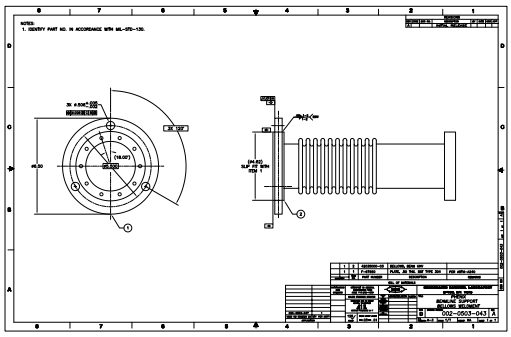

(a) Flange and bellows.

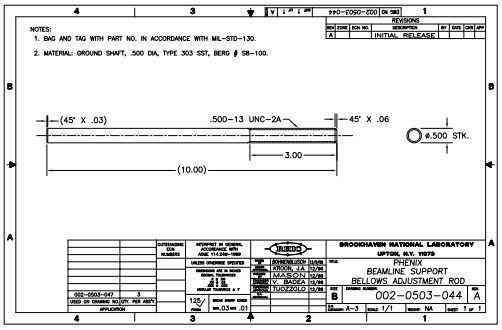

(b) Spreader rod

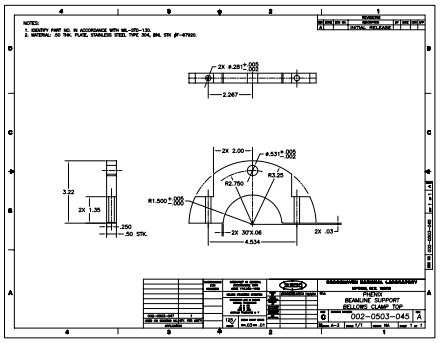

(c) Top spreader plate.

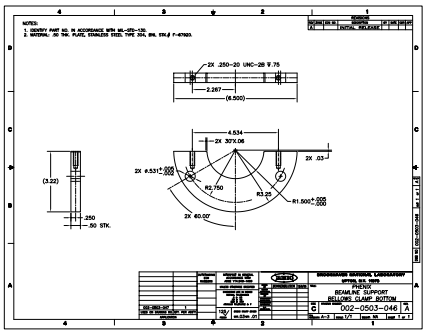

(d) Bottom spreader plate.

B.1.3 North Beampipe Support

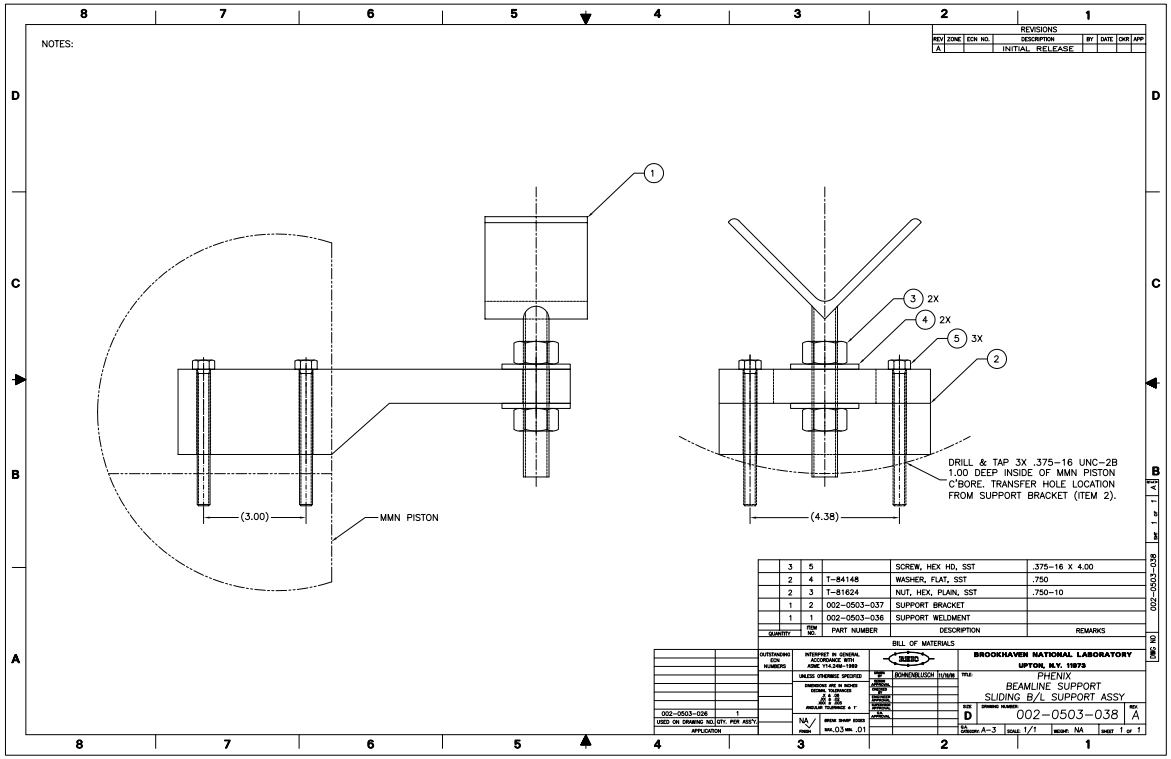

Figure B.3: Overall assembly of the North beampipe support. The transition piece is similar to the south, but without the spreaders.

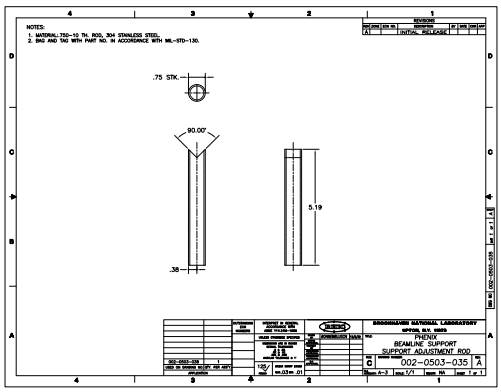

(a) Beamblock support rod.

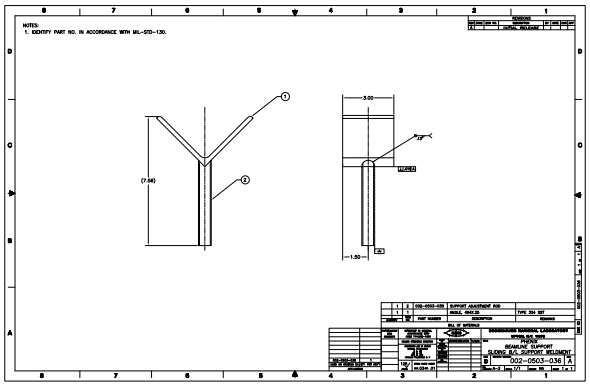

(b) Beampipe support rod.

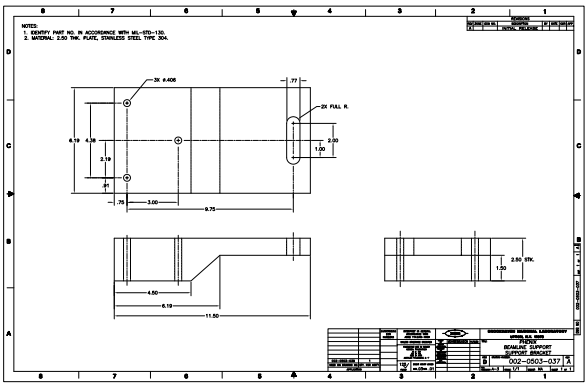

(c) Beampipe support block.

B.2 South MPC

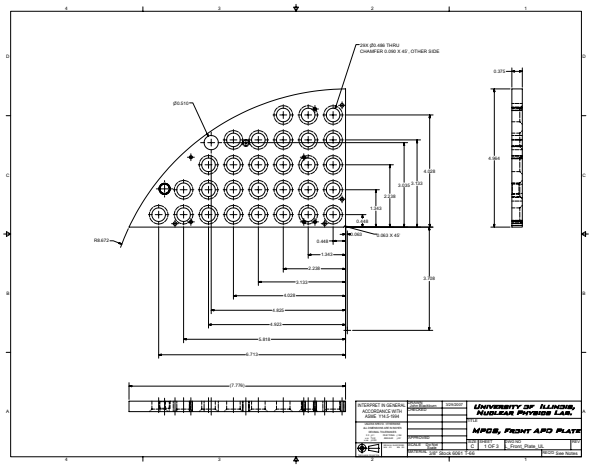

(d) Frontplate

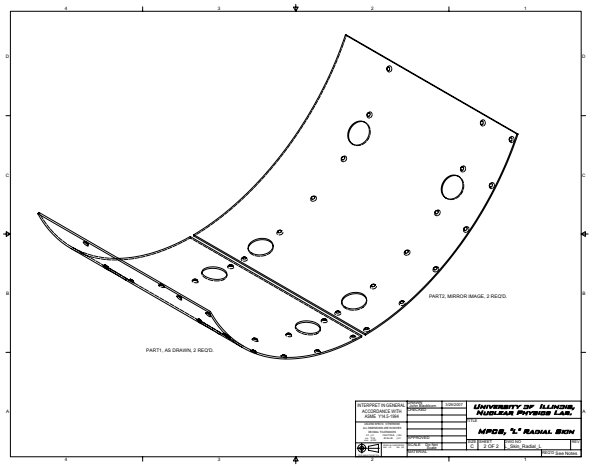

(e) Outer skin for "L" module

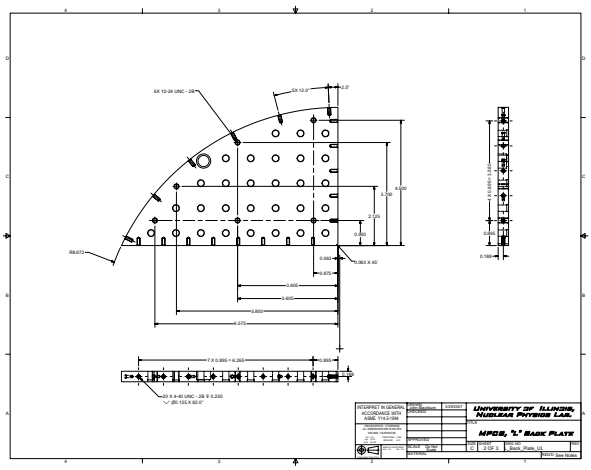

(f) Backplate

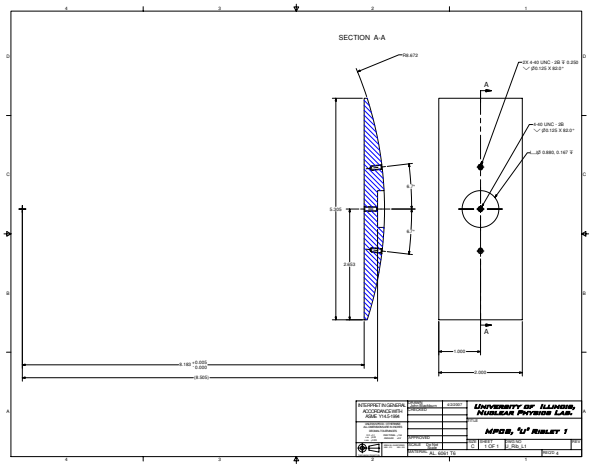

(g) Rib for "L" module

B.3 North MPC

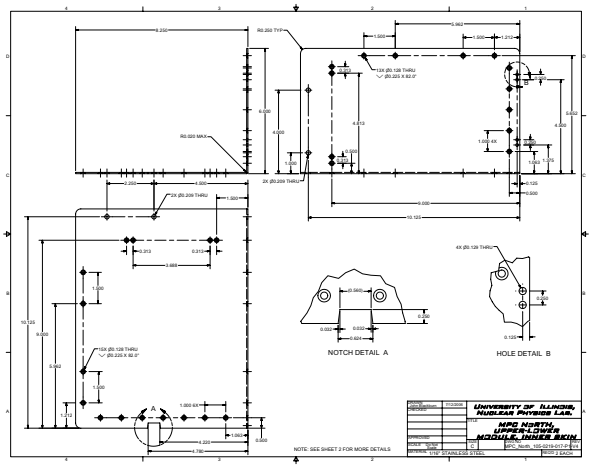

(h) Inner skin for "L" module.

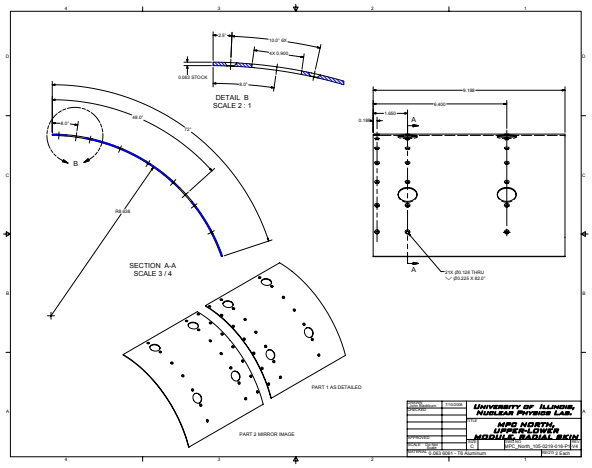

(i) Outer skin for "L" module.

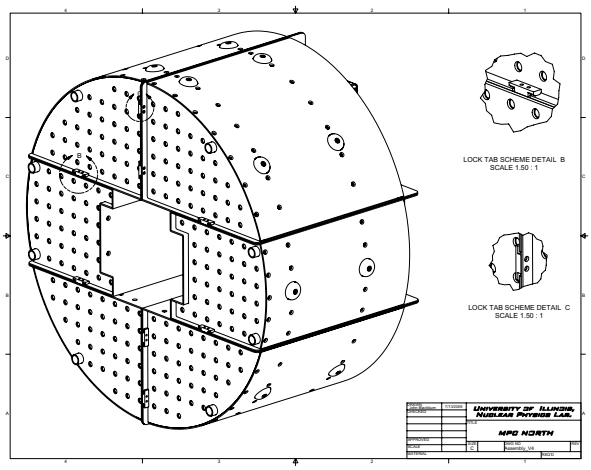

(j) Illustration of locking tab mechanism which locks the detector modules together at the far end of the muon piston bore.

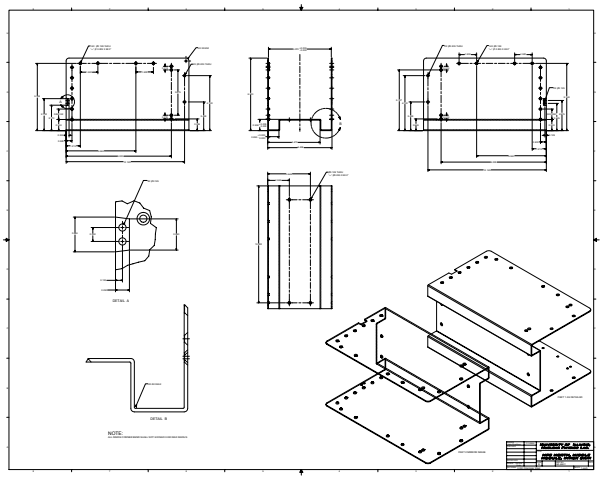

(k) Inner skin for "U" module.

B.4 MPC Monitoring System

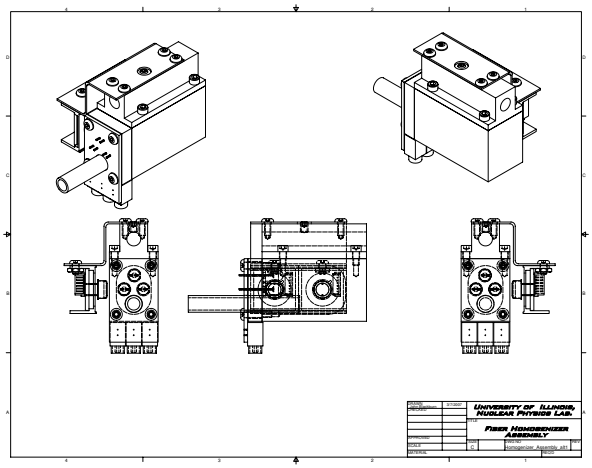

(l) Overall assembly.

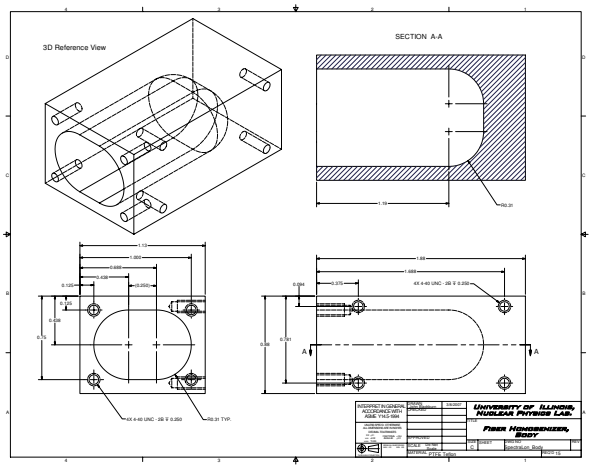

(m) Homogenizer Body.

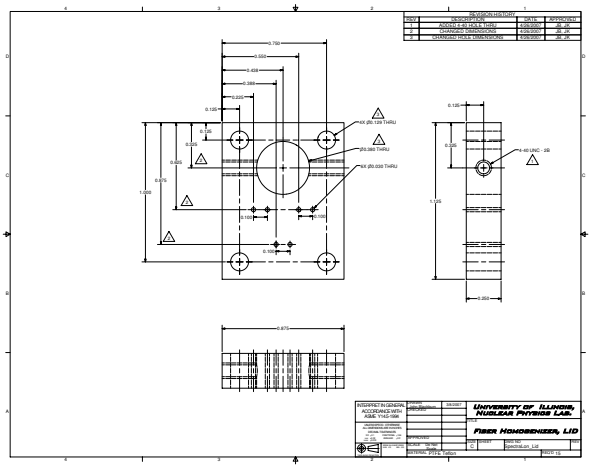

(n) Homogenizer Lid.

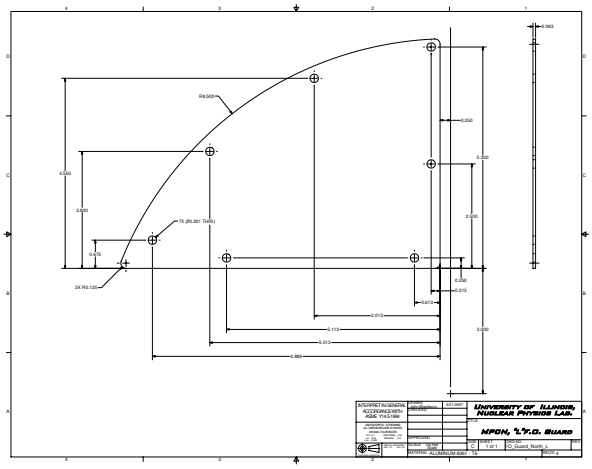

(o) Fiber optic guard for north "L" module.

References

[1] T. D. Lee and C.-N. Yang, "Question of Parity Conservation in Weak Interactions," *Phys. Rev.*, vol. 104, pp. 254–258, 1956.

[2] C. S. Wu, E. Ambler, R. W. Hayward, D. D. Hoppes, and R. P. Hudson, "Experimental Test of Parity Conservation in Beta Decay," *Phys. Rev.*, vol. 105, pp. 1413–1414, 1957.

[3] P. M. Nadolsky *et al.*, "Implications of CTEQ global analysis for collider observables," *Phys. Rev.*, vol. D78, p. 013004, 2008.

[4] C. Bourrely and J. Soffer, "Do we understand the single-spin asymmetry for π^0 inclusive production in p p collisions?," *Eur. Phys. J.*, vol. C36, pp. 371–374, 2004.

[5] D. de Florian, W. Vogelsang, and F. Wagner, "Single-Inclusive Hadron Production in Polarized pp Scattering at Next-to-Leading Logarithmic Accuracy," *Phys. Rev.*, vol. D76, p. 094021, 2007.

[6] T. Sjostrand, S. Mrenna, and P. Z. Skands, "PYTHIA 6.4 Physics and Manual," *JHEP*, vol. 05, p. 026, 2006.

[7] M. Hirai, S. Kumano, and N. Saito, "Determination of polarized parton distribution functions with recent data on polarization asymmetries," *Phys. Rev.*, vol. D74, p. 014015, 2006.

[8] D. de Florian, R. Sassot, M. Stratmann, and W. Vogelsang, "Global Analysis of Helicity Parton Densities and Their Uncertainties," *Phys. Rev. Lett.*, vol. 101, p. 072001, 2008.

[9] J. Blumlein and H. Bottcher, "QCD analysis of polarized deep inelastic scattering data and parton distributions," *Nucl. Phys.*, vol. B636, pp. 225–263, 2002.

[10] T. Gehrmann and W. J. Stirling, "Polarized Parton Distributions in the Nucleon," *Phys. Rev.*, vol. D53, pp. 6100–6109, 1996.

[11] D. de Florian, R. Sassot, M. Stratmann, and W. Vogelsang, "Extraction of Spin-Dependent Parton Densities and Their Uncertainties," *Phys. Rev.*, vol. D80, p. 034030, 2009.

[12] G. L. Kane, J. Pumplin, and W. Repko, "Transverse Quark Polarization in Large p(T) Reactions, e+ e- Jets, and Leptoproduction: A Test of QCD," *Phys. Rev. Lett.*, vol. 41, p. 1689, 1978.

[13] W. Dragoset, J. Roberts, J. Bowers, H. Courant, H. Kagan, *et al.*, "Asymmetries in Inclusive Proton-Nucleon Scattering at 11.75-GeV/c," *Phys.Rev.*, vol. D18, pp. 3939–3954, 1978.

[14] C. Allgower, K. Krueger, T. Kasprzyk, H. Spinka, D. G. Underwood, *et al.*, "Measurement of analyzing powers of pi+ and pi- produced on a hydrogen and a carbon target with a 22-GeV/c incident polarized proton beam," *Phys.Rev.*, vol. D65, p. 092008, 2002.

[15] J. Antille, L. Dick, L. Madansky, D. Perret-Gallix, M. Werlen, *et al.*, "SPIN DEPENDENCE OF THE INCLUSIVE REACTION p p (POLARIZED) $\rightarrow \pi^0$ X AT 24-GeV/c FOR HIGH $p_T\pi^0$ PRODUCED IN THE CENTRAL REGION," *Phys.Lett.*, vol. B94, p. 523, 1980.

[16] S. Saroff, B. Baller, G. Blazey, H. Courant, K. J. Heller, *et al.*, "SINGLE SPIN ASYMMETRY IN INCLUSIVE REACTIONS polarized P, P GOES TO pi+, pi-, AND P AT HIGH P(t) AT 13.3-GeV/c AND 18.5-GeV/c," *Phys.Rev.Lett.*, vol. 64, p. 995, 1990.

[17] V. Apokin, Y. Arestov, O. Astafev, N. Belikov, B. Chuiko, *et al.*, "Observation of significant spin effects in hard collisions at 40-GeV/c," *Phys.Lett.*, vol. B243, pp. 461–464, 1990.

[18] D. Adams *et al.*, "High x_t single spin asymmetry in π^0 and eta production at $x_F = 0$ by 200-GeV polarized anti-protons and protons," *Phys.Lett.*, vol. B276, pp. 531–535, 1992.

[19] D. Adams *et al.*, "Comparison of spin asymmetries and cross-sections in π^0 production by 200-GeV polarized anti-protons and protons," *Phys.Lett.*, vol. B261, pp. 201–206, 1991.

[20] D. Adams *et al.*, "Analyzing power in inclusive pi+ and pi- production at high x_F with a 200-GeV polarized proton beam," *Phys.Lett.*, vol. B264, pp. 462–466, 1991.

[21] A. Bravar *et al.*, "Single spin asymmetries in inclusive charged pion production by transversely polarized anti-protons," *Phys.Rev.Lett.*, vol. 77, pp. 2626–2629, 1996.

[22] D. Adams *et al.*, "Large x_F spin asymmetry in π^0 production by 200-GeV polarized protons," *Z.Phys.*, vol. C56, pp. 181–184, 1992.

[23] D. Adams *et al.*, "Single spin asymmetries and invariant cross-sections of the high transverse momentum inclusive π^0 production in 200-GeV/c p p and anti-p p interactions," *Phys.Rev.*, vol. D53, pp. 4747–4755, 1996.

[24] D. Adams *et al.*, "Measurement of single spin asymmetry for direct photon production in p p collisions at 200-GeV/c," *Phys.Lett.*, vol. B345, pp. 569–575, 1995.

[25] D. Adams *et al.*, "Measurement of single spin asymmetry in eta meson production in p (polarized) p and anti-p (polarized) p interactions in the beam fragmentation region at 200-GeV/c," *Nucl.Phys.*, vol. B510, pp. 3–11, 1998.

[26] M. Chiu, "Single spin transverse asymmetries of neutral pions at forward rapidities in $\sqrt{s} = 62.4$-GeV polarized proton collisions in PHENIX," *AIP Conf. Proc.*, vol. 915, pp. 539–542, 2007.

[27] M. Chiu *et al.*, "PHENIX Analysis Note 596, Neutral Pion Single Spin Asymmetries with the MPC in $p^{\uparrow}$+p collisions at 62 GeV,"

[28] B. I. Abelev *et al.*, "Forward Neutral Pion Transverse Single Spin Asymmetries in p+p Collisions at $\sqrt{s}$=200 GeV," *Phys. Rev. Lett.*, vol. 101, p. 222001, 2008.

[29] S. S. Adler *et al.*, "Measurement of transverse single-spin asymmetries for mid- rapidity production of neutral pions and charged hadrons in polarized p + p collisions at $\sqrt{s} = 200$-GeV," *Phys. Rev. Lett.*, vol. 95, p. 202001, 2005.

[30] I. Arsene *et al.*, "Single Transverse Spin Asymmetries of Identified Charged Hadrons in Polarized p+p Collisions at $\sqrt{s} = 62.4$ GeV," *Phys. Rev. Lett.*, vol. 101, p. 042001, 2008.

[31] D. W. Sivers, "Hard scattering scaling laws for single spin production asymmetries," *Phys. Rev.*, vol. D43, pp. 261–263, 1991.

[32] J. C. Collins, "Fragmentation of transversely polarized quarks probed in transverse momentum distributions," *Nucl. Phys.*, vol. B396, pp. 161–182, 1993.

[33] R. Seidl *et al.*, "Measurement of Azimuthal Asymmetries in Inclusive Production of Hadron Pairs in e^+e^- Annihilation at $\sqrt{s} = 10.58$ GeV," *Phys. Rev.*, vol. D78, p. 032011, 2008.

[34] A. V. Efremov and O. V. Teryaev, "On Spin Effects in Quantum Chromodynamics," *Sov. J. Nucl. Phys.*, vol. 36, p. 140, 1982.

[35] A. V. Efremov and O. V. Teryaev, "QCD Asymmetry and Polarized Hadron Structure Functions," *Phys. Lett.*, vol. B150, p. 383, 1985.

[36] J.-W. Qiu and G. F. Sterman, "Single transverse-spin asymmetries in hadronic pion production," *Phys. Rev.*, vol. D59, p. 014004, 1999.

[37] Y. Kanazawa and Y. Koike, "Chiral-odd contribution to single-transverse spin asymmetry in hadronic pion production," *Phys. Lett.*, vol. B478, pp. 121–126, 2000.

[38] K. Kanazawa and Y. Koike, "New Analysis of the Single Transverse-Spin Asymmetry for Hadron Production at RHIC," 2010.

[39] X. Ji, J.-W. Qiu, W. Vogelsang, and F. Yuan, "A unified picture for single transverse-spin asymmetries in hard processes," *Phys. Rev. Lett.*, vol. 97, p. 082002, 2006.

[40] M. Anselmino, U. D'Alesio, S. Melis, and F. Murgia, "Constraints on the gluon Sivers distribution via transverse single spin asymmetries at midrapidity in $p(transv.polarized)p \to \pi^0 X$ processes at BNL RHIC," *Phys. Rev.*, vol. D74, p. 094011, 2006.

[41] J. J. Aubert *et al.*, "The ratio of the nucleon structure functions $F2_n$ for iron and deuterium," *Phys. Lett.*, vol. B123, p. 275, 1983.

[42] I. Arsene *et al.*, "On the evolution of the nuclear modification factors with rapidity and centrality in d + Au collisions at $\sqrt{s_{NN}}$ = 200-GeV," *Phys. Rev. Lett.*, vol. 93, p. 242303, 2004.

[43] S. S. Adler *et al.*, "Nuclear modification factors for hadrons at forward and backward rapidities in deuteron gold collisions at $\sqrt{s_{NN}}$ = 200-GeV," *Phys. Rev. Lett.*, vol. 94, p. 082302, 2005.

[44] S. S. Adler *et al.*, "Azimuthal angle correlations for rapidity separated hadron pairs in d + Au collisions at $\sqrt{s_{NN}}$ = 200-GeV," *Phys. Rev. Lett.*, vol. 96, p. 222301, 2006.

[45] I. Alekseev *et al.*, "Polarized proton collider at RHIC," *Nucl. Instrum. Meth.*, vol. A499, pp. 392–414, 2003.

[46] A. Zelenski, "Polarized Sources at RHIC." Talk at 2007 RHIC/AGS User Meeting.

[47] A. Zelenski, J. G. Alessi, A. Kponou, and D. Raparia, "High-Intensity Polarized H- (Proton), Deuteron and 3He++ Ion Source Development at BNL," EPAC'08, 11th European Particle Accelerator Conference, 23-27 June 2008, Genoa, Italy.

[48] Brookhaven National Laboratory - Collider Accelerator Department, "RHIC Run Overview," June 2010. `http://www.agsrhichome.bnl.gov/RHIC/Runs/`.

[49] A. Kponou, A. Zelenski, S. Kokhanovski, and V. Zubets, "Sona transition studies in the RHIC OPPIS," *AIP Conf. Proc.*, vol. 980, pp. 241–247, 2008.

[50] A. Zelenski, S. Kokhanovsky, A. Kponou, J. Ritter, and V. Zubets, "The RHIC optically-pumped polarized H- ion source," *AIP Conf. Proc.*, vol. 980, pp. 221–230, 2008.

[51] A. Zelenski *et al.*, "Absolute polarized H-jet polarimeter development for RHIC," *Nucl. Instrum. Meth.*, vol. A536, pp. 248–254, 2005.

[52] H. Okada (Iinuma), *Measurement of the Analyzing Power A_N in pp Elastic Scattering in the CNI Region with a Polarized Atomic Hydrogen Gas Jet Target*. PhD thesis, Kyoto University, 2007.

[53] H. Huang *et al.*, "Commissioning of RHIC p carbon CNI polarimeter," *Nucl. Phys.*, vol. A721, pp. 356–359, 2003.

[54] M. Togawa, *Measurements of the leading neutron production in polarized pp collision at $\sqrt{s}$=200 GeV*. PhD thesis, Kyoto University, 2009.

[55] A. Bazilevsky *et al.*, "Single transverse-spin asymmetry in very forward and very backward neutral particle production for polarized proton collisions at $\sqrt{s}$=200 GeV," *Phys. Lett.*, vol. B650, pp. 325–330, 2007.

[56] C. Adler, A. Denisov, E. Garcia, M. J. Murray, H. Strobele, and S. N. White, "The RHIC zero degree calorimeters," *Nucl. Instrum. Meth.*, vol. A470, pp. 488–499, 2001.

[57] H. Akikawa *et al.*, "PHENIX muon arms," *Nucl. Instrum. Meth.*, vol. A499, pp. 537–548, 2003.

[58] S. H. Aronson *et al.*, "PHENIX magnet system," *Nucl. Instrum. Meth.*, vol. A499, pp. 480–488, 2003.

[59] K. Adcox *et al.*, "PHENIX central arm tracking detectors," *Nucl. Instrum. Meth.*, vol. A499, pp. 489–507, 2003.

[60] M. Aizawa *et al.*, "PHENIX central arm particle ID detectors," *Nucl. Instrum. Meth.*, vol. A499, pp. 508–520, 2003.

[61] L. Aphecetche *et al.*, "The PHENIX calorimeter," *Nucl. Instrum. Meth.*, vol. A499, pp. 521–536, 2003.

[62] A. Bazilevsky *et al.*, "PHENIX PbGl Cluster Identification," *PHENIX Technical Note: 386*.

[63] G. David *et al.*, "Pattern recognition in the PHENIX PbSc electromagnetic calorimeter," *IEEE Trans. Nucl. Sci.*, vol. 47, pp. 1982–1986, 2000.

[64] K. Imai, "Possible Polarimetry at Collision Point (PHENIX)," in *RHIC Spin Meeting*, August 1999. `http://spin.riken.bnl.gov/rsc/write-up/Imai/imai1.html`.

[65] M. Chiu *et al.*, "Muon Piston Calorimeter," *PHENIX Letter of Intent*, 2005. `https://www.phenix.bnl.gov/WWW/p/draft/chiu/mpc/MPC_LOI_v3.pdf`.

[66] E. Segre, *Nuclei and Particles*. 1977.

[67] R. Fernow, *Introduction to experimental particle physics*. 1990.

[68] C. W. Fabjan and T. Ludlam, "Calorimetry in High-Energy Physics," *Ann. Rev. Nucl. Part. Sci.*, vol. 32, pp. 335–389, 1982.

[69] C. W. Fabjan and F. Gianotti, "Calorimetry for particle physics," *Rev. Mod. Phys.*, vol. 75, pp. 1243–1286, 2003.

[70] B. Martin and G. Shaw, *Particle Physics*. 1990.

[71] F. Berger *et al.*, "Particle identification in modular electromagnetic calorimeters," *Nucl. Instrum. Meth.*, vol. A321, pp. 152–164, 1992.

[72] A. A. Lednev, "Separation of the overlapping electromagnetic showers in the cellular GAMS type calorimeters," IFVE-93-153.

[73] A. A. Lednev, "Electron shower transverse profile measurement," *Nucl. Instrum. Meth.*, vol. A366, pp. 292–297, 1995.

[74] R. Y. Zhu *et al.*, "A Study on the properties of lead tungstate crystals," *Nucl. Instrum. Meth.*, vol. A376, pp. 319–334, 1996.

[75] M. Ippolitov *et al.*, "Lead tungstate crystals for the ALICE/CERN experiment," *Nucl. Instrum. Meth.*, vol. A537, pp. 353–356, 2005.

[76] M. Ippolitov *et al.*, "Studies of lead tungstate crystals for the ALICE electromagnetic calorimeter PHOS," *Nucl. Instrum. Meth.*, vol. A486, pp. 121–125, 2002.

[77] P. A. Semenov *et al.*, "First study of radiation hardness of lead tungstate crystals at low temperatures," *Nucl. Instrum. Meth.*, vol. A582, pp. 575–580, 2007.

[78] R. W. Novotny *et al.*, "Radiation hardness and recovery processes of PWO crystals at -25-degrees C," *IEEE Trans. Nucl. Sci.*, vol. 55, pp. 1283–1288, 2008.

[79] S. Burachas *et al.*, "Temperature dependence of radiation hardness of lead tungstate (PWO) scintillation crystals," *Radiat. Meas.*, vol. 45, pp. 83–88, 2010.

[80] Toyoda Gosei, "LED E1L51-3B0A2-02."

[81] Hamamatsu Photonics, "Si PIN photodiode S1233 Series."

[82] E. Specht, "Packomania," March 2010. `http://hydra.nat.uni-magdeburg.de/packing/`.

[83] CAD Cut Incoporated. `www.cadcut.com`, 116 Three Mile Bridge Road, Middlesex, VT, 05602.

[84] Harlan and Lash Machining, Inc. `http://hlmachining.com`, 1302 Parkland Ct., Champaign, IL 61821.

[85] Precision Tooling and Die Co. 445 West Main Street, Mount Zion, IL 62549.

[86] S. S. Adler *et al.*, "PHENIX on-line systems," *Nucl. Instrum. Meth.*, vol. A499, pp. 560–592, 2003.

[87] A. Bazilevsky, E. Kistenev, and M. Volkov, "PHENIX PbGl Cluster Identification," PHENIX Technical Note 385.

[88] E. Ramberg *et al.*, "Fermilab Test Beam Facility." `http://www-ppd.fnal.gov/MTBF-w/`.

[89] J. Koster, M. Chiu, and A. Kazantsev, "PHENIX Technical Note 440, MPC Run08 Monitoring System," `http://www.phenix.bnl.gov/WWW/publish/jkoster4/note/led_writeup/`.

[90] A. Bazilevsky, B. Fox, Y. Goto, K. Okada, and H. Torii, "Updated Absolute Cross Section for Neutral Pion Production in Proton-Proton Collisions at *sqrts*=200 GeV with the PbSc Calorimeter," PHENIX Analysis Note 176.

[91] M. Chiu, M. Große Perdekamp, J. Koster, M. Meredith, and S. Wolin, "PHENIX Analysis Note 927, MPC Calibration,"

[92] H. Spinka, "Note on RHIC polarimetry," ANL-HEP-TR-99-113.

[93] T. Kempel, J. Lajoie, and F. Wei, "Formulae for Single Transverse Spin Asymmetries in Limited Acceptance," PHENIX Analysis Note 753.

[94] S. Dairaku, J. Koster, and Y. Goto, "PHENIX Analysis Note 929, PHENIX Local Polarimeter Analysis in Polarized proton-proton Collisions at $\sqrt{s}$=200 GeV from RHIC Run-6 and Run-8,"

[95] A. Vossen and J. Koster, "PHENIX Analysis Note to be submitted, Mpc Cluster Decomposition,"

[96] J. Koster, M. Chiu, and M. Große Perdekamp, "PHENIX Analysis Note 823, Cluster Single Spin Asymmetries with the MPC in $p^{\uparrow} + p$ collisions at 200 GeV,"

[97] P. Skands. `http://home.fnal.gov/~skands/leshouches-plots/LHPlotsFrontpage.html`.

[98] A. Adare *et al.*, "Inclusive cross section and double helicity asymmetry for π^0 production in p+p collisions at $\sqrt{s}$=200 GeV: Implications for the polarized gluon distribution in the proton," *Phys. Rev.*, vol. D76, p. 051106, 2007. `http://www.phenix.bnl.gov/phenix/WWW/info/data/ppg063_data.html`.

[99] R. Bennet and K. Okada, "Run-6 Direct Photon Double Longitudinal Spin Asymmetry Measurement," Run5 subtraction method, table 4.

[100] J. Adams *et al.*, "Forward neutral pion production in p+p and d+Au collisions at $\sqrt{s}$=200 GeV," *Phys. Rev. Lett.*, vol. 97, p. 152302, 2006. `http://drupal.star.bnl.gov/STAR/files/starpublications/62/data.html`.

[101] I. Arsene *et al.*, "Production of Mesons and Baryons at High Rapidity and High p_T in Proton-Proton Collisions at $\sqrt{s}$=200 GeV," *Phys. Rev. Lett.*, vol. 98, p. 252001, 2007.

[102] S. Heppelmann, "Measurement of Transverse Single Spin Asymmetry A_N in Eta Mass Region at Large Feynman x_F with the STAR Forward Pion Detector," 2009.

[103] A. Boyle, K. Bazilevsky, A. Deshpande, and Y. Fukao, "PHENIX Analysis Note 567, Results on invariant cross section and double helicity asymmetry (A_{LL}) in pi^0 production in polarized proton-proton collision at $sqrts = 200$ GeV from Run5,"

[104] K. Boyle, A. Bazilevsky, and A. Deshpande, "PHENIX Analysis Note 602, Results on the double helicity asymmetry (A_{LL}) in pi^0 production in polarized proton-proton collision at $sqrts = 200$ GeV from Run-6,"

[105] J. Seele, F. Ellinghaus, and D. Kinney, "PHENIX Analysis Note 649, Double Helicity Asymmetry of Mid-rapidity *eta* Mesons in Run-6 p+p at $sqrts = 200$GeV,"

[106] J. Koster *et al.*, "PHENIX Technical Note 442, Run08 Central Arm EMC Time of Flight Calibration," `http://www.phenix.bnl.gov/WWW/publish/jkoster4/note/TNToF/`.

[107] J. Koster, S. Hu, X. Li, M. Große Perdekamp, R. Yang, and S. Zhou, "PHENIX Analysis Note 864, pi^0 and *eta* Single Spin Asymmetries with the Central Arm in $p^\uparrow + p$ collisions at 200 GeV,"

[108] K. Boyle, A. Bazilevsky, and A. Deshpande, "PHENIX Analysis Note 721, Final Results on the double helicity asymmetry (A_{LL}) in pi^0 production in polarized proton-proton collision at .s = 200 GeV from Run-6 and resulting constraints on the polarized gluon distribution,"

[109] RHIC Polarimetry Group. `http://www.phenix.bnl.gov/WWW/publish/shura/RSC/CNI/Run8Pol/`.

[110] C. Aidala, "PHENIX Analysis Note 293, Single-spin Asymmetry A_N in Neutral Pion Production from Run-02 pp Data,"

[111] M. Anselmino *et al.*, "Transversity and Collins functions from SIDIS and e+ e- data," *Phys. Rev.*, vol. D75, p. 054032, 2007.

[112] M. Anselmino *et al.*, "Update on transversity and Collins functions from SIDIS and e+ e- data," *Nucl. Phys. Proc. Suppl.*, vol. 191, pp. 98–107, 2009.

[113] O. Martin, A. Schafer, M. Stratmann, and W. Vogelsang, "Tranverse double-spin asymmetries for muon pair production in p p collisions," *Phys. Rev.*, vol. D60, p. 117502, 1999.

[114] Z.-B. Kang, "Single transverse-spin asymmetry in inclusive hadron production (Talk at Brookhaven Nucleon Spin Physics Summer Program)." `http://www-nsdth.lbl.gov/~fyuan/spin10/Zhongbo_Kang.pdf`, July 2010.

[115] E-906/SeaQuest Experiment, "Drell-Yan Measurements of Nucleon and Nuclear Structure with the Fermilab Main Injector: E906," 2006.

[116] PAX Collaboration, "Technical Proposal for Antiproton-Proton Scattering Experiments with Polarization," 2005. `http://www.fz-juelich.de/ikp/pax/public_files/tp_PAX.pdf`.

[117] J. Chiba *et al.*, "Measurement of High-Mass Dimuon Production at the 50-GeV Proton Synchrotron," *Proposal for measurement at JPARC*, 2006. `http://www.j-parc.jp/jhf-np/pac_0606/pdf/p04-Peng.pdf`.

[118] A. N. Vasiliev *et al.*, "New Polarization Program at U70 (SPASCHARM Project)," 2007.

[119] G. V. Trubnikov *et al.*, "Project of the Nuclotron-based Ion Collider Facility (NICA) at JINR," EPAC'08, 11th European Particle Accelerator Conference, 23-27 June 2008, Genoa, Italy.

[120] C. Adolph *et al.*, "COMPASS-II Proposal," 2010.

[121] L. Bland *et al.*, "Transverse-Spin Drell-Yan Physics at RHIC.," 2008. http://spin.riken.bnl.gov/rsc/write-up/dy-final.pdf.

[122] E. Aschenauer *et al.*, "Letter of Intent: Feasibility Test of Large Rapidity Drell-Yan Production at RHIC [collider mode]," http://www.bnl.gov/npp/docs/pac0610/Crawford_LoI.100524.v1.pdf.

[123] K. N. Barish *et al.*, "Measurement of Dimuons from Drell-Yan Process with Polarized Proton Beams and an Internal Target at RHIC," http://www.bnl.gov/npp/docs/pac0610/Goto_rhic-drell-yan.pdf.

[124] A. Vossen *et al.*, "First Measurement of the Interference Fragmentation Function in e^+e^- at Belle," 2009.

[125] Ruggiero, Rich, "PHENIX Drawing DB," December 2009. http://www.phenix.bnl.gov/~ruggiero/.